ROBUST MODAL FILTERING

FOR CONTROL OF FLEXIBLE AIRCRAFT

A Ph.D. Dissertation
Presented to
The Academic Faculty

by

Peter Suh

In Partial Fulfillment
of the Requirements for the Degree
Doctor of Philosophy in the
School of Aerospace Engineering

Georgia Institute of Technology
May 2014

ROBUST MODAL FILTERING

FOR CONTROL OF FLEXIBLE AIRCRAFT

Approved by

Dr. Dimitri Mavris, Advisor
School of Aerospace Engineering
Georgia Institute of Technology

Mr. John Burken
Controls Branch
NASA Dryden Flight Research Center

Dr. Daniel Schrage
School of Aerospace Engineering
Georgia Institute of Technology

Dr. Dewey Hodges
School of Aerospace Engineering
Georgia Institute of Technology

Mr. Martin Brenner
Aerostructures Branch
NASA Dryden Flight Research Center

Date Approved: January 03, 2014

For my family

ACKNOWLEDGEMENTS

I would like to take this opportunity to thank those special individuals who gave me invaluable advice and contributed to my work. My foremost and sincere appreciation goes to Dr. Dimitri Mavris, my thesis advisor for his course corrections and thoughtful input which shaped my dissertation. Special thanks to Mr. Steve Jacobson, Branch Chief of NASA's Dryden Flight Research Center (DFRC), who inspired the thesis concept. Gratitude is owed to Mr. Martin Brenner for confirming that the modal filtering approach was mathematically sound from the beginning. I would like to acknowledge thesis committee members Dr. Daniel Schrage, Mr. Martin Brenner, Mr. John Burken and Dr. Dewey Hodges for their suggestions and constructive comments.

I acknowledge Georgia Institute of Technology's Co-op program. With the help of Assistant Director of the Graduate Cooperative Education Program, Mr. Ken Little and Dr. Mavris I was able to work terms at DFRC gaining practical experience. The work I did and the people I met improved my career development path. It also readied me for challenging aerospace applications.

At DFRC I had excellent mentors. I acknowledge Mr. Yohan Lin, then chief engineer of X-43A, and Mr. Jamie Wilhite of DFRC for introducing me to digital avionics systems during a four-month tour of the Systems Branch in 2007. Many thanks are given to Mr. Joe Pahle who introduced me to practical aspects of classical and modern control theory during an eight-month tour of the Controls & Dynamics Branch of DFRC in 2009.

From January, 2011 to present, my mentors in the Controls & Dynamics and Aero-Structures Branches, Mr. Chris Regan, Mr. John Bosworth, and Mr. Marty Brenner have guided me through research into controls and aeroservoelasticity. Dr. Jack Ryan has

improved my understanding of mu-optimal control and spent time correcting my publications.

Others at DFRC supported the dissertation modeling effort. Dr. Chan-gi Pak and Mr. Alexander Chin have graciously developed the X-56A state space models for this work. They worked on getting them into a format which I required for this research.

Mr. Allen Parker, Mr. John Bakalyar, Mr. Patrick Chen, and Mr. James Moore, co-developers of the fiber optic measurement systems at NASA have all contributed to my understanding of distributed sensing in meetings and through email. Mr. John Bakalyar has been especially helpful by giving me data and thoughtfully answering my questions.

I thank the Co-op directors I have had the pleasure to work with. Special acknowledgements go to former Human Resources Director Ms. Patsy Smith, and Ms. Everlyn Cruciani who have my eternal gratitude for being directly responsible for my being able to stay at DFRC in extended co-op terms. Acknowledgements are given to NASA Dryden's astute librarians, Mr. Karl Bender and Mr. Freddy Lockarno, who were invaluable assets during the literature review.

Additionally, I am grateful to Dr. Sriram Rallabhandi, Dr. Scott Duncan and Dr. Jung-Ho Lewe at the Aerospace Systems Design Laboratory (ASDL), who inspired me with their vision for the future, challenging discussions, and wealth of knowledge. Finally, I would like to thank my dad for his review and final edit remarks.

TABLE OF CONTENTS

LIST OF TABLES

LIST OF FIGURES

LIST OF SYMBOLS

A	state matrix
A_b	balanced and reduced-order plant state matrix
A_o	rational approximation matrix
A_1	rational approximation matrix
A_2	rational approximation matrix
a_Δ	additive uncertainty signal
B	control input matrix
B_b	balanced and reduced-order input matrix
B_k^{nf}	bias on k^{th} sensor near the fiber break
B_1	disturbance input weighting matrix for balanced and reduced-order plant
B_2	control input matrix for balanced and reduced-order plant
b	current M-step
b_f	number of M-steps
C	state space output matrix
C_b	balanced and reduced-order plant output matrix
C_m	output matrix transformation for accelerometers
C_1	state-regulated goal matrix for balanced and reduced-order plant
C_2	output matrix for balanced and reduced-order plant
c	current concentration step
$\bar{c}$	mean aerodynamic chord
c_f	number of concentration steps
D	direct feed-through matrix
D^2	squared Mahalanobis distance

$D^2(\cdot)$	squared Mahalanobis distance of the argument
D_{ub}^2	upper bound of D^2
D_ω	frequency weighting matrix
D_{12}	control-regulated goal matrix for balanced and reduced-order plant
D_{21}	output noise weighting matrix for balanced and reduced-order plant
d	vector of deformations
$d(x_C, y_C, z_C, t)$	vector of deflections defined over x_c, y_c, z_c at time t
$\ddot{d}(x_C, y_C, z_C, t)$	vector of accelerations defined over x_c, y_c, z_c at time t
d_m	vector of virtual measurement deformations
E	rational approximation matrix of lag terms
e_k	finite residual of the k^{th} sensor
F	set of all faulty sensors
F_i	objective function for the i^{th} mode
F_l	lower linear fractional transformation
G	plant
G_{des}	design plant
G_{gust}	gust model
$G_I(s)$	class of all generalized plants with multiplicative input uncertainty
$G_O(s)$	class of all generalized plants with multiplicative output uncertainty
G_V	set of plants over a velocity range
$G_{wz}(K)$	matrix transfer function from disturbance to regulated output over all controllers K
$G_{wz}(s)$	matrix transfer function from disturbance to regulated output
g	structural damping coefficient
H	sensor projection matrix (also referred to as hat matrix)

H_∞	h infinity control type
h_{ii}	scalar elements of the i^{th} column and row of H
h_O	tuning constant for weight function of M-estimator
I	identity matrix
$Im(\cdot)$	imaginary part
$\hat{\imath}$	imaginary number
i_Δ	input uncertainty signal
J	generalized damping matrix
K	controller
K_c	control gain matrix
K_e	filter gain matrix
k	reduced frequency or non-dimensional frequency
k_m	system stability margin
k_O	threshold to identify a faulty sensor
L	global stiffness matrix
$\tilde{L}$	modal stiffness matrix
L_e	elemental stiffness matrix
l	row vector index
l_r	row index vector of Φ for reference deformations
M	global mass matrix
$\widetilde{M}$	generalized mass matrix
M_e	elemental mass matrix
M_{index}	indexing of modal coordinates
M_u	multiplicative noise input matrix
M_Δ	matrix transfer function

$MED(\cdot)$	median of the argument
m_r	column index vector of Φ for reference modal displacements
m_T	total mass of the wing
N	number of degrees of freedom in finite element model
$N(\cdot,\cdot)$	normal distribution with argument parameters
N_Δ	matrix transfer function
n_{AF}	airframe sensor noise
n_d	noise vector added to plant outputs
n_f	bias induced by simulated FOS failure on sensors
n_s	simulated fiber optic sensor noise
n_u	input control noise
O	lower linear fractional transformation of generalized plant and K
O_s	original sensor position before modal deformation
O_s'	original sensor position after modal deformation
$\overline{OP}$	line segment distance from point O to point P
$\overline{O'P'}$	line segment distance from point O' to point P'
o_Δ	output uncertainty signal
P	sensor location point
P_c	tuning constant
$P_f(x_C, y_C, z_C)$	position of fiber break
P_g	generalized plant
P_I	generalized plant with multiplicative input uncertainty
Pmm_i	percent modal mass of the total mass m_T for the i^{th} mode shape
$P_{nf}^s(x, y, z)$	positions of sensors in a radius r_{nf} upstream of the fiber break

P_O	generalized plant with multiplicative output uncertainty
P_+	sensor position on the fore side of original sensor before modal deformation
P'_+	sensor position on the fore side of original sensor after modal deformation
P_-	sensor position on the aft side of original sensor before modal deformation
P'_-	sensor position on the aft side of original sensor after modal deformation
$Proj_{\vec{u}(\overrightarrow{O_sP_+})}\overrightarrow{O'_sP'_+}$	projection of $\overrightarrow{O'_sP'_+}$ on unit vector in the direction of $\overrightarrow{O_sP_+}$
$Proj_{\vec{u}(\overrightarrow{O_sP_-})}\overrightarrow{O'_sP'_-}$	projection of $\overrightarrow{O'_sP'_-}$ on unit vector in the direction of $\overrightarrow{O_sP_-}$
$Proj_{\vec{u}(\overrightarrow{OP})}\overrightarrow{O'P'}$	projection of $\overrightarrow{O'P'}$ on unit vector in the direction of $\overrightarrow{OP}$
Q	left singular matrix W_o
$Q(k)$	generalized aerodynamic force matrix
$\tilde{Q}(s)$	rational function approximation of the generalized aerodynamic forces
q	vector of modal displacements
$\hat{q}(\tau)$	estimated modal displacements at discrete time τ
$q(t)$	vector of modal displacements at time t
$\dot{q}(t)$	vector of modal velocities at time t
$\ddot{q}(t)$	vector of modal accelerations at time t
q_{est}	estimated modal displacements from modal filter in simulation
$q_i(t)$	i^{th} modal displacement defined at time t
q_m	indexed modal displacements for input to controller
q_∞	free-stream dynamic pressure
R	diagonal matrix of lag roots
$Re(\cdot)$	real part
r	number of reference deformations
r_{nf}	radius of sensors affected near the fiber break

r_o	relative uncertainty magnitude at steady state
r_∞	relative uncertainty magnitude at high frequency
$(\cdot)_{ref}$	reference command of the argument
S	set of all sensors
S_g^c	set of good sensors in concentration step c
$S_g^{c_f}$	set of good sensors in the c_f concentration step
S_I	input sensitivity matrix
S_k	absolute number of σ_g away from μ_g for the k^{th} sensor
S_k^f	faulty sensor binary decision variable
S_{nf}	set of sensors upstream and near the fiber break
S_O	output sensitivity matrix
$S_{\infty c}$	solution of control algebraic Ricatti equation
s	Laplace variable
$s(x, y, z, t)$	strain measurement vector at time t
$\hat{s}(x_C, y_C, z_C, \tau)$	estimated strain at x_C, y_C, z_C, τ
$s_k(x_C, y_C, z_C, \tau)$	strain measurements defined over x_C, y_C, z_C at time τ
$s_k(x_C, y_C, z_C, t)$	strain measurements at defined over x_C, y_C, z_C at time t
$s_k^{af}(x_C, y_C, z_C, \tau)$	measured strain of k^{th} sensor after the fiber break
$s_k^{nf}(x_C, y_C, z_C, \tau)$	strain of k^{th} sensor in a radius r_{nf} upstream of the fiber break
$s_m(x_C, y_C, z_C, t)$	strain at measurement locations at time t
T	location vector
T_I	input complementary sensitivity matrix
T_O	output complementary sensitivity matrix
$T(\cdot)$	right-hand-rotation matrix

$(\cdot)^T$	transpose of argument
TE_{ref}	reference trailing edge deflection at wing tip
t	time
u	control signal vector
$u(t)$	vector of control signals at time t
u_d	reference unit vector of deformations and rotations
u_n	control signal noise
u_Δ	output to uncertainty block
$\vec{u}(\cdot)$	unit vector
$\frac{\partial u}{\partial x_l}$	derivative in axial beam deformation in coordinate direction x_l
V	sample estimate of population variance-covariance
V_{des}	design speed
V_∞	free-stream velocity
V-f	frequency versus velocity
V-g	damping versus velocity
v	input signal to controller
W	weighting
W_A	matrix of proper additive weights
W_c	controllability Gramian matrix
W_I	matrix of proper input weights
W_O	matrix of proper output weights
W_o	observability Gramian matrix
W_S	matrix of proper sensitivity weights
W_T	matrix of proper complementary sensitivity weights

W_u	matrix of proper control output weights
w	vector of disturbances
$w(t)$	vector of disturbances at time t
$w_g(t)$	gust velocity at time t
$\dot{w}_g(t)$	gust acceleration at time t
$w_i(s)$	weight functions on diagonals of W_I and W_O
w_k	sensor weight
$w_k(\cdot)$	sensor weight as a function of argument
X	explanatory or data matrix
X_k	k^{th} row of X
x	state vector of plant model
$x(t)$	state vector at time t
$\dot{x}(t)$	time derivative of $x(t)$
$\hat{x}(t)$	estimated states of balanced and reduced-order plant
$x_{act}(t)$	vector of actuator displacements, velocities and accelerations at time t
x_{AF}	vector of airframe states
$x_{AF}(t)$	vector of airframe states at time t
x_{AF}^{ref}	reference airframe states
$x_{as}(t)$	state vector of modal aero lags belonging to $x(t)$
$x_b(t)$	balanced and reduced-state vector of plant model at time t
$\dot{x}_b(t)$	time derivative of $x_b(t)$
x_C	Cartesian coordinate
x_{cg}	c.g. location of the aircraft in the x_C direction
x_e	vector of modal displacements
$x_e(t)$	vector of modal displacements at time t

$\dot{x}_e(t)$	vector of modal velocities at time t
$\tilde{x}_e$	estimated modal displacement states
$\hat{x}_e(\tau)$	estimated modal displacement state vector at discrete time τ
x_k	sensor data vector
x_l	uni-axial coordinate in a moving frame always in the direction of the SFOS layout
$x_{lag}(t)$	vector of aero lag states at time t
x_o	initial state at time 0
$x_q(t)$	state vector of modal coordinate displacements belonging to $x(t)$
$x_{\dot{q}}(t)$	state vector of modal coordinate velocities belonging to $x(t)$
x_u	un-deformed location of the aircraft nodes in the x_C direction
x_ϕ^i	deformed location of aircraft nodes for the i^{th} mode shape in x_C
Y	rational approximation matrix of lag terms
y	output sensor vector
$y(t)$	output sensor vector at time t
y_C	Cartesian coordinate in the y-direction
y_{cg}	c.g. location of the aircraft in the y_C direction
y_u	un-deformed location of the aircraft nodes in the y_C direction
y_ϕ^i	deformed location of aircraft nodes for the i^{th} mode shape in y_C
y_Δ	input to uncertainty block
z_{cg}	c.g. location of the aircraft in the z_C direction
z_C	Cartesian coordinate in the z-direction
$z(t)$	goal regulated outputs at time t
z_{KS}	goal regulated KS states
z_S	goal regulated sensitivity states

z_T	goal regulated complementary sensitivity states
z_u	un-deformed location of the aircraft nodes in the z_C direction
z_ϕ^i	deformed location of aircraft nodes for the i^{th} mode shape in z_C
α	angle of attack
β	angle of sideslip
γ	air density
Γ	diagonal matrix of singular values of J
Δ	structured uncertainty block
Δ_I	structured input uncertainty block
Δ_O	structured output uncertainty block
δ_i	i^{th} uncertainty
δV	change of velocity
$\delta\alpha$	change of angle of attack
$\delta\theta$	change in pitch angle
δx_C	scalar global displacement in x_C
δx_{cm}	forward change of aircraft's center of mass from trim
δy_C	scalar global displacement in y_C
δy_{cm}	side change of aircraft's center of mass from trim
δz_C	scalar global displacement in z_C
δz_{cm}	heave change of the aircraft's center of mass from trim
$\delta\theta_C$	scalar global angle about y_C axis
$\delta\phi_C$	scalar global angle about x_C axis
$\delta\psi_C$	scalar global angle about z_C axis
$\delta LWLE$	change in deformation at LWLE
$\delta LWTE$	change in deformation at LWTE

$\delta RWLE$	change in deformation at RWLE
$\delta RWTE$	change in deformation at RWTE
$\delta SW1T$	change in SW1T modal displacement
$\delta SW1B$	change in SW1B modal displacement
$\delta WF1R$	change in WF1R rotation
$\delta WF1L$	change in WF1L rotation
$\delta WF2R$	change in WF2R rotation
$\delta WF2L$	change in WF2L rotation
$\delta WF3R$	change in WF3R rotation
$\delta WF3L$	change in WF3L rotation
$\delta WF4R$	change in WF4R rotation
$\delta WF4L$	change in WF4L rotation
ε	measurement error
ε_k	k^{th} measurement normal error distribution
ε_{xx}	axial strain
ε_{xx}^{+}	axial strain measured on fore side of a sensor
ε_{xx}^{-}	axial strain measured on aft side of a sensor
ζ	viscous damping ratio
θ	pitch angle
$\vartheta(\cdot)$	arbitrary increase in Q distribution of squared Mahalanobis distance as a function of argument
Λ	diagonal matrix of eigenvalues
λ	vector of eigenvalues
λ_i	i^{th} system eigenvalue
μ	structured singular-value vector

μ_g	weighted mean of the residuals of sensors contained in $S_g^{c_f}$
μ_m	coordinate-wise population location
μ_n	mean of normal error distribution
ρ	spectral radius
ρ_∞	free-stream density
$\rho(\cdot)$	objective function of the arguments
Σ_m	population variance-covariance matrix
σ_g	weighted standard deviation of the residuals of sensors contained in $S_g^{c_f}$
σ_i	i^{th} Hankel singular value of the system triple (A, B, C)
σ_k	median absolute deviation
$\bar{\sigma}(\cdot)$	maximum singular values
σ_n	standard deviation of a normal error distribution
τ	discrete time
$\varphi(\cdot)$	derivative of $\rho(\cdot)$ and influence function
$\phi_i(x_C, y_C, z_C)$	i^{th} natural mode shape vector defined over x_C, y_C, z_C
Φ	deformation modal matrix, a collection of mode shapes, ϕ_i
ϕ	bank angle
ϕ_i	i^{th} natural deformation mode shape
Ψ	matrix of strain mode shapes, $\psi_i(x_C, y_C, z_C)$
Ψ_{FOS}	strain matrix defined at SFOS measurement locations
$\Psi_k(x_C, y_C, z_C)$	k^{th} row of strain modal matrix
ψ	yaw angle
ψ_i	i^{th} strain mode
$\psi_i(x_C, y_C, z_C)$	i^{th} strain mode shape defined over x_C, y_C, z_C

ψ_m	m^{th} strain mode
ω	natural frequency
:	total column vector index (i.e., all columns included)
$\mathcal{H}_\infty$	Hardy space norm
$(\cdot)^\dagger$	Moore-Penrose generalized inverse
$(\cdot)^{(b,c)}$	argument in the b M-step and concentration step c

LIST OF ABBREVIATIONS

AAW	active aeroelastic wing
Accel	accelerometer
AF	airframe
AFFDL	Air Force Flight Dynamics Laboratory
AFS	active flutter suppression
AFW	active flexible wing
AFWAL	Air Force Wright Aeronautical Laboratories
AGARD	Advisory Group for Aerospace Research and Development
ALDCS	Active Lift Distribution Control System
AoA	angle of attack
ARMD	Aeronautics Research Mission Directorate
ASC	active structural control
ASE	aeroservoelasticity
AW1B	antisymmetric wing first bending
AW1T	antisymmetric wing first torsion
AWBT	antisymmetric wing bending and torsion flutter
AWTC	aeroelastic wing tip controls
BACT	Benchmark Active Controls Technology
BFF	body freedom flutter
BFL	body flap left
BFR	body flap right
BWB	blended wing body
CCD	charged-coupled device
CM	constrained m-estimator

CME	concentrated modal estimator
DARPA	Defense Advanced Research Projects Agency
DAST	Drones for Aerodynamic and Structural Testing
DFRC	Dryden Flight Research Center
DGK	First letters of authors
DLM	doublet lattice method
DOF	degree of freedom
DR	deepest regression
EBM	equivalent beam model
EI	effective independence
EOM	equations of motion
ERA	Environmentally Responsible Aviation
EuRAM	European Research Aeroelastic Model
FAA	Federal Aviation Administration
FAR	federal acquisition regulation
FBG	fiber bragg grating
FCH	No translation (author has not defined yet)
FCS	flight control system
FEM	finite element model
FMCD	fast minimum covariance determinant
FOS	fiber optic sensors
FOSS	fiber optic shape sensors
freq	frequency
GAF	generalized aerodynamic force
GE	Gaussian efficiency

GLA	gust load alleviation
GM	generalized M-estimation
GPS	global positioning system
GR	generalized rank
GVT	ground vibration test
HALE	high altitude long endurance
HARW	high aspect ratio wing
HB	high breakdown
HFS	hot-film sensors
ICAO	International Civil Aviation Organization
I-FEM	inverse finite element method
IMU	inertial measurement unit
INS	inertial navigation system
KBF	Kalman-Bucy filter
KF	Kalman filter
LE	leading edge
LFT	linear fractional transformation
LMS	least median of squares
LQG	linear quadratic Gaussian
LQR	linear quadratic regulator
LQS	least quartile of squares
LTA	least trimmed sum of absolute deviations
LTI	linear time-invariant
LTS	least trimmed squares
LWLE	left-wing leading edge

LWTE	left-wing trailing edge
MAC	modal assurance criterion
MB	median ball
MBA	median ball algorithm
MCD	minimum covariance determinant
MCS	Monte Carlo Simulation
MD	modal displacement
MED	Median
MEMS	microelectromechanical systems
MIMO	multiple-input multiple-output
MLD	multivariate location and dispersion
MLR	multiple linear regression
MS	minimum state
MVE	minimum volume ellipsoid
NACA	National Advisory Committee for Aeronautics
NASA	National Aeronautics and Space Administration
NN	neural network
NP	nominal performance
NS	nominal stability
OLS	ordinary least squares
PI	proportional Integral
PSC	peak seeking control
RC	controls branch at DFRC
REWLS	robust and efficient weighted least squares
RFA	rational function approximation

RM	repeated median
RM	repeated median
RNN	recurrent neural network
RP	robust performance
RS	robust stability
RWLE	right-wing leading edge
RWTE	right-wing leading edge
SFOS	simulated fiber optic sensors
sim	simulation
SISO	single-input single-output
SMI	structural modal interaction
SOF	summation of forces
SP	short-period mode
SST	supersonic transport
SVD	singular-value decomposition
SW1B	symmetric wing first bending
SW1T	symmetric wing first torsion
SWBT	symmetric wing bending and torsion flutter
TDT	transonic dynamics tunnel
TE	trailing edge
UAV	unmanned aerial vehicle
Vel	velocity
VLM	vortex lattice method
WF	wing flap
WF1L	wing flap first left

WF1R	wing flap first right
WF2L	wing flap second left
WF2R	wing flap second right
WF3L	wing flap third left
WF3R	wing flap third right
WF4L	wing flap fourth left
WF4R	wing flap fourth right

SUMMARY

The work in this dissertation comprises aeroservoelastic simulation development, two modal filter design case studies and theoretical improvement of the modal filter. The modal filter is made robust to sensor bias. Studies have shown that the states estimated by the modal filter can be integrated into active structural control. The integration of modal filters into aircraft structural control systems is explored.

Modal filters require distributed sensing to achieve accurate modal coordinate estimates. Distributed sensing technology has progressed to the point, where it is being tested on aircraft such as Ikhana and the upcoming X-56A. Previously, the modal filter was criticized for requiring too many sensors. It was never assessed for its potential benefits in aircraft control. Therefore it is of practical interest to reinvestigate the modal filter.

The first case study shows that under conditions of sensor normality, the modal filter is a Gaussian efficient estimator in an aeroservoelastic environment. This is a fundamental experiment considering the fact that the modal filter has never been tested in the airflow.

To perform this case study a linear aeroservoelastic code capable of modeling distributed sensing is developed and experimentally validated. From this code, a computational wing model is fitted with distributed sensing. A modal filtering design methodology is developed and applied.

With distributed sensing and modal filtering feedback control is achieved. This is also compared and contrasted with a controller using state-of-the-art accelerometers. In

addition, new methods of active shape control are introduced for warping an aeroelastic structure utilizing the modal filter and control surfaces.

The next case study takes place in a realistic setting for an aircraft. Flexible aircraft bring challenges to the active control community. Increased gust loads, possibility of flutter, and off-design drag may detrimentally affect performance and safety. Aeroservoelastic tailoring, gust load alleviation (GLA) and active flutter suppression (AFS) may be required on future flexible air vehicles. It is found that modal filters can theoretically support these systems.

The aircraft case study identifies additional steps required in the modal filtering design methodology. Distributed sensing, the modal filter and modal reference shape control are demonstrated on the X-56A flutter-unstable simulation model. It is shown that control of deformations at potentially millions of points on an aircraft vehicle can be achieved through control of a few modal coordinates.

Finally modal filter robustness is theoretically improved and computationally verified. State-of-the-art modal filters have high bias sensitivity. In fact, this is so critical that state-of-the-art modal filters may never be certified for aircraft implementation. This is especially true within a flight critical control system. The solution to this problem is found through derivation of the robust modal filter.

The filter combines good properties of concentration algorithms with robust re-descending M-estimation. A new trim criterion specific to the strain based modal sensing system is derived making the filter robust to asymmetric or leverage point outliers. Robust starts are introduced to improve convergence of the modal estimation system to the globally optimal solution in the presence of 100s of biased fiber optic sensors.

CHAPTER 1

INTRODUCTION

The dissertation begins with a background on modal structures, filtering and control. Modal filtering is a method of estimating modes through some form of estimation. Due to technological barriers modal filters have not been adequately represented on aircraft. It is shown by way of recent developments in distributed sensing that modal sensing is a technology which must be reassessed. This is especially true for more flexible aircraft.

A simple example is given first, to demonstrate the properties of modal coordinates. This is followed by a background review on historical modal filtering methods and aircraft modal control. Next a discussion is given on the current state of distributed sensing and shape sensing. This is followed by development of dissertation research questions and the organization of the dissertation.

1.1 Background

The number of degrees of freedom (DOF) of an analytical structure is theoretically infinite. To approximate the continuous structure, the finite element is typically employed. This is done by discretizing the structure into elemental shapes of known mass and stiffness matrices. A buildup of local mass and stiffness matrices leads

to global mass and stiffness matrices. The global mass and stiffness matrices can be used to analyze the original complex structural model generally with good accuracy.

Mathematically, this is the same as approximating the continuous structure as a lumped system. In a lumped system, continuous mass and stiffness properties are lumped at discrete locations resulting in n DOF. The size of n can be on the order of millions for large complex structures [1]. Due to finite element model size, a reduced set of coordinates known as generalized coordinates or modal coordinates are typically employed for analysis.

The modal model of the larger system assumes that the deflection at all points of a structure in forced or unforced conditions is equal to a linear combination of an infinite number of mode shapes. Thus the deformation can be approximated by a reduced set of modal coordinates and mode shapes which dominate the response as in Eq. (1.1),

$$d(t) \approx q_1(t)\phi_1 + q_2(t)\phi_2 + \cdots + q_m(t)\phi_m \tag{1.1}$$

where $q_1(t), q_2(t), \dots, q_m(t)$ are modal coordinate scalars varying with time t and $\phi_1, \phi_2, \dots, \phi_m$ are constant boundary satisfying shape functions with dimensions, $n \times 1$.

By casting the structural equations of motion into a modal form, the number of degrees of freedom, n, reduces to m, where generally $m << n$ after modal truncation. Each mode shape corresponds to a particular natural frequency. The frequency and action location of environmental forces tend to determine what mode shapes will be excited. Thus, with careful consideration, certain mode shapes can be included in the modal modal and certain mode shapes can be ignored. The low frequency mode shapes tend to be excited more often and also dominate the response in most environments.

A computational example taken from the author's simulation model demonstrates this effect. Consider a model constructed of 100 finite elements with 300 DOF (assuming bending, torsion and vertical degrees of freedom (DOF) per node). Six mode shapes and corresponding modal coordinates are used to characterize the deflected shape of a cantilevered plate under a point load. Figure 1.1 shows the structure in its un-deformed shape at the beginning of the static force test.

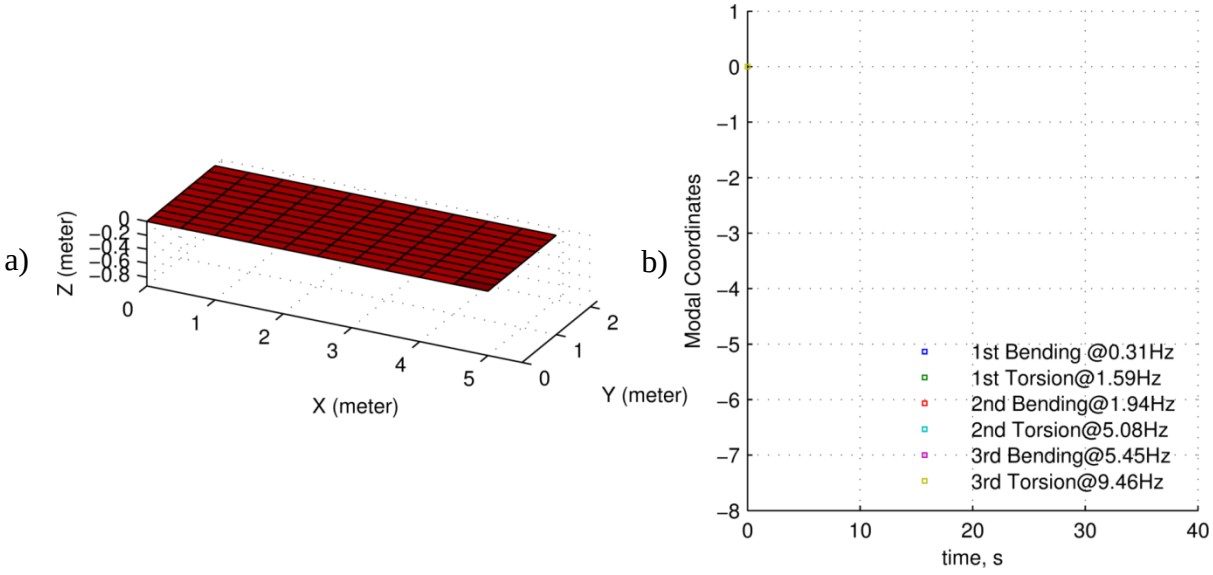

Figure 1.1: Plate Structure Model a) Undeformed Structure; and b) Modal Coordinates at Time 0.

Initially the structure is in static equilibrium with no external forces applied and thus, the modal coordinates start at zero at time 0. Any amplitude change in the modal coordinates represents a movement from the initial undeformed state of the structure.

The motion of the modal coordinates can be excited by an external force. This force can be represented through aerodynamic forces or other external loads. For demonstration of how the modal coordinates respond, a point force is applied to the corner of the structure.

The application of the force to the corner of the plate causes it to initially twist and bend as would be expected. The response can be mostly characterized by two modal coordinates, as shown in Fig. 1.2.

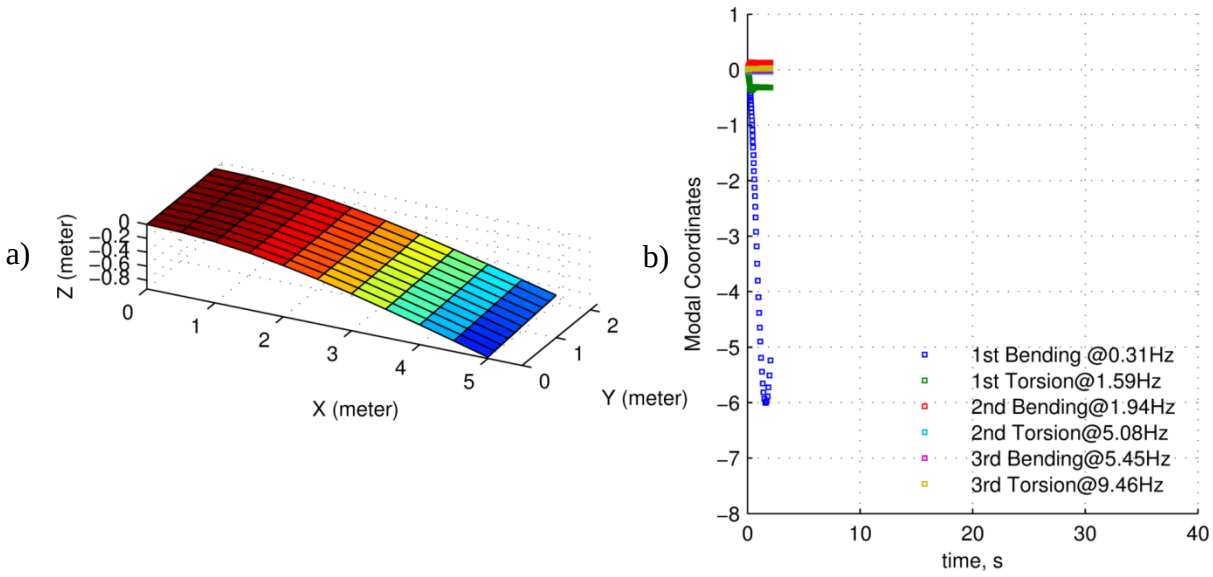

Figure 1.2: Deformed Structure a) Structural Deformation Initial Stage; and b) Modal Coordinates up to 2 s.

The two modal coordinates which moved substantially are: 1st bending and 1st torsion. It is not unusual that these particular coordinates responded to the point load. Lower frequency modes tend to dominate the response of most structures when excited with low frequency applied forces. Indeed, the bending and torsional coordinates tend to resonate at low natural frequencies of 0.31 Hz and 1.59 Hz respectively.

Note that the natural frequency of the bending mode is lower than that of the torsional mode. It is also interesting that the bending mode moves more than the torsional mode. The point force was applied at points of maximum modal deflections, for both mode shapes.

Therefore this demonstrates for this case how it is easier to move a lower frequency modal coordinate. The modes with higher frequencies move very little, showing only a small contribution to the deformation.

The modal coordinates also characterize the dynamics of a structure. They may be used to represent velocity and acceleration of a system. Therefore, they have a dynamic nature, which if controlled could be very useful in moving the shape of the structure.

Most structures have a certain amount of damping. In aircraft, this damping comes from natural structural damping as well as aerodynamic damping. For this cantilevered plate, ten percent damping is modeled in the system. When solving the equations of motion the surface develops a restoring force (also due to stiffness) and the structure moves back almost towards its starting point as shown in Fig. 1.3.

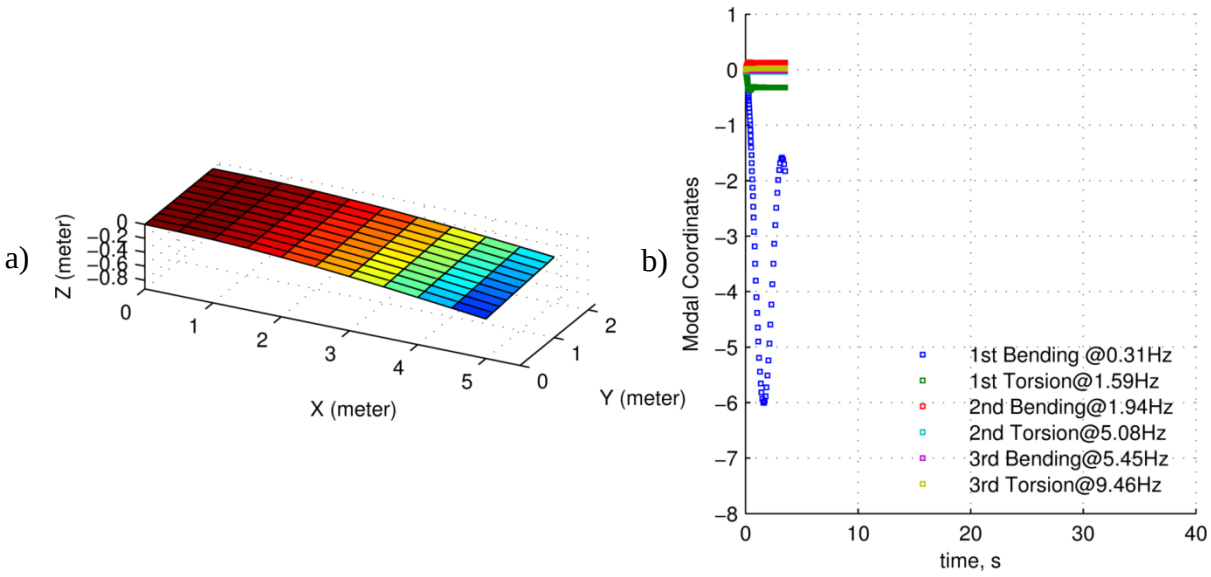

Figure 1.3: Deformed Structure a) Structural Deformation Intermediate Stage; and b) Modal Coordinates up to 3.5 s.

Modal motion is often characterized by vibration or oscillations. As the oscillations damp out, the steady state response is revealed. If the movements are from an applied external force, the structure will likely achieve a new equilibrium displacement state.

For this example, the structure moves to a static equilibrium under the forcing static point load. The modal coordinates or modal displacements move into steady-state positions. This is significant, because if these modal displacements can be controlled, then the structure can be forced approximately into a unique shape.

The steady state response of the cantilevered plate is achieved from the point load and the final position is mostly characterized by a bending and torsion type shape as shown in Fig. 1.4.

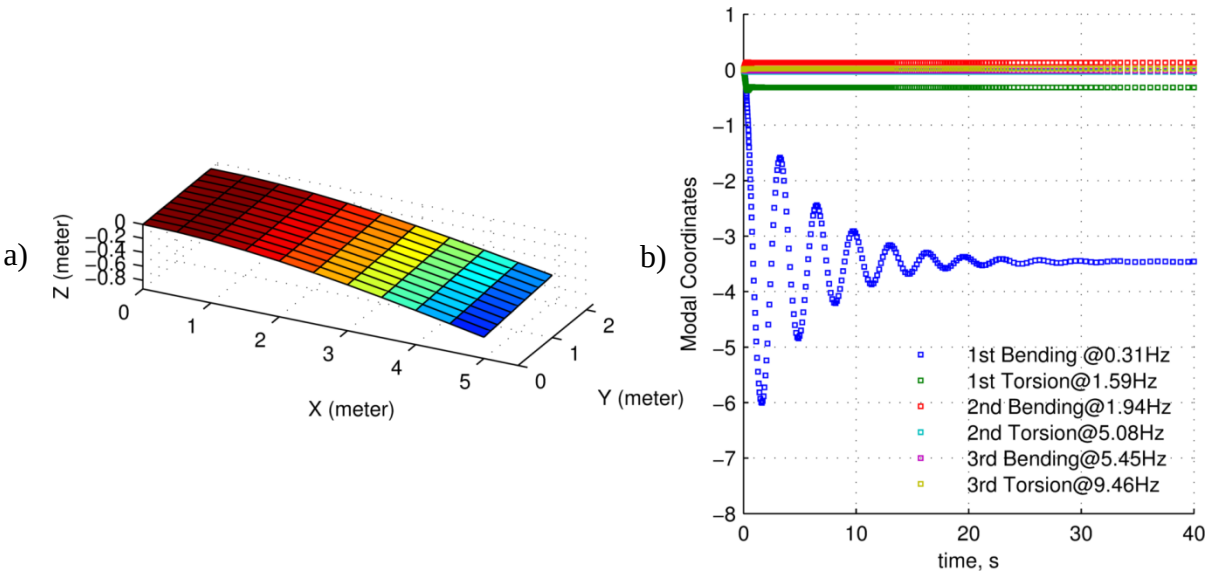

Figure 1.4: Deformed Structure a) Static Equilibrium of Structure Under Forced Condition; and b) Modal Coordinates up to 40 s.

The power of modal coordinates draws from the principle of superposition. This principle assumes that the contribution of each modal displacement to the system

response is strictly additive. With knowledge of only a few low frequency modal coordinates, a majority of the global response can be characterized. In a structure, the response can be associated with strain, loads etc. Thus with knowledge of modal coordinates, internal load and strain distributions can be approximated.

Aerodynamic forces and point load forces share a similar principle. They may be treated as external forces on the structure. Aircraft are essentially flying structures subject to most forces used to model any structure, but with external aerodynamic forces. It is true that aerodynamic forces change the modal frequencies and the mode shapes. But mathematically, these forces may be treated as external forces. Thus superposition of mode shapes must still characterize deformation even under aerodynamic forces. This is true only for small deformations, however.

In summary, modal coordinates allow for significant model reduction and improve analysis capabilities. As shown above, there were near to 300 DOF in the finite element model, but only two modal coordinates were required to characterize the motion of the system. If modal coordinates can approximate deformation, then commanding modal coordinates in flight control systems could be of interest.

1.1.1 Modal Filtering

The above example describes the significance of the modal coordinate. Estimates of modal coordinates can capture the contribution of both static and dynamic deformation in a structure. The literature has shown the modal coordinates can be measured and used for purposes of control, analysis and structural monitoring etc. Accounts vary on how the

modal coordinates should be measured. But one thing is clear: they are important and their measurement facilitates several aspects of structural control.

Indeed, Sumali et al. [2] stated that modal sensing (also known as modal filtering) has gained so much importance in structural dynamics that it is now seen as its own field within the structural discipline. Several of these methods are briefly reviewed here, taking note of their limitations. They include frequency based, dynamic state estimation, spatial and continuous modal filters. The following section introduces frequency based modal filtering.

1.1.1.1 **Frequency Based Methods**

For structures with distinct natural frequencies far apart, low and high pass filters may be used with single point sensors such as accelerometers to estimate local modal states [1]. The use of frequency based filtering has worked quite well in SISO and cascaded SISO type modal control configurations.

However, flexible structures may have interacting modes which need to be controlled. Furthermore, the frequencies of a structure tend to drift overtime and modal frequencies may appear close together in complex structures. It is also likely that production aircraft may experience variations which shift structural natural frequencies from one aircraft to the next and from one flight to the next [3].

S-plane filters also introduce additional dynamics into control designs. Indeed, in some instances, low pass filters at the output of a sensor induces dynamics into the plant and can lead to instability in feedback control systems [4]. Due to their limiting

application to SISO type control techniques for relatively rigid aircraft, frequency based methods are not reviewed further.

1.1.1.2 **Dynamic State Estimators**

Various types of dynamic state observers have been employed to estimate modal states [5], such as the Kalman Filter (KF) which is the optimal estimator in the presence of plant and sensor noise. These filters are made possible through the modal state space representation and truncation. However, due to modal truncation the introduction of the KF can induce observation spillover into the system potentially resulting in instability [6].

Observation spillover is a case where truncated modes show up in the response and provide a misleading representation of the controlled modal states. Consider the composite system [7] described by controlled modes, error and residual modes $(x_c, e_c, x_r)^T$, where $e_c = x_c - \hat{x}_c$. The governing equation is as in Eq. (1.2).

$$\begin{pmatrix} \dot{x}_c \\ \dot{e}_c \\ \dot{x}_r \end{pmatrix} = \begin{pmatrix} A_c - B_c G_c & B_c G_c & 0 \\ 0 & A_c - K_c C_c & -K_c C_r \\ -B_r G_c & B_r G_c & A_r \end{pmatrix} \begin{pmatrix} x_c \\ e_c \\ x_r \end{pmatrix} \tag{1.2}$$

The spillover terms can be identified in this formulation to result from the $K_c C_r$ term (observation spillover) and the $B_r G_c$ term (control spillover). The sensor output is contaminated by the residual modes and feedback control excites the residual modes.

It is possible to reduce observation spillover to a minimum in the observer by appending truncated modal states to the estimator. But doing so has the property of increasing the size and complexity of the resulting estimator and/or controller depending on the control synthesis technique.

One solution to this problem given by Sezak and Likins [8] was to design the KF with a modified measurement noise intensity matrix accounting for residual modes as in Eq. (1.3),

$$V + C_r V_1 {C_r}^T \tag{1.3}$$

where V is the standard measurement noise intensity matrix and C_r is the output measurement matrix for the residual modes and

$$E[x_r, x_r] = V_1 \tag{1.4}$$

This procedure tends to desensitize the reconstructed states to the residual modes, but the procedure works better if many sensors are available [7]. Many other methods and techniques have been given for both observation and control spillover, but are not reviewed here in detail.

Attention must also be given to the fact that a KF is only an optimal filter if the sensors are not significantly biased. Therefore if significant bias corrupts sensor measurements, the Kalman type filters will break down unless precautionary steps are taken. For practical modal filtering for an aircraft, a robust method is required.

1.1.1.3 **Spatial Filtering**

Spatial modal filters take a step towards robustness, with their ability to compress thousands of sensor measurements into a modal estimate. Spatial modal filters were first proposed by Meirovitch and Baruh [9] as alternatives to observer techniques. Modal filters represent the quasi-static estimation technique, and at any instant of time, the modal coordinates may be determined from motion variable information measured at that same instant of time. Meirovitch and Baruh's modal filter was derived strictly from the modal expansion theorem [10] as given as in Eq. (1.5),

$$\bar{d}(t) = \sum_{r=1}^{n} q_r(t)\bar{\phi}_r(x) \tag{1.5}$$

where the time varying modal states $q_r(t)$ may be determined by Eq. (1.6).

$$q_r(t) = \bar{\phi}_r{}^T M\bar{d}(t) \tag{1.6}$$

Calculation of the modal coordinates requires knowledge of the system mass matrix $M \in \mathbb{R}^{n\times n}$, the mass normalized eigenvectors $\bar{\phi}_r \in \mathbb{R}^{n\times 1}$ as well as deflections and rotations $\bar{d}(t) \in \mathbb{R}^{n\times 1}$ at every point n in the structure in either a continuous or distributed FEM sense. The method is exact if all of the displacements of the structure are known in real time.

However, distributed data is not always available and thus approximations of the DOF at unmeasured locations were applied by Meirovich and Baruh by the use of interpolation functions. The interpolation functions include Lagrange and Chebyshev polynomials [11], splines [12], as well as those used in the finite element method [13], among others. Assuming Rayleigh-Ritz guidelines are employed using global admissible interpolation functions the modal states were calculated by Meirovich and Baruh as in Eq. (1.7),

$$q_r(t) = \int_D M(p)\phi_r(p) \sum_{j=1}^{k}\sum_{s=1}^{k} \psi_s(p)\, U^{-1}\left[d(p_j) + v(p_j)\right] dD \tag{1.7}$$

where $M(p)$ is the mass distribution taken at point p, $\psi_s(p)$ is a globally admissible interpolation function evaluated at p, $U \in \mathbb{R}^{k\times k} = [\psi_1, \psi_2, \ldots \psi_s]$ is the matrix of interpolation functions evaluated at sensor locations p_j, k is the number of sensors points in the structure, p_j is the sensor point location, $v(p_j)$ represents zero-mean Gaussian,

independent, and uncorrelated stochastic noise, and D is the domain of the physical system and the eigenvectors of the system ϕ_r.

Meirovitch and Baruh's formulation depends upon having as many admissible interpolation functions as sensors, in order to take an inverse. Note that an admissible function is an arbitrary function satisfying all the geometric boundary conditions of the eigenvalue problem and are differentiable (to a specified order) over domain D.

Hence, this method only applies to simple structures where structural properties can be analytically defined, such as a simple plate/beam/truss etc. Meirovitch and Baruh also suggested the use of the finite element method to apply the method to more complex structures. In the finite element sense, the modal coordinates may be evaluated by breaking the domain D into smaller sub-domains $D_t, t = 1..T$. This represents a slightly more practical approach for larger and more complex structures with varying geometry.

Modal coordinate calculation with the finite element method is analytically represented as in Eq. (1.8),

$$q_r(t) = \sum_{t=1}^{T} \int_{D_t} M(p)\phi_r(p){L_t}^T \left[d^t(p_j) + v^t(p_j)\right] dD_t \tag{1.8}$$

where L_t is a vector of interpolation functions for element D_t, $d^t(p_j)$ is the measured deflections on the t^{th} element at sensor location p_j, $v^t(p_j)$ is the zero-mean Gaussian, independent, and uncorrelated stochastic noise for the t^{th} element at sensor location p_j

It is clear that the finite element build-up represents a more practical representation since it is not intuitive how to generalize global differentiable interpolation functions for a large complex structure such as an aircraft. However, the equation in this

form is not handy in its implementation, and would likely require quite a great deal of manual effort to set up.

Indeed, the continuous mass distribution is assumed to be known at every point on the structure and this may be uncertain in complex structures. This technique is also subject to errors such as that from: system parameter uncertainty, interpolation functions, eigenfunction error, and a finite number of sensors. In a study on the effect of these types of errors on independent mode control, it was shown that as the magnitude of modal filter errors increase, the stability of the closed loop vibration control system degrades [14].

Some improvements to this technique can be found in the literature in the work of Zhang et al. [15] and Shelley et al. [16]. They introduce two experimental approaches to modal filtering, which includes the frequency response function (FRF) method and the pseudo-inverse method.

The FRF method begins with the calculation of the reciprocal modal vectors by calculating the weighted sum of a number of FRFs which most closely approach the FRF of a single degree of freedom (DOF) system, in a least squares manner. With knowledge of the input forces and the reciprocal modal vectors, the modal coordinate calculation may be expressed in the time invariant (stationary) form as in Eq. (1.9),

$$q_r(t) = \int_0^t e^{\lambda_r(t-\tau)}\{\phi_r\}^T\{f(\tau)\}d\tau + \{\psi_r\}^T\{\phi_r^*\}\int_0^t e^{\lambda_r^*(t-\tau)}\{\phi_r^*\}^T\{f(\tau)\}d\tau \qquad (1.9)$$

where $\{\psi\}$ represents the r^{th} reciprocal modal vector, λ_r is the r^{th} complex eigenvalue corresponding to the r^{th} mode ϕ_r, $f(\tau)$ is the input forcing function vector, and $(*)$ indicates the complex conjugate. Shelley et al. tested this off-line modal filter technique on a five meter truss structure and achieved accurate modal acceleration results.

However, the primary purpose of the technique as indicated by Freudinger [17] is to complete the modal model and check the orthogonality of the modal vectors given in Meirovitch's work. Direct implementation of the method for modal sensing may be difficult without exact knowledge of the forcing functions in the system, and this application does not appear to be its sole purpose.

For real time mass and force independent modal filtering, Zhang et al. [15] proposed the pseudo-inverse technique given as in Eq. (1.10).

$$\bar{q} = (\Phi^T \Phi)^{-1} \Phi^T \bar{d} \tag{1.10}$$

This technique was tested upon the same 5 meter truss as in Shelley et al.'s work. In the tests, they chose to record 24 modes, and varied the number of accelerometer sensors for this task.

They found that the low frequency modes were estimated quite well but higher frequency modes were not. This was attributed to spatial aliasing, as the higher modes are not as spatially independent. Indeed, higher modes were also more coupled than lower order modes.

Rigid body modes were also not estimated accurately, due to errors in the modal matrix with respect to rigid body modes. They suggested that since the modal matrix Φ may consist of several hundred rows, that this technique was not practical without sensor reduction.

Modal filtering has also extended into adaptive works. An adaptive modal filtering scheme for controlling the Big Darby Creek bridge in Ohio [18] and a 4.5 meter vertically hung truss [19], in which the control input forces were assumed to be known and measured. The system depended upon a Luenberger observer for estimation of the true modal coordinate, which was used to adapt the modal filter vector. Further

adaptation was accomplished with a Least Mean Square (LMS) algorithm, which estimated an optimum weighting vector by minimizing a least mean square error term.

In Slater and Shelley's [20] health monitoring study, they proposed to use the adaptive filter in the presence of sensor faults. However the filter was only tested for a single sensor fault. It took nearly 5 seconds for the filter to adapt the system after the fault, which is too slow for critical control applications.

It has been shown that ordinary least squares (OLS) modal filter designs [16] require a large number of point sensors: typically at least two times the number of modes used to analyze the system. At a time when each sensor had its own hardware, cost and syncing issue it became paramount to minimize the number of sensors while achieving accurate modal coordinate estimates. Several sensor placement optimization strategies have been developed to support the modal filter implementation [21, 22, 23]. In any case, increasing the number of sensors has tended to improve modal filtering performance. In a test on a truss [16] the sensors were chosen for modal filtering from 8, 16 and 24 sensor locations. Each time they were selected from an optimal sensor placement technique. The modal filters with a higher number of sensors consistently outperformed the modal filters with fewer sensors.

However the modal filters to date have primarily relied on the assumption that the sensor errors are normal. The most robust modal filter relied on LMS. Both filters minimize an error function which increases without bound which increases without bound. Thus they will be highly sensitive to outlying sensor observations. Therefore OLS modal filters must be made robust for practical applications.

1.1.1.4 **Continuous Modal Filtering**

The modal filters, KFs and frequency based methods may all may be implemented with discrete sensor arrays, such as accelerometers, strain gauges, piezoelectric patches, etc. However, discrete sensor arrays have several shortcomings: firstly it complicates the hardware since each sensor requires its own electronics and secondly the discrete nature of the array can result in spatial aliasing [24].

Spatial aliasing [25] is the counterpart of the more well-known time aliasing and occurs: when the wave number k of one mode exceeds the number of sensors n regularly spaced in that direction, the sensor output appears as generated by a mode with a lower wave number $(2n - k)$. Elka and Bucher show that the use of piezoelectric patches and linear combiner [2] results in spatial aliasing at higher frequencies.

Current research is addressing the shortcomings of discrete sensor arrays with continuous distributed sensors [26, 27, 28, 29, 30] such as piezoelectric films and optical fibers. These methods are not reviewed here, but it seems that the future of modal sensing will likely include continuous type distributed sensing techniques for high frequency applications [30].

1.1.2 Modal Sensing Key Observations

A comparison of modal sensing techniques is summarized in Table 1.1. Continuous modal filtering and methods are not included as it is understood that continuous filters are used primarily to address the issue of spatial aliasing, which is not a major concern in aircraft modal control. The natural frequencies of aircraft modes are far below the frequencies where spatial aliasing could become a concern.

Table 1.1: Modal Sensing Table

	Positive	Negative
Frequency-Based	1) Simple to implement	1) Frequency dependent; frequencies shift over life of structure more than mode shapes
	2) Modal frequencies are known better initially	2) Requires very distinct natural frequencies in structure
	3) Good for SISO type applications	3) Difficult to implement in control system for MIMO systems with many states
Dynamic state estimator	• KF good for low signal to noise ratio feedback	1) Sensitive to uncertainty
	• Error asymptotic stability	2) Observation spillover issues
	3) Integrating effects on the estimates	3) Sampling rate dependent
	4) Good for MIMO applications	4) Sensor bias may lead to overall erroneous results
Modal Filters	1) Eliminates observation spillover	1) Large number of sensors required for accurate estimation
	2) Sampling rate does not affect accuracy of estimation	2) Cross-coupling error leads to inaccurate estimates of modal coordinates
	3) Designed independently of controller	3) Lacks integrating effects on the estimates
	4) Good for MIMO Applications	4) Sensor bias may lead to overall erroneous results

From Table 1.1, it is clear that frequency based techniques will only apply for SISO type applications of structures with distinct natural frequencies and thus, only state estimators and modal filters are considered. The modal filter techniques were proposed to eliminate observation spillover, but fell out of use due to the requirement for a large number of sensors and other issues listed in Table 1.1.

The modal filter is attractive because it relies directly upon the modal matrix. The same modal matrix can be used to design the state space equations for a structure. This includes the aircraft structure. The next section overviews some of the reasoning behind modal filtering and how it relates to control of structures.

1.1.3 Modal Filtering for Structural Control

Many control strategies in the structures field have been developed for modal coordinate feedback [9, 16, 31, 25, 19, 32]. Performance of integrated systems applied to active vibration and noise control can be substantially improved by the use of high quality modal filters [33, 30]. Several techniques have emerged making use of discrete sensor arrays and include the modal filter [15] and the dynamic state estimator [34].

In the structures community, it was found that controllers relying on state observers such as the KF tend to introduce observation and control spillover into the problem with non-collocated actuators and sensors [25]. Likewise flight controllers can induce structural mode interaction (SMI) or control spillover in aerospace. Typically spillover is rejected through notching structural frequencies, but this leads to additional phase lag.

Spillover can occur even though the margins of designing controllers with the LQG/LQR methods are substantial. According to Preumont [25], the margins provide good protection against delays and nonlinearities in the actuators. But he states that "they are not sufficient to guarantee against spillover instability, because the phase uncertainty associated with a residual mode often exceeds 60 degrees."

To address this issue, spatial modal filters were developed to remove observation spillover [9] relying upon projection and the important property of orthogonality among the mode shapes. Several types of spatial modal filters were demonstrated on a few test articles, but fell out of interest. They were criticized for requiring too many sensors and also suffered from spatial aliasing.

To date, a spatial modal filter has not been utilized in an aircraft for modal control. Nevertheless, the structures community has continued research into modal filters since the early 90s. This has resulted in unique solutions to address effects of spatial aliasing with continuous distributed sensing, such as piezoelectric films and fiber optics [26, 27, 28, 29].

Enough background material and testing on modal filtering has been accomplished to make it a prime candidate for aircraft implementation. The question is where modal filtering fits into the aircraft control paradigm. This really depends on what the modal filter brings to the table. A brief review of aircraft modal control is given in the following section.

1.1.4 Aircraft Modal Control

Modal control of aircraft is not a new topic. That is not to say that a spatial modal filter has been used for control feedback in an aircraft. For the most part, output feedback and state feedback control has seen various experimental applications. Some of the aircraft which have been used for this purpose include the B-2, YF-17, F-4F, B-52 and Boeing SST [35, 36, 37, 38, 39, 40]. Historically, flexible motion suppression controllers have relied upon point sensors, frequency filters and/or estimators for control feedback [41, 42, 43]. But few of these methods have seen production level aircraft testing.

The experimental control techniques fall under various classes of classical, modern and adaptive methods. Classical approaches seemed to be taken early on, followed by a few MIMO methods. Estimators for MIMO control design have often taken the form of Kalman-Bucy Filters [44] and corresponding discrete Kalman Filters (KF), accompanied by significant control order reduction. Even less adaptive methods have been experimentally flown. Much of the analysis and control design relied primarily on the fact that the flexible aircraft may be cast into modal form. The major difference between a structure on the ground and one passing through the air is that the modes are coupled through aerodynamic forces for an aircraft [45].

Modal sensing and modal control is still a very relevant topic today. NASA has announced their next X-plane [46], which turns out to be a flexible aircraft with aeroelastic instability within its flight envelope. The purpose of the program is to demonstrate robust flutter suppression using modern technologies. To this end, it will carry onboard distributed sensing capabilities and have multiple control surfaces dedicated to flutter suppression. NASA's prototype flutter testing aircraft, the X-56A

inspires renewed interest in modal sensing for modal control applications. Primarily, this is because of the onboard distributed sensing systems.

Recall that modal filters fell out of favor due to the requirement of many (potentially 1,000s) of sensors. The need to reassess the modal filter's utility becomes quite obvious as distributed sensing is actively being tested.

The next section gives the reason for why modal filtering must be reassessed for aircraft implementation. The link is drawn between modal filtering and dynamic shape estimation. A brief overview of the emerging field of dynamic shape estimation is given below.

1.1.5 Dynamic Shape Estimation

With the advent of increased digital computing, distributed measurement systems such as fiber optic sensor (FOS) arrays have received flurried interest and work is ongoing. In particular, FOS multiplexed with FBGs may enable futuristic capabilities like intelligent vehicle highway systems and adaptive structures. The development of the FOS has been reported to be a major breakthrough in sensing technology [47].

Since the first demonstration of photosensitivity in fiber optic waveguides [48], fiber optics have seen many applications such as structural and material process control, adaptive structural positioning, chemical and biomedical processing and many other applications [31]. They have also been used to estimate loads [49].

The benefits of FOS over traditional strain gauges are many and include that they: have low electromagnetic sensitivity, have high signal to noise ratios, are lightweight and efficient, and cover a much larger sensing area than traditional sensors [50]. The

algorithms developed to process strains from wavelength changes are accurate and efficient. The process is based upon the strain to wavelength relationship as in Eq. (1.11),

$$\frac{\delta\lambda}{\lambda} = (1 - p_e)\varepsilon + (\alpha + \zeta)\Delta T + n\Delta P \tag{1.11}$$

where $\delta\lambda$ is the change in wavelength at a fiber bragg grating, ε is the flexural strain, ΔT is the change in temperature from the initial calibration, ΔP is the change in pressure from the initial calibration, p_e is the effective photoelastic coefficient, α is the attenuation coefficient, ζ is the thermooptic coefficient, and n is the Young's Modulus coefficient.

The strains processed from the fiber optic wavelength measurements may be further processed to achieve overall deflections (x,y,z) using simple mathematical techniques such as OLS [51] and Euler-bernoulli beam theory integration [52]. The FOS accurately predicts deformations on Ikhana aircraft's wing, as shown in Fig. 1.5.

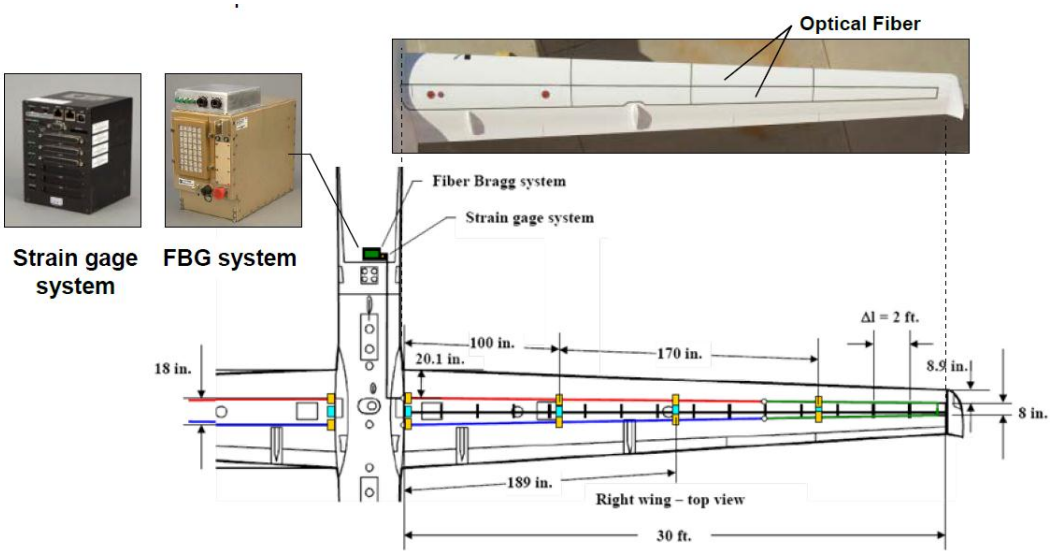

Figure 1.5: Fiber Optic Sensors with Fiber Bragg Gratings Laid on Ikhana Wing[1].

[1] Dr. Lance Richards, Allen R. Parker, Dr. William L. Ko, Anthony Piazza, Space Sensors and Measurements Techniques Workshop, Nashville, TN, August 5, 2008

Strain and shape are very useful information now available for control related studies. But control systems may also benefit from distributed acceleration measurements as well. Distributed acceleration is reaching technology readiness levels (TRLs) where they may be used on an aircraft, without introducing the noise and weight of standard accelerometers.

Microacclerometers designed with piezoelectric thin films were theoretically demonstrated on a FEM beam structure with good results [53, 54]. Indeed, microelectromechanical systems (MEMS) accelerometers based on piezo films have been machined to be less than the size of a penny with a similar thickness [55]. They have analyzed modes of a structure up to 45 Hz, which means they are certainly applicable for aircraft modal sensing. MEMS accelerometers have also been utilized on Lockheed's body freedom flutter vehicle for feedback in a flutter controller.

The Helios accident [56] is one inspiration for distributed sensing, as it could have been used to monitor the increasing wing dihedral leading up the accident. A common goal in the literature has been to determine the full dynamic deflection field of a structure in real time. This can serve multiple purposes and is most often linked with structural monitoring [57, 58, 59, 60].

A brief review of shape algorithms is given in the next section for comparison. These methods include the Euler-Bernoulli integration type, quasi-static strain-mode shape, and inverse-FEM. Primarily these methods are available to be used with distributed FOS data. Photogrammetry and the three-core fiber are also discussed.

1.1.5.1 **Integration Methods**

Several works have taken advantage of multiplexing capability of FOS with Bragg gratings. These works have utilized classical beam-bending theory to formulate displacement as a function of flexural strain [61, 52, 62]. Ko et al. [61] derives a form of the curvature-strain relationship for the non-uniform beam as in Eq. (1.12),

$$\frac{d^2w(x)}{dx^2} = \frac{\varepsilon(x)}{c(x)} \tag{1.12}$$

where $c(x)$ represents the half depth the beam at location x, $\varepsilon(x)$ is the measured bending strain at the x location along the beam and $w(x)$ is the vertical displacement along the beam

The tapered beam half depth and the bending strain may be assumed to be linear functions of x between the i^{th} and $(i-1)$ measurement stations. And the tapered beam may be divided into n sections with sectional length $\Delta l = l/n$. The following formulas result given in Eqs. (1.13) and (1.14).

$$c(x) = c_{i-1} - (c_{i-1} - c_i)\frac{x - x_{i-1}}{\Delta l};\ x_{i-1} < x < x_i \tag{1.13}$$

$$\varepsilon(x) = \varepsilon_{i-1} - (\varepsilon_{i-1} - \varepsilon_i)\frac{x - x_{i-1}}{\Delta l};\ x_{i-1} < x < x_i \tag{1.14}$$

After substitution of Eqs. (1.13) and (1.14) into (1.12) and integrating twice with respect to x a formula for the deflection of the i^{th} sensor station may be derived as in Eq. (1.15).

$$y_i = \frac{(\Delta l)^2}{6}\sum_{j=1}^{i}\frac{1}{c_{j-1}}\left\{\left[3(2j-1)-(3j-2)\frac{c_{i-j+1}}{c_{i-j}}\right]\varepsilon_{i-j}+(3j-2)\varepsilon_{i-j+1}\right\}+y_0+(i)\Delta l tan(\theta_0) \quad (1.15)$$

For a cantilever beam, the deflection y_0 and slope θ_0 at the built-in end are zero for all i. Forms of the bending angles at the i^{th} stations were also given but are not reviewed here. The cross-sectional torsion angle at any i^{th} station is given in Ko et al.'s as in Eq. (1.16).

$$\phi_i = arcsin\frac{y_i - y_i'}{d_i} \quad (1.16)$$

where y_i' is the deflection measurement precisely forward or aft of the measurement y_i and d_i is the chord-wise distance between the measurement stations. This method can be very useful for finding distributed rotations and deformations along high aspect ratio wings.

However, Ko's displacement method makes the assumption that the sensor error of all sensors on the FOS is normal and unbiased. If large strain bias is injected at any point in the algorithm, all remaining shape data after the biased sensor point must also be biased.

1.1.5.2 **Quasi-static strain displacement method**

Vibration mode shapes have been utilized in many works, to reconstruct the elastic deflection field [63, 64, 65, 66]. The strain/displacement mode shape matrices were used to form a quasi-static transformation matrix between strain and displacement. The primary assumption is the same used for modal transformations as in Eq. (1.17),

$$d(t) = \Phi q(t)$$
$$s(t) = \Psi q(t) \tag{1.17}$$

where $s(t) \in \mathbb{R}^{n\times 1}$ is the n dof strain vector, $d(t) \in \mathbb{R}^{n\times 1}$ is the n dof deformation displacement vector, $\Psi \in \mathbb{R}^{n\times m}$ is the strain mode shape matrix with m strain modes, $\Phi \in \mathbb{R}^{n\times m}$ is the displacement modal matrix with m displacement modes, and $q(t) \in \mathbb{R}^{m\times 1}$ is the vector of modal coordinates (equivalent for strain and displacement).

The deformations may be cast into the following form with a least squares approximation as in Eq. (1.18),

$$d(t) = [\Phi(\Psi^T\Psi)^{-1}\Psi^T]_m s_m(t) \tag{1.18}$$

taking note that the rank of $(\Psi^T\Psi)^{-1}\Psi^T$ cannot exceed the number of used strain sensors. Notice that the subscript m indicates measurements, so any rows in the modal matrices which are unrelated to the measurement DOF must be removed.

The displacement modal matrix may be calculated from the eigenvalue solution of the un-damped structural equations of motion in the usual way. In order to calculate strain mode shapes, the linear displacement equations of motion must first be cast into the strain generalized form through linear strain to displacement relationships [63, 67] before calculating the eigensolution.

One of the main disadvantages of the quasi-static strain-displacement method has been shown to be the noise and error components in the signal and structural model data. The modal matrices must include a large number of modes and many sensors are required for accurate solutions.

The Kalman Filter has been introduced to filter the modal measurement noise (derived from strain errors) in a recursive filtering step [68, 69]. However, the disadvantage of the KF in shape prediction is that it is highly sensitive to modeling errors,

as was shown by Treiber et al. [68] where a 1% thickness variation of the underlying mathematical model caused a tenfold increased deviation of estimation of the real shape.

As with integration methods, this method is also sensitive to strong bias in any single sensor. However, in this case, the estimates of "all" deformations will be biased. This is because OLS feature estimates are offset proportional to the maximum error bias in any sensor. The feature estimates in Eq. (1.18) are directly used to form estimates of all deformations.

1.1.5.3 **Inverse FEM for full-field reconstruction**

Whereas some works utilize model/structurally dependent vibration mode shapes to determine deflection, other researchers try to use strain-displacement relations directly. It can be argued that this is a more robust method, since its accuracy is not subject to the number of mode shapes retained in the modal matrices.

Several researchers are employing the material independent inverse FEM for full-field reconstruction [51, 70, 71]. In their original work, Tessler and Spangler constructed a Mindlin three-node, inverse-shell element with six conventional DOF at each node. They formed a least squares functional for the three-node element as in Eqs. (1.19)-(1.22),

$$\Phi_e^{\lambda}(d) = \|e(d) - e^{\varepsilon}\|^2 + \|k(d) - k^{\varepsilon}\|^2 + \lambda\|g(d) - g^{\varepsilon}\|^2 \tag{1.19}$$

$$\|e(d) - e^{\varepsilon}\|^2 = \frac{1}{n}\int_{A_e}\sum_{i=1}^{n}[e(d)_i - e_i^{\varepsilon}]^2 dxdy \tag{1.20}$$

$$\|k(d) - k^{\varepsilon}\|^2 = \frac{(2t)^2}{n}\int_{A_e}\sum_{i=1}^{n}[k(d)_i - k_i^{\varepsilon}]^2 dxdy \tag{1.21}$$

$$\|g(d) - g^{\varepsilon}\|^2 = \frac{1}{n}\int_{A_e}\sum_{i=1}^{n}[g(d)_i - g_i^{\varepsilon}]^2 dxdy \tag{1.22}$$

where $e(d)$ is the membrane strain measure of the element as a function of the kinematic variables d, $k(d)$ are the bending curvatures of the element, $g(d)$ are the transverse shear strains of the element, $e_i^{\varepsilon}, k_i^{\varepsilon}, g_i^{\varepsilon}$ is the measured membrane, bending curvature, and transverse shear strains, respectively at i inside the element ε is the measurement error and n is the number of sensors within the element boundaries.

The measurement strains are taken by putting the strain measurement sensors on the top and bottom of each shell element. The relationships of local coordinate derivatives between strain and displacement were formed for each type of strain as in Eq. (1.23).

$$\begin{aligned} e(d) &= L^m d \\ k(d) &= L^b d \\ g(d) &= L^s d \end{aligned} \tag{1.23}$$

Shape functions were derived for a triangular element, assuming the out-of-plane bend displacement of the element is assumed to be interpolated with a quadratic polynomial in the local element coordinate system. The in-plane local coordinate displacement functions may also be derived from shape functions and included into matrix N as in Eq. (1.24).

$$d = Nd_e, \qquad \left({d_e}^T = \{u_i, v_i, w_i, \theta_{xi}\theta_{yi}\}, i = 1,2,3\right) \tag{1.24}$$

This approach is a standard one used to form the element strain-displacement matrix in most finite element books such as *Understanding Finite Element Stress Analysis* [13]. Substituting the local coordinate displacement relationships d into the strain-displacement relationships: $e(d)$, $k(d)$, and $g(d)$, and taking derivatives in the local coordinate directions, the element strain to displacement relationship is derived as in Eq. (1.25).

$$K_e d_e = \varepsilon_e \tag{1.25}$$

By assembling the element matrices and vectors in the typical finite element assembly operation, the global matrices and vectors may be formed into a least squares problem. The OLS solution of the displacements for measured strains can be readily found. Rows corresponding to unmeasured strains must be removed in order to proceed with the calculation. Once the displacements have been found, it is a simple matter to then find the smoothed strains as well as the stresses [49] assuming material relations are available.

As with modal and integration methods, the inverse FEM technique for shape estimation is also subject to problems if even one sensor becomes strongly biased. Clearly a pattern of sensitivity to sensor bias is emerging in all of the reviewed works thus far.

1.1.5.4 **Photogrammetry**

Other methods of shape estimation are also being assessed in the aerospace community. Photogrammetry has been receiving interest recently for aircraft

implementation, due to their potential capability to estimate deflections from processed visual images. There are several camera setups available and one may use the single camera multi-view system, or single camera, single view, or multi-camera single view setups, etc. Each setup has its own pluses and potential drawbacks, but the single camera, single view seems to be winning out due to its simplifications of the collinearity equations.

Recently, the single camera, single view system was installed onto an F/A-18 for the purpose of measurement of deflections [72]. They demonstrated the capability to process the deflections of the aircraft for many frames of data, and also identified potential error sources. For improved observability during nonlinear LCO, NASA Langley decided to complement their accelerometer feedback in the Transonic Dynamics Wind Tunnel (TDT) with the intelligent videogrammetric measurement method [73].

The close range videogrammetric measurement method uses charged coupled device (CCD) cameras to calculate out of plane displacement at the reflective patches adhered to the surface of the wing [74]. The use of videogrammetry has also been applied to the measurement of flutter mode shapes [75]. They utilized the Modal Assurance Criterion (MAC) for comparisons between calculated and measured flutter mode shapes.

A photogrammetry procedure involves placing targets on the wing with known locations and solving the collinearity equations which map pixel coordinates (x,y) to three-dimensional vehicle coordinates in (X,Y,Z). A nonlinear least squares algorithm (linear for two cameras single view) may be used to solve for the Euler angles relating the different coordinate systems as well as the optimal camera location.

After this initial setup process, the deformations may be found by taking the difference in deflections from a reference picture. The deformation angles may be found through arcsine approximations with chord-wise opposing target deformations or least squares as suggested in Farrell et al.'s [72] work. In order to identify the targets well, the targets must be distinct from their surrounding surface (black targets on white surface etc.). Then the target (x,y) coordinates are found by employing computationally intensive image analysis methods on the current picture such as the edge-finding method.

Unfortunately, the image processing step makes the photogrammetry system in general a near-real or next-day measurement time method. However, real time processing of video imaging has been utilized in some applications with advanced edge finding algorithms (running at 25 Hz) in the Automated Aerial Refueling (AAR) project [76], and has even been applied to missile detection which would require high frame rates.

Photogrammetry is sensitive to many other interacting factors such as the geometry of the object, the camera locations, the number of images and image resolution, the exposure and contrast of the targets, the camera and lens characteristics and how the equations are solved [77]. A cloudy day or the location of the sun has impacts on the accuracy of the results, as the sensitivity of the edge-finding algorithms plays a factor here.

As the wing bends or twists, a target may dip out of sight of the camera and become invisible, especially due to low camera inclination angles (10-15 deg.) required for out-of-window installations. The area of the targets also increases with increasing distance to the camera(s). Thus, this method may have some resolution issues for HALE class vehicles.

Photogrammetry has been making headway in many aerospace implementations such as for 3d mode shape determination [78] and for deflection-load calculations developed by interpolating strain-load relations from ground load tests [79]. Another interesting technology which purely estimates shape is the three-core fiber introduced next.

1.1.5.5 **Three-core Fiber**

Research is also progressing further into fiber optic sensor technology at NASA. Langley researchers: James Moore and Matthew Rogge [80], as well as Dryden researchers are working on the three-core FOS. It is a mounting with three fibers instead of the usual one, with the usual multiplexing of strain sensing. The use of three fibers allows the neutral axis to be calculated between the fibers themselves instead of the structure to which they are adhered to. Preliminary studies show that the three-core FOS is able to capture deformation (x,y,z) from its un-deflected position in real time with good accuracy, without any knowledge whatsoever of the structure to which it is adhered to. However, accuracy issues have arisen when the fiber twists significantly. The following section summarizes some of the observations made for dynamic shape estimation.

1.1.6 Shape Sensing Key Observations

Shape sensing techniques are described in Table 1.2. Some are direct shape sensing methods and others rely on transformations. It was observed that shape sensing methods are categorically integration methods, strain-mode shape, inverse FEM and photogrammetry. Each method either relies upon or can support modal filtering.

Table 1.2: Distributed Shape Sensing Comparison.

	Positive	Negative
Integration Methods	1) FEM independent techniques available	1) Shape calculation error grows towards end of fiber due to dependence of current shape estimate on all previous strain estimates along fiber
	2) Out-of-plane deflections calculated accurately over very long distances (ie. Global observer aircraft wing span)	Biased sensors may cause estimates of deformation to become biased
	3) Possible to calculate all translational coordinate directions (x,y,z) for modal filter with tri-core fiber	
	4) Noise filtered through shape calculation	
Strain-mode shape method	1) Highly accurate shape estimation when enough modes are used	1) Strain-displacement matrix must be experimentally verified
	2) Could be utilized to directly estimate modal deflections from strain	Biased sensors may cause modal estimates to become biased
Inverse-FEM	1) Calculation of full-field deflection of a FEM model (6 DOF per node)	1) Strain-displacement matrix must be experimentally verified
	2) Material independent (No mass/stiffness knowledge required)	2) Potentially difficult to set up LS problem for complicated geometry, without toolbox
	3) No mapping to modal nodes required since DOF are directly calculated	Biased sensors may cause shape estimates to become biased
Photogrammetry	1) Strain-independent translational DOF calculations	1) Mostly out-of-window applications and generally low sampling rates
		2) Subject to a great deal of internal/external error sources in flight (a target might dip out of sight if camera incidence is low such as for out-of-window applications)

Table 1.2 shows that there are at least four major types of shape prediction algorithms and technologies. Integration methods are suitable for beam-like structures. The strain mode and inverse-FEM techniques are general deformation prediction methods. Photogrammetry is of interest, but quite a lot of uncertainty exists from the possibility of visual interference.

Since most structures are cast into the modal form, the strain mode shape technique is the most compatible with aircraft controllers. By commanding these modes, it may be feasible to achieve desired shapes, as is predicted in Eq. (1.18). The strain based methods are for the most part subject to strong bias if even one sensor becomes biased.

Since these methods require many sensors, the chances for sensor failure could potentially increase. Indeed this will be an important subject to address. The following section summarizes what was learned from overviewing modal filtering and shape estimation. Specific research objectives to guide the work in this dissertation are identified.

1.2 Research Objectives

Modal filtering is an exciting field but its potential has yet been realized. By controlling modal coordinates, one may control the shape of the vehicle.

To date, spatial modal filters have not been applied in an aircraft setting. Some practical applications have been demonstrated on plates, beams and truss like structures. So any application of a spatial modal filter to an aircraft will represent a first application.

The modal filter has received criticism. In some studies, it has been suggested that modal filtering relies upon too many sensors for accurate estimation. So the thinking has been to reduce and optimize placement of the number of required sensors for modal estimation and control. Indeed many individual sensors may be subject to a large amount of sensor wiring and cost.

But FOS multiplexed with Bragg gratings do not require individual wires connected to each sensor. Photogrammetry only requires lightweight targets placed at sensor locations. Current technological advances in distributed sensing suggest major improvements in implementation.

For example, if a FOS system uses 2,000 sensors this will have the same weight penalty to the aircraft as if it only used 1 sensor. The cost will not be significantly different either. There is very little limitation on FOS placement over the aircraft wing skin or under it. With restrictions lifted on distributed sensing, modal filtering must be reinvestigated for aircraft structural control.

But before doing so, the modal filter must first be tested in a bench test aeroservoelastic setting, because it has never been done before. If this works, the modal filter must then be tested on an aircraft model.

Assuming both case study results are positive, this still does not guarantee that a modal filter is practical enough for aircraft applications. All modal filters in experimental

testing today have a significant shared weakness. That is, they have a high sensitivity to sensor bias. Therefore, something must be done to shore up this limitation.

From the brief background and discussion, three research objectives are identified:

- **Investigate how modal filtering performs on an aeroservoelastic problem as a first application**
- **Investigate distributed sensing and modal filtering in the control system of an aircraft**
- **Improve upon the sensor bias limitations of modal filtering**

These objectives are broad, and will be used to formulate an overall research problem and research questions in the next Chapter. Before doing so, further work must be done in fleshing out aircraft aeroservoelasticity problems and how they have been addressed. This will help identify applications for the modal filter.

It is posited that research fields where modal filtering will have the most impact are active flutter suppression (AFS), aircraft performance improvement, and loads alleviation design. The next Chapter will address these issues in detail. The following section gives an overview of how this dissertation is organized.

1.3 Dissertation Organization

The first Chapter, “Introduction” lays out the foundation for why modal filtering should be pursued in aerospace and why it has not up till now. The next Chapter titled “Literature Review” reviews how modal filtering fits into the aircraft control paradigm by

identifying the state-of-the-art in aeroservoelasticity. After this Chapter, design work is completed to make initial assessments of the modal filter in an aeroservoelastic environment.

To this end, an aeroservoelastic code is developed in the next Chapter titled, "Simulation Development." From this simulation architecture, the design of the wing model modal filter based control system follows in the Chapter titled, "Wing Model." Further design work is required to verify use of the modal filter and thus a modal filter is designed and implemented on an aircraft in the next Chapter titled, "X-56A."

After applications of the modal filter are complete, it is determined that enough evidence has been gathered to support modal filtering in aircraft. But the modal filter is not robust, and must be made so for practical application.

From here, the dissertation moves into the theoretical and a survey of robust regression methods is completed in the Chapter titled, "Theoretical Foundation." This Chapter includes a down-selection of the available robust methods. Variations of these methods are used to derive a robust modal filter in the Chapter titled, "Robust Modal Filtering." This is followed by other applications of a robust modal filter in the Chapter titled, "Other Applications of Robust Modal Filtering."

The research up to this point is guided by the research questions identified in the Literature Review. The answers to these questions are formally given as well as how the Hypotheses have changed are given in the Chapter titled, "Conclusions." This Chapter also includes a summary of the accomplishments included in this dissertation as well as how someone picking up from where this research leaves off should proceed. A flowchart representing the detailed organization is given in Fig. 1.6.

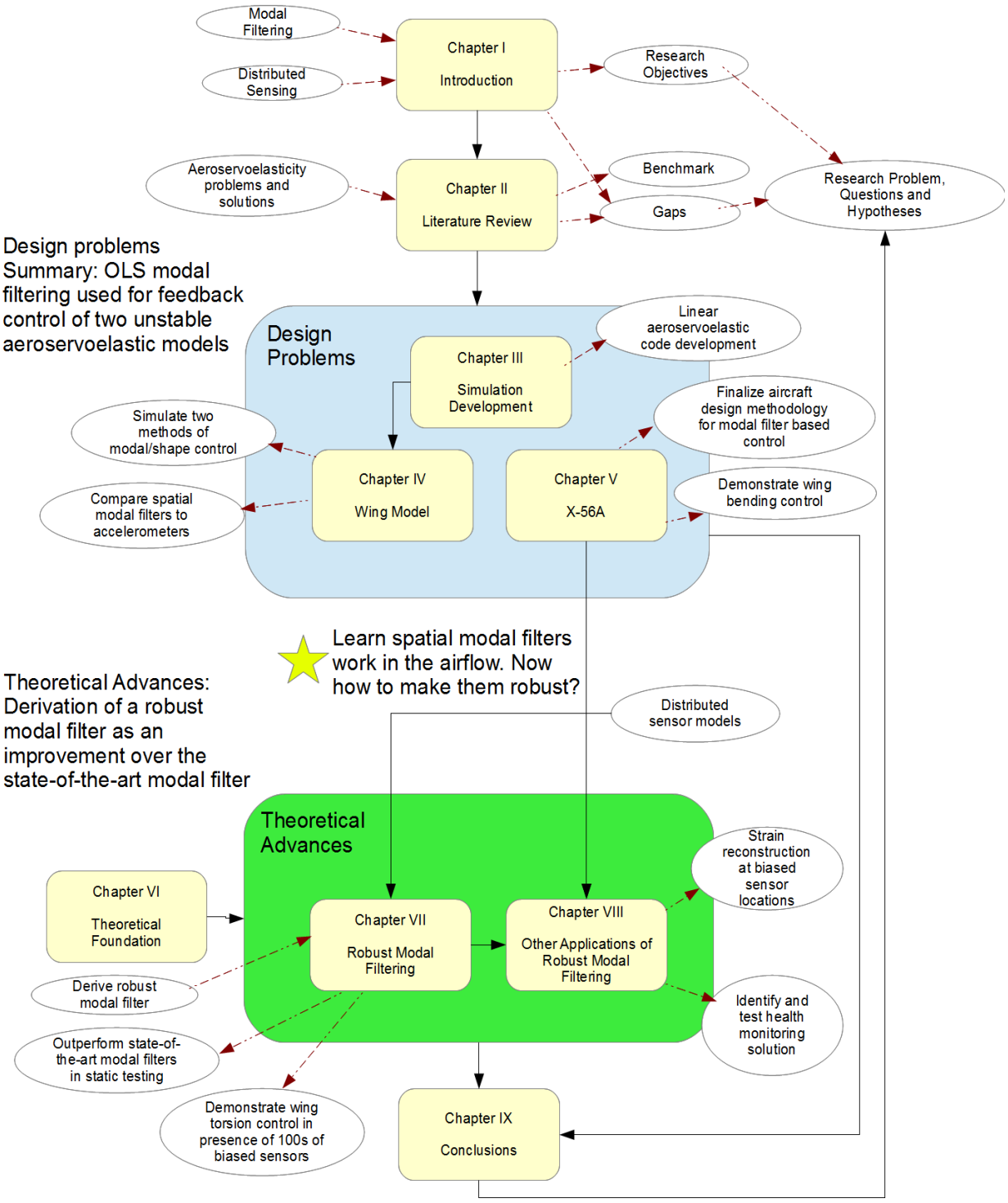

Figure 1.6: Dissertation Overview.

CHAPTER 2

LITERATURE REVIEW

The Introduction hinted at a link between modal coordinates and aircraft aeroservoelastic models. The research objectives require investigation of this link. In this Chapter, the relationships are identified through a brief literature review and cited mathematical models.

In search of the modal filter's niche problems in aeroservoelasticity are overviewed. Some of the major problem or improvement areas include flutter suppression, aircraft performance improvement and loads alleviation design. By reviewing these areas, benchmarks and gaps are identified. Using identified benchmarks and gaps and research objectives, the research problem, research questions and corresponding hypotheses are posed. The first section begins with an introduction to the most notorious aeroservoelastic problem, flutter.

2.1 Flutter Suppression

Paramount issues surrounding a flying structure include: flutter, modal vibration, hazardous maneuver loads and gust loads, wing buffet and limit cycle oscillations [81]. Flutter is listed first because it is perhaps the most safety critical issue in aerospace. There is so much concern surrounding flutter, that control of flutter is only conducted within the

context of aircraft experimental control studies. To date, commercial or military aircraft simply do not fly past the flutter boundary in the flight envelope. It can be postulated, that this is because the methods of flutter control used today are not to be relied upon with 100% confidence. Indeed this is why control of flutter is still an open problem.

The methods used to experimentally control flutter are reviewed in the following sections. Discussion is given on passive, single input single output (SISO) and multiple input multiple output (MIMO), and adaptive methods as well. Finally an introduction to aeroservoelastic modeling is given, as it characterizes the importance of the modal coordinates. The following section introduces the nature of flutter in aircraft.

2.1.1 A Brief Introduction to Flutter

Flutter is notoriously hazardous due to its ability to cripple or destroy aircraft. Flutter tends to occur when two or more structural modes couple and begin an increasing two way energy transfer with the air stream. When the energy input into the structure is greater than that which can be dissipated by structural damping, flutter occurs [82]. This is often physically characterized by very dangerous structural oscillations which lead to structural failure.

In order to reduce the possibility of flutter, the flutter speed must be known so that pilots do not accidentally cross the flutter boundary. For a proper safety margin, the flutter speed must be 1.2 times the diving speed according to FAR 25.629 [83]. Regulation on not crossing the flutter speed may someday change, however, especially with increasing fuel efficiency requirements. The following explains this logic.

Due to N+3 generation aircraft requirements new technologies and aircraft concepts are being introduced. NASA has proposed a 70% fuel burn reduction in future concept aircraft by 2025 [84]. From the suite of technologies available to meet this fuel burn objective, structure reduction or removal is of interest. This is related to removing structures in the wings and designing for strength instead of stiffness. However, by reducing stiffness, the modal frequencies will likely shift closer to rigid body frequencies. This can increase the possibility for flutter and cause it to appear at lower speeds.

Thus it appears that energy-efficient air transports, in order to realize the full benefits of weight savings technologies, may require active systems for flutter suppression [42]. This is not a new realization. Research into active control of flutter for weight savings has been a research priority for decades. But one must ask, "why are flutter suppression systems not available in almost every aircraft today?" The short answer is likely due to the lack of robustness of the controllers. There is a reason supporting this answer which will be elicited in the following sections. It is linked with what has historically been controlled, the point sensor not the true fluttering states. First a discussion is given on passive flutter suppression methods in the following section.

2.1.2 Passive Flutter Suppression

Historically in relatively stiff aircraft, notch filtering has been relied upon to suppress marginally stable flexible modes from interference/coupling with the control system. Unfortunately due to the variation of flexible modal frequencies in most aircraft from aging, maintenance, etc., notches were made excessively wide to consider modal

frequency uncertainty during operations. This had the effect of reducing phase margin, as well as a gain margin reduction to meet phase requirements.

This is a well-known and documented issue. Within fighter aircraft, improvements have been sought using phase advance filters and structural coupling/notch filters designs [85]. Reductions in the size of the notch filters have been made by some with adaptive notch filtering. [86].

For more flexible aircraft, notch filtering will become more difficult to implement due to increased performance degradation in the control system. Indeed, some researchers suggest that flexible modes should be controlled inside the flight control system of flexible aircraft and should no longer be suppressed with notch filters [87, 88]. This is absolutely true if the modes are unstable.

For unstable modes, flutter suppression may be achieved by adding mass ballast and structural stiffening [89]. However, these methods add weight, impacting performance. Trade studies performed by Boeing indicate that weight penalties as much as 2 to 4 % of total structural weight may be required to solve potential flutter problems [90]. Indeed, this spurred a steady amount of research into active flutter control in lieu of passive flutter methods on aircraft such as the SST, C-5A, 747, B-1, F-4, YF-16 and the Advanced Technology Transport [91].

2.1.3 SISO Flutter Suppression

Since the early 1970s, researchers have been developing algorithms to suppress flutter. One of the first useful approaches seems to be that of Nissim, who utilized the

aerodynamic energy concept method [37, 92, 93]. The idea was to suppress flutter by removing energy from the air surrounding the structure.

Other works utilizing classical SISO control methods were implemented such as that by Abel et al. [94]. Around the same time, controllers utilizing modern control theory were being developed [95]. Some of these implementations are discussed in the following section.

2.1.4 Modern Theory Flutter Suppression Methods

Many modal based controllers have been developed with various modern control techniques such as Linear Quadratic Gaussian (LQG) Theory [96], and Eigenspace methods [97]. Newsom's numerical study [98] on a high-aspect-ratio cantilever wind-tunnel wing model using full state linear feedback Linear Quadratic Regulation (LQR) showed that one could theoretically increase flutter dynamic pressure by at least 50%.

Recently, an LQG-based controller has been successfully tested on the Multi-utility Aeroelastic Demonstrator (MAD) known as the Multi-Utility Technology Testbed (MUTT) [99, 82]. The body freedom flutter (BFF) vehicle representing the full scale SensorCraft shown in Fig. 2.1 made use of its control system to suppress BFF using accelerometer feedback.

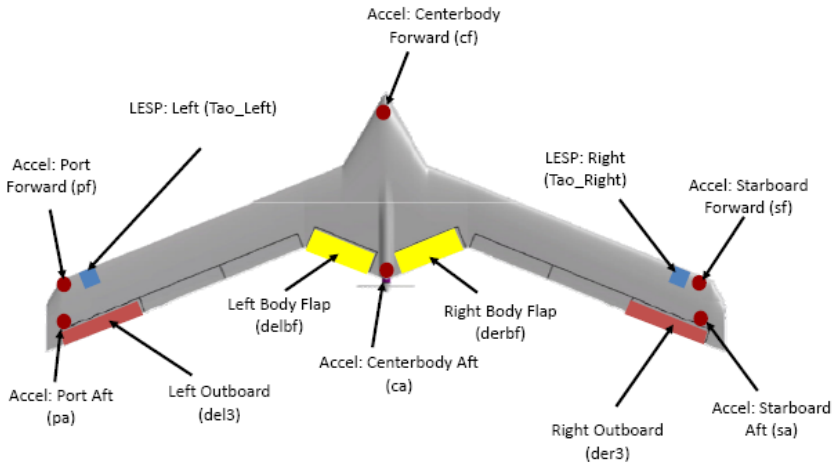

Figure 2.1: Multi-Utility Aeroelastic Demonstrator (Courtesy of Lockheed Martin).

The primary issues linked with state space methods is robustness. Most controllers are model based and therefore if the model is wrong, the controller may fail. If flutter occurs outside the predicted flutter speed region, the flutter suppression controller may not respond at all [100]. In fact, the variations in modal frequencies may lead to coupling of higher order modes [101] and flutter may appear at different speeds and with varying characteristics.

These problems are predicted to become more serious in production aircraft, which must undergo aging and maintenance. Presently, uncertainty is being addressed with advanced control techniques such as with H_∞ control [102] and adaptive methods. H_∞ control guarantees stability for specified disturbances making it a desirable solution for robustness. More advanced control such as μ-optimal control also guarantees stability for structured uncertainties and disturbance criteria [103]. The next section discusses the importance of control order reduction.

2.1.5 Control Order Reduction

Because of the superposition assumption in MIMO systems, the model order may become quite large. In a comparative paper published in 1990, Nissim [93] suggested that the SISO aerodynamic energy method should be used as an alternative to modern control theory based aeroservoelastic controllers which have a plethora of states, high sensitivity to modeling errors, and may be inaccurate at different flight conditions.

Proponents of modern control theory have developed several techniques to support practical implementation. The improvements are primarily through control law reduction [104, 105, 106, 107, 95, 108].

Order reduction is typically a process of retaining only the most important DOF of a system design, designing the reduced order controller from the reduced state space and then testing it on the larger system. However these techniques assume a very good model is available.

Order reduction is often related to the amount of interaction in a system. A controller which is focused on controlling all of the modes will be significantly more coupled than one which controls only the important modes. Order reduction might be significantly improved by modal filtering.

2.1.6 Adaptive Control

If one cannot guarantee robustness due to poor models, then adaptation may be the preferred route. Because flutter speeds change due to mass and stiffness variations, the academic community has been increasingly moving towards adaptive methods in

flutter control. Indeed, artificial intelligence in flutter control seems to be making headway as it proliferates into engineering spheres [109].

Fiber optic sensors with fiber Bragg gratings and piezo actuators placed near the wing root have also been applied to flutter control via a neuro-adaptive algorithm on a swept 330 mm span swept wing model [110]. The system control architecture for this study shown in Fig. 2.2 may be beneficial for its applicability to a wide range of conditions possibly adapting to uncertainty.

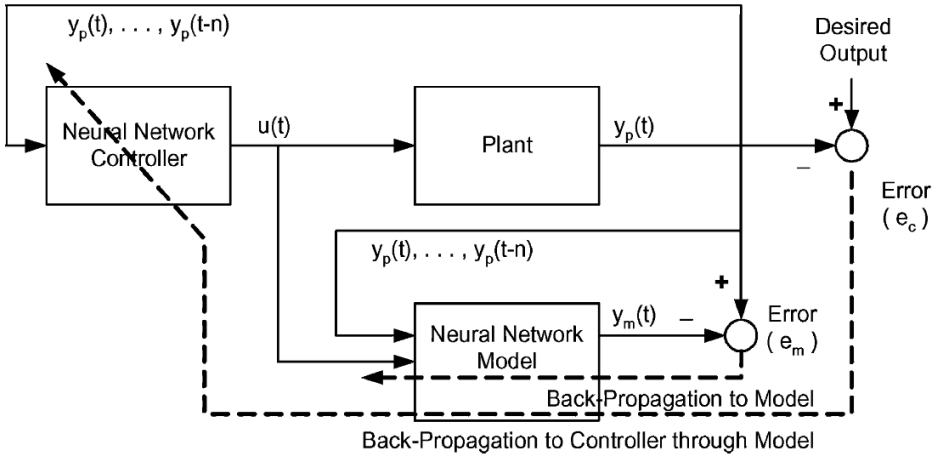

Figure 2.2: Neuro Adaptive Controller for Active Flutter Suppression.

The concept of this adaptive strategy is that it both learns changes in the plant and also adapts the controller to the varying plant. By adapting to both plant and controller, it is more likely to be applicable over the life of the vehicle. However, there are absolutely no guarentees on its robustness due to the use of the intractable neural network. There are many others pursuing these strategies however.

Active adaptive aeroelastic control has been approached by Scott and Pado [111] on the BACT model using a static NN. A nonlinear adaptive aeroelastic control synthesis technique [112] was proposed on a 2-d airfoil. Flutter control [113] has been achieved

with self-learning Recurrent Neural Networks (RNNs), which add feedback connections to classical NNs and use internal states that develop internal dynamics. A recent adaptive flutter suppression system based on the RNN was applied to a three-surface transport aircraft [114]. Model based reference adaptive control has also been applied using TE and LE control surfaces in a numerical simulation [115].

Many advanced adaptive techniques are being developed, but it will likely be difficult to certify them on future aircraft. This is primarily due to the harsh consequences of controller failure and a general distrust of adaptive concepts. Thus classical, modern and robust control concepts will likely remain an industry norm for some time.

2.1.7 Aeroservoelastic Modeling

Aeroservoelastic modeling is an integral step in the development of most non-adaptive modal based flutter controllers. It is expected that here, will be found the mathematical link to modal filters. This search begins with the aeroservoelastic equations of motion.

The formulation of the aeroservoelastic equations of motion has been addressed many times in literature [116, 117, 118, 119]. The unified formulation [120] developed by ZONA Inc. captures flexible vehicle rigid body interactions through the use of stability derivatives. Important platform specific choices must be made in dealing with rigid body and elastic interactions, as well as aerodynamic modeling. For mostly rigid aircraft, the mean axis equations [121] remove the inertial interactions of rigid body modes and elastic modes, so that only aerodynamic coupling is present.

The mean axis constraints assume that the change in inertia due to elastic deflection is negligible and also require that the modes are orthogonal to the mass matrix and to each other. Another requirement is that the modal deflections remain small. This helps to maintain the assumption that the deflection may be formed from a linear combination of modal displacements [122]. An example of the state space formulation is given here by Pototzky [123] as in Eq. (2.1),

$$\dot{x} = \begin{Bmatrix} \dot{x}_1 \\ \dot{x}_2 \\ \dot{x}_3 \\ \vdots \\ \dot{x}_6 \end{Bmatrix} = \begin{bmatrix} 0 & I & 0 & \dots & 0 \\ -\widehat{M}^{-1}\big(\widehat{K} & \hat{C} & \lambda I & \dots & \lambda I\big) \\ 0 & A_3 & -\beta_1\left(\frac{2V}{\bar{c}}\right) & 0 & 0 \\ \vdots & \vdots & 0 & \ddots & 0 \\ 0 & A_6 & 0 & 0 & \beta_4\left(\frac{2V}{\bar{c}}\right) \end{bmatrix} \begin{Bmatrix} x_1 \\ x_2 \\ x_3 \\ \vdots \\ x_6 \end{Bmatrix} + \begin{bmatrix} 0 & 0 & 0 \\ -\widehat{M}^{-1}\big(\widehat{K}_c & \hat{C}_c & \widehat{M}_c\big) \\ 0 & A_{c1} & 0 \\ \vdots & \vdots & \vdots \\ 0 & A_{c4} & 0 \end{bmatrix} \begin{Bmatrix} u_c \\ \dot{u}_c \\ \ddot{u}_c \end{Bmatrix} \tag{2.1}$$

where $x_1 \in \mathbb{R}^{m\times 1}, x_2 \in \mathbb{R}^{m\times 1}$represents the modal displacement and velocity states respectively, $x_3 \in \mathbb{R}^{m\times 1}, \dots x_6 \in \mathbb{R}^{m\times 1}$ are aerodynamic lag states, $\widehat{M} \in \mathbb{R}^{m\times m}, \hat{C} \in \mathbb{R}^{m\times m}, \widehat{K} \in \mathbb{R}^{m\times m}$ are the generalized aero-influenced mass, damping and stiffness matrix respectively, $u_c \in \mathbb{R}^{p\times 1}$, $\dot{u}_c \in \mathbb{R}^{p\times 1}, \ddot{u}_c \in \mathbb{R}^{p\times 1}$ are actuator displacement, velocity and acceleration states respectively. Control feedback for this system may assume various forms of Eq. (2.2),

$$u = Ky \tag{2.2}$$

where K represents a static or dynamic controller and y represents a set of measurements to feed back. For a flutter controller, the measurements would likely come from strain or accelerometer sensors. However, if a modal filter is present, the contributing modes

themselves could form the measurement. This would remove the possibility of observation spillover discussed previously and focus the control suppression energy.

Many of the methods used in practice make the assumption of the linear structure and linear aero (and rightly so for the most part). But many structures have local non-linearities and must be handled more carefully. For local nonlinearities, Karpel's fictitious mass method [124] may be employed, and local deformation modes may be obtained.

Other researchers are using geometrically exact formulations to capture aeroelastic properties of highly flexible vehicles, such as in Patil et al.'s [125] work, which are generally applicable to a wide range of flexibility.

The use of smart materials and structures is motivating many different formulations and modifications to state space equations. For example, the introduction of piezoelectric control modes in the aeroservoelastic equations of motion may be seen in Karpel and Moulin's [126] work. Another fascinating topic is how the elastic aerodynamic information is captured. Aerodynamic states may be cast into modal form as well and they are introduced in the next section.

2.1.8 Unsteady Aerodynamics and State Space Modeling

The size of the controller is highly dependent on how the aerodynamic forces are modeled as well as how many modes are controlled. Roger's approximation [117] of the unsteady aerodynamic forces results in as many aero states equal to 1-4 times the number of modes included in the analysis. As an example, an aeroelastic model with 10 modal displacement states may include as many as 10-40 additional aero states.

Higher order aerodynamics can be captured by including more states. The generalized aerodynamic forces (GAF) due to both rigid body perturbations and elastic modal states can be represented by a rational function approximation (RFA) as in Eq. (2.3)

$$\tilde{F}_{aero} \approx \gamma \left[A_0 + \bar{s}A_1 + \bar{s}^2 A_2 + \sum_{l=1}^{L} \frac{\bar{s}}{\bar{s} + \beta_l} A_l \right] \bar{q} \tag{2.3}$$

where $\bar{s} = i\frac{\omega \bar{c}}{2V} = \frac{s\bar{c}}{2V}$, and $\bar{c}$ is the reference chord length. s is the Laplace variable, $\bar{q} \in \mathbb{R}^{m\times 1}$ is a vector of modal displacements, $A_i \in \mathbb{R}^{m\times m}$ are GAF coefficient matrices and γ is the dynamic pressure.

To use the RFA, the GAFs are first calculated over a range of reduced frequencies, using the Doublet Lattice Method [127]. The complex GAF matrices are fitted with a least squares methodology to an s-plane polynomial containing pre-selected lag terms, resulting in matrix coefficients A_i.

The resulting aerodynamic damping, stiffness and lag matrices are then implemented in a state space format such as in Pototzky's [123] work. This is an accurate methodology for all but transonic and hypersonic speeds and has been used by many researchers for developing control laws.

Notice that in Eq. (2.3), that the aero lag forces are a function of modal coordinates. This suggests that with knowledge of the modal coordinates in real time it may be possible to estimate both steady and unsteady aero forces due to elasticity. This is yet another potential advantage of modal filtering.

The size of the plant state space matrices is considered by many to be burdensome due to the large number of aerodynamic lag states. In general, up to four aero states may

exist for each included mode. Karpel developed the Minimum State (MS) Method [128] which reduced the number of aerodynamic states down to one per mode, and optimized further from here.

The MS formulation requires nonlinear optimization methods and is based off of the Modified Matrix-Pade formulation [129]. While the setup of the system is more complex, the reduction in states can be considerable, which is preferable for control synthesis. The state space equations are not given here explicitly, but their development may be reviewed through this technical report [128].

The state space matrices are almost always based upon the modal displacement, velocity and aero lag states. Thus measurement of these states will be very beneficial for state feedback/tracking controllers. It could be that the feedback of these modal states are what will make flutter controllers truly robust. However, this is only speculation for now. This concludes the discussion of flutter. Next, a discussion of aircraft performance improvement is given.

2.2 Aircraft Performance Improvement

The following sections introduce the possibility of utilizing modal filtering for improving an aircraft's performance. Fuel efficiency is a major motivating factor in aircraft today. Some discussion is given on how drag and therefore fuel efficiency is affected by more elastic aircraft.

A few computational studies predict potential improvements of controlling elastic effects. Finally, a survey of aircraft shape control methods is given. Fuel efficiency is discussed first in the following section.

2.2.1 Fuel Efficiency

Fuel efficiency is paramount and improvements to fuel efficiency continue to be discovered. Since the late 1950's IPPC have shown that aircraft fuel burn per passenger decreased by 70%. From this, about 40% came from engine fuel efficiency improvements and 30% from airframe efficiency improvements [130]. Estimates suggest that the trend in fuel efficiency will continue its upward trend according to a 2010 International Civil Aviation Organization [131] report.

The primary source of improvement comes from the introduction of weight savings and drag reduction technologies. ICAO states that advanced alloys and composite materials will lead to significant weight reduction. Indeed, aircraft such as the Boeing 787 and Airbus A350 are made of as much as 70% of advanced materials which includes composite wings.

Advanced future aircraft concepts will likely be more flexible than traditional aircraft due to structure reduction and lightweight structures. Therefore, their fuel efficiency will improve just due to the relationship with lift, drag and weight. These aircraft will be lighter and thus require less lift to achieve equilibrium. Therefore the trim angle of attack will be lower and they will produce less drag relative to a stiffer aircraft.

However, more flexible aircraft will also vary in shape more than a relatively stiff aircraft. Therefore at off-design conditions, their structure may drift further from the optimum more so than a relatively stiff aircraft. Heinze [132] suggests that off design performance will be further degraded due to the effects of flexibility.

It is postulated here that some flexible aircraft will require active drag control for improved fuel efficiency at off-design conditions. The drag of a vehicle has a relationship

to shape, which in turn has a relationship with modal coordinates. An interesting link may exist here. First a discussion on passive drag reduction methods is given in the next section.

2.2.2 Passive Drag Reduction

Aircraft drag is inversely related to fuel savings and airline profit margins. Induced drag accounts for approximately 40% of the drag in cruise and 80-90% of the drag in climb [133]. Therefore drag reduction will continue to be of paramount importance for next generation aircraft. A 1996 estimate [134] states that a 1% fuel performance improvement for the United States fleet of wide-body transports would result in savings of approximately $100 million per year. An additional $20 million/yr for each $.10/gal increase in fuel price is also predicted in the same year. There are many ways to reduce drag.

Aircraft designers tailor local twist angles along the wing to produce a low-drag lift distribution [135]. A few example structural modifications include taper, twist and winglets. These are basic improvements, but the list goes on and becomes increasingly complex. What has intrigued many in academia and industry alike is the concept of controlling drag using active controls technology. This is discussed in the next section.

2.2.3 Active Drag Reduction

It was realized early on that conventional control surfaces could be used to re-optimize the vehicle at different flight conditions. Traditionally, control surface scheduling has been applied for relatively rigid aircraft in attempts to optimize the angle

of attack at different flight conditions. Weisshaar pointed out the three main properties of roll control, and thus lift distribution and drag wake optimization [136]. They are repeated here:

1) Aileron deflection: aileron deflection changes both wing lift and pitching moment so that the aileron effectiveness to roll the aircraft is reduced by increased dynamic pressure

2) Leading edge surfaces: The leading edge slat lift curve coefficient is extremely small compared to a similar size aileron because the aileron easily deflects the airflow downward to produce a momentum change while the leading edge surface does not. However, slat displacement produces local nose-up wing twist large enough to increase lift substantially if the wing is "flexible" and can be twisted.

3) Wing camber distortion (also called camber bending): This can be done by using either internal mechanical apparatus or active materials as an integral part of the wing structure to produce parabolic or higher order continuous camber bending distortion. The nose down torque is smaller than that produced by an aileron with a similar lift generation ability. The chordwise lift distribution also creates more evenly distributed loads.

A substantial body of research has followed to show that mechanical actuation devices may be used to reconfigure the drag profile of aircraft. The literature contains analytical, experimental and intelligent methods for active drag reduction methods.

In 1996, Gilyard used a drag minimization procedure on a test L-1011 at NASA's Dryden Flight Research Center [134]. This procedure utilized in-flight measurements for feedback along to a real-time performance optimization system. More specifically, the

throttle was held fixed in flight and the aircraft velocity was used as a drag estimator. Gradients of the drag with respect to control surface movements were computed and used to reduce the cost function. Controls were implemented with symmetrical ailerons. During flight tests, they averaged a 1% reduction in fuel consumption.

Artificial intelligence has also been employed for drag optimization with post flight data by Lin et al. [137]. The neural network was trained with the flight data and identified the optimal symmetric aileron position based on flight conditions and aircraft states. The automatic flight control system used the signal to command the symmetric outboard ailerons accordingly. From the analysis, this resulted in a minimum drag aircraft control surface configuration for fuel savings.

Other studies to find control increments for drag reduction include that of Heinze on a 737 transport wind tunnel model [132] in which a generating set search optimization technique was used. The method was analogous to a compass search method [138]. Griffin et al. employed a time varying Kalman Filter method to find control gradients with respect to a performance function in order to optimize drag performance on the X-48B [139]. These methods apply to any style of aircraft, whether it is flexible or not. The next section reviews methods of control of off-design drag for flexible aircraft.

2.2.4 Control of off-design Drag due to Flexibility

Aeroservoelastic tailoring with active control is recently becoming of interest. In 2006, Weisshaar and Duke extended their work on laminate tailoring [135, 136] to include active control surfaces in an effort to reduce drag to a minimum. They suggested

that an active wing shape control should be developed to tailor a flexible aircraft such that induced drag is minimized at off-design conditions.

They give a closed form solution of the required control surface deflections for a full span aileron to produce an elliptical lift distribution and thus minimum drag. They utilize the aerodynamic influence coefficient matrix and the wing structural flexibility matrix in the problem formulation. They also propose an optimization problem in lieu of the closed form solution for more practical applications.

Kumina et al. developed an objective function, where induced drag was related to circulation, through generalized coordinates of properly chosen modal shapes [140]. In a simulation model, control surface deflections were found which corresponded to minimal induced drag. They form the drag optimization problem as in Eq. (2.4),

$$minimize\ C_D(q_1, \dots, q_n) \tag{2.4}$$

$$s.t. \begin{matrix} C_L(q_1, \dots, q_n) = C_{L0} \\ m_y(q_1, \dots, q_n) = 0 \end{matrix} \tag{2.5}$$

where $C_D(q_1, \dots, q_n)$ is the drag coefficient as a function of generalized coordinates, $C_L(q_1, \dots, q_n)$ is the lift coefficient as a function of generalized coordinates, C_{L0} is the reference lift coefficient and $m_y(q_1, \dots, q_n) = 0$ is the pitching moment as a function of generalized coordinates. The drag objective function in modal coordinate form was given without explicit derivation as in Eq. (2.6),

$$C_D = q^T \widetilde{D} q \tag{2.6}$$

where q^T is a vector of control surface settings, and $\widetilde{D}$ is not given explicitly, but depends on the aerodynamic influence coefficient matrix (AICs) and is derived from Rodden et al.'s original work [141]. The elastic effects are wrapped into the $\widetilde{D}$ term which was not explicitly given.

Equation (2.6) shows a direct correlation between elastic modal coordinates and induced drag. In Kuzmina's [140] work, they did comparisons between a rigid and elastic transport aircraft and showed that structural deformations increased induced drag especially during maneuvers with high load factors.

Additionally, motivation for adaptive drag control was given in another paper discussing the utilization of adaptive wing tip control devices in lieu of trailing edge surfaces [142].

At off-design conditions, there seems to be some agreement in the literature that a more flexible aircraft will move further from its optimal wing shape. This indicates a need to address the problem directly.

2.2.5 Aircraft Shape Control

Active shape control (ASC) may be applicable for reducing drag at off-design conditions. With ASC the aircraft structure may be moved closer to an optimal shape at off-design conditions. ASC has been pursued in the literature, primarily with smart structure technologies. In the literature, ASC is often referred to as "morphing". This is often accomplished with technologies such as swing wings, Shape Memory Alloys (SMAs), piezoelectric or other distributed effectors.

Shape control for adaptive wings has been proposed by Austin et al. [143]. The purpose of their research was to reduce drag during transonic operations by varying the airfoil structure between the leading and trailing edges. They formulated an open loop control law for adaptive rib actuators assuming all forces (aerodynamic and stiffness forces) on the wing are known precisely. They form the closed loop control law which

minimizes the difference between a desired shape and the current shape of the wing. In this work, the shape deformation was measured with internal LVDTs.

Recently developed smart sensor & control technology has prompted further work in ASC. Piezoelectrics [144, 145, 83] have been receiving increasing attention. They are considered to be a collocated control effector. Recall that a collocated effector is an effector which affects the same point which is sensed. These control effectors guarantee against spillover effects. Heeg gives a full derivation of the piezoelectric aeroservoelastic equations of motion and derives the state space and a controller.

Ehlers and Weisshaar conducted a comprehensive analytical study to discover how active control using piezoelectric patches could reshape the wing to improve aerodynamic performance and control static aeroelastic characteristics [146]. An extensive survey of the use of strain actuated control may be found in Chee et al.'s work [147]. A book based upon the finite element approach to piezo control by Bandyopadhyay et al. [148] is also very useful to understand the complex issues involved. Morphing-capable adaptive structures based on SMA technology has been applied to shape trailing edge surfaces of a UAV [149].

In 2005, scientists and engineers [150] exploited the aeroelasticity of a F/A-18 wing using inboard and outboard leading edge flaps. A picture of this aircraft is given in Fig. 2.3. The Air Force program manager commented that, "With wing warping, the control surface deflections can be chosen to produce an aeroelastic shape that minimizes load on the structure and results in reduced structural weight. It also minimizes drag on aircraft, improves range and maximizes maneuver rates of aircraft"

Figure 2.3: NASA Active Aeroelastic Wing F/A-18 (Redesignated X-53) Technology Testbed Aircraft[2].

In 2010, Nguyen at NASA Ames proposed a control allocation scheme based modal suppression/drag reduction controller [151], relying on conformal trailing edge control surfaces. The model used to design the controller was designed retaining flexible modes, and the drag representation includes elements of flexibility.

Nguyen's research may be interpreted to suggest that modal sensing may be becoming increasingly important as aircraft shape control research progresses. The same author addresses the need for advanced sensing specifically in a NASA tech brief [152]:

"New sensors should be able to measure both static and dynamic components of the wing deflection. The sensor bandwidth should be sufficiently fast to enable sensors to be used for providing data to an active wing shape control system"

---

[2] http://www.dfrc.nasa.gov/Gallery/Photo/AAW/HTML/EC03-0039-1.html

However, using active shape control to improve aerodynamic properties will likely remain difficult without local sensors which truly indicate the aerodynamic properties of the flow. Aerodynamic sensor packages such as the DASP toolbox [153] are being developed to address the sensor deficiencies.

The previous sections may be used to deduce that modal filtering will benefit aircraft performance. By controlling the modal coordinates and thereby the shape, the aerodynamics of the aircraft can be adjusted. If this can be done actively and intelligently, aircraft inflight shape optimization may become a reality. The modal filter may benefit aircraft in other ways as well. The following section reviews loads alleviation and links modal coordinates to an aircraft load controls scheme.

2.3 Modal Coordinates for Loads Calculation

As aircraft are designed to be increasingly flexible in an effort to reduce weight, elastic frequencies may couple dangerously with gust frequencies. This may lead to resonance and structural cracks.

Loads and gust load alleviation (GLA) have been important issues for decades. GLA studies began in the early 70s when cracks were discovered in the Lockheed C-5A Galaxy. An example of which is shown in Fig. 2.4. After initial investigation, active gust load alleviating ailerons was fitted to the re-winged Lockheed C-5As in the early 80s [154].

Since then, various active gust load alleviation devices and techniques have been implemented on aircraft such as the Lockheed L-1011-500, Airbus 320, Boeing 787, and the B-2 [155, 156, 157, 158]. To address the gust load alleviation problem, lead sensors are generally required if using conventional control surfaces [159]. However, the same is not generally true for maneuver related loads alleviation [160], which is more of a steady state effect.

Modal coordinates have also been used for internal load calculations, through the use of the modal displacement (MD) method. The MD method recovers the loads directly from the modal displacements, and has been used for loads-alleviation control design [161]. When used carefully under fairly well-distributed loads such as in a gust case and with a sufficient number of modes taken into account, the MD method has been shown to calculate the actual loads quite well [162].

Figure 2.4: A United States Air Force C-5A Galaxy in flight[3].

[3] http://www.af.mil/shared/media/photodb/photos/021205-O-9999G-001.jpg

The MD approach makes the modal superposition assumption, which is parallel to the modal displacement assumption. Each modal coordinate represents a specific load. Since the modes are orthogonal, the modal contributions to the load may be summed directly, as the interaction terms are assumed to be zero. Hence if enough modal coordinates are measured it may be possible to recover the net-load distributions.

The use of load modes may be employed along with the discrete coordinate stiffness matrix to calculate the net load on the structure such as in Eq. (2.7),

$$L(t) = \Phi_L{}^T K \Phi q(t) \tag{2.7}$$

where $\Phi_L \in \mathbb{R}^{m \times n}$ is a matrix of load modes which is calculated apriori, $K \in \mathbb{R}^{n \times n}$ is the discrete coordinate stiffness matrix, $\Phi \in \mathbb{R}^{n \times m}$ is the matrix of mode shapes and $q(t) \in \mathbb{R}^{m \times 1}$ is a vector of modal coordinates. With knowledge of the modal coordinates in real time, it may become possible to calculate the majority of the net loads contribution at a particular instant in time. By actively controlling net loads via modal coordinates in GLA systems, wings may be designed lighter and fuel efficiency may be improved.

2.4 Summary of Application of Modal Filtering in Aircraft

From the previous sections it is possible to identify several motivating concepts as well as potential pitfalls. Due to increasing flexibility, next generation aircraft will be more susceptible to aeroelastic instability and gust loads. It will become more difficult to implement passive flutter suppression methods. This is especially true if flutter occurs is

in the flight envelope. AFS may become a requirement in more flexible aircraft. Furthermore, ASC and GLA may become requirements.

2.4.1 Benchmark

Experimental vibration controllers have relied on modal information in one form or another. The benchmark today is in the use of single point sensors for control in aeroservoelasticity. For example, all experimental flutter methods propose control of flutter with only snapshots of the true aeroelastic states. These snapshots are taken with point sensors such as accelerometers. The true states are not measured and have never been used for AFS control feedback.

There are other problems with using single point sensors. Suppressing single sensor outputs may lead to observation and control spillover issues (SMI in aircraft). It is also common that single point sensors require additional dynamics such as low pass filters. This is problematic as modal frequencies tend to shift with time. Mode shapes change required by spatial modal filters change very little.

Modal filtering can estimate the true modal states of a structure. To date, benchmark spatial modal filters have been implemented in structural studies out of the airflow. It remains of interest to see if modal filters accurately capture the true modal states in the presence of aerodynamic forces. It is also of interest to see whether distributed sensing supports this objective.

The benchmark in modal filtering is the OLS type or LMS type modal filter. Both filters assume that the sensor error distribution is approximately normal. Therefore these filters are not practical for implementation in aircraft applications. This suggests a need to

make the modal filter robust. Several gaps can be identified given these benchmarks. They are presented in the next section.

2.4.2 Gaps

It is postulated that there are gaps in the point sensor design methodology. Aeroelastic state space models typically represent structural states with modal displacements, modal velocities and modal aero lags [123]. By sensing and controlling linear combinations of these states, the overall objective may not be satisfactorily met.

Researchers in structures have suggested that spillover can occur in sensing and feedback control. In aircraft, flight controllers have induced SMI. To reduce this interaction, notch filters are typically employed, leading to increased phase lag. To meet phase requirements, the controller bandwidth is typically reduced. Here this gap may be filled, simply by controlling only that which needs to be controlled and leaving the rest alone.

Another gap is simply robustness. A controller which uses an exact estimate of a distributed state is more trustworthy than one which does not. A single sensor simply gives less information than 1,000s of sensors placed at many locations on a structure. It makes sense that AFS will likely be improved by modal sensing techniques, allowing control energy to be focused on the interacting modes. Otherwise, some energy is focused on modes which are not necessarily contributing. Furthermore, more accurate and reliable modal estimation may improve loads alleviation control design systems.

Another gap which has been postulated for flexible aircraft is the need for shape control to improve fuel economy. Active shape control may be required to maintain an

optimal wing shape or slightly perturb the shape in order to reduce drag in future flexible vehicles at off-design conditions. One of the methods of shape prediction relies heavily on accurate estimation of modal coordinates. Therefore improved modal sensing can support active shape control and drag reduction, in the future.

Another gap already identified is that modal filters require a large number of sensors for accurate modal coordinate estimation. This has prevented the spatial modal filter from being used in aircraft. Fast forward and today, experimental studies are being conducted with distributed sensing on aircraft with sampling rates up to 100 Hz. Indeed, high density distributed sensors will support modal filtering designs [20]. Thus it is postulated that this gap can be filled just by the utilization of modern distributed sensing technology.

Another gap follows from this immediately. A modal filter has not yet been tested in an aeroservoelastic environment. The modal frequencies and modal shapes change with air speed. Therefore it remains of interest to see whether a spatial modal filter is still applicable in an aeroservoelastic environment. Assuming this is possible, it is still not clear whether modal filtering can be of any use on an aircraft without experimentation. Much speculation is already seen in the previous sections, however.

Finally and perhaps most importantly a gap in modal filters is that they rely upon OLS for estimation. This requires that the sensor error distributions should always be normally distributed. However, practical applications are never perfect. Sensors fail and the unexpected happens. Therefore, modal filters must be improved to be robust under these circumstances. This becomes especially important if modal filtering is relied upon for feedback flutter control. To address these gaps, while supporting research objectives,

a specific research problem, research questions and hypotheses are formulated within the following section.

2.5 Research Problem, Research Questions & Hypotheses

The previous section identified gaps which must be addressed in both modal filtering and flexible aircraft. Much of this has been brought about by new requirements from the Aeronautics Research Mission Directorate. The N+3 fuel efficiency objectives has generated interest in investigating all available technologies. Perhaps the most beneficial and potentially the most dangerous technology is light weight structures. Such aircraft with this technology may require ASC or AFS.

Suppression of structural vibration is the most common motivation, when considering structural control. A more active way of thinking would be to consider how to take advantage of the structure's ease of movement. This dissertation will prepare the way for practical structural shape optimization in aircraft.

Aircraft aerodynamics are highly affected by the shape of the wing. More optimal shapes have been achieved through the usage of taper, aspect ratio, and twist. However, these shapes are often fixed and may not be optimal at some flight conditions. It is postulated that flexible structural control could be one method of improving performance characteristics of flexible aircraft. This could come about by controlling shape at off-design conditions and through load control.

Demonstrating global shape optimization of the aircraft is beyond the scope of this dissertation however. It would be more efficient to focus on how distributed sensing can be utilized to achieve inner loop control objectives first. It seems that reasonable near term objectives are to demonstrate AFS, GLA and ASC by way of the modal filter. In future work, an optimizer can be built around these inner loop control concepts.

But research suggests that modal filters are highly sensitive to sensor bias. This could raise substantial questions about their implementation and certification in commercial aircraft. Therefore, the thesis research problem is posed in a careful way which supports high level research objectives and addresses some of the identified gaps while accounting for the practical requirement of safety.

Research Problem:

How can high resolution distributed sensing and modal filtering be safely utilized for control feedback in flexible aircraft?

In support of this research problem, the first research question is posed:

Research Question 1. Is the OLS modal filter efficient for control feedback when it is utilized within an aeroservoelastic problem?

A hypothesis is formulated in response to this question as follows:

Hypothesis 1. The OLS modal filter will perform the same as it would on a static structure out of wind flow.

The relationship of $d(t) = \Phi q(t)$ holds true at all times. When considering the aeroservoelastic problem, the modal filter should not perform any differently. However, the modal filter has never been applied in an aeroservoelastic setting before. A wing model without rigid body modes should be sufficient to address this question fully. The next research question follows the proof of concept theme:

Research Question 2. How should a modal filter be incorporated into the control system of a aircraft?

A hypothesis is formulated in response to this question as follows:

Hypothesis 2. The modal filter is a partial state filter in the aeroservoelastic problem. It can be placed in series with a traditional control system estimator.

The literature search revealed the typical aeroservoelastic state space model and its states. It was found that modal states are directly measured by the modal filter implemented by Shelley et al. Therefore, the series connection appears natural. Answering this question addresses several concerns about a modal filter's utilization on a flying vehicle. Perhaps the most important one is whether the modal filter is still applicable when an aircraft's modes become complex due to aerodynamic interaction.

The OLS modal filter is one which is precariously used. The residuals strongly bias the estimates, and therefore it is not robust. Thus, the following research question is posed:

Research Question 3. How can the OLS modal filter be improved to be robust to sensor bias?

The following hypothesis is formulated in response to this question:

Hypothesis 3. A robust regression technique will provide a real time estimator which proves to be efficient and resilient to faulty sensors

The modal matrix of a structure can be identified to be a data matrix A with explanatory data. The strain or shape measurements can be identified to be the output data, b in the relationship, $Ax = b$. So, a real time robust parameter estimation technique appears to be a natural solution.

Additional Research Questions are given next which do not have associated hypotheses. They are given under the assumption that the previous hypotheses are correct.

Research Question 4. What methods of shape control may the modal filter be utilized for?

Research Question 5. Can a fully coupled rigid and flexible controller be designed with the modal filter?

Research Question 6. Are there other uninvestigated uses for a robust modal filter?

CHAPTER 3

SIMULATION DEVELOPMENT

The previous Chapter identified six research questions which must be addressed. In fact, the first must be answered in order to proceed with the next five. The next five depend on whether or not the modal filter can be used for control feedback in an aeroservoelastic environment. To formulate an answer to this question, it was necessary to code up a linear aeroservoelastic simulation environment. This was done, rather than using open source simulations, because most simulations do not have models of high density distributed sensing.

The simulation environment supports the development, control design and testing of the wing model in the next Chapter. It allows user inputs for varying numbers of control surfaces and structural layouts as well as mass and stiffness properties. Since the simulation environment is extensive, it has not yet been fully documented. An overview of the simulation is given instead, with salient features such as the state space modeling environment given for review. In future work, the simulation environment will be fully documented and published. The following section introduces some of the major steps taken in designing the simulation. A verification and validation study of the simulation is given at the end of this Chapter.

3.1 Summary of Wing Model Simulation Development

The steps taken to generate the wing model simulation environment are given and summarized briefly. A full recounting of the model development will be published at a future date. References are given, where important equations were derived. Any verification or validation steps taken are referenced to the source of verification material. The building blocks of the simulation include:

1) Development of a FEM and linear solver in MATLAB with 2 node 6 DOF isotropic beam elements, 4 node 12 DOF isotropic plate elements and 2 node 6 DOF isotropic spring elements
    a. Modal frequencies of 12 DOF plate [163] model verified against ANSYS FEM software [164]. Deflection is verified with cantilever beam theory.
    b. 6 DOF beams verified with cantilever beam theory.
    c. Developed variable geometry representing rectangular wing with outer skin, linearly tapering spars/rips, and control surfaces using FEM elements
2) Development of a 3d Vortex Lattice code and planar Doublet Lattice code in MATLAB
    a. VLM verified by matching parabolic lift distributions for rectangular wings, and comparing total lift with the standard lift equation for various aspect ratios
    b. DLM verified for the planar case [165]
        i. Quartic approximation of and verification of kernel [127]
        ii. Normalwash defined [166]
        iii. Chord-wise box layout improvements [167]

3) Generalized Force Coefficient build-up and rational function approximation in MATLAB
    a. Generalized forces calculated [168, 169]
    b. RFA utilizes Roger's least squares approximation of the unsteady aerodynamics [117]
    c. RFA verified by matching the experimental flutter speed and frequency of rectangular plate [164]
    d. Visualization completed with V-g and V-f analysis [170]
4) State space model for elastic modes modeled and simulated in MATLAB/Simulink
    a. State space [123] designed for Roger approximation of unsteady aerodynamics
    b. Verified instability of state space from positive real parts of complex eigenvalues at and beyond the predicted flutter speed from V-g analysis
    c. Gust loads modeling with sinusoidal gust columns [171]

Many of the steps just mentioned are not accounted for in detail within this paper; although these were the major steps taken by the author to design the simulation. Important steps, such as the aeroservoelastic state space model and verification and validation are discussed. The following section elucidates the simulation functions.

3.2 Simulation Modules

The full functional capability of the aeroservoelastic analysis for the wing model is presented in Fig. 3.1.

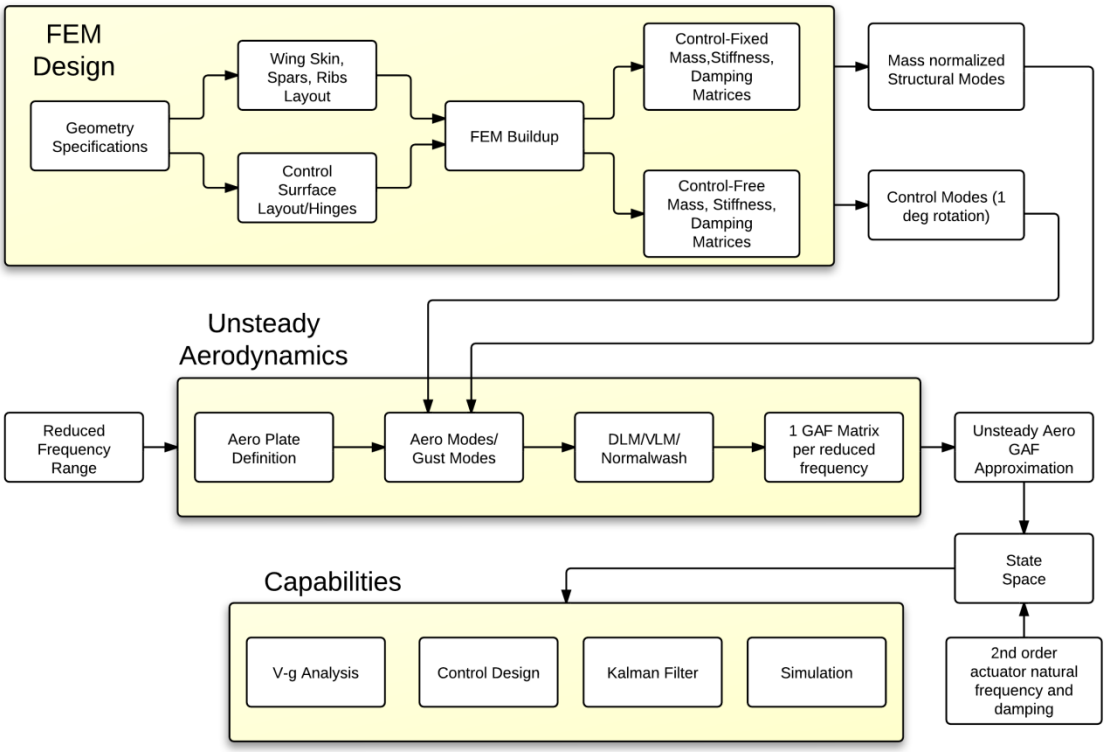

Figure 3.1: Wing Model Design, Aeroservoelastic Analysis and Controller Development Tool.

To start the FEM design, the user must input the geometry of the structure, such as the wing span and aspect ratio. The number of structural panels in the chord-wise and span-wise directions are variable giving the user some control of the structural layout. The spars are then assumed to lie along the ¼ chord and at control surface connections. Ribs are spaced every panel width. All properties including material type and thicknesses are user defined.

The aero module includes several components such as aero paneling, aero modes and gust modes, as well as GAF calculation and RFA design. The aero module is used to support state space design.

Direct simulation can also be achieved by inputting forces directly into the finite element model, or they can be done using the state space matrices themselves. A limitation of the simulation model is that it cannot simulate aerodynamic forces onto a node in a time simulation. The finite element aerodynamic force relationships have not yet been developed. This would require a wake model which is not currently implemented.

The following section details the aeroservoelastic state space model development which the simulation tool was designed to support. Actuators and gust modeling are also overviewed in the sections to follow.

3.2.1 Aeroservoelastic State Space Model

The derivation of the plant, input influence matrix and sensor output matrices is given here, using similar notation found in [45]. The relevant displacement matrix equation of motion for structures is given as in Eq. (3.1),

$$M\ddot{x} + C\dot{x} + Kx + \bar{q}A(k)x = P(t) \tag{3.1}$$

where $M \in \mathbb{R}^{n\times n}$ is the inertia matrix, $C \in \mathbb{R}^{n\times n}$ is the damping matrix, $K \in \mathbb{R}^{n\times n}$ is the stiffness matrix, λ is the dynamic pressure, $A(k)$ is the aerodynamic influence coefficient matrix calculated calculated from for a given Mach number and a set of reduced frequency values $k = \frac{\omega \bar{c}}{2V}$, $\bar{c}$ is the mean chord length, ω is the circular frequency and V is the freestream velocity, $x \in \mathbb{R}^{n\times 1}$ is the physical displacement vector of rotational and translational DOF, and $P(t)$ is the external forcing function.

The free vibration of the unforced system in equilibrium is given as in Eq. (3.2).

$$M\ddot{x} + Kx = 0 \tag{3.2}$$

The eigenvalue solution of the system produces the natural frequencies and eigenvectors (dry mode shapes) of the system. The following transformation may then be applied to Eq. (3.2) assuming mean axis constraints are satisfied, as shown in Eq. (3.3),

$$x = \Phi q \tag{3.3}$$

where $\Phi \in \mathbb{R}^{n\times m}$ is the matrix of eigenvectors corresponding to elastic, rigid and control modes. The transformation results in Eq. (3.4).

$$M\Phi\ddot{q} + C\Phi\dot{q} + K\Phi q + \lambda A(k)\Phi q = P(t) \tag{3.4}$$

Pre-multiplying by Φ^{T}, the matrix equation of motion becomes as in Eq. (3.5).

$$\Phi^{\mathrm{T}}M\Phi\ddot{q} + \Phi^{\mathrm{T}}C\Phi\dot{q} + \Phi^{\mathrm{T}}K\Phi q + \lambda\Phi^{\mathrm{T}}A(k)\Phi q = \Phi^{\mathrm{T}}P(t) \tag{3.5}$$

This is typically rewritten in the following generalized form as in Eq. (3.6).

$$\tilde{M}\ddot{q} + \tilde{C}\dot{q} + \tilde{K}q + \lambda \mathrm{Q}(k)q = \tilde{P}(t) \tag{3.6}$$

From here, decisions must be made in how the generalized aerodynamic force (GAF) matrix will curve fitted.

There are several ways of doing this including Roger's RFA [117] and Karpel's Minimum State method [172]. The RFA of the generalized unsteady aerodynamic forces in the Laplace domain may be written as in Eq. (3.7),

$$\hat{Q}(k) = A_0 + \bar{s}A_1 + \bar{s}^2 A_2 + \sum_{l=1}^{L} \frac{\bar{s}}{\bar{s} + \beta_l} A_l \tag{3.7}$$

where $\bar{s} = i\frac{\omega \bar{c}}{2V} = \frac{s\bar{c}}{2V}$, $\bar{c}$ is the reference chord length, and s is the Laplace variable. The matrix coefficients A_i may be found through a least squares approximation of a set of GAF matrices each calculated at a specified reduced frequency. For slower speeds analysis the largest reduced frequency is chosen to be high and for faster speeds, the largest reduced frequency may be chosen lower due to the inverse relationship with freestream velocity.

The GAF matrices are calculated through a doublet lattice procedure with aero mode shapes and modal shape derivatives taken in the chord-wise direction. To improve the accuracy of the approximation for higher Mach numbers, Rodden's quartic kernel approximation [127] is utilized. In addition, the number of aero panels for each generalized force matrix calculation are constrained in the streamwise direction to be at least $50k/\pi\bar{c}$, as Rodden et al. [167] recommends for improved accuracy.

Roger's RFA is chosen for computing the RFA. To implement the RFA, the lag constants β_l are user defined but typically chosen from the lower range of the predefined set of reduced frequencies. For an accurate fit of the generalized force matrix, usually at least 2 lag states are required, although this number tends to vary from 1 to 4 in the literature.

Inserting (3.7) into (3.6), the equations of motion are rewritten assuming simple harmonic motion as in Eq. (3.8),

$$\widetilde{M}\ddot{q} + \tilde{C}\dot{q} + \widetilde{K}q + \lambda\left[\mathrm{A}_0 + \frac{s\bar{c}}{2V}A_1 + \left(\frac{s\bar{c}}{2V}\right)^2 A_2 + A_3x_3 + A_4x_4 + \cdots\right]q = 0 \tag{3.8}$$

where the lag states are given as in Eq. (3.9).

$$x_j = \frac{sq}{s + \frac{2V}{\bar{c}}\beta_j};\ \ j = 3 \ldots 6 \tag{3.9}$$

Equation (3.9) may be rewritten in the form of matrix ODEs as in Eq. (3.10).

$$\dot{x}_j + \frac{2V}{\bar{c}}\beta_j x_j = \dot{q} \tag{3.10}$$

Like terms are grouped in (3.8) and the equation may be rewritten as in Eq. (3.11).

$$\left(\widetilde{K} + \lambda A_0\right)q + \left(\tilde{C} + \lambda\frac{\bar{c}}{2V}A_1\right)\dot{q} + \left(\widetilde{M} + \lambda\left(\frac{\bar{c}}{2V}\right)^2 A_2\right)\ddot{q} + \lambda A_3x_3 + \lambda A_4x_4 + \cdots = 0 \tag{3.11}$$

Condensing variables results in Eq. (3.12).

$$\widehat{K}q + \hat{C}\dot{q} + \widehat{M}\ddot{q} + \lambda A_3x_3 + \lambda A_4x_4 + \cdots = 0 \tag{3.12}$$

Equations (3.10) and (3.12) represent a set of ordinary differential equations and may be converted to state space form in the usual way. Before doing so, it is important to understand that the modal coordinates may include control modes, rigid body modes, elastic modes and gust modes. The matrices are partitioned accordingly. Assuming only the presence of elastic modes, control modes and gust modes in the analysis, the state space equations are presented as in Eq. (3.13).

$$\dot{\boldsymbol{x}} = \begin{Bmatrix} \dot{x}_1 \\ \dot{x}_2 \\ \dot{x}_3 \\ \vdots \\ \dot{x}_6 \end{Bmatrix} = \begin{bmatrix} 0 & I & 0 & \dots & 0 \\ -\widehat{M}^{-1}(\widehat{K} & \hat{C} & \lambda I & \dots & \lambda I) \\ 0 & A_3 & -\beta_1(\frac{2V}{\bar{c}}) & 0 & 0 \\ \vdots & \vdots & 0 & \ddots & 0 \\ 0 & A_6 & 0 & 0 & -\beta_4(\frac{2V}{\bar{c}}) \end{bmatrix} \begin{Bmatrix} x_1 \\ x_2 \\ x_3 \\ \vdots \\ x_6 \end{Bmatrix}$$
$$+ \begin{bmatrix} 0 & 0 & 0 \\ -\widehat{M}^{-1}(\widehat{K}_c & \hat{C}_c & \widehat{M}_c) \\ 0 & A_{c1} & 0 \\ \vdots & \vdots & \vdots \\ 0 & A_{c4} & 0 \end{bmatrix} \begin{Bmatrix} u_c \\ \dot{u}_c \\ \ddot{u}_c \end{Bmatrix} \tag{3.13}$$
$$+ \frac{1}{V} \begin{bmatrix} 0 & 0 \\ -\widehat{M}^{-1}(\widehat{K}_g & \hat{C}_g) \\ 0 & A_{g1} \\ \vdots & \vdots \\ 0 & A_{g4} \end{bmatrix} \begin{Bmatrix} w_g \\ \dot{w}_g \end{Bmatrix}$$

The states x_1 and x_2 replace the modal state displacement and velocity vectors respectively. The remaining states make up the aerodynamic lag terms. The control surface states $u_c, \dot{u}_c, \ddot{u}_c$ may be replaced with actuator transfer function dynamics, in order to convert the input states into control command format. The gust velocity and acceleration are represented by w_g and $\dot{w}_g$ respectively.

The sensor output equation is typically modeled based on the position and type of sensors in the system. Certainly, there are many ways to form the output sensor equation, and here one intuitive way is reviewed. Assuming that the measurements are linear combinations of the modal states Eq. (3.14) results,

$$\begin{aligned} q_s &= T_s \Phi = \mathrm{C}_0 q \\ \dot{q}_s &= T_s \Phi \dot{q} \\ \ddot{q}_s &= T_s \Phi \ddot{q} \end{aligned} \tag{3.14}$$

where q_s, $\dot{q}_s$ and $\ddot{q}_s$ represent the measured displacements, velocities and accelerations respectively on the wing, Φ is the modal matrix, q is a vector of modal coordinates, and T_s is an interpolation matrix used if the sensors are not exactly placed at the FEM node

locations. Accelerometers and rate sensors can be used in flutter control problems, the sensor matrices are related to the state vector derivative as in Eq. (3.15).

$$\begin{aligned}\begin{Bmatrix}\dot{q}_s\\ \ddot{q}_s\end{Bmatrix} &= \begin{Bmatrix}T_s\Phi\\ T_s\Phi\end{Bmatrix}\begin{Bmatrix}\dot{q}\\ \ddot{q}\end{Bmatrix}\\ &= \begin{bmatrix}T_s\Phi & 0 & 0 & 0\\ 0 & T_s\Phi & 0 & 0\end{bmatrix}\dot{x}\\ &= C_1\dot{x}\end{aligned} \tag{3.15}$$

Notice that the sensors are related to the state space formulation matrices, which means that a direct feed-through matrix must be introduced. Pre-multiplying the state space form by C_1

$$\begin{aligned}C_1\dot{x} &= C_1Ax + C_1Bu\\ &= C_2x + D_2u\end{aligned} \tag{3.16}$$

The output equation may then be formed as in Eq. (3.17).

$$y = \begin{Bmatrix}q_s\\ \dot{q}_s\\ \ddot{q}_s\end{Bmatrix} = \begin{bmatrix}C_0\\ C_2\end{bmatrix}x + \begin{bmatrix}0\\ D_2\end{bmatrix}u \tag{3.17}$$

3.2.2 Actuators

For each control surface, a second order actuator is utilized. To prepare for actuator command time delay a 1st order lag filter $1/(Ts+1)$ is multiplied with the 2nd order actuator transfer function. This also has an additional effect of removing direct feedthrough from the sensor output matrix, when accelerometers are used for feedback. Each 3rd order actuator function from input command to output is shown as in Eq. (3.18),

$$\frac{u_c}{u_{com}} = \frac{1}{Ts+1}\left(\frac{\omega^2}{s^2+2\omega\xi s+\omega^2}\right) \tag{3.18}$$

where T is a scalar time constant, ω is the circular frequency, ξ is the damping ratio.

For all results, the time constant is set to .02 sec; ω was set to 74 rad/sec; and ξ was set to 0.58. The actuator settings were chosen very close to those for an experimental fighter aircraft's aileron actuators. This was not done for any particular reason, other than the convenience of having a similar model. A linear time invariant (LTI) transformation of the actuators may be used to augment the state space equations given in Eq. (4.4). The actuator bode and step is given in Fig. 3.2a) and 3.2b) respectively.

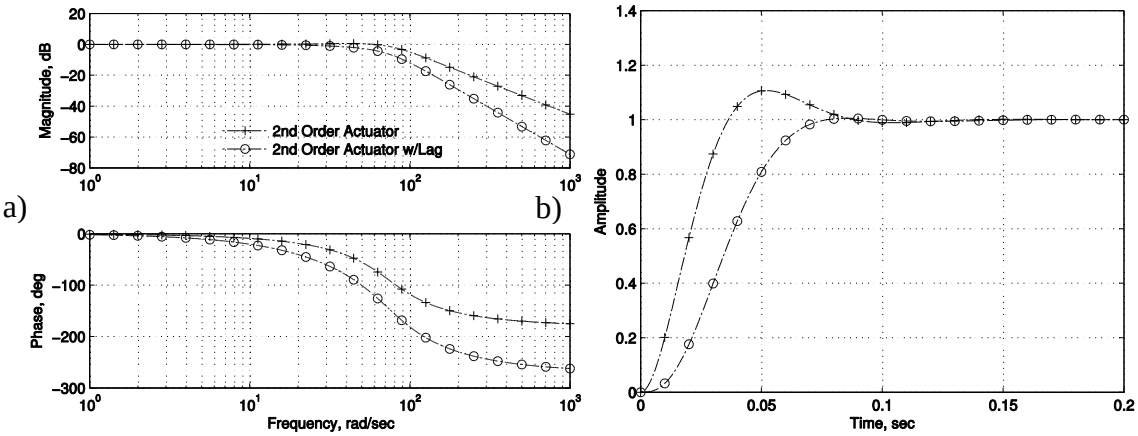

Figure 3.2: Actuator a) Bode Comparison; and b) Step Comparison.

The lag filter makes the actuator behave more like a first order filter. The time response is closer to what a transport control actuator looks like. The following section describes the gust model which is used in the simulation.

3.2.3 Gust Model

Gust modes are important to test the models for their performance in GLA. The gust modes are found by modeling the phase lag between individual panels and the beginning of the gust [171]. For a coordinate system with origin at the trailing edge and increasing x in the leading edge direction, the gust mode is given as in Eq. (3.19),

$$g_{mode} = -exp\left(i\frac{2k}{\bar{c}}\left(x_{CP} - \bar{c} + \bar{x}_{gust}\right)\right) \tag{3.19}$$

where x_{CP} is the vector of stream-wise coordinates at the control points of each aerodynamic panel. $\bar{x}_{gust}$ is the chord-wise distance between leading edge of the model and the start of the gust. Note that there is no phase lag, at the start of the gust. For this gust model, it is assumed that $\bar{x}_{gust} = 0$. This means the gust starts to build at leading edge of the wing.

Here is presented the $1 - cos(x)$ gust model, which is used to drive the gust input matrix of the state space equations. The standard temporal variation gust model [170] is given as in Eq. (3.20),

$$w_g(t) = \frac{w_{g,0}}{2}\left(1 - \cos\left(\frac{\pi V}{H}t\right)\right) \tag{3.20}$$

where $w_{g,0}$ is the design gust velocity, V is the aircraft speed, H is the gust gradient, or half the distance of the total gust span. For this wing test model it was desirable to design for a known maximum gust velocity and acceleration at the design operating condition. So the gust velocity was specified as in Eq. (3.21),

$$w_g(t) = \frac{w_{g,max}}{2}\left(1 - \cos(Ct)\right) \tag{3.21}$$

where C is a design constant and $w_{g,max}$ is the maximum gust velocity. A derivative in time of Eq. (3.21) gives the gust acceleration model shown in Eq. (3.22).

$$\dot{w}_g(t) = \frac{w_{g,max}}{2}\sin(Ct)C \tag{3.22}$$

By inspection, it is clear that the maximum value occurs when $\sin(Ct) = 1$, and thus the constant C is chosen as in Eq. (3.23).

$$C = 2\frac{\dot{w}_{g,max}}{w_{g,max}} \tag{3.23}$$

The period for the gust disturbance is therefore given as in Eq. (3.24).

$$P = \frac{2\pi}{C} \tag{3.24}$$

For the simulation, the same gust model is used. A maximum velocity of 5 m/sec and an acceleration of 1g is used for all studies. The model utilized for gust disturbance simulation is given in Fig. 3.3.

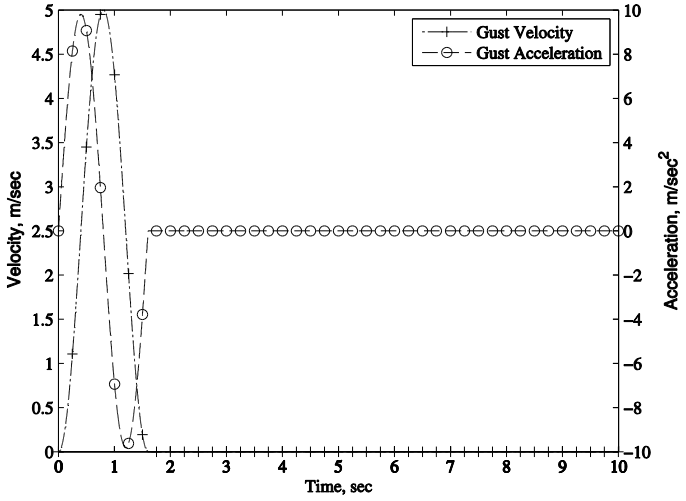

Figure 3.3: $1 - cos(x)$ Gust Model for Control Design and Simulation.

The gust model used here represents a fairly large disturbance. However, the parameters are adjustable. More reasonable disturbances may be input for other flight conditions. The next section describes the verification and validation procedures followed before putting trust in the simulation.

3.3 Simulation Verification & Validation

The simulation requires verification and validation. Therefore, pertinent aspects of the aeroservoelastic tool are tested against published material or theoretical relationships. First, it is shown that the deflected finite element model of the beam matches cantilever beam deflection theory results. Second, the modal frequencies and flutter speed prediction modules are compared with that of an experimental model. First, the beam verification results are presented.

3.3.1 Beam Verification

Here it is demonstrated that the finite element model force to displacement relations are satisfactorily matching cantilever beam theory results. Two beams are simulated under the same static loading conditions of {F_z=-100N, M_y=-100N-m} at beam tip where F_z is a force in the vertical direction and M_y is a torsion-like torque applied to the tip. The cubic dimensions of the beam are $(l, w, h) = (1m, 0.5m, 6.35mm)$, with a built-in boundary condition at one end.

One beam is a simple continuous isotropic cantilever beam. The second is a finite element beam, used in the structures module. The beam was discretized length-wise into 30 finite isotropic beam elements. The comparison shows that under the same forcing conditions, the FEM beam model deflection and torsion corresponds precisely to the cantilever beam deflection and torsion as is presented in Fig. 3.4.

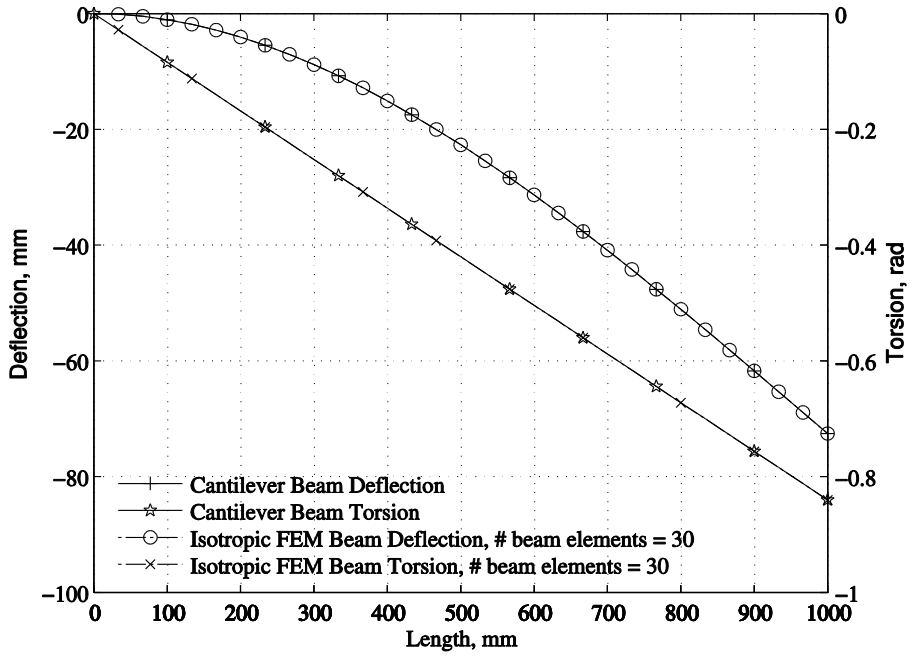

Figure 3.4: Beam Model Verification,{Force, Moment} = {-100N, -100N-m} at Beam End.

The nearly perfect overlay gives confidence that the beam properties of the structure are modeled correctly. This is very important in the generation of accurate mode shapes for the modal filtering process. It is also important when deriving aero mode shapes used to compute GAFs. The next section compares experimental data to the simulation results for modal frequencies and flutter speed and frequency prediction.

3.3.2 Modal Frequencies and Flutter Validation

Validation is completed for a published theoretical/experimental modal analysis and flutter results for a clamped .3048m x .1524m x 0.001588m polybicarbonate plate. The experimental wind tunnel and modal frequency analysis was conducted at Duke University by Conyers et al. [164]. The simulation code modal frequency predictions are compared to that from both the ANSYS code (which they computed) and the

experimental measurements. The simulation code nearly matches the first 5 modal frequencies calculated from ANSYS software and comes very close to experimentally measured frequencies collected into Table 3.1.

Table 3.1: Modal Frequency Code Comparisons and Experimental Results

	ANSYS Frequencies, Hz	Simulation FEM Frequencies, Hz	Duke Univ.'s Experimental Frequencies, Hz
Mode # 1	3.99	3.99	4.13
Mode # 2	16.96	16.97	17.24
Mode # 3	24.86	24.89	24.38
Mode # 4	55.33	55.40	54.25
Mode # 5	69.84	69.92	69.00

They also conducted experimental flutter testing and prediction with their in-house code. The flutter speed and frequency comparisons are presented in Table 3.2.

Table 3.2: Flutter Code Comparisons and Experimental Results

	Duke Univ.'s in-house Flutter Code	Simulation Flutter Code	Duke Univ.'s Wind Tunnel Experimental Results
Flutter speed , m/sec	20.8	19.9	20.05
Flutter frequency, Hz	10.3	10.9	11.50

Table 3.2 shows that the theoretical flutter frequency and speed calculated from the simulation code are very close to Duke's wind tunnel experimental results. In fact, they are closer than the theoretical results from Duke's in-house aeroelastic flutter code. It is postulated that this is due to the increased aero paneling at higher reduced frequencies used in the Simulation code developed herein. These improvements were suggested by Rodden et al. [167].

Within Duke Univ.'s paper, 10 modes were modeled in the aeroelastic analysis to find the theoretical flutter speed and frequencies of the rectangular plate without a hole, but a V-g and V-f plot was not shown. V-g and V-f analyses are presented here in Fig. 3.5 as they were plotted with the simulation flutter code.

a) b)

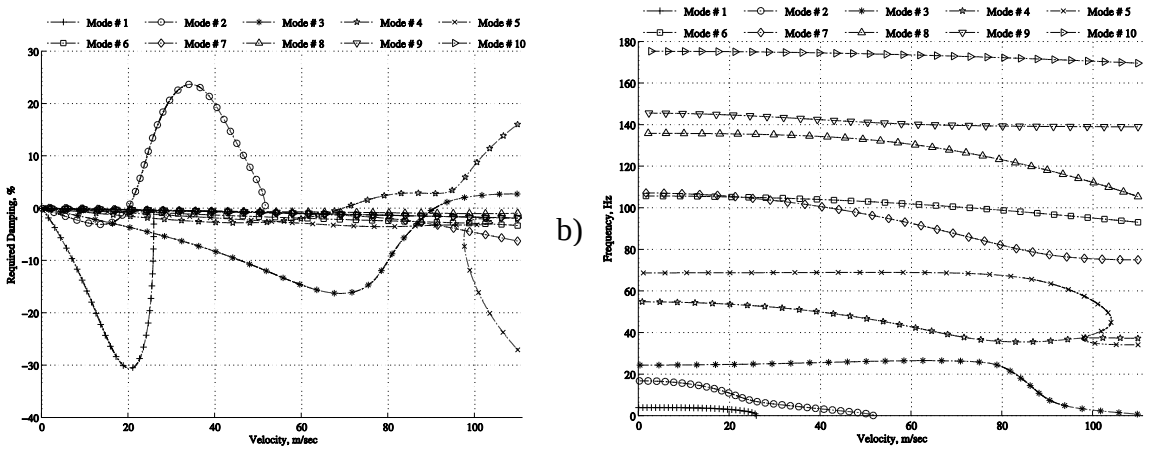

Figure 3.5: Flutter Analysis of Theoretical Plate Model a) V-g Plot; and b) V-f Plot.

It is clear from the V-g analysis in Fig. 3.5(a) that the first two modes (1st bending and 1st torsion) interact. At 19.9 m/sec the 1st torsion mode's damping goes to zero and begins to theoretically flutter. The flutter frequency is found to be 10.9 Hz through inspection of the 1st torsion mode in the V-f plot given in Fig. 3.5(b) at the flutter speed. The closeness of the simulation results with experimental results validates the simulation model for flutter analysis of rectangular wing structures.

CHAPTER 4

WING MODEL

The simulation model developed previously is an excellent tool for testing the modal filter. The question to address is whether or not the modal filter is applicable in an aeroservoelastic setting. Therefore, this chapter directly addresses Research Question 1.

To this end, a methodology for how modal filtering is incorporated into the aeroservoelastic controller is given. To compare the modal controller, its results are given side by side with a controller designed using benchmark accelerometers.

A computational wing model is developed in this Chapter utilizing the simulation from the previous Chapter. The model is fitted with both accelerometers and fiber optic sensors. Two separate controllers are developed for each sensor type for a benchmark comparison. Their robustness to structured uncertainty is compared. This is done with a mu analysis [103]. The performance is analyzed by two simulations. The first simulation compares the controllers' ability to reject gust disturbances and the second demonstrates their aptitude in suppressing flutter.

Both controllers perform almost equally well, which was somewhat unexpected. However, it turns out that modal controllers tended to be much lower order for this particular case study. This Chapter also specifically addresses Research Question 4 by formulating two methods of wing shape control. Shape control is a practical benefit of using a modal filter based controller. The first section introduces the modal filtering design methodology.

4.1 Modal Filtering Design Methodology

The methodology for incorporating the modal filter into the control design of an aeroservoelastic model is divided into three phases. These three phases include the Control Design Phase, Modal Filtering Design Phase and the Shape Reference Signal Design Phase. The phases are presented in the following flow chart in Fig. 4.1.

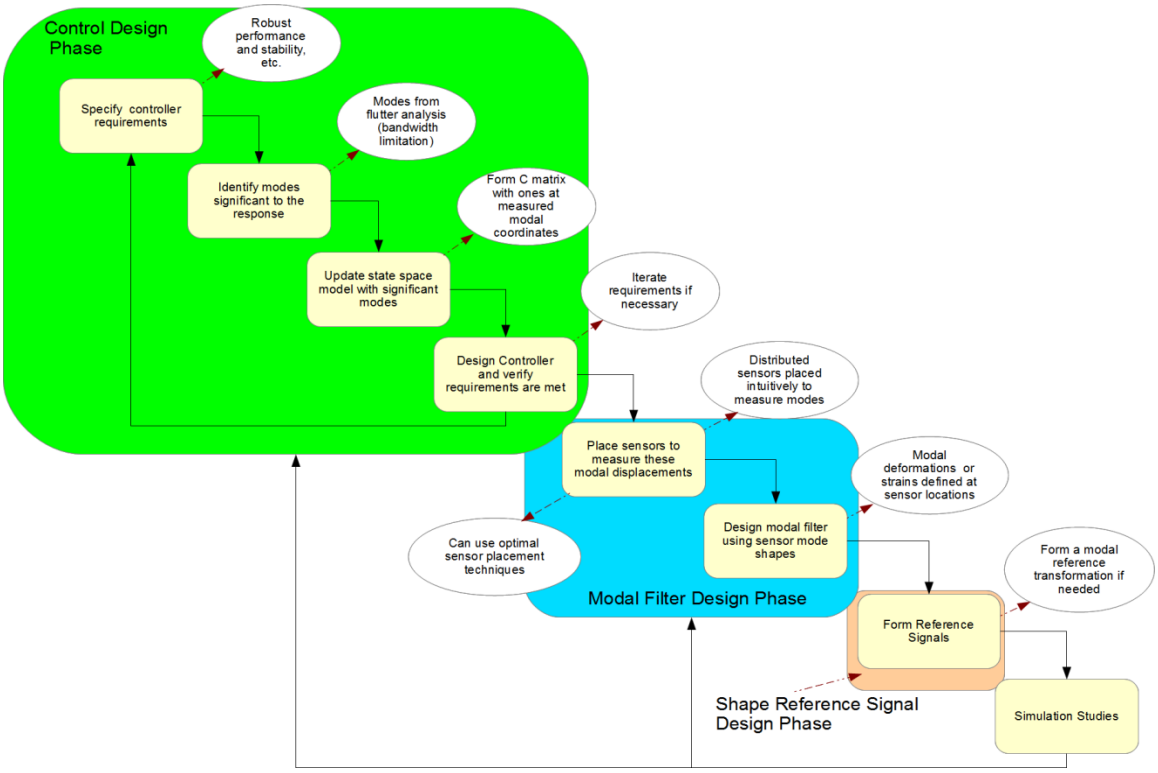

Figure 4.1: Modal Filtering Design Methodology Flow Chart.

The phases introduced in Fig. 4.1 are sequential, because each depends on results of the other. During control design, significant modes are identified and controlled. No structural sensors need to be in place, because the estimation and control design problems

are separate. After it is verified that control of these modal displacements is intelligent, the modal filter design phase ensues.

In the beginning of the modal filter design phase, the sensors are placed in an intuitive sense to measure the modal displacements. For example, if a 1st Bending modal displacement is desired, then it would be intuitive to place FOS span-wise along the wing. If a 1st Torsion modal displacement is required, it would be pertinent to have chord-wise sensor measurements at several different span-wise stations. Once sensors are placed appropriately and modal coordinates are estimated well, reference signal design phase ensues.

The reference signal design phase is necessary depending on what the requirements are for the control design. If suppression only is desired, then no modal reference shaping is required. If it is desired to command a shape, at many specific locations, then a modal transformation it required. That is, a transformation must be performed on the desired deformation references.

After these phases are complete, simulation of the overall system is needed to ensure that all components work together and meet design objectives. Otherwise, iteration on any or all design phases may be required. This concept is captured by the feedback arrows in Fig. 4.1. The following sections give some more details on a modal filter based control design, beginning with the control design phase.

4.1.1 Control Design Phase

Control design can be approached in many ways, so only a general overview of the process is given here. The first step for modal filtering control design is to specify

performance and robustness requirements. For performance, this typically includes specifying targets or bounds for rise time, overshoots, settling time and the overall shape of the response. Robustness must also be achieved in a control design and is approached from varying points of view in the literature. A mu-analysis and Monte Carlo Simulation is recommended.

4.1.1.1 **Identifying Significant Modal Coordinates**

With requirements set, identification of important modes for control feedback must be completed. Significant modes are defined as those modes which contribute strongly to the response and fall within actuator bandwidth. In a structure, the magnitude of the modal mass is often a proportional indicator of modal contribution to the response.

The percent of the total modal mass for the i^{th} mode may be calculated as shown in Eq. (4.1),

$$Pmm_i = \frac{1}{m_T}\frac{\phi_i(x,y,z)^T M u_d}{\phi_i(x,y,z)^T M \phi_i(x,y,z)} \tag{4.1}$$

where m_T is the total mass of the structure, and u_d is an $N \times 1$ reference vector of unit deflections and rotations. Modes with the highest percent modal mass must be selected for feedback, since they may contribute heavily to the response [7]. A good rule of thumb is to include modes which sum to approximately 90% of the total mass of the structure.

But things change when aerodynamic forces are present. In an aeroelastic setting, a flutter analysis (V-g or V-f plots) or convergence study must determine the importance of modal coordinates. Pak [173] shows how to expand the flutter mode as a linear combination of the natural modes and calculate the percent contribution of each mode to flutter. This is necessary due to the fact that modal contributions change with air speed.

So the modal contribution at one dynamic pressure can be completely different than the contribution at another dynamic pressure.

Once the design flight condition and modal displacement feedbacks are decided upon, then the state space models can be modified. This process is given in the following two sections, starting with a definition of the states of a typical aeroservoelastic state space model.

4.1.1.2 **State Definition**

The aeroservoelastic wing model may be represented by a linear time-invariant (LTI) system of finite dimensions as in Eq. (6.9),

$$\begin{matrix} \dot{x}(t) = Ax(t) + Bu(t) \\ y(t) = Cx(t) + Du(t) \end{matrix} \quad x(0) = x_o \tag{4.2}$$

with the initial state $x(0) = x_o$. The n-dimensional vector $x(t)$ is referred to as a state vector and at any time during a simulation can be accessed to give the current "state" of the system about an equilibrium condition. The o-dimensional vector y is the system measurements. The A, B, C and D matrices are real constant matrices with $n \times n$, $n \times c$, $o \times n$ and $o \times c$ dimensions.

According to Eq. (6.9), only the current state and the c-dimensional input u is required to know the state in the next time step. The state vector may be defined as in Eq. (4.3),

$$x(t) \triangleq \{x_q(t), x_{\dot{q}}(t), x_{as}(t), x_{act}(t)\}^T \tag{4.3}$$

where $x_q(t) \in \mathbb{R}^{m\times 1}$ is a vector of modal coordinate displacements, $x_{\dot{q}}(t) \in \mathbb{R}^{m\times 1}$ is a vector of modal coordinate velocities, $x_{as}(t) \in \mathbb{R}^{e\times 1}$ is a vector of aerodynamic lag

states and $x_{act}(t) \in \mathbb{R}^{z\times 1}$ may be formed from a vector of actuator accelerations, velocities, and displacements. The modal filter may be used to sense some or all of the states in the $x_q(t)$ vector, as shown in Eq. (3.10). Any of these states (or combinations of these states) can be used to form the output matrix if the appropriate sensor is utilized. In turn, the output matrix is used during control design.

4.1.1.3 **Modal Coordinate Sensor Output Matrix**

The output matrix C is a matrix of row vectors relating the output sensor to the state vector, x. Since the modal filter directly measures some or all of the x_q state, the output matrix may be cast into the form shown in Eq. (4.4), assuming all modal coordinates are measured.

$$C \triangleq [I_{m\times m} \quad 0_{m\times m} \quad 0_{m\times e} \quad 0_{m\times z}] \tag{4.4}$$

Directly measuring all modes is not required. Higher-order modes which do not significantly contribute to the overall modal deformation in the system may be ignored to reduce the row dimension of the output matrix. This is one of the strengths of the modal filter, to filter out modes which do not matter.

4.1.1.4 **Model Reduction**

There is a multitude of literature on the topic of reducing the order of a controller; two references are given here [104, 107]. Some researchers reduce the plant and design the controller around the reduced order plant. Others reduce the controller after it has been designed around the full plant. It is typical to preserve the dominant eigenvalues in the reduced order model.

A common method of order reduction is to first balance and then then reduce the plant based on the Hankel singular values [174]. This method was selected for the current model. The following discussion pertains to the balancing completed on the stable portion of the plant after partitioning of the plant into stable and unstable parts.

The Hankel singular values $\left\{\sigma_i = \sqrt{\lambda_i(W_c W_o)}, i = 1 \ldots n\right\}$ are derived from the eigenvalues $\{\lambda_i, i = 1 \ldots n\}$ of the square root of the product of the controllability Gramian, W_c ,and observability Gramian, W_o. The Gramians are found from a solution of algebraic equations known as Lyapunov equations, shown in Eq. (4.5).

$$\begin{aligned} AW_c + W_c A^T + BB^T &= 0 \\ A^T W_o + W_o A + C^T C &= 0 \end{aligned} \tag{4.5}$$

The Gramians give a degree of relative observability and controllability if the plant is internally balanced. To balance the plant a transformation on the states $x = Rx_b$ may be found so that the controllability and observability Gramians are both diagonal and equal. The diagonality means that each state has its own independent measure of controllability and observability. The equality of the Gramians indicates that each balanced state is equally controllable and observable (is excited to the same degree to which it is sensed).

The transformation is found by decomposing the solutions of Eq. (4.5): W_c and W_o of the unbalanced system using a singular value decomposition (SVD). The left singular matrix, Z , of W_c may be multiplied with left singular matrix, Q ,of W_o, as in Eq. (4.6).

$$J = QZ \tag{4.6}$$

Another SVD of J may be performed to arrive at $J = V\Gamma U^T$. The transformation matrix is presented as in Eq. (4.7).

$$R = ZU\Gamma^{-1/2} \tag{4.7}$$

The transformed state space matrices are given by the method as is shown in Eq. (4.8).

$$\begin{aligned} A_b &= R^{-1}AR \\ B_b &= R^{-1}B \\ C_b &= CR \end{aligned} \tag{4.8}$$

To reduce the order of the system, states (rows or columns) of the balanced system may be removed which correspond to relatively low Hankel singular values. From the reduced-order model, the reduced-order controller and estimator are designed as it would be from the original plant matrices.

4.1.1.5 **Control Design and Iteration**

Control design can proceed with any desired control methodology. For the wing model, the H_∞ Optimal design methodology is chosen. It is chosen because it can lead to very robust control designs.

The important step of any controller is to verify requirements are met for the controller on the full order plant model. Requirements must also be achieved on a nonlinear simulation model if it is available. Often, to meet the requirements it is necessary to retain more states in the plant used for control design.

Sometimes the requirements are too stringent and must be changed, however. One output of the control design phase is to identify which modal displacements must be used for feedback. Once a controller is accepted, then the modal displacements are also accepted. The design of the modal filter is discussed in the next section.

4.1.2 Modal Filtering Design Phase

The means of estimating the modal coordinates is probably one of the most important aspects of the modal coordinate feedback controller design. The sensors could come in the form of piezoelectric materials [2], fiber optics [66], strain gauges [175], or, potentially, photogrammetry [78]. Each sensor type has different characteristics, which may make some sensors more appropriate for certain systems than others.

For the wing model, the modal matrix, Φ is composed of the natural mode shapes of the system. These mode shapes are mass normalized, making them orthogonal. The measurement of the modes proceed as in Eq. (4.9),

$$\hat{q}(t) = \Phi(l,:)^{\dagger}\, d_m(x_C, y_C, z_C, t) \tag{4.9}$$

where l is the indexed locations of the modal matrix Φ where sensors are located, † is the Moore-Penrose pseudo-inverse and $d_m(x_C, y_C, z_C, t)$ are the measured deformations. For the wing model, it is assumed that the sensors measure deformations directly. This is certainly possible considering the shape algorithms available. The following section describes how the sensors are placed which will be used to compute $d_m(t)$.

4.1.2.1 **Sensor Placement**

One of the discussed gaps was that single point sensors only take snapshots of the true aeroelastic states. Another fact is that single point structural sensors must be optimally placed in order to confidently use them.

This strict rule can be relaxed, when distributed sensors such as the FOS are incorporated onto the structure. With so many sensors, the sensors can be placed in ad

hoc manners, using intuition, rather than complex optimization programs. That is the approach which is to be taken here.

After setting up the sensors to intuitively capture the modal displacements, the modal matrices can be computed. This is done by computing displacements at the sensor locations corresponding to the normal modes in the finite element model. These sensor modes shapes can then be collected into the modal matrix and used as in Eq. (4.9).

A rather important concept is how many modes must be included in the modal matrix. This depends on how many modes are interacting in the system. Enough residual modes must be accounted for or the pseudo-inverse solution of the controlled modal displacements will become biased. After estimation of all modal displacements, the required modal displacements to be controlled can be indexed.

In some cases, reference signal design can be important as was previously discussed. This is especially the case when modal displacements must be tracked. These issues are discussed in the next section.

4.1.3 Reference Signal Design Phase

A modal tracking controller can be used for the purpose of shape control. By controlling modal displacements, the shape of the structure can be uniquely commanded. Deformations are linearly related to modal displacements, assuming small perturbations. A least squares optimal reference signal can be designed. This is achieved by converting the reference deformations at any or all points of the vehicle, into modal references. Only the modes to be controlled must be included in this transformation corresponding to

sensor locations defined in the reference deformation signal. This relationship is given as in Eq. (4.10),

$$q_{ref}(t) = \Phi^{\dagger}(l,:)d_{ref}(x,y,z,t) \tag{4.10}$$

where † is the Moore-Penrose pseudo-inverse operator, and l are indices corresponding to locations where deformations are desired to be controlled.

The problem of forming the vector $d_{ref}(x,y,z,t)$ depends on application. If the desire is to control a specific point on the wing to stay at a specific point, then this vector will have only a few components. If the problem is to globally optimize the shape with some aerodynamic criterion involved, then the vector may have many components. The formation of the vector $d_{ref}(x,y,z,t)$ remains an open problem to be explored. Here the vector is assumed to be known.

The presented design methodology is not easy to accept without an example. So a case study is presented next which follows the three phases which were introduced here. However, some liberties are taken where appropriate.

4.2 Wing Model

The modal filtering design methodology presented previously, serves as a practical guide for the rest of the work in this Chapter. The work begins with the development of a computational test article for proof of concept of the application of modal filtering to the aeroservoelastic problem. This is also a requirement for answering Research Question 1.

To this end, a notional elastic aluminum based rectangular wing clamped at one side is developed the first case study. The dimensions were selected such that the half-span was several times longer than the chord, which would be typical of an aircraft wing.

4.2.1 Geometry

The structure of the wing includes the fore and aft spars, ribs and wing skin, present in many aircraft. The ribs and spars are modeled with structurally equivalent beams. The wing's purpose is to be able to simulate aeroelastic phenomena well and not to mimic any particular vehicle, so details such as shear webs and stringers etc. have been neglected. The geometry for the clamped wing model is presented in Fig. 4.2.

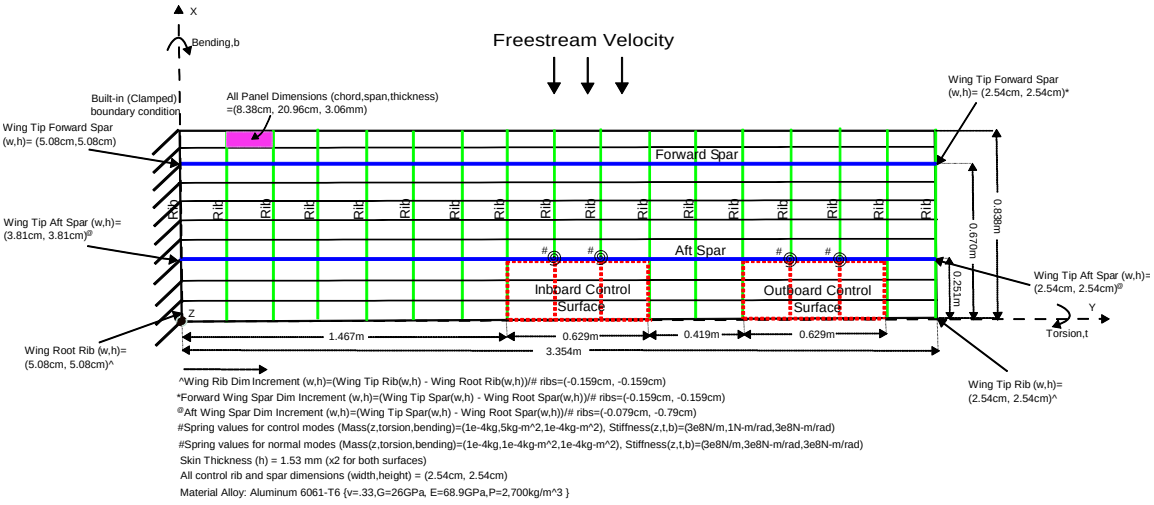

Figure 4.2: Wing Model Geometry and Structural Specifications.

The wing half span was modeled as a 3.354m x .838 m aluminum rectangular plate clamped at the wing root, and made from 6061-T6 aluminum metal alloy traditionally utilized in aircraft flying today. Complete specifications of the structural aspects of the wing are given in Table 4.1.

Aluminum ribs and spars were added to reinforce the structure giving it structural properties similar to an aircraft wing. The leading edge spar was made thicker than the trailing edge spar as it would likely carry more of the lift load. To simulate a more realistic wing where structure would be built up to carry more load near the root, the spars and rib dimensions were linearly tapered towards the wing tips. Control surface panels shown outlined in red dots were also stiffened with leading edge and trailing edge spars, as well as cross-wise ribs along the dotted lines. Each control surface was connected to the wing structure by two 6 DOF springs. The connection joined the wing and control surface at 1/3 and 2/3 of the control surface span.

Table 4.1: Example Geometry Specifications.

	Specifications
Wing Span	6.7m (22ft.)
Wing Chord	0.84m (2.75ft)
Aspect Ratio	8
Control Surface (CS) Span[4]	0.63m (2.06ft)
Control Surface Chord	0.25m (.83ft)
Spar Length	3.35m (11ft.)
Rib Length	0.84m (2.75 ft.) In front of CS - 0.59m (1.94ft.)
Wing Tip Forward Spar	2.54cm.x2.54cm. (1in.x1in.)
Wing Root Forward Spar	5.08cm.x5.08cm. (2in.x2in.)
Wing Tip Aft Spar	2.54cm.x2.54cm. (1in.x1in.)
Wing Root Aft Spar	3.81cm.x3.81cm. (1.5in.x1.5in.)
Wing Tip Rib	2.54cm.x2.54cm. (1in.x1in.)
Wing Root Rib	5.08cm.x5.08cm. (2in.x2in.)
Control Surface Upper Spar	2.54cm.x2.54cm. (1in.x1in.)
Control Surface Lower Spar	2.54cm.x2.54cm. (1in.x1in.)
Control Surface Rib	2.54cm.x2.54cm. (1in.x1in.)
Skin Thickness	1.53mm. (0.06in.)
Material Alloy	Aluminum 6061-T6[5] (v=.33, G=26GPa,E=68.9GPa P=2,700kg/m^3)
Wing Root Boundary Condition	Built-in at centerline (3.35m)

[4] The four control surfaces have exactly the same geometrical specifications and actuators

[5] http://asm.matweb.com/search/SpecificMaterial.asp?bassnum=MA6061t6

4.2.2 Normal Modes

The elastic modes are generated in a control fixed configuration, where the spring connecting the control surface to the wing is assumed to have a stiffness of several magnitudes higher than any component of the global stiffness matrix. The modal frequencies are given in Fig. 4.3.

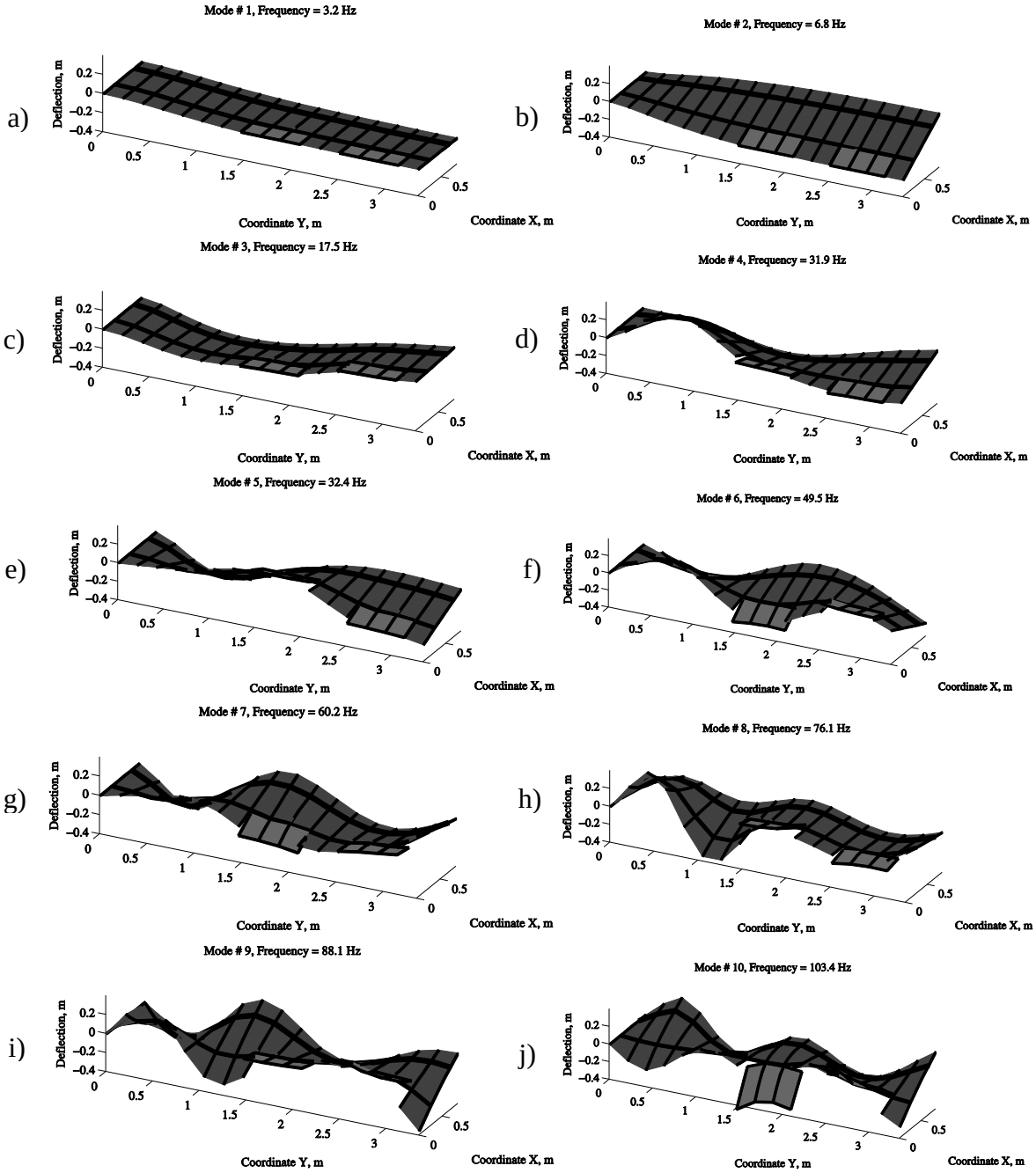

Figure 4.3: Modal Representation of Wing Model: a) 1st Bending (Mode 1); b) 1st Torsion (Mode 2); c) 2nd Bending (Mode 3); d) 2nd Torsion (Mode 4); e) Mode 5; f) Mode 6; g); Mode 7; h) Mode 8; i) Mode 9; and j) Mode 10.

The first 4 modes, in order of appearance and from visual inspection appear to be: 1^{st} wing bending, 1^{st} wing torsion, 2^{nd} wing bending, and 2^{nd} wing torsion. The remaining modes could be considered higher order residual modes. The control modes (1 per control surface) are not shown here, but they are calculated by enforcing a 1 deg. rotation boundary condition on their respective actuators. The next section describes in detail the state space model developed for the wing model in the aero module (See Fig. 3.1).

4.2.3 Aeroelastic Modal Analysis

The Velocity versus damping (V-g) and Velocity versus frequency (V-f) plots are the standard representation of the aero-structural interaction at a particular Mach number and altitude. These charts are essential in a flutter analysis. They can also be used to select design flight conditions.

The V-g plot shows the flight condition at which the structure requires positive damping, and the structure becomes unstable. The V-f plot may be utilized to identify the flutter frequency. To generate the plots, one must specify a reduced frequency range. The GAFs for the aero fit were calculated at reduced frequencies with intervals of 0.2 along $C[0,1.2]$ and Roger's RFA [117] and least squares procedure was utilized to find the aero coefficients. For the following results, compressibility was simulated at a Mach number of 0.25. The altitude was set to 1,000ft standard atmosphere. Both plots are presented in Fig. 4.4.

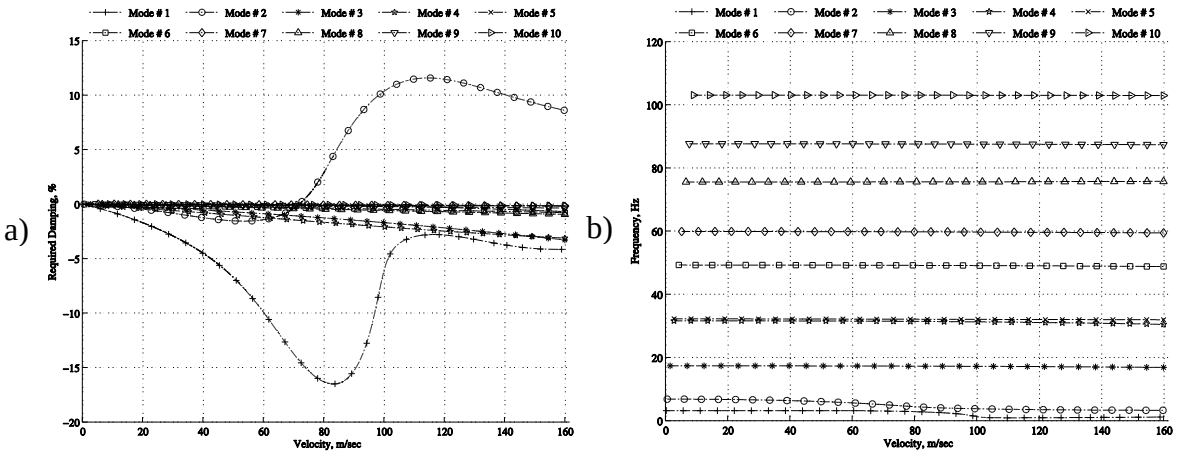

Figure 4.4: Flutter Analysis of Wing Model a) Damping versus Velocity, V-g ; and b) Frequency versus Velocity, V-f.

Notice that the beginning frequency of each mode corresponds to its natural frequency. The frequency of the modes changes with speed as aerodynamic coupling increases. At flutter, two or more modes begin to oscillate at a common frequency. This frequency is determined by the mode which crosses the zero damping line.

From observation of the V-g analysis, the 1st wing bending (mode 1) and 1st wing torsion (mode 2) begin fluttering around 72 m/sec at a frequency of about 4.9Hz. The interaction of the two modes is typical, where the margin of instability of one mode substantially increases and the margin of stability of another mode also increases.

Because further work with modal filtering must also take place on a flutter sensitive flight vehicle, it was desired to select a flight condition for the model after flutter. Therefore, the flight condition was selected to be at 80 m/sec, which is about 8 m/sec past the bending/torsion flutter boundary and at an altitude of 302 m or roughly 1,000 ft. This also represents a feasible flight condition for a lightweight flexible small UAV type aircraft. The characteristics of the model at this flight condition is presented in the next section.

4.2.4 Open Loop Flutter

The aeroelastic wing model is in an open-loop flutter condition, based on the prediction made by the V-g analysis (See Fig. 4.4a) at the freestream velocity of 80 m/s and altitude of 305 m.

To observe the characteristics of the flutter instability, the model was perturbed from equilibrium at time 0 s by a unit deflection command to the control surfaces which lasted for 0.01 s. The time history of the modal coordinates is shown in Fig. 4.5.

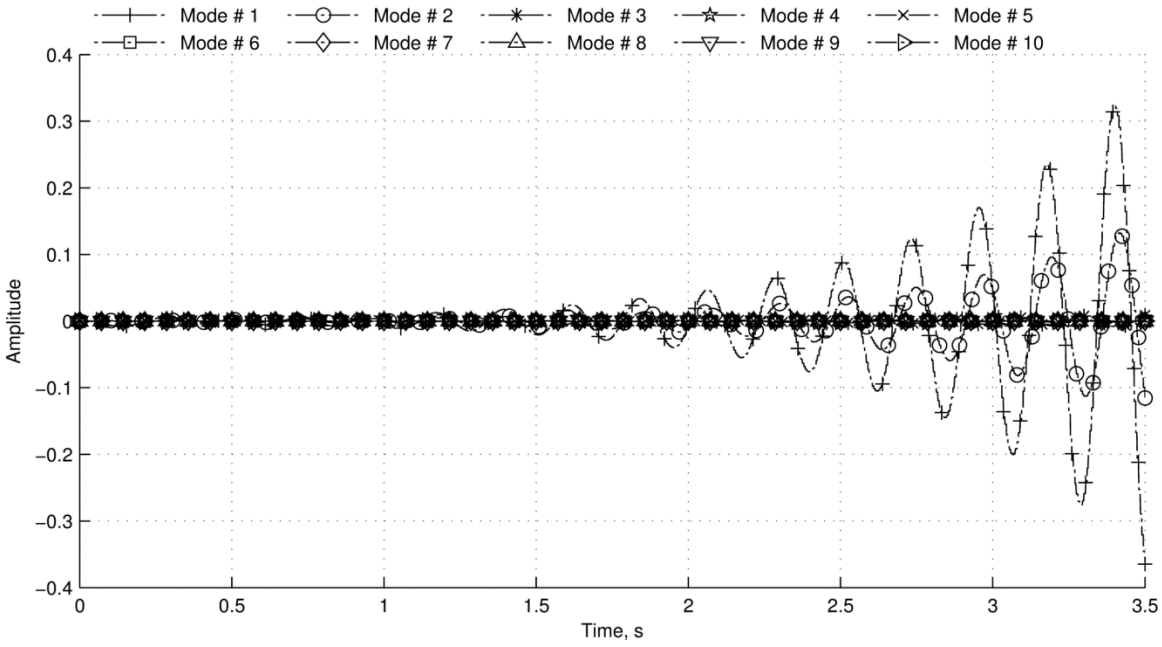

Figure 4.5: Wing Model in Open Loop Flutter.

The first mode corresponds to 1st wing bending. The second mode corresponds to 1st wing torsion. The modal amplitudes oscillate at 4.49 Hz, which was almost predicted by the V-f analysis (See Fig. 4.4[b]). The damping ratio for this mode (from a controls perspective) was -5.3%, which gives it a higher margin of instability than that which was

predicted in the V-g analysis (See Fig. 4.4[a]). The time to double amplitude is 0.46 s, meaning the flutter instability is relatively mild. The bending mode reaches higher amplitudes than the torsion mode, which is expected due to its lower natural frequency. The torsion mode is slightly out of phase with the bending mode. From the above results (See Figs. 4.4 and 4.5), it is apparent that active control is required.

4.2.5 Comparative Control Study

A brief introduction is needed for the following sections. First, it is clear that active control is required for the model. It was decided that in order to properly answer Research Question 1, a comparative control study should be taken. By comparing a modal controller to the benchmark controller with accelerometers, it is easier to evaluate the modal filter based controller. This is preferable to the strategy of simulating the modal filter controller and stating that it is either working or is not working.

To this end, the simulation aeroservoelastic wing model is fitted with either accelerometers or a modal filter (with fiber optic inputs). Plants are designed for both systems with the same inputs. Both plants are different only in that one is using a modal filter and the other is using accelerometers for output. The plants are reduced in order and differences are noted for each.

Several objectives were defined to guide the controller designs so that the controllers could be qualitatively compared. The first objective was for each to stabilize the plant. Figure 4.5 predicts that the wing model undergoes strong open-loop flutter at the flight condition.

The second objective was to reduce the controller order as far as possible. This has the effect of reducing the computational burden in the flight computer. It is also useful from numerical perspectives.

A third objective was for the controller to have good disturbance rejection properties, especially from low-frequency turbulence. Passenger comfort can be improved by actively rejecting gust disturbances [159].

The fourth objective of the controller design was that it must be robust to modeled uncertainty. A controller designed about a linearized model rarely performs the same way in practice as it does in the laboratory [103]. Below, the control design is described in detail, beginning with the sensor system design.

4.2.6 Sensor System Design

Two regulators for the fluttering wing model must be developed. The regulators are given accelerometer inputs and modal coordinate inputs, respectively. The sensor placement strategy for each is described beginning with the accelerometer placement.

4.2.6.1 **Accelerometer Placement**

The first controller was allowed input from two accelerometers. Two were thought to be enough to capture the torsional and bending motion contributing to the flutter mode of the wing model.

The accelerometers were placed using Kammer's Effective Independence (EI) procedure [176]. The EI procedure begins by forming the sensor projection matrix, $H = \Phi(\Phi^T\Phi)^{-1}\Phi^T$ from the modal matrices. Large diagonals, h_{ii} of the projection

matrix H correspond to relatively important sensor locations i on the finite-element wing model.

The EI sensor reduction procedure begins by removing the row of the modal matrix, Φ corresponding to the smallest h_{ii}. The reduced projection matrix is then recalculated and the row corresponding to the smallest h_{ii} is again removed.

This reduction process can be iterated to the desired number of sensors, which are then used to form the index l used in Eq. (4.12). The EI procedure tends to select sensors that carry the highest amount of the desired modal information. The resulting sensor placements are shown in Fig. 4.6.

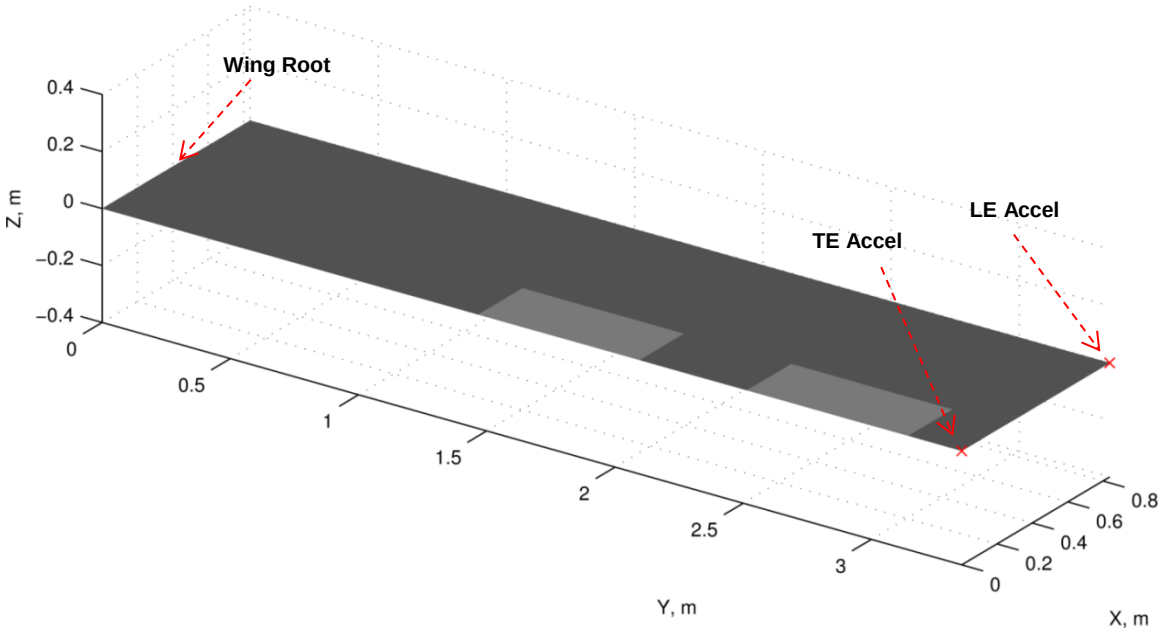

Figure 4.6: Accelerometer placement on wing model.

By down-selecting the rows of the modal matrix to the wing tips, the EI procedure indicates that the wing tips (both leading edge and trailing edge) carry the most modal information. "The most modal information" in this case means that the first wing bending and wing torsion modes had the highest deformation at these points (See Fig. 4.3[a-b]).

The EI procedure is only a first step and was used for its simplicity. The EI procedure contains flaws in that it does not attempt to optimize sensor layout for residual modes. It has been shown that residual modes tend to corrupt the sensor signal, leading to observation spillover [25]. Thus, optimization procedures, such as the modified EI procedure [177], have been developed to place sensors on a BWB-type aircraft while minimizing residual mode information.

The EI procedure is also sensitive to structure with many nodes, because nodes tend to be very close together and many good locations may fall in the same spot. The severity of this problem can be reduced by using correlation matrices to select sensor locations that maximize modal information without redundancy [174]. The next section demonstrates how accelerometers were modeled in the state space matrices.

4.2.6.2 **Accelerometer Sensor Output Matrix**

The output matrix must be adjusted to account for accelerometer measurements. Rather than measuring directly any part of the state vector, accelerometers measure linear combinations of modal coordinate accelerations. The relationship between the accelerometers and the state of the system is often modeled as shown in Eq. (4.11).

$$y(t) \triangleq C_m \dot{x}(t) = C_m(Ax(t) + Bu(t)) \tag{4.11}$$

The matrix $C_m \in \mathbb{R}^{a \times n}$ has as many rows as accelerometers, a, and as many columns as the state space vector size. The matrix C_m is defined (See Ref. [45]) as shown in Eq. (4.12),

$$C_m \triangleq [0_{a\times m} \quad \Phi_{a\times m}(l,:) \quad 0_{a\times e} \quad 0_{a\times z}] \tag{4.12}$$

where $\Phi_{a\times m}(l,:)$ is the displacement modal matrix row indexed by l. The next section reviews the development of the modal coordinate selection process for the controller.

4.2.6.3 **Modal Coordinate Selection**

The second controller is designed with modal coordinate feedback. The modes which dominate the deformation of the structure and can be easily controlled and observed should be selected for feedback. It is also important that the normal modes' natural frequencies are within the actuator bandwidth.

For curiosity's sake, the percent of the modal mass for each mode was calculated by Eq. (4.1) and is given in Fig. 4.7.

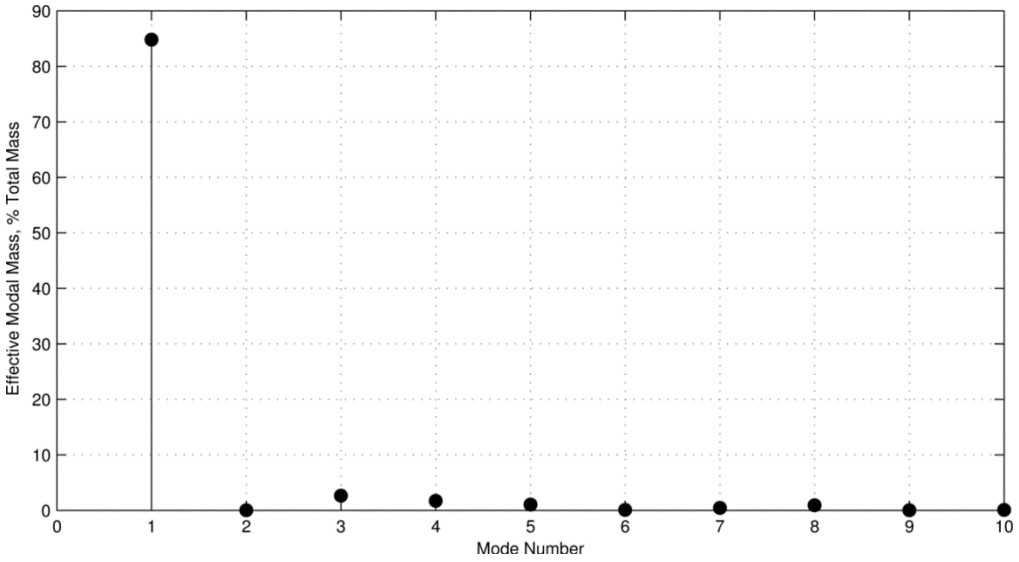

Figure 4.7: Percent Modal Mass per Mode Shape.

Recall that the modal mass is a strong indicator of a modes ability to be excited. The percent modal mass of the first bending mode is the highest at 85%, indicating that it will be a mode which both contributes significantly to the modal response and can likely be easily controlled and observed [170]. It is difficult to state an exact measure of observability and controllability of modes, as the measure of observability and controllability will be determined by the placement of the control effectors and sensors

(See Refs. [7] and [178]). It is also important to consider the interaction of aerodynamic forces and modal frequencies.

Recall that the airflow interacts with the structure (See Fig. 4.4) near flutter so that some modes tend to dominate the structural deformation more than others. The flutter analysis at the selected flight condition indicates that the torsion mode will also be highly mobile near flutter. As such, based on the observation of the flutter interaction 1st wing bending and 1st wing torsion modal coordinates were selected for feedback.

4.2.6.4 **Fiber Optic Sensor Placement**

Since FOS has already been tested on aircraft (See Ref. [179]) this distributed sensor was selected for the true sensor feedback to the modal filter. The selected modes for feedback include strong bending and torsion effects. The fibers were placed intuitively so that this modal information could be estimated. The modeled layout on the wing model is shown in green in Fig. 4.8.

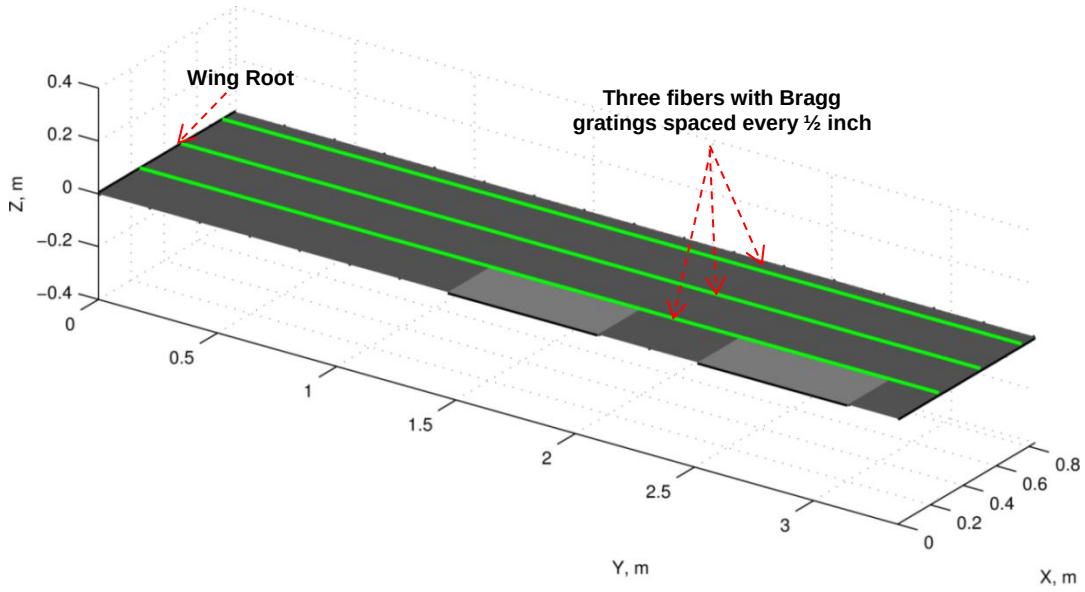

Figure 4.8: Fiber Optic Sensor Placement on Wing Model.

To capture sufficient bending information, the sensors are placed span-wise along the entire wing. To capture torsional effects, three fibers are placed chord-wise. The spacing between each sensor location along each fiber was set at ½-inch intervals, which is the same spacing used on the NASA Ikhana Predator B unmanned aircraft [179].

The use of a strain-shape algorithm need not be required to use the FOS for modal coordinate estimation. Work by Kang et al. [66] has shown that FOS measurements can be utilized to estimate modal coordinates. But instead of a modal matrix, Φ, a strain mode matrix, Ψ ,is formed, which can then be utilized as shown in Eq. (1.10). The strain mode matrix is simply the modal representation in units of strain.

For the wing model, it is assumed that deflections are directly measured at FOS locations. This was done because strain mode capabilities were not available in the developed finite element model. Assuming deflections are measured instead of strains is not a big assumption. Several methods described previously have been developed for the purpose of estimating deflection from strain. In fact, Eq. (1.18) shows precisely how strain can be used to estimate deflections at FOS locations.

4.2.7 Controller Design

Up to this point the selection of accelerometer placements and FOS placements has been completed. The process of control design is discussed here. This is a little out of order than that which was given in the methodology. This is done in order to keep the discussion of the modal coordinate based controller and accelerometer based controllers

in the same areas. In fact, before placing the FOS, the controller design was already completed.

In any case results of reducing the order of the plant are discussed for each sensor type. The controller methodology used for each model is discussed. The robust stability is also analyzed for each closed loop system with two structured uncertainty cases. The following section discusses the results of model reduction for both plants.

4.2.7.1 **Model Reduction**

Sensor selection is very important in control order reduction. The transformation matrix R [See Eq. (4.7)] is directly dependent on the SVD of J [See Eq. (4.6)]. The matrix J is, in turn, directly dependent on the SVD of W_o. Therefore, Eq. (4.5) gives a direct relationship between the output matrix C and W_o.

The use of either modal coordinates or accelerometers affects the form of the output matrix and thus will affect the relative Hankel singular values through the eigensolution. To illustrate this effect more clearly, the relative unit-normalized Hankel singular values of the balanced systems with accelerometer outputs and modal coordinate outputs are given in Fig. 4.9.

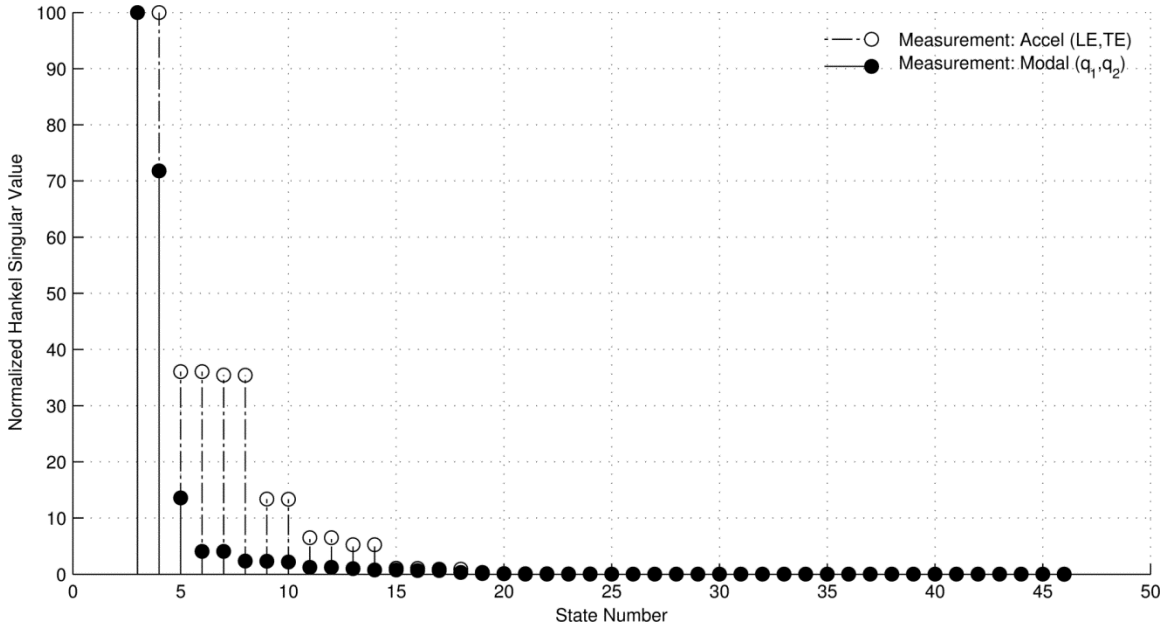

Figure 4.9: Comparison of Normalized Hankel Singular Values for Two plants.

The first plant with accelerometer outputs has significant unit-normalized Hankel singular values out to state 14. The Hankel singular values for the second plant with modal coordinate outputs show a very steep drop-off after the 5^{th} state.

It is not precisely known why this occurs. The steep drop-off may be accounted for by the fact that no relationship in the output matrix is given for modes past the first two modal states. Since the higher modes are not as observable to the system, their input-output contribution is less.

The presentation of the Hankel singular values in this form may indicate that the controller order could be reduced based only on the relative magnitude of the singular values. It was found, however, that proceeding thus blindly could lead to an unstable controller.

A more rigorous approach was taken, by reducing the order of the controller by removing states corresponding to the lowest Hankel singular values until the reduced-

order controller performance diverged significantly from the performance of the original full controller (See Ref. [174]). The pole comparison of the two plants is given in Fig. 4.10.

a)

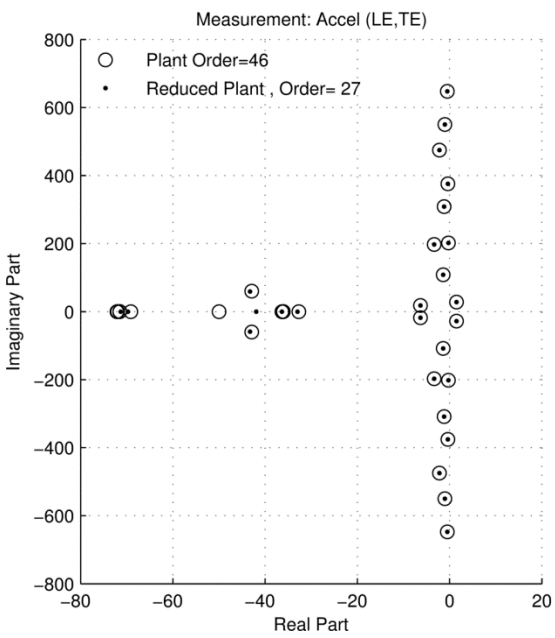

b)

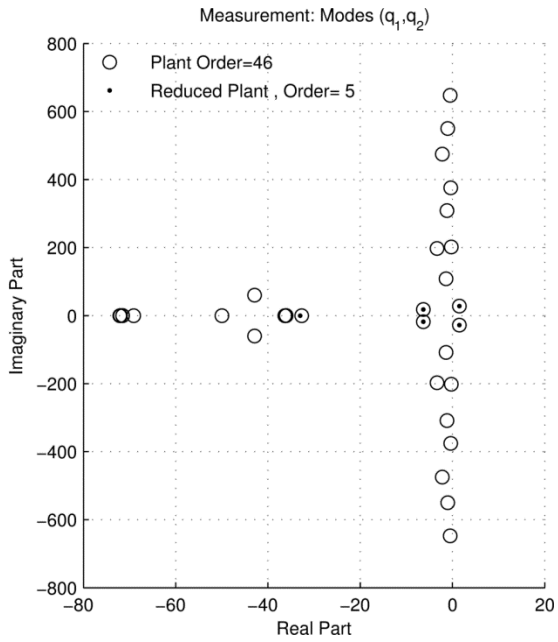

Figure 4.10: Order reduction: a) Plant with Accelerometer Output; and b) Plant with Modal Coordinate Output.

The plant with accelerometer outputs was not reduced as far as was the plant with modal coordinate outputs. The final order of the plant with accelerometer outputs was 27. The final order of the plant with modal coordinate outputs was 5. The plant poles shown in Fig. 4.10 qualitatively compare well to many structures, in which lightly damped modes are very near the imaginary axis [7]. Sometimes these lightly-damped modes can become unstable due to interaction with a flight control system, described previously as SMI.

For the present case, aerodynamic coupling (See Fig. 4), is the cause of the pole migration to the right half-plane (RHP). Simulation results in Fig. 4.5 indicated that two

modes are unstable in the model. The poles in Fig. 4.10 which have moved into the RHP characterize this instability as a flutter instability. One of the primary objectives of the present work is to actively suppress this flutter mode. That process is described below.

4.2.7.2 **H-Infinity Optimal Control**

Many choices for control design are available once a state space model has been defined as in Eq. (3.13). The H_∞ optimal controller [103] was chosen for this study because it has a wide range of applicability. One excellent feature is that it is not assumed that the disturbances are collocated with the control inputs. The locations of controlled outputs are not necessarily collocated with the location of system performance as they are in the LQG controller design [174].

The H_∞ Optimal controller was designed for both reduced-order plants shown in Fig. 4.10(a-b). The reduced order plants were cast into the state-space realization shown in Eq. (4.13),

$$\begin{aligned} \dot{x}_b(t) &= A_b x_b(t) + B_1 w(t) + B_2 u(t) \\ z(t) &= C_1 x_b(t) + D_{12} u(t) \\ y(t) &= C_2 x_b(t) + D_{21} w(t) \end{aligned} \tag{4.13}$$

where $A_b \in \mathbb{R}^{n_r \times n_r}$ is the reduced-order state matrix, $B_1 \in \mathbb{R}^{n_r \times w}$ is the disturbance matrix, $B_2 \in \mathbb{R}^{n_r \times c}$ is the control input matrix, $C_1 \in \mathbb{R}^{e \times n_r}$ is the state-regulated goal matrix, $D_{12} \in \mathbb{R}^{e \times u}$ is the control-regulated goal matrix, $C_2 \in \mathbb{R}^{m \times n_r}$ is the measurement matrix, $D_{21} \in \mathbb{R}^{m \times w}$ is the measurement noise matrix. The reduced-order states, $x_b(\mathrm{t}) \in \mathbb{R}^{n_r \times 1}$ are driven by the disturbances, $w(t) \in \mathbb{R}^{w \times 1}$ and the control inputs, $u(t) \in \mathbb{R}^{c \times 1}$.

The goal of the H_∞ optimal control methodology is to find the controller K which minimizes the H_∞ norm of the transfer function $G_{wz}(K)$ from disturbance w to regulated

output z, over all possible controllers [174]. Recall that the H_∞ norm of a transfer function is defined as the supremum or least upper bound of the transfer function over all frequencies. So, more simply stated, the H_∞ synthesis routine results in a controller which best suppresses the peak of $G_{wz}(s)$, where s is the Laplace variable.

The suboptimal Ricatti solution of the H_∞ problem requires that two algebraic Ricatti equations must be solved in which the observer and the controller matrices are coupled by an inequality constraint on the spectral radius ρ. Another constraint is also included to assure that the Hamiltonian matrices do not have eigenvalues on the imaginary axis, which may cancel poles or zeros on the imaginary axis and lead to instability.

Typically, the objective function is minimized with a local optimization technique such as the bi-section method, which generally performs well since the objective function is convex [103]. The resulting H_∞ controller may then be represented as in Eq. (4.14),

$$\begin{gathered}\dot{\hat{x}}(t) = (A + \rho^{-2}B_1B_1^TS_{\infty c} - B_2K_c - K_eC_2)\hat{x}(t) + K_ey(t) \\ u(t) = -K_c\hat{x}(t)\end{gathered} \tag{4.14}$$

where $S_{\infty c} \in \mathbb{R}^{n\times n}$ is the solution to the control algebraic Ricatti equation, K_e is the filter gain matrix, and $\hat{x}(\mathrm{t}) \in \mathbb{R}^{n_r\times 1}$ is the estimated state vector of the reduced-order plant. For more detail on the H_∞ problem formulations and solutions, refer to Refs. [103] and [174].

For control design the two reduced-order plants were subjected to the same disturbance input matrix, B_1. The matrix was formed from a gust model and process noise weights. The gust model representing the interaction of a wind gust with the modal velocities was derived from a sinusoidal gust column [180]. The sinusoidal gust column is initialized from 0 m/s wind speed at the leading edge of the wing model building in

strength towards the trailing edge of the wing. The derived gust basis represents the physical effect of the gust in modal space and is used in the weighting scheme as well as for simulation later on.

The first column of disturbance weighting matrix B_1 was represented as the velocity basis of the gust weighted with a sustained gust velocity, $w_g(t)$,of 5 m/s. The second column of B_1 was represented by the acceleration basis of the gust weighted with a sustained gust acceleration, $\dot{w}_g(t)$, of 9.81 m/s^2. This is chosen very large on purpose to improve the controller's disturbance rejection. The weighting matrix B_1 was also augmented with unit vectors characterizing the presence of process noise.

For control design on both reduced-order plants, the goal state matrix C_1 was modified so that the first two modes would receive highest weights. The first two modes were weighted highest since Fig. 4.4 indicates that these two modes will have a flutter interaction. By giving the first two modes higher weightings, the optimization technique emphasizes the reduction of the peaks of the first two modes due to the gust disturbance across the frequency range of $G_{wz}(s)$ as much as possible. The control-regulated goal matrix D_{12} was given equal weightings which penalized high control surface movement.

The measurement matrix C_2 was set for each controller respectively to either Eq. (4.4) for the controller with modal coordinate input or Eq. (4.12) for the controller with accelerometer input. The controller's sensitivity to measurement noise was also reduced by modifying the weighting matrix D_{21} with moderately high weights corresponding to each sensor.

4.2.7.3 **Robust Stability**

The H_∞ synthesis does not always result in a controller which meets performance specifications; thus the controller design process is an iterative one. To bound the design process, objectives were defined for both control designs. Assuming an initially-stable control design, two objectives for the controllers were that each should be robust to structured uncertainty and also have good disturbance rejection properties.

More specifically, the first goal for both controllers was that they be robust to at least 5% multiplicative uncertainty on the inputs or outputs of the plant at a low frequency of 1Hz. They should also be robust to at least 25% multiplicative uncertainty near the higher flutter frequency of 4.49 Hz. Secondly, each controller was designed to mitigate the modeled sinusoidal gust disturbance described in the section above.

A quantitative measure of the robust stability margin of both controllers is the structured singular values (SSV) or μ. The SSV is defined as shown in Eq. (4.15) [103],

$$\mu(O) \triangleq \frac{1}{min\{k_m | \, det(I - k_m O\Delta) = 0 \text{ for structured } \Delta, \bar{\sigma}(\Delta) \leq 1\}} \qquad (4.15)$$

where k_m is the stability margin defined as $k_m = 1/\mu(O)$, O is the lower linear fractional transformation (LFT) of the generalized plant P, Δ represents a structured uncertainty block, and the maximum singular value of Δ is defined by $\bar{\sigma}(\Delta)$. The value of $\mu = 1$ occurs when there is a perturbation with $\bar{\sigma}(\Delta) \leq 1$, which is just large enough to make $I - O\Delta$ singular.

A larger value of μ is undesirable, as it means that a smaller perturbation makes $I - O\Delta$ singular. The "generalized small gain theorem" (See Ref. [103]) states the robust stability (RS) condition, as shown in Eq. (4.16).

$$RS \Leftrightarrow \mu\big(O(\hat{\imath}\omega)\big) < 1 \; and \; \bar{\sigma}\big(\Delta(\hat{\imath}\omega)\big) < 1, \forall\omega \tag{4.16}$$

To verify RS for both plants, both reduced-order plants were subjected to multiplicative input or output uncertainty. The class of all generalized plants for multiplicative input uncertainty is given as shown in Eq. (4.17).

$$G_I(s) = G(I + W_I\Delta_I) \tag{4.17}$$

The class of all generalized plants for multiplicative output uncertainty is given as shown in Eq. (4.18).

$$G_O(s) = (I + W_O\Delta_O)G \tag{4.18}$$

The structure of the input and output weights is defined to be diagonal; that is $W \triangleq diag\{w_i(s), i = 1 \ldots b\}$. For W_I, b is a scalar equal to the dimension of the inputs. For W_O, b is set equal to the scalar dimension of the outputs. The uncertainty block Δ for both input and outputs is defined to be diagonal, $\Delta \triangleq diag\{\delta_i, i = 1 \ldots b\}$, where b is set accordingly for inputs and outputs. The uncertainties on the diagonal δ_i are also defined to be < 1, so that the RS condition shown in Eq. (4.16) always holds.

Generally, uncertainty is greater at higher frequencies, so the uncertainty is made to vary with frequency by weight functions, as shown in Eq. (4.19).

$$w_i(s) = \frac{\tau s + r_o}{\left(\frac{\tau}{r_\infty}\right)s + 1} \tag{4.19}$$

The constant r_o is the relative uncertainty magnitude at steady state; and $1/\tau$ is approximately the frequency where the relative uncertainty reaches 100%. The constant r_∞ is the magnitude of the weight at higher frequencies. The constants were selected so that the uncertainty would be greater than 5% at 1 Hz and greater than 25% near the flutter frequency of 4.49 Hz.

The plant with input multiplicative uncertainty is modeled as that given in Fig. 4.11.

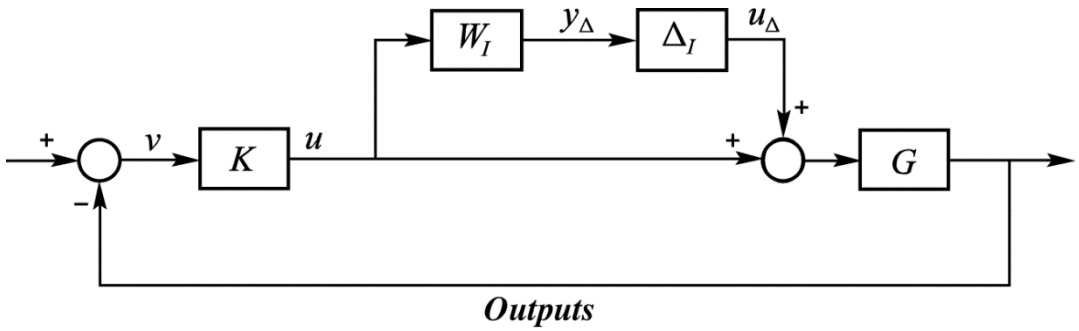

Figure 4.11: Generalized Plant with Structured Input Uncertainty.

For the inputs $[y_\Delta, u]^T$ and the outputs $[u_\Delta, v]^T$, the generalized plant with multiplicative input uncertainty defined above may be shown to be as presented in Eq. (4.20).

$$P_I = \begin{bmatrix} 0 & W_I \\ -G & -G \end{bmatrix} \tag{4.20}$$

The O structure may be formed from a lower LFT of P_I and K represented as $F_l(P_I, K)$. By carrying out the matrix operations it can be shown that $O = -W_I KG(I + KG)^{-1} = -W_I T_I$, where T_I is the input complementary function. The $\mu(O)$ for the H_∞ controllers with multiplicative control input uncertainty is given in Fig. 4.12.

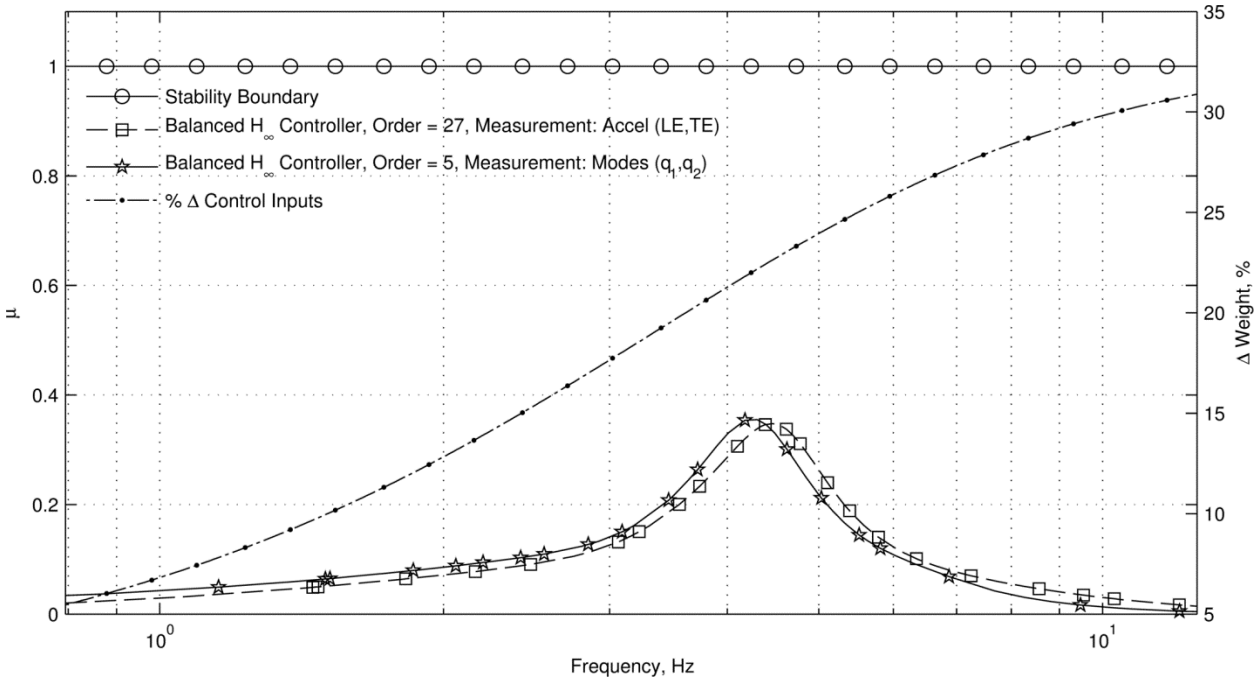

Figure 4.12: Structured Singular Value Analysis with Input Multiplicative Uncertainty.

The stability boundary is defined to be 1 for μ as is a requirement for RS from Eq. (4.16). The maximum μ for the controller with modal coordinate inputs is approximately 0.36 at 2.14 Hz. The maximum μ for the controller with accelerometer inputs was approximately 0.35 at 2.23 Hz. The μ for both controllers was bell-shaped across the frequency range. The H_∞ controller with accelerometer inputs resulted in a closed-loop system which was slightly more robust to input uncertainty.

The difference is not substantial, however. Both controllers seemed to experience a peak in μ near 2.2 Hz. One might expect the peak to occur at the open-loop flutter frequency of 4.49 Hz; however, the frequencies correspond to the closed-loop pole locations. From this analysis, it was determined that both controllers meet and exceed expectations with respect to input multiplicative uncertainty. They also perform very similar.

Output uncertainty is also of interest, since different measurement systems are being utilized. The plant with output multiplicative uncertainty is modeled as that given in Fig. 4.13.

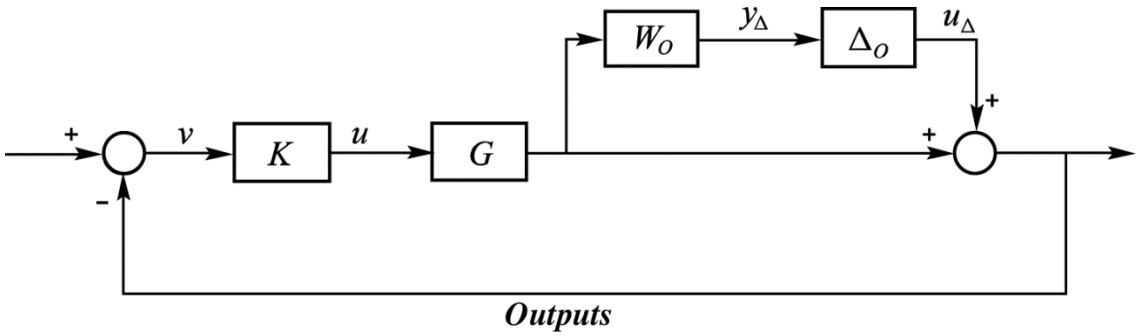

Figure 4.13: Generalized Plant with Multiplicative Output Uncertainty.

For inputs, $[y_\Delta, u]^T$ and outputs $[u_\Delta, v]^T$, the generalized plant with multiplicative output uncertainty defined above may be shown to be as presented in Eq. (4.21).

$$P_O = \begin{bmatrix} 0 & W_O G \\ -I & -G \end{bmatrix} \tag{4.21}$$

The O structure may be formed from a lower LFT of P_O and K represented by $F_l(P_O, K)$. By carrying out the matrix operations, it can be shown that $O = -W_O(I + GK)^{-1}GK = -W_O T$, where T is the output complementary sensitivity function. The $\mu(O)$ calculated for both H_∞ controllers with multiplicative measurement output uncertainty is given in Fig. 4.14.

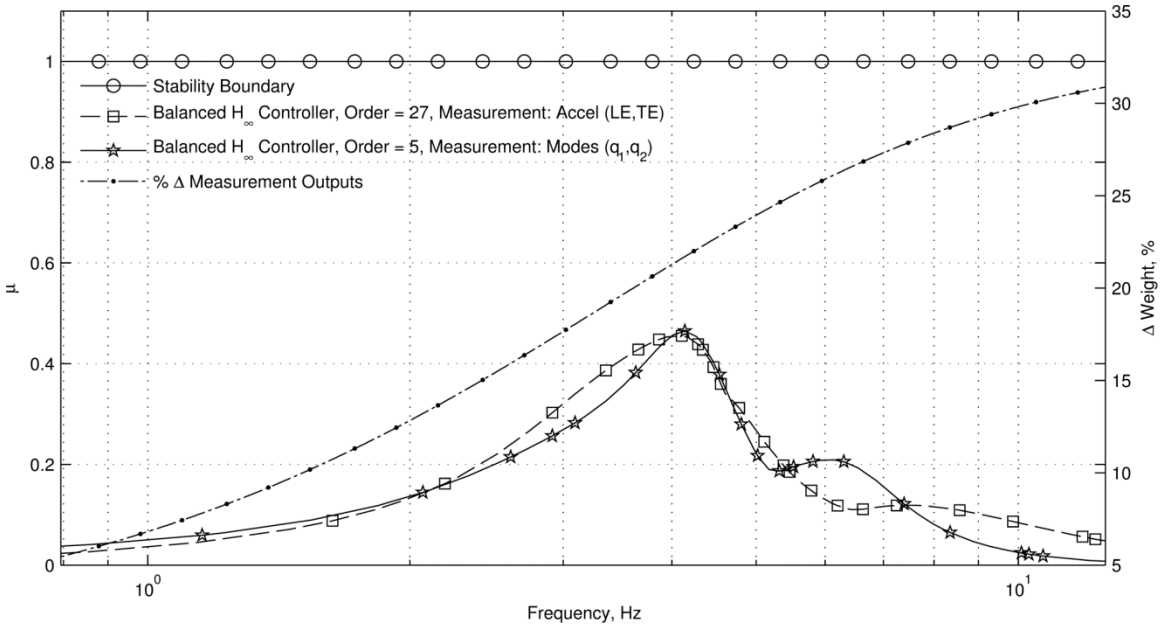

Figure 4.14: Structured Singular Value Analysis with Output Multiplicative Uncertainty.

The maximum μ for the controller with modal coordinate inputs is approximately 0.47 at 2.10 Hz. The μ for the controller with modal coordinate inputs experienced a second peak near a frequency of 3.38 Hz. The maximum μ for the controller with accelerometer inputs was approximately 0.46 at 2.08 Hz. The μ for the controller with accelerometer inputs was nearly bell-shaped across most of the frequency range, and descended until a frequency of 3.54 Hz, at which point it climbed for a short time. Overall, the characteristics of the μ for both controllers indicate that the H_∞ controller with accelerometers resulted in a closed-loop system which was slightly more robust to output uncertainty. However, the relative stability margin difference between the two controllers is negligible.

Both controllers meet and exceed expectations with respect to output multiplicative uncertainty. In fact, both controllers performed almost equally well. This

seems to indicate that no great benefit is obtained in the control architecture from using either sensor type.

It was observed that the modal filter based controller was lower order. The hypothesis is that the lower order is due to the modal filter's focused suppression of the first two modes. Keeping in mind that no significant benefits or detriments are seen as yet by using either sensor, simulations can now be performed.

4.3 Simulation

The time simulation of controllers is a reliable way to diagnose performance and make comparisons. It is also useful for determining if a controller must be redesigned or if the requirements must be moved.

Several case studies were selected to be performed with different objectives. The first two case studies pertain to GLA and AFS. The next two case studies focused on the use of modal filtering for virtual deformation estimation and tracking on the wing. The original plants designed at 80 m/s at an altitude of 302 m were upgraded with "integral of modal position" states and reduced.

New controllers were then derived using the same methodology presented for the regulators. The first controller tracks virtual deformations from a modal command; the second controller tracks the same virtual deformations with a virtual deformation modal approximation. These two methods of shape control were simulated in an effort to answer Research Question 4. First, the gust disturbance simulation results are presented.

4.3.1 Gust Disturbance

The regulators described above were tested in a simulation environment, with a gust disturbance input. The simulation structure that was used to model the gust disturbance for the controller with modal coordinate inputs is given in Fig. 4.15.

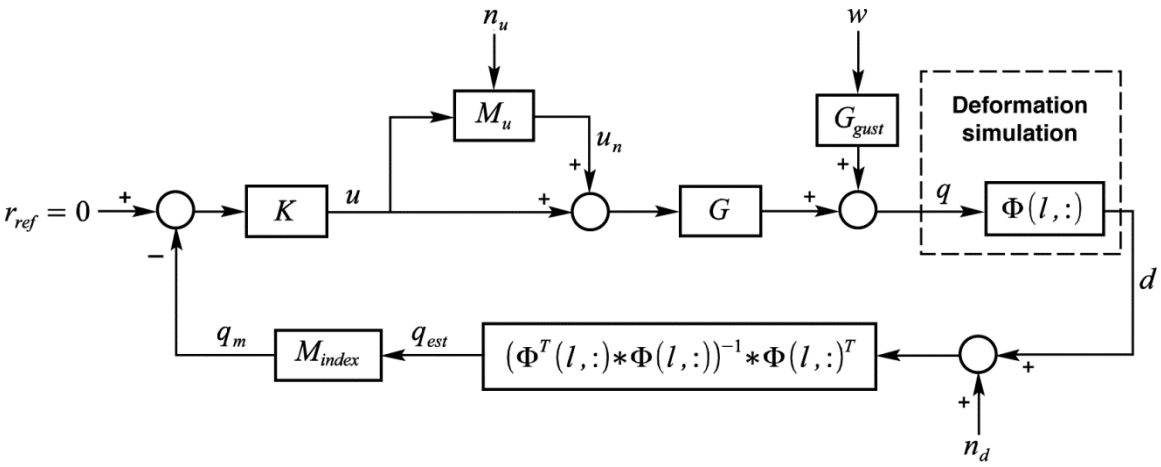

Figure 4.15: Control Simulation with Modal Filter for Gust Modeling.

The simulation structure for the accelerometer inputs is the same except that the connection after the gust inputs is input directly into the summing block with the reference input. The exogenous inputs to the system are $[n_u, w, n_d]^T$ corresponding to input multiplicative noise, gust disturbance states, and additive measurement noise. Zero mean multiplicative Gaussian noise, n_u, with a standard deviation of 0.1, is modeled on each control input for both control systems, making M_u in Fig. 4.15 the identity matrix of size c.

The standard $1 - \cos(x)$ gust profile (See Ref. [180] and Fig. 3.3) is modeled to characterize the transient shape of the gust disturbance $w = \{w_g(t)\ \dot{w}_g(t)\}^T$ which lasts for 1.6 s. The gust velocity and acceleration at time 0 are both initialized to zero. The gust

is shaped to achieve a maximum velocity, $w_g(t)$ of 5 m/s and a maximum acceleration $\dot{w}_g(t)$ of 9.81 m/s^2. The signals, $w_g(t)$ and $\dot{w}_g(t)$ are input to the LTI gust system G_{gust} which acts as a disturbance on the output of the plant, G.

For the controller with modal coordinate inputs, zero mean Gaussian noise n_d with a standard deviation of 1 cm was added to the measurement signals. Deformations are used instead of strain because strain was not available directly in the model. When accelerometers were used in place of the deformation measurements, it was assumed that the additive noise had a standard deviation of 1.0 m/s^2.

For the controller with modal coordinate inputs, the noise was added to the simulated deformations at locations shown in Fig. 4.8. Accelerometer measurements tend to be somewhat noisy, whereas fiber optic measurement systems are expected to produce measurements with a very high signal-to-noise ratio [181].

This model being a simulation model, true displacement measurements were not available. The controller with modal coordinate inputs makes use of a deformation simulation, by multiplying the modal matrix Φ indexed at measurement index stations l with the true modal coordinates, q.

The modeled displacement information and additive displacement noise is input into the least-squares modal filter introduced in Eq. (4.9). The estimated modal coordinates are then indexed ($M_{index} = \{1,2\}$) to obtain q_m. This signal is then used to form the control signal input to the H_∞ controller, K.

Since GLA is the objective of the controller, the reference on each measurement is set to 0. The gust simulation results are presented in Fig. 4.16 for the controllers with acceleration inputs and modal coordinate inputs respectively.

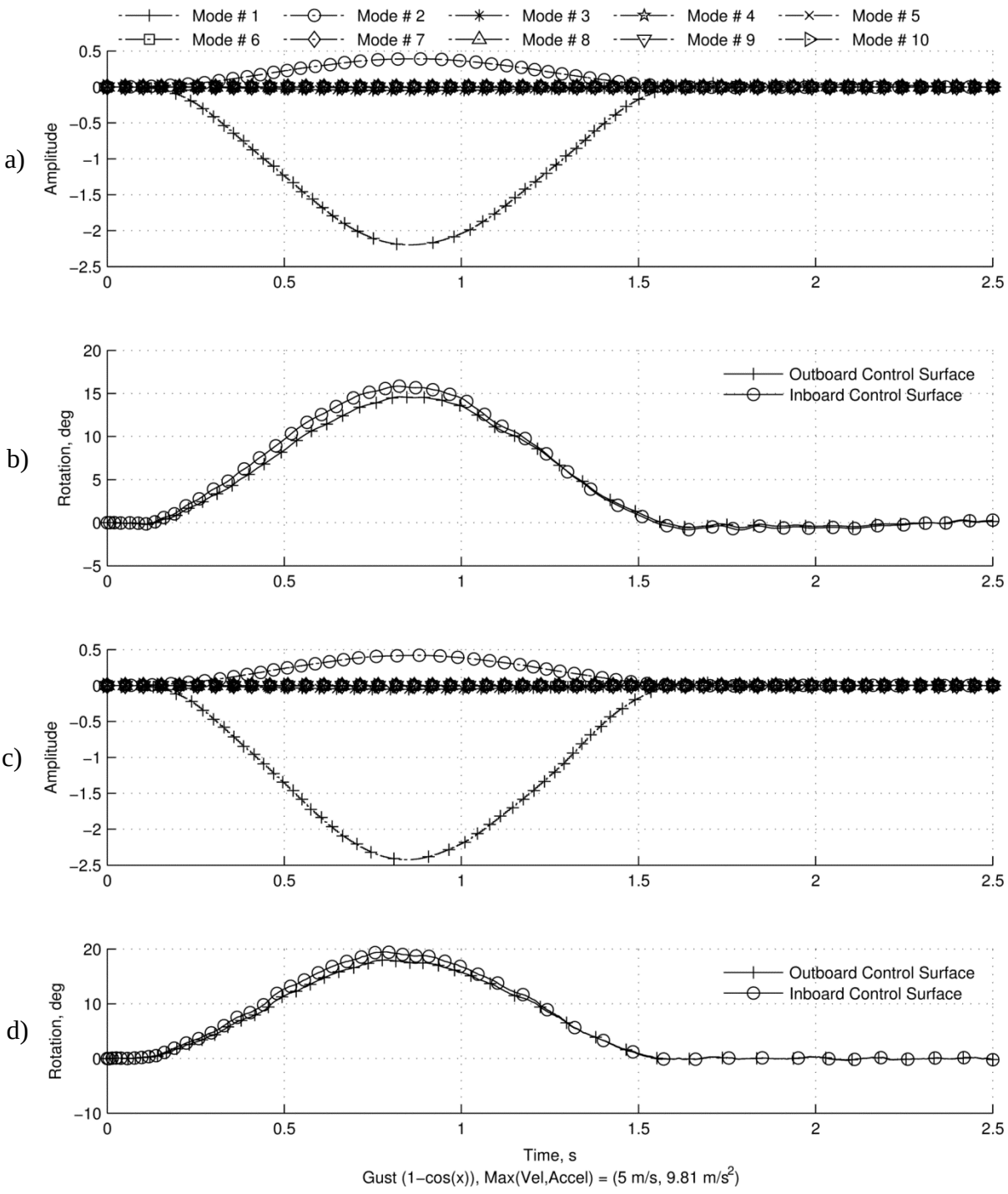

Figure 4.16: Controller Performance in a Gust: a) Controller with Accelerometer Inputs, Modal Amplitude Time History; b) Controller with Accelerometer Inputs, Control Surface Time History; c) Controller with Modal Coordinate Inputs, Modal Amplitude Time History; and d) Controller with Modal Coordinate Inputs, Control Surface Time History.

The modal response to the gust for the controller with accelerometer inputs (See Fig. 4.16[a]) indicates that the first two modes (first wing torsion and first wing bending) responded most to the gust as expected. The peak amplitude of the bending mode was approximately -2.2, which corresponds to roughly a 44-cm-upward bending deflection at the wing tip. A negative bending modal coordinate corresponds to a positive wing tip deflection (See Fig. 4.3[a]). The twist mode moves to a maximum amplitude of 0.4, which corresponds to approximately 10 deg. of positive wing twist, leading-edge up.

Over the gust time history, the control surfaces move to counteract the effect of the gust (See Fig. 4.16[b]). As the wing experiences a lift increase, the control surfaces rotate upward to reduce the angle of attack of the wing and reduce lift. The rotation of the control surfaces stayed well within the bounds of reason for wing control surface rotations.

The gust disturbance rejection performance of the controller with modal coordinate inputs was comparable to that of the controller with accelerometer inputs, shown in Fig. 4.16(c); the peak amplitude of the bending mode was slightly higher at -2.4. The torsion angle was nearly the same at approximately 10 deg. Little can be said as to which controller has better disturbance rejection. The differences were negligible. Both controllers rejected the specified gust disturbance adequately with little differences. The next section discussed the results of AFS simulations.

4.3.2 Active Flutter Suppression

A major theme in this study has been to demonstrate that the controller with the modal coordinate inputs may be used for AFS. Figure 4.5 shows that the model is open-

loop unstable, resulting in modal motions characteristic of flutter. This occurs at a flight condition of 80 m/s at an altitude of 302 m.

The same simulation structure (See Fig. 4.15) that was used for the gust disturbance modeling was used for flutter suppression with very small changes. The gust model inputs *w* were set to zero. A small control input at time 0 was introduced to perturb the wing model from its trim state. The modal amplitudes of the model are allowed to increase without control input until 3.5 s.

The controller was linearly phased-in from 3.5 s to 4.5 s. The controller was not turned on to full instantly at 3.5 s to avoid large oscillations due to the output magnitudes being far from the reference condition of zero. The simulation results are presented in Fig. 4.17 for the controllers with acceleration inputs and modal coordinate inputs respectively.

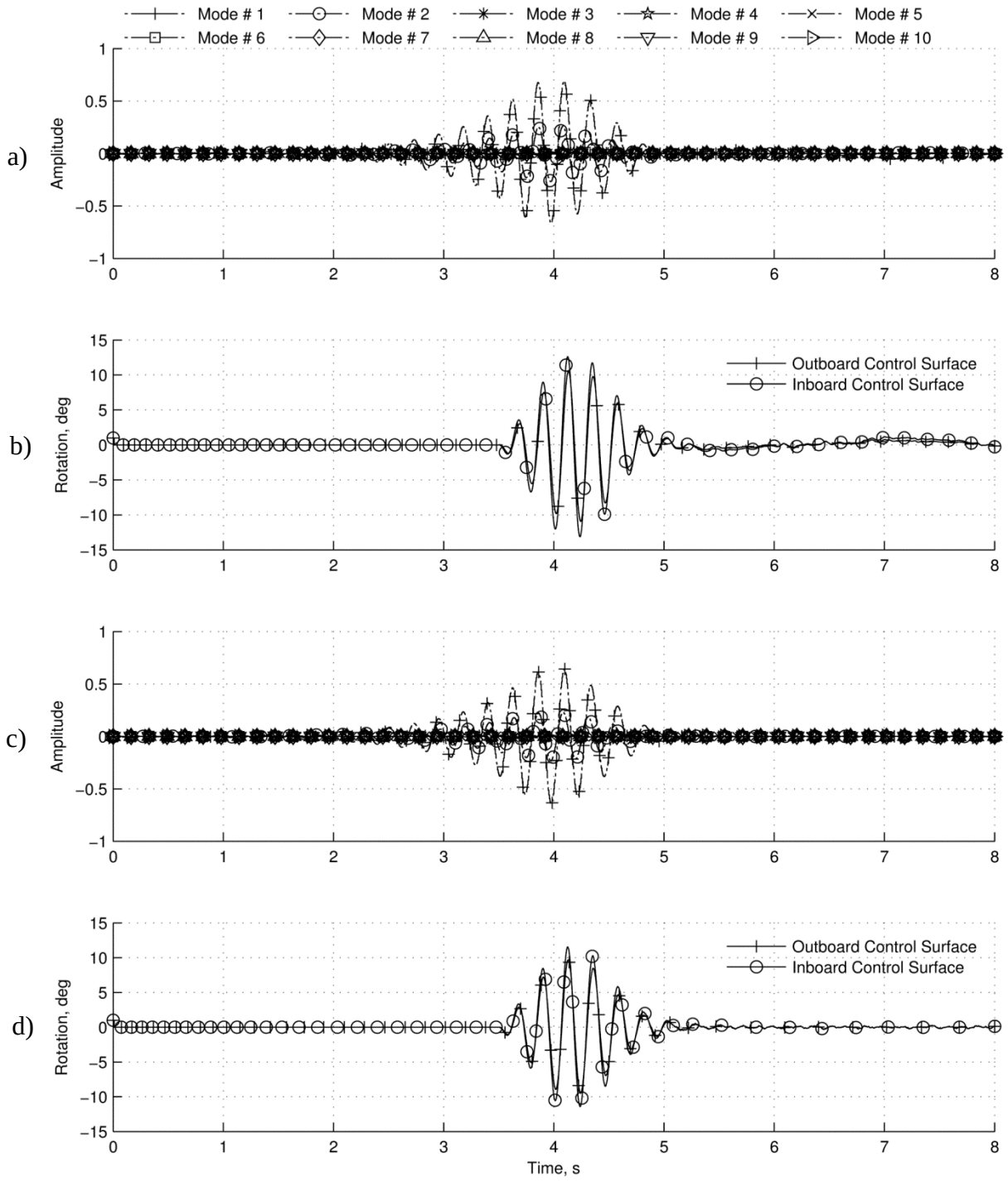

Figure 4.17: Controller Performance in a Flutter Suppression: a) Controller with Accelerometer Inputs, Modal Amplitude Time History; b) Controller with Accelerometer Inputs, Control Surface Time History; c) Controller with Modal Coordinate Inputs, Modal Amplitude Time History; and d) Controller with Modal Coordinate Inputs, Control Surface Time History.

The time history for the controller with accelerometer inputs is examined first in Fig. 4.17(a). The modal amplitudes oscillate with a frequency of 4.49 Hz increasing in amplitude until approximately 4.2 s. At this time, the controller force begins to remove a sufficient amount of energy from the flutter mode to begin to reduce the amplitudes of the modes. The oscillations die out quickly at approximately 5 s.

The time history of the controller matches what would physically be required to reduce flutter in the wing. As the wing bends upward (See Fig. 4.17[a]) the control surfaces rotate upward (See Fig. 4.17[b]) to reduce the angle of attack of the wing and reduce lift. The net aerodynamic force has the effect of moving the wing downward. As the wing moves down, the control surfaces rotate downward to increase the lift on the wing. This counterbalancing effect performs work and removes energy from the flutter mode. The overall effect asymptotically stabilizes the structure.

After the flutter mode stabilizes, the control surface movements appear to oscillate at low frequency and the modal coordinates remain near zero. The movement from equilibrium is in response to the additive noise on the accelerometers.

The controller with modal coordinate inputs performed similarly to the controller with accelerometer inputs, as before with the gust inputs. Figure 4.17(c) shows that the modal coordinates begin to flutter up to 3.5 seconds and are slowly damped out once the controller is enabled.

As before, the control surface movements worked to extract energy from the flutter mode as seen in Fig. 4.17(d). The modal coordinates also stay near zero as expected. From time analyses it was clear that both controllers performed well in meeting the primary objective to suppress the flutter mode at the selected flight condition.

So far, the actual modal coordinate time histories are presented in each plot, representing the motion of the model in either a gust or fluttering condition. To satisfy curiosity, the modal coordinates which were given to the controller for feedback during the flutter suppression, q_m, are presented in Fig. 4.18.

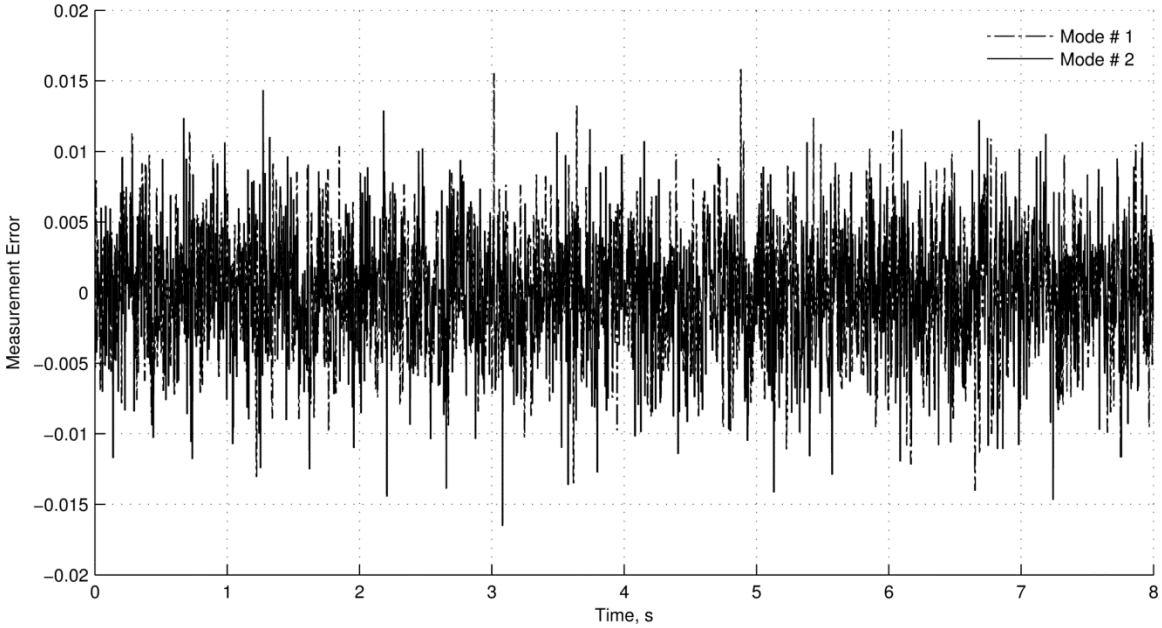

Figure 4.18: Modal Coordinate Measurement Error.

Recall that zero mean Gaussian noise with a standard deviation of 1 cm was added to all deflections that were used to estimate the modal coordinates. This means that the error can likely go up about 3 cm for the deformations some of the time, assuming that some data points will fall roughly 3 standard deviations away. All of the deflections with error were put through a least-squares modal filter [See Fig. 4.15 and Eq. (4.9)].

The measurement error of the modal coordinates indicates that a typical least-squares smoothing has taken place, as the modal amplitudes measurement error tended to stay near 0.01. Although this smoothing is not substantial enough to raise eyebrows, it does show that the errors tend to average out when many sensors are utilized in forming the least squares estimates. It is also clear that the increasing amplitude of the modal

coordinates did not affect the modal coordinate estimation error, even during open-loop flutter.

4.3.3 Virtual Deformation Control –Modal Reference Tracking

Until this point, much of the focus of this study has been to compare regulators with accelerometer inputs or modal coordinate inputs. It was observed that the controllers had similar performance during GLA and AFS. In this section, shape control is demonstrated. This is required in response to Research Question 4, which asks for various methods of shape control via modal filtering. Recall that shape control has been pursued in other works as well; two references are given here [143, 182].

Further work using accelerometers is not continued. While the controller with accelerometers might be able to track deformations by double-integrating the accelerations, it is not a natural fit; the deformations predicted with accelerometers may start to drift and require deformation updates. Thus what follows is only the modal controller.

The modal controller may be a suitable match for shape control since modes are linearly-related to deflections [See Eq. (1.5)]. The first form of shape control is implemented through forming a modal reference. If a set of reference deflections d_{ref} are known at specific locations, l_r, these deformations may be transformed to modal coordinate reference values, q_{ref}.

By tracking modal references, deflections may be indirectly tracked, even if those deflections are not directly measured. These deflections are referred to as virtual deformations, and the control of these deformations as virtual deformation control. The

simulation for deformation control through modal reference tracking is presented in Fig. 4.19.

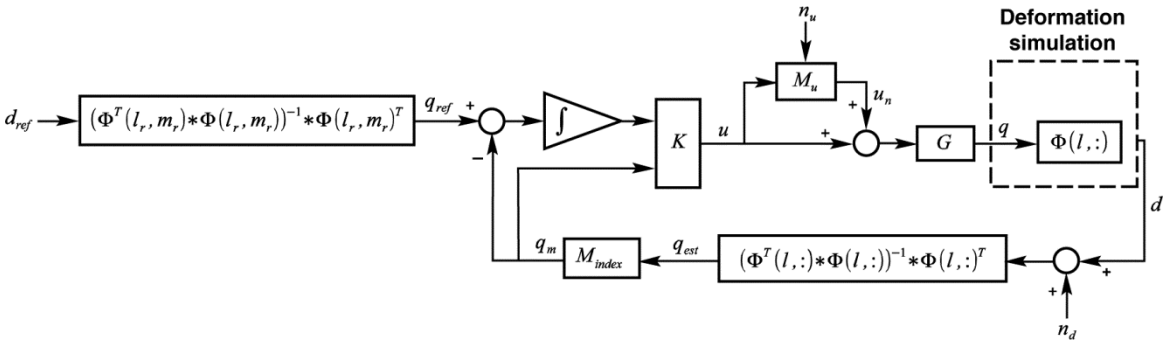

Figure 4.19: Control Simulation for Virtual Deformation Control: Modal Reference.

The modal tracker is designed to achieve zero steady-state tracking error by using integral states of the tracked modal coordinates. All modes are estimated by the modal filter and indexed (i.e., $M_{index} = \{1,2\}$) to give q_m. Recall that all contributing modes must be estimated before filtering in order to more accurately estimate the first two. This is done to reduce projection error.

The modal measurements are input to a differencing junction with the modal reference and sent through a single continuous-time integrator. To simulate a small torsion angle command, $d_{ref} = \{TE_{ref}, LE_{ref}\}$ was set to $\{1\,mm, -1\,mm\}^T$, which represents a leading-edge-down rotation.

Since small deformations are used as references, the noise was adjusted accordingly, so that the standard deviation of the multiplicative control noise was set to 0.001. The standard deviation on the deformation measurements was assumed to be 1 mm. These noise settings allows one to better see what the controller is doing in the resulting plots; this was not done to simulate actual sensor noise characteristics. The simulation results are presented in Fig 4.20.

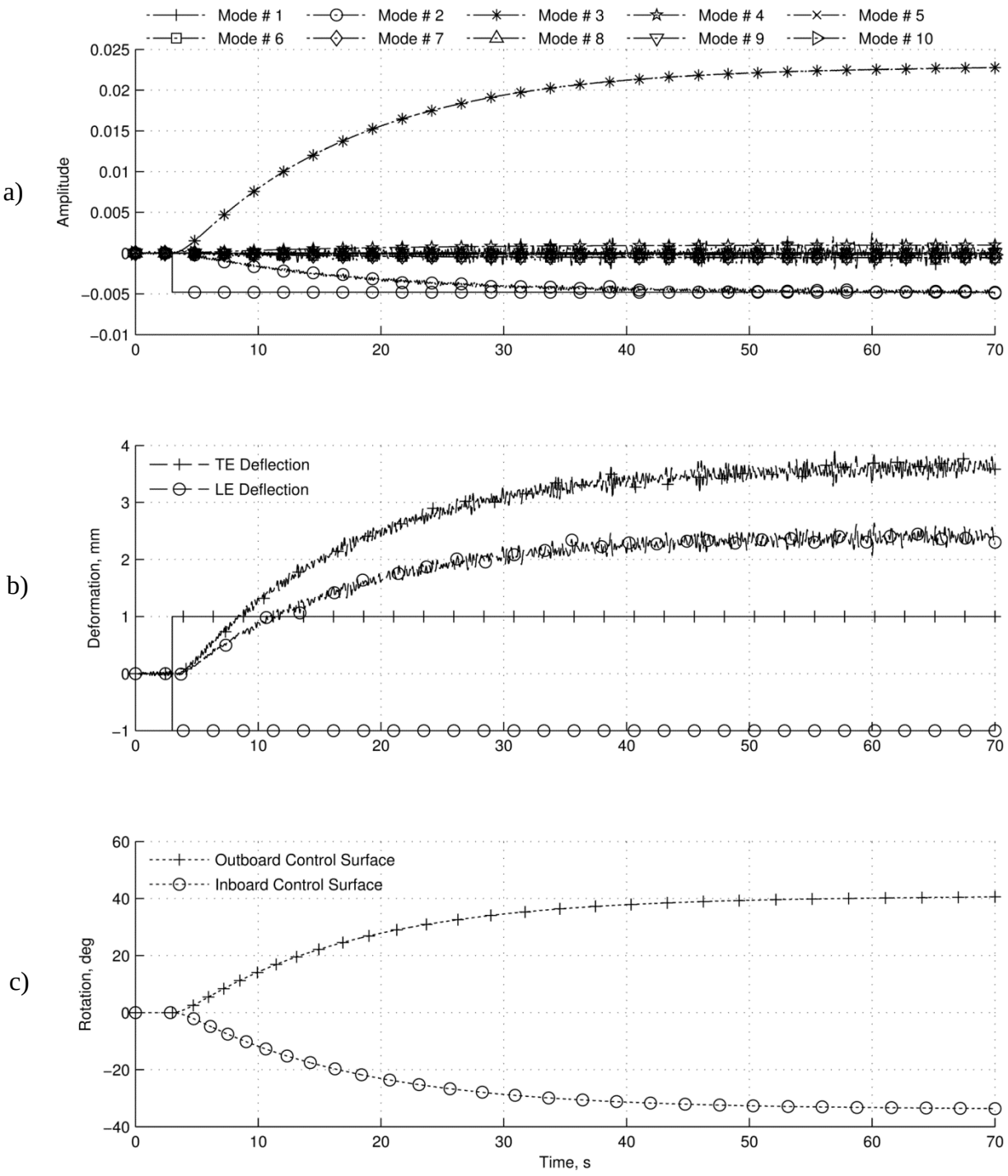

Figure 4.20: Virtual Deformation Control: Modal Reference- a) Modal amplitudes; b) Deformations and Predicted Deformations at Wing Tip; and c) Control Surface Rotations.

Figure 4.20(a) shows that the first torsion modal coordinate overlays the reference torsion modal coordinate within 50 s. The bending modal coordinate reference is near zero and is also tracked within 50 s. The other eight modal coordinate time histories are also plotted so that the effects of residual modes may be observed. The second bending mode becomes highly excited. The deformations achieved through modal tracking are presented in Fig. 4.20(b). The deflections achieve what would be a torsional angle with the leading edge down, but the net deformations of both are up approximately 2 mm.

There is significant error between the desired deformations of {1 mm, -1 mm} and what is achieved {3.6 mm, 2.2 mm}. The prominent second bending modal coordinate is clearly to blame for this error. From desktop simulations it was observed that to reduce this error, the second bending mode (See Fig. 4.3[c]) could be tracked if more actuators were available. Note that the deformations to be tracked were at the same locations as where the accelerometers were placed. They were not measured by the fiber optics themselves. The action of tracking a deformation which is not directly measured is observed here.

Figure 4.20(c) indicates that to achieve small deformations, very large control surface rotations were required, almost up to 40 deg. The large rotations are a result of either high stiffness in the wing or potentially low control surface steady-state effectiveness. For this reason, the deflection references were kept small to ensure the control surfaces rotated within reasonable limits. These results indicate that wings with low torsional modal mass (See Fig. 4.7) may be difficult to structurally morph using only trailing edge aerodynamic effectors.

4.3.4 Virtual Deformation Control – Predicted Deformation Reference Tracking

In the previous case study, the deformation command was transformed to a reduced modal command and the modes were tracked. Due to the effect of residual modes, the wing deformation reference command was tracked poorly. To reduce this effect, the modal filter can also be used to form a predicted estimate of the deformation of the structure at any point by including residual modes into the estimate. To prepare the controller, the output matrix in the state space may be defined to have the form shown in Eq. (4.22),

$$y \triangleq [\Phi(l_r, :) \quad 0_{r\times m} \quad 0_{r\times e} \quad 0_{r\times z}]x \tag{4.22}$$

where r is the number of deformations (or virtual deformations) desired to be tracked. This method of definition has the effect of making the outputs of the plant equivalent to the deformations. A similar transformation is used to model the accelerometers, where the sensors are assumed to measure linear combinations of the modal states.

The simulation for tracking deformations estimated by modal coordinates is similar to the modal tracking simulation presented above (See Fig. 4). The difference is that the estimated modal coordinates are used to estimate desired virtual displacements at location indices, l_r.

This method of tracking is named predicted deformation because all of the modes are used to form the deformation prediction. Therefore, Since all modes are utilized to estimate the virtual deflections, $q_m = q_{est}$. Alternatively it can be stated that, $M_{index} = \{1,2,3,4,5,6,7,8,9,10\}$. Therefore predicted deformation tracking is the second answer to

Research Question 4. The simulation scheme used for virtual deformation tracking by way of predicted deformation tracking is presented in Fig. 4.21.

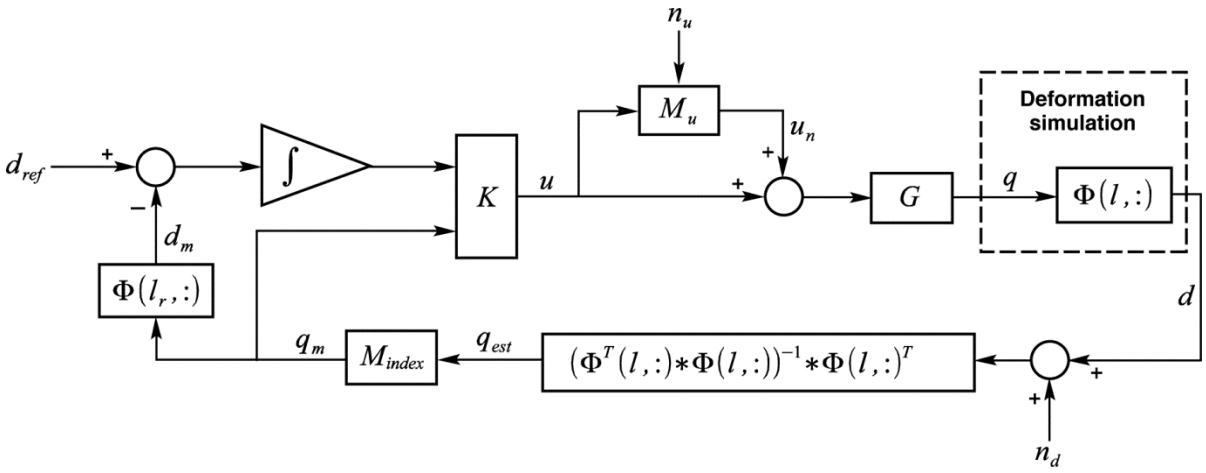

Figure 4.21: Control Simulation for Virtual Deformation Tracking: Predicted Deformation Reference Control.

For testing, the noise levels in the previous simulation are also used, as were used previously for modal reference tracking. The same reference values of {1mm,-1mm} were used for the deformation reference and the simulation results are presented in Fig 4.22.

a)

b)

c)

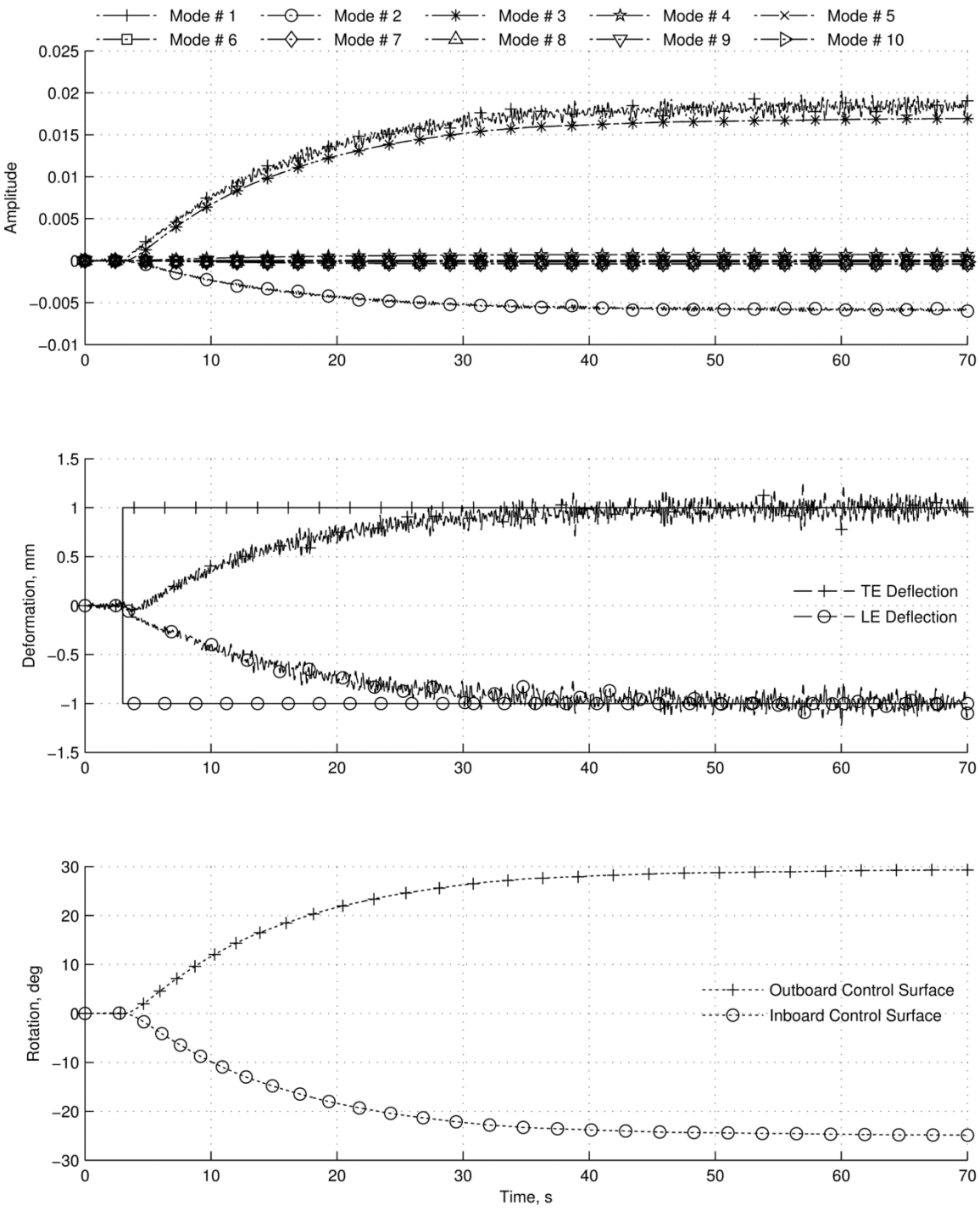

Figure 4.22: Virtual Deformation Control: Predicted Deformation Reference- a) Modal Amplitudes; b) Deformations and Predicted Deformations at Wing Tip; c) Control Surface Rotations.

The time history of the modal coordinates in Fig. 4.22(a) shows that the torsion modal coordinate moved comparative to the way it did previously (See Fig. 4.20[a]). The second wing bending modal coordinate also moved positively; however, this time, the first wing bending moves from zero to a large positive value, which has the effect of offsetting the second wing-bending effects. The net effect was that the actual virtual deformations and reference virtual deformations were overlaid as seen in Fig. 4.22(b).

Figure 4.22(c) indicates that the control surface movements were lower than they were previously (See Fig. 4.20[c]). The outboard control surface moved to about 30 degrees and the inboard surface moved to -25 deg.

The use of either the tracking strategy presented here or that presented in the previous section may depend on the application. If a multitude of points on the wing are required to be tracked or moved to a particular shape, then the strategy first presented may be more useful. The reduction of the reference signals to a few modal coordinates may alleviate the control design effort.

If only a few virtual deflections at a few points on the structure (i.e., 2-4) are required to be tracked, then the strategy presented in this section may be more applicable. The selection of the appropriate tracking strategy will be application dependent.

4.4 Summary of Wing Model Design Work

It is clear that the modal filter shows promise in an aeroservoelastic environment, which satisfactorily answers Research Question 1. For the reduced plants, H_∞ optimal

regulators were designed for each plant with the objective of being robustly stable to input and output multiplicative uncertainty and having good disturbance rejection properties. The controllers were tuned, such that similar characteristics are achieved for each. No significant difference was noted, other that the order of the modal controller was significantly lower order than the controller with accelerometer inputs.

The proposed two shape control techniques also provide two answers to Research Question 4. It was observed that one of the two methods of shape control is more appropriate for an aircraft. For an aircraft, such as the X-56A, the modal displacement reference tracking strategy is the most appropriate. This method does not require the control of all modal displacements in the model. Tracking high frequency modes will lead to robustness issues.

The modal displacement reference tracking strategy requires only that the first few low frequency modes be controlled. It is also readily applicable to track potentially millions of displacements points using the modal reference transformation given in Eq. (4.10). The X-56A modal filtering control design is demonstrated next.

CHAPTER 5

X-56A

The wing model introduced in the previous chapter is a model used to determine how the modal filter operates on a pure elastic model. However, a shortcoming of this model is its boundary conditions. There are no aircraft trim requirements for a clamped wing model. Only flexible modes are modeled and rigid body interactions remain unexplored. The wing model is also too structurally simple to verify use of the modal filter for aircraft.

The X-56A model was a platform chosen to test the modal filter on a complex aircraft. Simulations on this model are used to give answers to both Research Question 2 and Research Question 5. The first question asks whether modal filtering supports aircraft control systems. The second asks for the properties of merging flexible (modal) and rigid body control.

The Chapter begins with a design methodology to incorporate modal filtering into an aircraft control system. The design of the controller follows and finally simulations are given demonstrating virtual deformation control and AFS on the vehicle.

5.1 Modal Filtering Design Methodology

It is slightly more challenging to implement a modal filter onto an aircraft than the wing model, but the principles are roughly the same. A methodology for incorporating a modal filter into a controller has been given in Tzafestas's [183] book. However, it was not specific for an aircraft or for shape control. The presented design methodology is tailored for an aircraft analyzed with free-free modes. Free-free modes are computed such that rigid body and flexible modes are orthogonal to each other.

The modal reference simulation which the methodology is constructed for is given in Fig. 5.1.

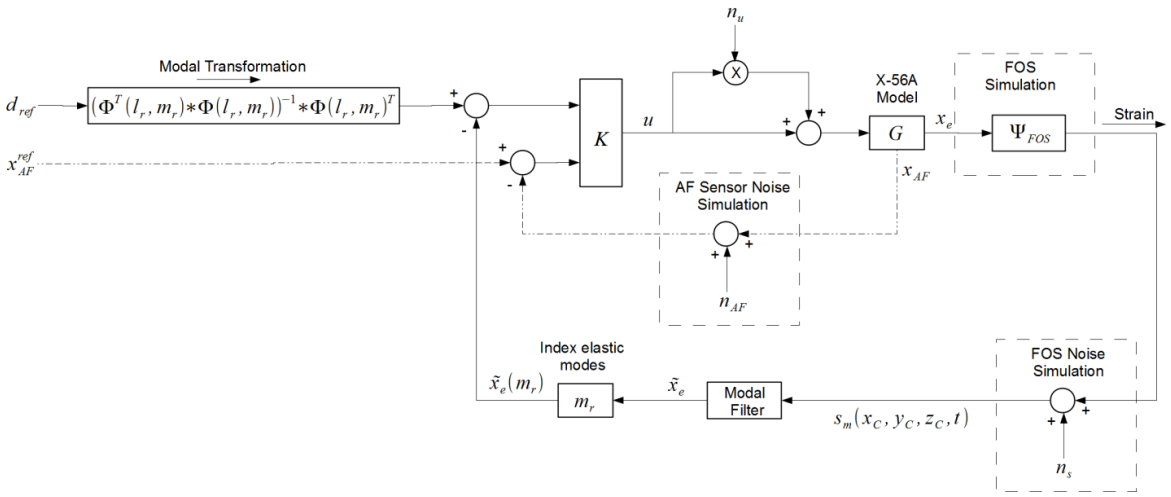

Figure 5.1: The Virtual Deformation Control Architecture for the X-56A Model.

This architecture assumes that a virtual deformation control architecture with modal reference tracking is used. It was determined that this was the most practical method of shape control in the previous Chapter.

In many ways the phases of modal filtering design provided in the previous Chapter are the same (See Fig. 4.1). In the architecture provided in Fig. 5.1, there are

three important design phases. First, the controller, K, must be developed (Phase I). Second, the modal filter and simulated fiber optic sensors (SFOS) models must be constructed (Phase II); and third, the reference signal transformation must be computed (Phase III). The following sections describe these phases, from the perspective of aircraft modal filtering design. The first section begins with the control design phase.

5.1.1 Control Design Phase

As before, the first step for modal filtering control design is to specify performance and robustness requirements. For performance, this typically includes specifying targets for rise time, overshoots, settling time and the overall shape of the response. Robustness must also be achieved in a control design and is approached from varying points of view in the literature. A mu-analysis and Monte Carlo Simulation is recommended.

5.1.1.1 **Identifying Significant Modes**

Identification of significant modes in an aircraft structure is again similar for a wing model. Again, the V-g and V-f plots or equivalent are used to determine interacting modal coordinates. Modal coordinates must be selected for feedback which contribute to flutter, modal vibration and are within the actuator bandwidth.

Selection of these modes can be an iterative process due to the need to meet robustness requirements. If modal coordinates at high frequencies are fed back, the bandwidth of the controller may be required to be too high. Once feedback modes have

been decided upon, the state space matrices must be updated. First the state space model development and airframe state definitions are discussed in the next section.

5.1.1.2 **State Space Modeling**

Mathematically, the matrix equation of motion of the aeroelastic system in discrete coordinates is given as in Eq. (5.1).

$$[M_{hh}]\{\ddot{q}\} + [C_{hh}]\{\dot{q}\} + [K_{hh}]\{q\} + [M_{hc}]\{\ddot{\delta}\} = q_\infty[Q_{hh}(ik)]\{q\} + q_\infty[Q_{hc}(ik)]\{\delta\} \tag{5.1}$$

Analogous to Euler's first law, $F = ma$ (or in this case $ma = F$), the left side of the aeroelastic system equation represents the structure's mass properties and applied motion while the right side represents the aerodynamics forces.

The generation of aerodynamic transfer functions in the time domain by solving unsteady aerodynamics can be a very complicated procedure. For this reason, unsteady aerodynamic methods are often formulated in the frequency domain by assuming simple harmonic motion.

The doublet lattice method (DLM), the unsteady flow extension of the vortex lattice method (VLM), was developed by Albano and Rodden [184] and is traditionally used to determine the unsteady aerodynamic forces [141, 185, 186].

However, ZAERO uses ZONA6 as an unsteady-flow extension of Woodward's Method, which is described as a similar but higher order singularity distribution than the vortex lattice method [187, 188, 189]. The aero model is presented in Fig. 5.2.

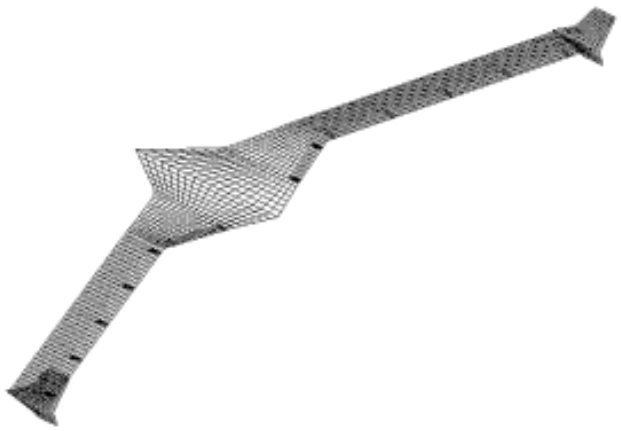

Figure 5.2: Aero Panel Model of X-56A.

Points between the FE model and aero model are selected that accurately represents the force transferal from the aerodynamic control points to the structural grid points. This allows calculation of the GAFs from modal deformation at structural grid points.

It becomes necessary to convert the frequency-domain GAF to the Laplace domain. However, the Laplace-domain unsteady aerodynamics must be in a rational function form to be incorporated into the time-domain state-space equations of the aeroelastic system. Therefore, the unsteady aerodynamic forces are approximated through the following RFA as in Eq. (5.2).

$$\left[\tilde{Q}(ik_l)\right] \approx [A_o] + [A_1](ik_l) + [A_2](ik_l)^2 + [D]\left[ik_l[I] - \frac{V}{L}[R]\right]^{-1}[E](ik_l) \tag{5.2}$$

From principles of analytic continuation, the unsteady aero modeled in terms of reduced frequencies can be expanded into the entire Laplace domain through the following substitution given in Eq. (5.3),

$$\frac{L}{V}s = g + ik \tag{5.3}$$

where s is the Laplace Variable and g is the non-dimensional damping. Aero lags are used to model the delayed force effects of the unsteady aerodynamics. The aero lags are modeled as zeros along the negative real axis of the Laplace domain since the aero force translation to the structure is not real time. By setting $g = 0$, for the non-dimensional damping, the aerodynamic forces are now expressed in the Laplace domain as in Eq. (5.4).

$$\begin{aligned}\left[\tilde{Q}(s)\right] &= \begin{bmatrix} Q_{hh} \\ Q_{hc} \end{bmatrix} \\ &= [A_o] + \frac{L}{V}[A_1]s + \frac{L^2}{V^2}[A_2]s^2 + [D]\left[s[I] - \frac{V}{L}[R]\right]^{-1}[E]s\end{aligned} \tag{5.4}$$

The two most common methods to perform the RFA are Roger's [117] method and the minimum state method by Karpel [172]. RFA is least squares fit technique that approximates the GAF matrices at several discrete reduced frequencies, k. In general, the least square fit procedure solves for $[A_0]$, $[A_1]$, $[A_2]$, [D], and [E]. Roger's method was chosen to compute the RFA.

Constraints are applied at specific reduced frequencies (such as at zero) and aerodynamic derivatives are matched in ZAERO. In general, ZAERO's theoretical manual recommends running open-loop ASE analysis in frequency domain first (normal flutter analysis) and compare with open-loop analysis in time domain (using state-space models) to ensure RFA is accurate. Otherwise, additional tweaking in the RFA process must be performed.

The state space model description given in Eq. (4.2) is used for the X-56A with state vector defined as in Eq. (5.5),

$$x(t) \triangleq \{x_{AF}(t), x_e(t), x_{\dot{e}}(t), x_{lag}(t), x_{act}(t)\}^T \tag{5.5}$$

where $x_{AF}(t) \in \mathbb{R}^{AS\times 1}$ is a vector of airframe states, $x_e(t) \in \mathbb{R}^{m\times 1}$ is a vector of modal displacements, $x_{\dot{e}}(t) \in \mathbb{R}^{m\times 1}$ is a vector of modal velocities, $x_{lag}(t) \in \mathbb{R}^{f\times 1}$ is a vector of aerodynamic lag states and $x_{act}(t) \in \mathbb{R}^{z\times 1}$ is formed from a vector of actuator accelerations, velocities, and displacements.

5.1.1.3 **Trim Conditions**

The trim conditions were applied to the nonlinear equations of motion to develop the state space models. The trim analysis ensures gravity is included into the model to provide more accurate flight responses for rigid body motion. Two trim conditions include:

1) Applied 1G gravitational force
2) Only free variable is angle of attack

These conditions lead to a trim angle of attack and a trimmed elastic solution. Therefore all the state space models' states are considered to be perturbations about this point.

A limitation is identified here. ZAERO is not capable of trimming the aircraft in unstable conditions. Therefore all models past flutter are trimmed for a single flight condition which occurs before the flutter speed. This results in the aircraft model sinking due to an imbalance of lift with gravity.

5.1.1.4 **Actuators**

The state space models must also model actuator dynamics. Actuator dynamics can drastically impact the elastic aircraft states. A third order transfer function of the actuators is formulated for each control surface to incorporate the actuator dynamics into the system. Indeed, ZAERO requires a 3rd order actuator model to remove the direct-feed through from the sensor output matrix when accelerometers are used for feedback [190].

Unfortunately, a 4th order (not 3rd order) experimentally verified actuator model was provided by Lockheed Martin. So Matlab's System ID toolbox was used to convert the 4th order actuator model into a 3rd order model with balanced truncation. The actuator transfer function is represented here as in Eq. (5.6).

$$\frac{\delta_1(s)}{u_{ac_1}(s)} = \frac{a_{i3}}{s^3 + a_{i1}s^2 + a_{i2}s + a_{i3}} \tag{5.6}$$

The LTI transformation resolves the transfer function into actuator state space matrices of the following as in Eq. (5.7).

$$\{\dot{x}_{act}\} = \begin{bmatrix} 0 & 1 & 0 \\ 0 & 0 & 1 \\ -a_{i3} & -a_{i2} & -a_{i1} \end{bmatrix} \{x_{act}\} + \begin{Bmatrix} 0 \\ 0 \\ a_{i3} \end{Bmatrix} u_{ac_i} \tag{5.7}$$

These models are appended to the state space models for all ten control surfaces, increasing the state space order by the order of the actuator transfer function multiplied by ten.

5.1.1.5 **Sensors**

Sensors which measure position, velocity, and acceleration can be defined in ZAERO. These sensors are used to determine translational or rotational motion which

becomes the outputs of the state-space models. Accelerometer sensor and control surface locations used for the X-56A state-space model are shown in Fig. 5.3. Accelerometer locations are labeled in red, control surfaces are labeled in black.

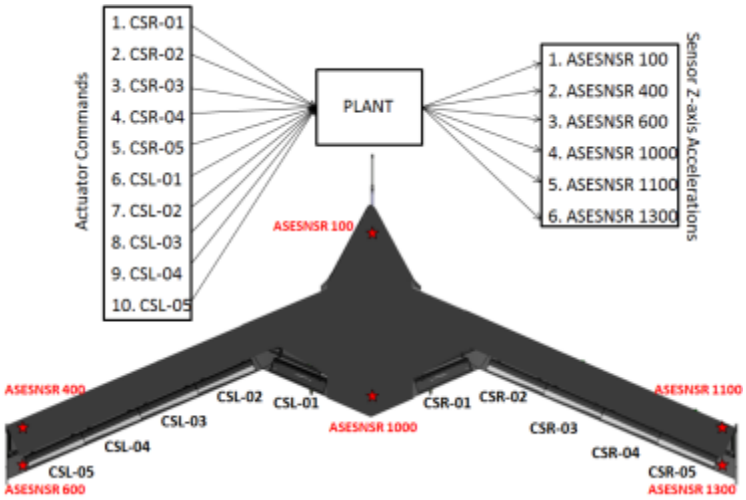

Figure 5.3: X-56A Control Surfaces and Sensor Locations.

Currently, the X-56A has available to it six accelerometers. However these accelerometers are not utilized for control feedback in this study. The focus is instead on utilizing the modal displacement states, $x_e(t)$ for feedback. Further sensor layouts are given in the design section, specifically for the SFOS. With the state space models so developed, they can be modified to feedback modal coordinates as presented in the next section.

5.1.1.6 **Modifying State Space Matrices**

The modification of the state space matrices for modal coordinate feedback is very similar to how the wing model state space matrices are modified. Consider the relationship of the strain-based modal filter (See Ref. [66]) to the modal displacement state vector $x_e(t)$ as in Eq. (5.8),

$$x_e(t) = q(t) = (\Psi^T\Psi)^{-1}\Psi^T s_m(x_C, y_C, z_C, t) + \varepsilon \tag{5.8}$$

where $\Psi = \{S_d\phi_i(x_C, y_C, z_C), i = 1 \ldots N\}$ is a $N \times N$ strain matrix with N strain modes, $s_m(x_C, y_C, z_C, t) \in \mathbb{R}^{N\times 1}$ is the measured strain and ε is a normal error. This represents the modal filter in its pseudo-inverse form. Since the modal filter gives a partial state estimate of the full state vector, $x(t)$ as defined in Eq. (5.5) the form of the output matrix is simply identity for measured modes.

The sensor output matrix, C, is a matrix of row vectors relating the sensory information to the state vector, $x(t)$. For the wing model methodology, the output matrix was developed for the case where rigid body motion was restrained. Here, the output matrix is adjusted for rigid body state feedback concurrent with modal deformation state feedback. It is assumed that m modes are retained for measurement. The output matrix is formed assuming all modal displacements, x_e , and airframe states, x_{AF}, are measured, as shown in Eq. (5.9).

$$C \triangleq \begin{bmatrix} I_{AS\times AS} & 0_{AS\times m} & 0_{AS\times m} & 0_{AS\times f} & 0_{AS\times z} \\ 0_{m\times AS} & I_{m\times m} & 0_{m\times m} & 0_{m\times f} & 0_{m\times z} \end{bmatrix} \tag{5.9}$$

As with the wing model, there is no requirement to measure all flexible states (or rigid states) to adequately sense the vehicle state. Higher frequency modes generally do not significantly contribute strongly to the deformation [7, 183]. These modes may be cautiously ignored to reduce the size of the C matrix.

5.1.1.7 **Model Reduction**

After selecting and modeling modal coordinates, the state space matrices can be reduced in order and used to design the control laws. The same model reduction

philosophy of partitioning the plant into stable and unstable parts and then using balanced truncation [174] is used as for the wing model. From here a control design methodology can be taken.

5.1.1.8 **Control Design and Iteration**

As with the wing model, control design can proceed with any desired control methodology. For the wing model, the μ-Optimal [103] design methodology was chosen. This methodology is very flexible and allows the designer to simultaneously satisfy many requirements at once.

As with the wing model, once a controller has been designed which meets requirements, the modal coordinates are also fixed. They can be used in the modal filter design phase which is discussed in the next section.

5.1.2 Modal Filter Design Phase

Phase II requires the development of the modal filter. The difference between the modal filer for the wing model and that used on the X-56A, is that the former is in displacement units and the latter is in units of strain.

The wing model assumed deformations are computed from any shape algorithm at SFOS locations, while the X-56A assumes strain is measured directly. This is representative of what the FOS actually measure. To utilize the strain mode matrix for modal filtering, the strain modes must be computed. But it was not known how to compute strain modes directly from MSC NASTRAN.

Instead an approximation for strain was made using the computed deformations for each mode shape at the sensor locations. The close proximity of the sensors (of approximately one-half-inch) along the SFOS gives a unique opportunity to calculate axial strain modes directly from the deformation at the sensor locations.

Recall the axial strain in a beam element [191], where x_l is along the length of the beam axis (as in a fictitious beam connecting two sensor locations), shown in Eq. (5.10):

$$\varepsilon_{xx} = \frac{\partial u}{\partial x_l} \tag{5.10}$$

The FOS measure axial strain, so a fictitious beam is assumed to exist between sensor locations. Assuming beams between each sensors, 1,000s of fictitious beams must be modeled. This concept is best described using Fig. 5.4. This is presented as a visual aid for the breakdown of Eq. (5.10) into the conversion of deformation to strain discussed next.

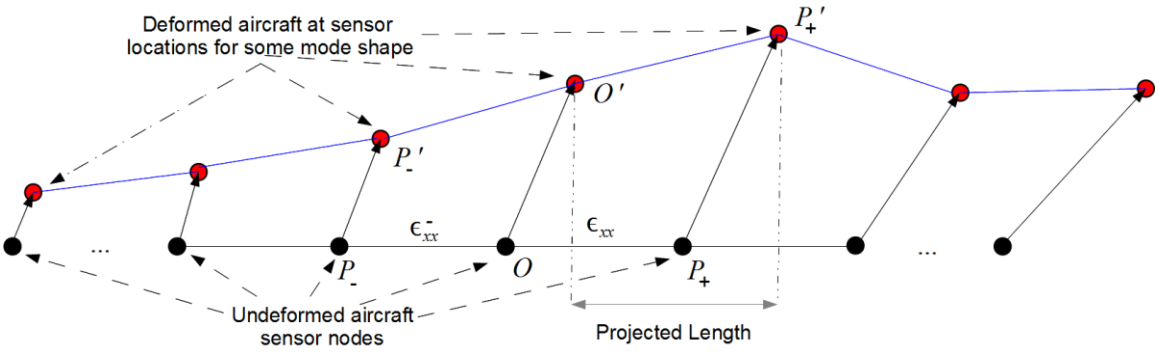

Figure 5.4: The Fiber Optic Sensor Locations Deformed for Notional Mode Shape.

Each dark dot in Fig. 5.4 represents sensors from the SFOS along the aircraft wing, which have been labeled for clarity. Each sensor has a line drawn between it, where a fictitious isotropic beam is assumed to exist. The deformed sensors shown as red dots

are connected with blue lines. The blue lines represent the beams in some deformed state due to the mode shape it corresponds to.

Linear algebra may be used to show that the strain in any fictitious beam element of the SFOS shown in Fig. 5.4 is calculated as shown in Eq. (5.11):

$$\varepsilon_{xx} = \frac{Proj_{\vec{u}(\overrightarrow{OP})}\overrightarrow{O'P'} - \overline{OP}}{\overline{OP}} \tag{5.11}$$

where $\overrightarrow{OP}$ is a directed line segment from the un-deformed sensor location $O \epsilon \mathbb{R}^3$ to the un-deformed sensor location $P \epsilon \mathbb{R}^3$, and $\overrightarrow{O'P'}$ is a directed line segment from the deformed sensor location $O' \epsilon \mathbb{R}^3$ to the deformed sensor location $P' \epsilon \mathbb{R}^3$ and $\vec{u}$ is the unit vector.

The projection (See Fig. 5.4) computes the final length of the beam section with respect to its original beam orientation. The difference between the original length and the deformed length, divided by the original beam length, gives the strain in the beam element.

The strain in one beam may differ from the strain in the beam next to it. Therefore the strain from modal deformation on the r^{th} sensor (or sensor location O) may be defined to be the average of the strain computed on either side of it (See Fig. 5.4) as shown in Eq. (5.12),

$$\varepsilon_r(s) \triangleq \frac{1}{2}[\varepsilon_{xx}^{+} + \varepsilon_{xx}^{-}]$$

$$= \frac{1}{2}\left[\frac{Proj_{\vec{u}(\overline{O_sP_+})}\overrightarrow{O_s'P_+'} - \overline{O_sP_+}}{\overline{O_sP_+}}\right. \tag{5.12}$$

$$\left. + \frac{Proj_{\vec{u}(\overline{O_sP_-})}\overrightarrow{O_s'P_-'} - \overline{O_sP_-}}{\overline{O_sP_-}}\right], s\varepsilon S$$

where ε_{xx}^{+} is the axial strain measured at a sensor using the left fictitious beam and ε_{xx}^{-} is the axial strain measured at the same sensor using the right connected fictitious beam (See Fig. 5.4). To compute the strain at point O with good precision, candidate sensor locations P_+' and P_-' must be selected close to the original sensor.

This operation can be carried out for each mode and at each sensor node, and sensor strain modes ψ_m may be formed by collecting component strains Eq. (5.12) for each sensor. The sensor strain modes are collected into the desired strain mode matrix defined at SFOS sensor locations, as shown in Eq. (5.13).

$$\Psi_{FOS} \triangleq [\psi_1, \psi_2 \dots \psi_i \dots \psi_m] \tag{5.13}$$

With the strain mode matrix defined, the modal filter can be set up in the following way as in Eq. (5.14),

$$q(t) = \Psi_{FOS}^{\dagger} s_m(x_C, y_C, z_C, t) \tag{5.14}$$

where $s_m(x_C, y_C, z_C, t)$ is the measured strain at the sensor locations. The next section describes how the reference transformation must be defined.

5.1.3 Shape Reference Signal Design Phase

A reference transformation is required in Phase III of the modal filtering design methodology. However the development of this transformation on an aircraft model is

not as straightforward because of free-free mode shapes. The normal mode shapes are infused with strong rigid body motion to satisfy mean axis constraints.

Therefore, the use of these modes to recreate the modal reference signal will lead to large displacement errors. The mode shapes required in Eq. (5.16) are calculated by an optimization procedure on the original mode shapes. The optimization procedure rotates and translates every node in the mode shape about the aircraft center of gravity (cg).

Recall that a mode shape corresponds to deformations at N grid points. At each grid point, the mode shape is defined for six DOF, so each mode shape technically has $6N$ DOF. The number of DOF are increased with global DOF parameters so the total DOF in each mode equate to $6N + 6$ DOF. The global DOF are the only variables in the objective function defined for the i^{th} mode shape given by Eq. (5.15):

$$F_i = \left\| \left\{ \begin{bmatrix} x_{cg} \times \mathbf{1^T} \\ y_{cg} \times \mathbf{1^T} \\ z_{cg} \times \mathbf{1^T} \end{bmatrix} + T(\delta\theta_C)T(\delta\phi_C)T(\delta\psi_C) \begin{bmatrix} \left(x_u + x_\phi^i - x_{cg} \times \mathbf{1}\right)^T \\ \left(y_u + y_\phi^i - y_{cg} \times \mathbf{1}\right)^T \\ \left(z_u + z_\phi^i - z_{cg} \times \mathbf{1}\right)^T \end{bmatrix} + \begin{bmatrix} \delta x_C \times \mathbf{1^T} \\ \delta y_C \times \mathbf{1^T} \\ \delta z_C \times \mathbf{1^T} \end{bmatrix} \right\} - \begin{bmatrix} x_u^T \\ y_u^T \\ z_u^T \end{bmatrix} \right\|_2^2 \tag{5.15}$$

where x_{cg}, y_{cg} and z_{cg} are the scalar coordinates of the cg of the aircraft, $T(\cdot)$ is a right-hand-rotation matrix operator, x_u, y_u and z_u are $N \times 1$ coordinate vectors of the un-deformed aircraft, x_ϕ^i, y_ϕ^i, and z_ϕ^i are $N \times 1$ coordinate vectors of the i^{th} modal deformation vector, ϕ_i. The six scalar variables in the optimization function include translational coordinates: δx_C, δy_C, and δz_C , and rotations about all three axes: $\delta\theta_C$, $\delta\phi_C$, and $\delta\psi_C$.

By minimizing the objective function [See Eq. (5.15)] for the i^{th} mode,with respect to these six scalar variables the relative distance between the un-deformed aircraft and the deformed aircraft is minimized. Since the squared Euclidean norm is a strictly convex function of its respective arguments, the objective function is also convex [138]; therefore, there are numerous discrete optimization methods available in the literature which can be used to solve it. For each mode i, the objective function is minimized with a locally convergent random search technique known as the compass method [138].

The transformed mode shapes defined at sensor locations are collected to form the modal matrix. These mode shapes are pure elastic and thus are used to form a proper modal reference transformation. The modal reference command is shown in Eq. (5.16):

$$q_{ref}(t) = \Phi^{\dagger}(l_r, m_r) d_{ref}(x_C, y_C, z_C, t) \tag{5.16}$$

where $d_{ref}(x_C, y_C, z_C, t)$ is a vector of deformations from the un-deformed aircraft corresponding to the index vector, l_r , in the pure elastic deformation modal matrix, Φ.

Recall that each row of the modal matrix corresponds to a physical location on the aircraft, (x_C, y_C, z_C). The index of modes, m_r , corresponds to the index of modes within the modal matrix, which the controller is designed to track. The selection of l_r is a research topic within itself. However, here it is recommended to select points with high deformation in the commanded mode shapes identified in Phase I. This may reduce coupling with residual modes, although this concept must be fully investigated.

This completes the modal filter design methodology. The following sections put the presented modal filter design methodology into practice on the X-56A vehicle. The case study, which addresses both Research Question 2 and Research Question 5, begins with a brief history and description of the vehicle.

5.2 Design

The Air Force Research Laboratory's (AFRL) Multi-utility Aeroelastic Demonstration (MAD) Program has developed the Multi Utility Technology Test-bed (MUTT) also known as the X-56A with Lockheed Martin being the prime contractor for design and development of the vehicle. The X-56A builds on previous work between Lockheed Martin and AFRL to design and develop new high altitude, subsonic, long endurance autonomous aircraft [99, 192].

The goal of this test vehicle is to perform flight research on active aeroelastic control technologies such as flutter suppression and gust load alleviation. The X-56A will be capable of a variety of configurations. This vehicle has a detailed FEM developed by Lockheed Martin and will provide a basis for future work in analyzing new structural configurations based on the initial X56A design. The initial design of the X-56A is shown in Fig. 5.5.

Figure 5.5: Initial Configuration of the X-56A (Picture Courtesy of Lockheed Martin).

The X56A is intentionally designed to encounter three flutter instabilities within its operating flight envelope: body freedom flutter (BFF), symmetric wing bending torsion flutter (SWBT), and antisymmetric wing bending torsion flutter (AWBT). BFF is a phenomenon where the rigid body mode of pitch and plunge couples with the elastic mode of first wing bending. The other two modes are traditional elastic flutter modes.

The vehicle is equipped with water tanks on its wings for mass variation simulation. Water in the wing makes control design more difficult because the controller will either need to adapt or be robust to the varying modal properties. This challenge may be compared to the wing stores AFS problem of the Northrop YF-17 airplane [41]. For simplicity, the simulation model used here assumes that the water tanks are empty.

The yaw model is also ignored. This is because the effects of pressure drag are not modeled. Since the aircraft has no rudder, its yaw control will be limited. To yaw, the control surfaces must move in opposing directions to generate more drag on one side of the vehicle.

Salient features of the modeling process are described in the following sections. This begins with the computation of the normal modes and a flutter analysis. These are also first steps in the modal filter design methodology.

5.2.1 Normal Modes

The normal modes analysis was completed in MSC Nastran [193] (MSC Software Corporation, Santa Ana, California) on a detailed finite element model (FEM) provided by Lockheed Martin. The FEM corresponding to the water-empty full fuel case was utilized. The detailed FEM is shown in Fig. 5.6.

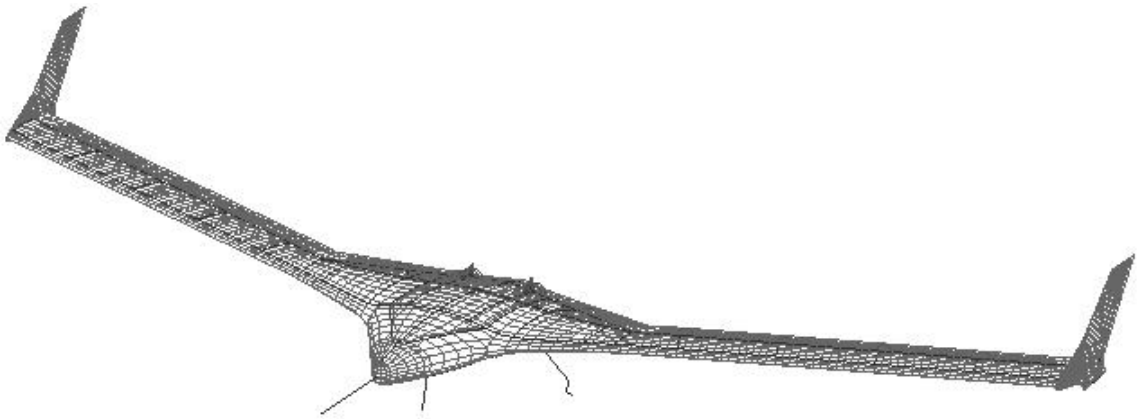

Figure 5.6: The Finite Element Model of the X-56A Aircraft.

The FEM contains over 8,000 nodes. Although accurate, the FEM has not yet been updated through a ground vibration test. Therefore the X-56A model in this paper has aircraft characteristics, but does not represent completely the procured flight vehicle. The free-free modes are shown here amplified by a large amount (for visualization) in Fig. 5.7.

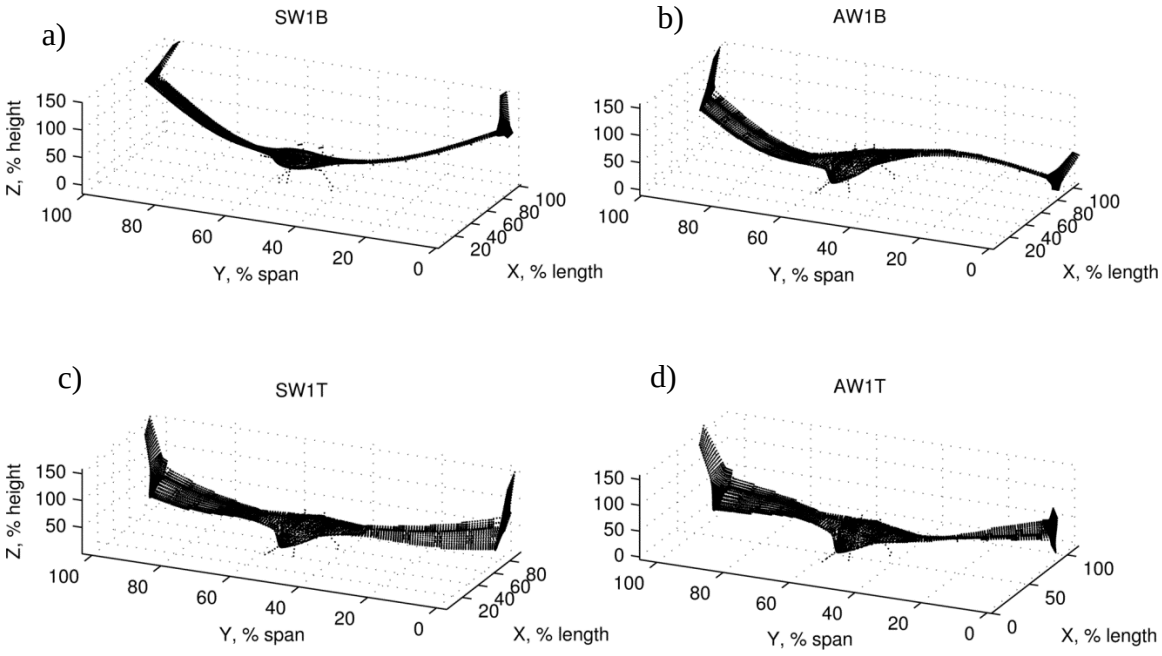

Figure 5.7: Normal Mode Shapes of the X-56A Model: a) SW1B; b) AW1B; c) SW1T; and d) AW1T.

Only four modes are shown here, but 14 flexible modes were included in all of the X-56A models. Fourteen were found to be sufficient to capture the salient flexible motion characteristics.

Visual inspection reveals that the first two mode shapes appear strongly coupled with rigid body motion. The coupling is pronounced in the symmetric wing first bending (SW1B) mode, where rigid body pitch and heave are observed. The antisymmetric wing first bending (AW1B) mode has a substantial rigid body roll component. The symmetric first wing torsion (SW1T) mode has a slight pitch coupling which is difficult to see. The antisymmetric wing first torsion (AW1T) is slightly coupled with roll. The next section introduces the flutter analysis. This is required for selecting an appropriate flight condition and modal coordinates for feedback.

5.2.2 Flutter Analysis

As the modal frequencies shift due to coupling aerodynamic forces, they may move from stable to unstable regions. Therefore, it is important to determine where this occurs so that the flutter margins of the vehicle can be computed. To determine the theoretical flutter margins of the vehicle the eigensolution of the aeroelastic system equation [See Eq. (5.1)] was solved [172].

The accuracy of the solution is paramount for the development of a model based control system. Thus it is important to verify that the frequency and time domain aerodynamics match. Further validation can be done in wind tunnel and flight test environments, but these are not completed here. Both frequency and time domain modal aeroelastic solutions are presented in Fig. 5.8.

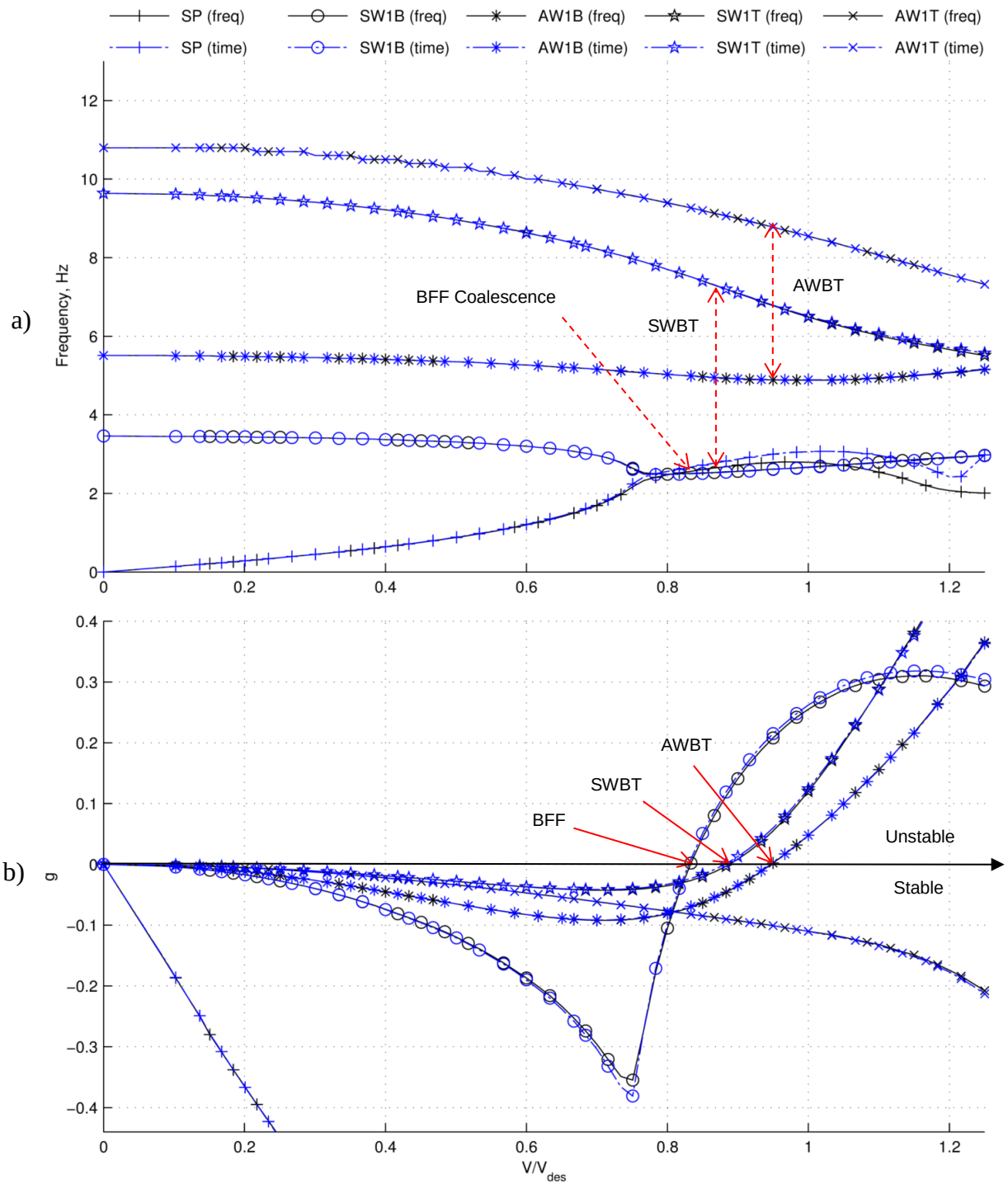

Figure 5.8: Flutter Analysis of X-56A Model: a) Frequency versus Velocity, V-f ; and b) Damping versus Velocity, V-g.

Figure 5.8 shows an overlay of the aerodynamic approximation for the state space models with the frequency domain aerodynamic solutions. This verifies that the RFA is good and analysis can continue with confidence.

Figure 5.8(b) reveals that three flutter modes exist. The first mode that goes unstable (that is, crosses $0g$) is BFF at a ratio of design speed, V_{des} , of approximately 0.82. The BFF frequency is 2.7 Hz (16.9 rad/s). The viscous damping ratio for the BFF is -0.13. Recall that the g value is equal to the negative of twice the viscous damping [170]. Therefore, positive g corresponds to an unstable flight condition.

The SWBT mode appears at approximately 89 percent of design speed at a flutter frequency of 6.5Hz (41 rad/s). The viscous damping ratio of the SWBT is lower than the BFF at -0.06. The velocity versus frequency plot, V-f, indicates that unfavorable coupling occurs between the SW1B and SW1T normal modes, similar to what one might expect when performing a flutter analysis on a clamped plate [170]. Typically, the coupled modes' frequencies shift down but do not coalesce.

The AWBT mode appears at 94 percent of design speed at a flutter frequency of 4.9 Hz (30.7 rad/s). The damping ratio of the AWBT is -0.024. This represents another unfavorable coupling between the AW1B and AW1T normal modes.

The viscous damping of each mode decreases (margin of instability grows) very quickly, relative to velocity changes. This is especially true for the BFF. In practice, flutter predicted in this way is conservative, as structural damping is unaccounted for. However it is useful for picking a design speed to design a controller as it is. Further tweaking comes later.

It is desired to pick a design speed which is subject to all three flutter instabilities. Therefore the design plant is chosen at a ratio of design speed of one. To verify that the flutter modes are present at the design speed, the X-56A state space model was perturbed with a unit-scaled control deflection command to the right-wing control surfaces (See Fig. 5.3), lasting 0.001 s. The pertinent state space variations are plotted in Fig. 5.9.

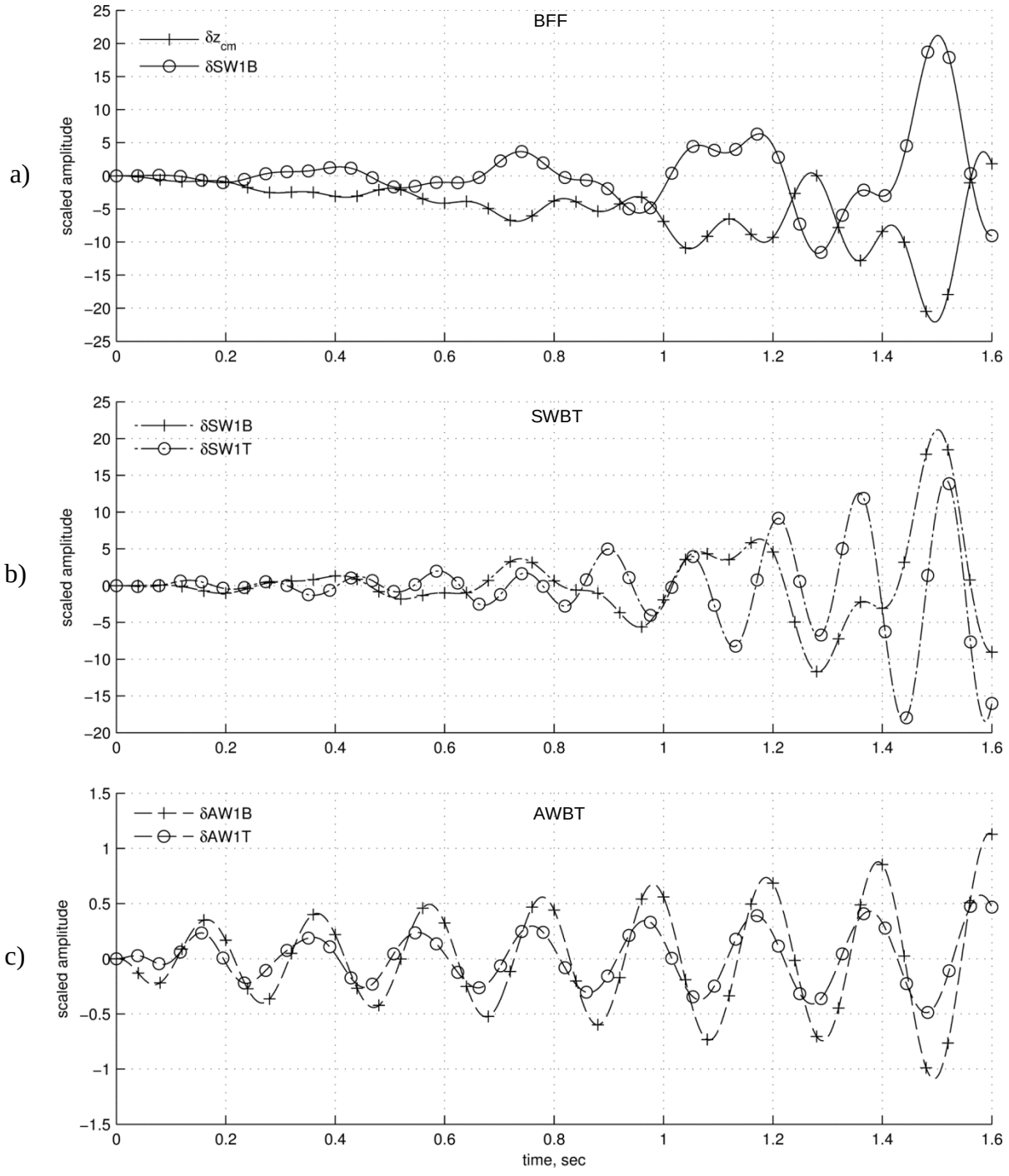

Figure 5.9: The X-56A Model in Open Loop Flutter at Design Speed: a) BFF; b) SWBT; and c) AWBT.

The BFF mode in Fig. 5.9 (a) is demonstrated by the interaction of the scaled states, rigid body heave state, δz_{cm} , and modal displacement $\delta SWB1$. The flutter characteristics of the BFF mode are divergent oscillations of contributing modes at the same frequency, out of phase.

The SWBT mode also illustrates the unfavorable coupling of modal displacements: $\delta SW1B$ and $\delta SW1T$ (See Fig. 5.9[b]). The nature of the coupling is difficult to discern because it appears random in nature. This means that there is an interaction with another mode, likely the BFF mode.

The AWBT mode shows an in-phase interaction of modal displacements: $\delta AW1B$ and $\delta AW1T$. The scaled modal amplitudes are small but clearly grow in time, verifying that this flutter mode also exists at the design flight condition. Without control, the aircraft will experience strong flutter instability and will require AFS at this speed.

One important characteristic should be noted, other than flutter. Note that altitude is lost over time (See Fig. 5.9[a]). This could be due to the fact that the impulse energy is in one direction. It could also be due to trim conditions. The trim angle of attack was computed at a lower speed where the model is stable. However, this is not expected to dramatically affect the application of the modal filtering design methodology.

The flutter modes indicate that four flexible modal displacements should be used for control feedback, including $\delta SW1B$, $\delta SW1T$, $\delta AW1B$ and $\delta AW1T$. However, the frequencies of the anti-symmetric modes are prohibitively high and close to the actuator bandwidth. Therefore only the symmetric 1st bending and 1st torsional modal displacements are selected for feedback. The requirements of the vehicle controller are

now overviewed, and a μ-optimal controller is designed, which can track both rigid body states and the first two modal displacements.

5.2.3 Control Design

It is desired to suppress the flutter modes (See Figs. 5.8 and 5.9) and track the rigid-body commands of the X-56A aircraft. This is especially important in consideration of Research Question 5 which asks for if a full coupled modal and rigid body controller can be designed.

In addition, one of the primary objectives is to demonstrate virtual deformation control on a flight vehicle to satisfactorily confirm one answer to Research Question 4, which inquires as to what shape control methods the modal filter enables. With these concepts in mind the aircraft controller is designed. The following two sections provide an overview for how the control design phase is accomplished. The first step of Phase I is to define the robustness and performance requirements.

Since flutter is a potentially destructive phenomenon, the modal controller must be robust to uncertainty. This is especially important for a modal controller, since during a ground vibration test, mode shapes are typically not predicted exactly [7]. In fact, cross-coupling is a primary argument against using a modal filter for control. Cross-coupling can occur when any one mode shape in the modal matrix is not accurate and propagates into other modal displacement estimates through projection [194].

To reduce these uncertainties, the following uncertainty requirements were defined: 10 percent multiplicative uncertainty on the inputs and outputs, and 10 percent additive uncertainty on the scaled plant. Since flutter speeds are hard to predict precisely

and structural damping is not modeled, the controller requirements must also be satisfied at off-design conditions.

A notional requirement is that the controller must be robust to a 3-percent speed variation. This requirement seems limited. However, it is practical considering the other uncertainties and considering the design speed is at flight condition with a high margin of instability (See Fig. 5.8).

Robustness to parameter uncertainty is highly desirable, but the controller must also meet performance specifications. The tracked measurements must respond to doublet inputs with low rise times and small overshoots. Quality performance must also be achievable in the aforementioned uncertainty conditions to demonstrate robust performance. The uncertain plant and required control system is summarized in Fig. 5.10.

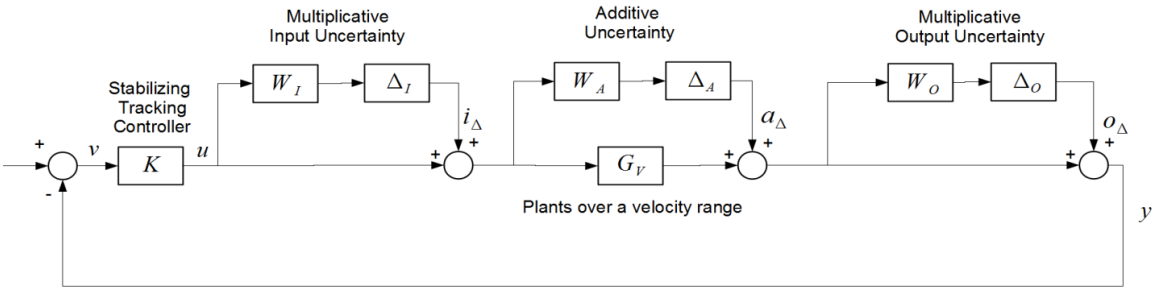

Figure 5.10: The Uncertain Plant and the Required Controller for the X-56A Model.

Considering the uncertainties in Fig. 5.10(a) μ-Optimal [103] control approach was taken. The design approach uses a hybrid of performance weights and uncertainty weights. Robust stability (RS) is achieved if and only if a system is stable for all perturbed plants about the nominal model up to the worst-case uncertainty. The robust stability condition which must be met for the μ-optimal controller is given as in Eq. (5.17).

$$RS \iff \mu\left(M_\Delta(\hat{\imath}\omega)\right) < 1, \forall\omega \tag{5.17}$$

The μ is calculated over the frequency range with the relation shown in Eq. (5.18),

$$\mu\left(M_\Delta(\hat{\imath}\omega)\right) = \frac{1}{min\{k_m | det(I - k_m M_\Delta(\hat{\imath}\omega)\Delta) = 0 \; for \; structured \; \Delta, \bar{\sigma}(\Delta) \leq 1\}} \tag{5.18}$$

where k_m is the stability margin, $\bar{\sigma}$ is the maximum singular value, and Δ is the structured uncertainty. The transfer function matrix from the input of the uncertainty blocks to the outputs of them as shown in Fig. 5.10 is presented as in Eq. (5.19),

$$M_\Delta = \begin{bmatrix} -W_I T_I & -W_I K S_O & -W_I K S_O \\ W_A S_I & -W_A K S_O & -W_A K S_O \\ W_O G S_I & W_O S_O & -W_O T_O \end{bmatrix}, G\mathcal{E}G_V \tag{5.19}$$

where W_I is a matrix of proper input weights, W_A is a matrix of proper additive weights, W_O is a matrix of proper output weights, and K is the controller. From this matrix, the salient sensitivity and complementary sensitivities from the M_Δ structure are identified which correspond to the requirements. The magnitude of the singular values predict the performance of the control system. These closed loop transfer functions are defined as in Eq. (5.20),

$$\begin{aligned} T_I &= KG(I + KG)^{-1} \\ KS_O &= K(I + GK)^{-1} \\ S_O &= (I + GK)^{-1} \\ S_I &= (I + KG)^{-1} \\ T_O &= GK(I + GK)^{-1} \end{aligned} \tag{5.20}$$

where T_I is the input complementary sensitivity, S_O is the output sensitivity, S_I is the input sensitivity, and T_O is the output complementary sensivitiy. To improve rejection of control input uncertainty, the controller was designed around the plant as shown in Fig. 5.11.

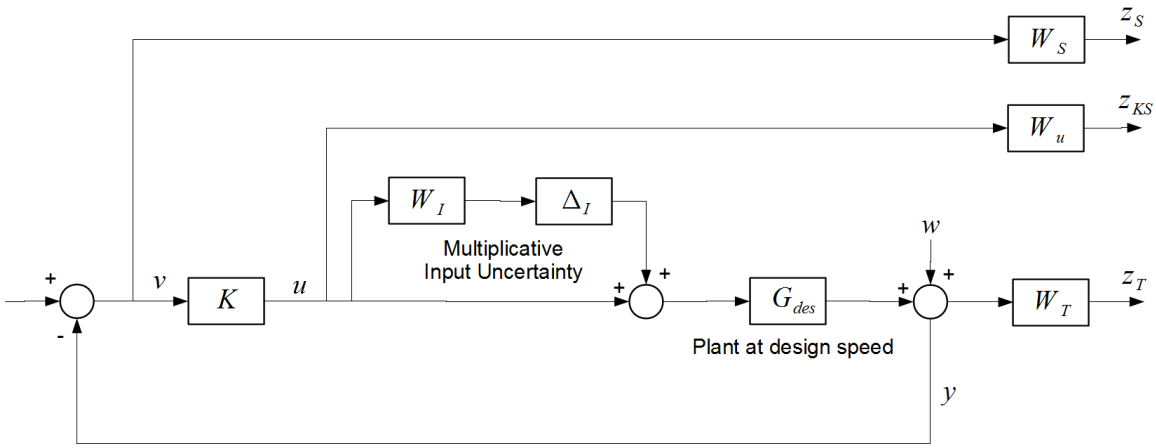

Figure 5.11: The Control Design Framework for the X-56A Model.

The design plant, G_{des} , at the design speed, V_{des} , was of order 130. To improve controller synthesis G_{des} was scaled by the full range of actuator movement and expected sensor output changes. The translational states, δx_{cm}, δy_{cm}, and δz_{cm}, and the velocity state were removed from the model.

With the resulting 126th-order model, balanced reduction [174] was performed to bring the model order to 90 states. The selected states to be tracked were: $SW1B$ and $SW1T$ modal displacements, pitch angle, θ, and bank angle, ϕ. The angle of attack α, angle of sideslip β, and yaw angle, ψ were also sensed but were chosen to be suppressed.

Traditional proper weights from a mixed $\mathcal{H}_\infty$ synthesis were utilized along with multiplicative uncertainty at the plant inputs. The input uncertainty weight, W_I, was adjusted to achieve maximum amplitude near the actuator break frequency. Sensitivity weight, W_S, was adjusted for integral tracking on tracking states and for suppression on suppression states.

It was found that the break frequencies of the modal displacement performance weights had to be increased 10 rad/s relative to the airframe state weight break

frequencies of 1 rad/s. The break frequency of the control weight, W_u, was adjusted to 5 rad/s for reduced control surface movement. The break frequency of the complementary sensitivity weight, W_T, was set to 30 rad/s to improve high frequency noise rejection. The uncertainty transfer function, N_Δ , was calculated (See Fig. 5.11) to be as shown in Eq. (5.21):

$$N_\Delta = \begin{bmatrix} W_I T_I & -W_I K S_O \\ -W_S G S_I & -W_S S_O \\ -W_u T_I & -W_u K S_O \\ W_T G S_I & -W_T T_O \end{bmatrix} \tag{5.21}$$

One may verify that all of the pertinent closed-loop transfer functions corresponding to those shown in Eq. (5.20) are present in Eq. (5.21). Thus, by reducing the $\mathcal{H}_\infty$ norm of N_Δ, the specified uncertainties (See Fig. 5.10) can be rejected.

For this control design architecture, the μ-optimal controller was computed using MATLAB's Robust Control Tool Box. To find the controller, DK-iteration (See Ref. [103]) was performed, which solves the iterative optimization problem shown in Eq. (5.22).

$$\min_K \left(\min_{D_\omega} \left\| D_\omega N_\Delta(K) {D_\omega}^{-1} \right\|_\infty \right) \tag{5.22}$$

The DK-iteration resulted in a 162th-order controller after some trial and error with the weights in Fig. 5.11. The controller was then internally balanced [174] and truncated to 44 states without a substantial loss of robustness or performance. This resulted in an $\mathcal{H}_\infty$ norm of 3.29.

It was difficult to meet both performance and robustness requirements with the scaled plant. Therefore, the desired $\mathcal{H}_\infty$ norm of 1 was not achieved. Rescaling may

improve the controller. The next section discusses the controller stability and performance.

5.2.4 Controller Stability & Performance

Nominal stability (NS) was verified for the reduced order controller by verifying that eigenvalues of the closed-loop system had real negative parts. An analysis of the singular values of the loop gain as well as the closed loop sensitivity functions given in Eq. (5.20) are presented in Fig. 5.12.

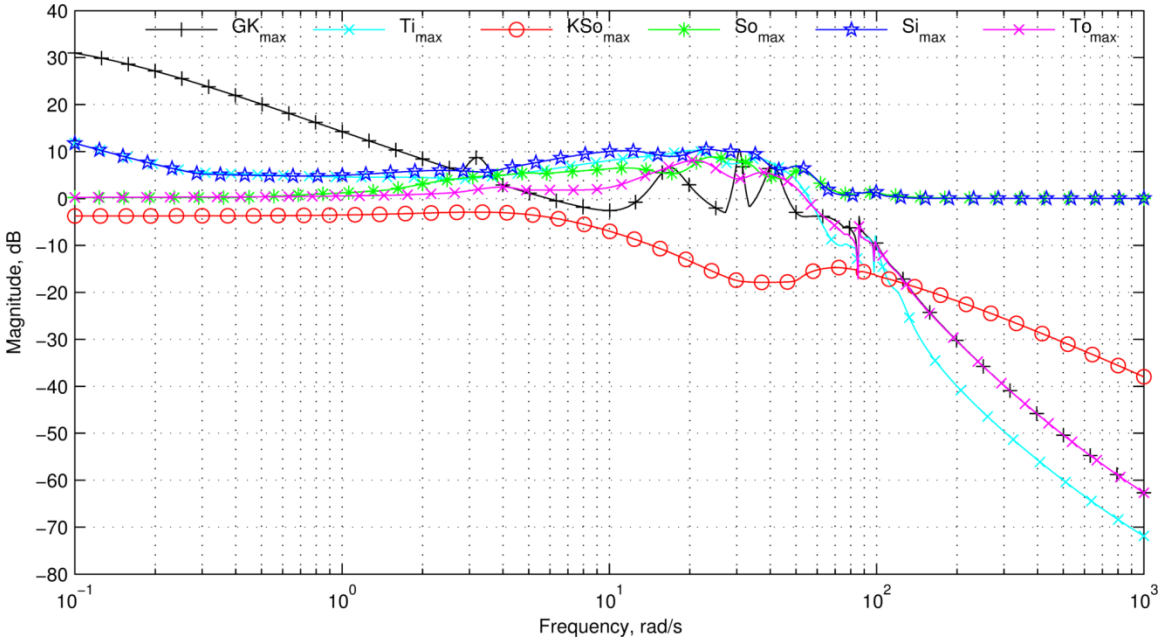

Figure 5.12: Maximum Singular Values of Open Loop (GK) and Closed Loop Sensitivity Functions.

At first glance, Fig. 5.12 reveals that most of the closed loop transfer functions stay at or beneath 10 dB, corresponding to a magnification of the inputs to these transfer functions of approximately 3.2. The controller bandwidth is 25 rad/s which is high but

below the actuator break frequency. After this frequency, the complementary sensitivities fall sharply at 60 dB/decade. Therefore, noise will be attenuated well past 25 rad/s.

Recall that it is desired that the controller be robust to uncertainty and, of course, disturbances. Robustness to input multiplicative uncertainty is strongly impacted by the maximum singular values of T_I [See Eq. (5.19)]. The maximum singular value of T_I within the bandwidth of the controller has a magnitude of 10 dB. Therefore the controller will amplify input uncertainties at frequencies where flutter is most likely to occur.

Robustness to additive uncertainty or gust responses is strongly affected by the peak of the closed-loop transfer function, KS_O. Over the entire bandwidth, the singular values of KS_O are below 0 dB and, thus, gust-like disturbances will be attenuated. The magnitude of the singular values of KS_O fall off quickly after 6 rad/s. This predicts that higher frequency turbulence will be rejected.

Robustness to sensor uncertainty is predominantly dependent on the peaks of S_O and T_O. From 0.1 rad/s to 1 rad/s the singular values of S_O show that plant uncertainty is neither amplified nor reduced; however, near flutter frequencies the plant uncertainty is amplified. The singular values of T_O indicate that sensor noise or output uncertainty will not be strongly amplified past 25 rad/s.

Some aspects related to tracking may also be identified from Fig. 5.12. For best tracking accuracy, T_O must be equal to 0 dB over most of the controller bandwidth. Figure 5.12 shows that there are several peaks above 0 dB, which may lead to overshoots or poor performance. The tracking history can be investigated by inputting doublet reference inputs to the controller. The set of charts presented in Figs. 5.13-5.15 expands on the performance and robustness characteristics of the controller.

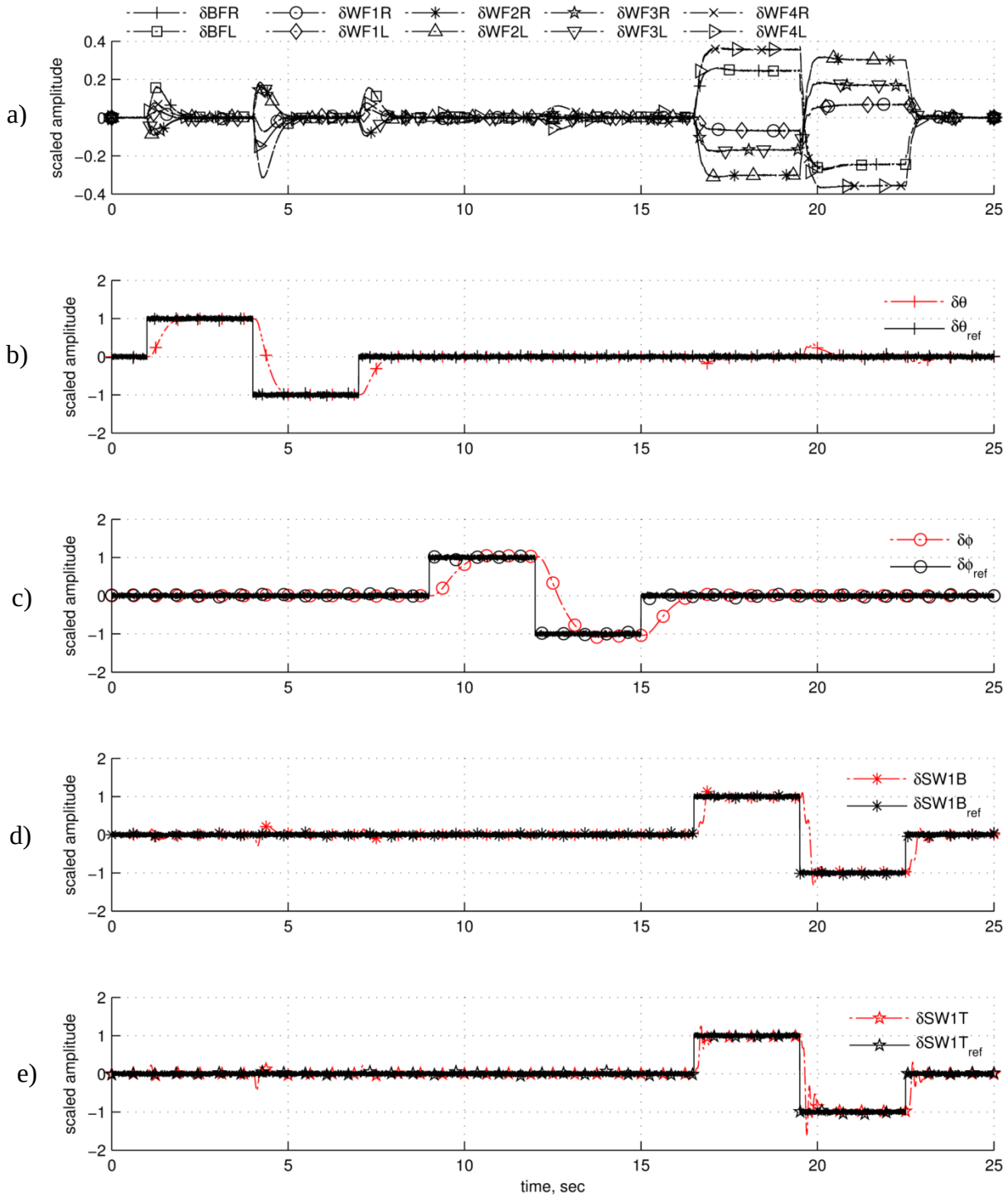

Figure 5.13: Performance Chart for Doublet Inputs to Tracked Variables on X-56A: a) Control Surfaces; b) Pitch Angle Tracking; c) Bank Angle Tracking; d) SW1B Modal Displacement Tracking; and e) SW1T Modal Displacement Tracking.

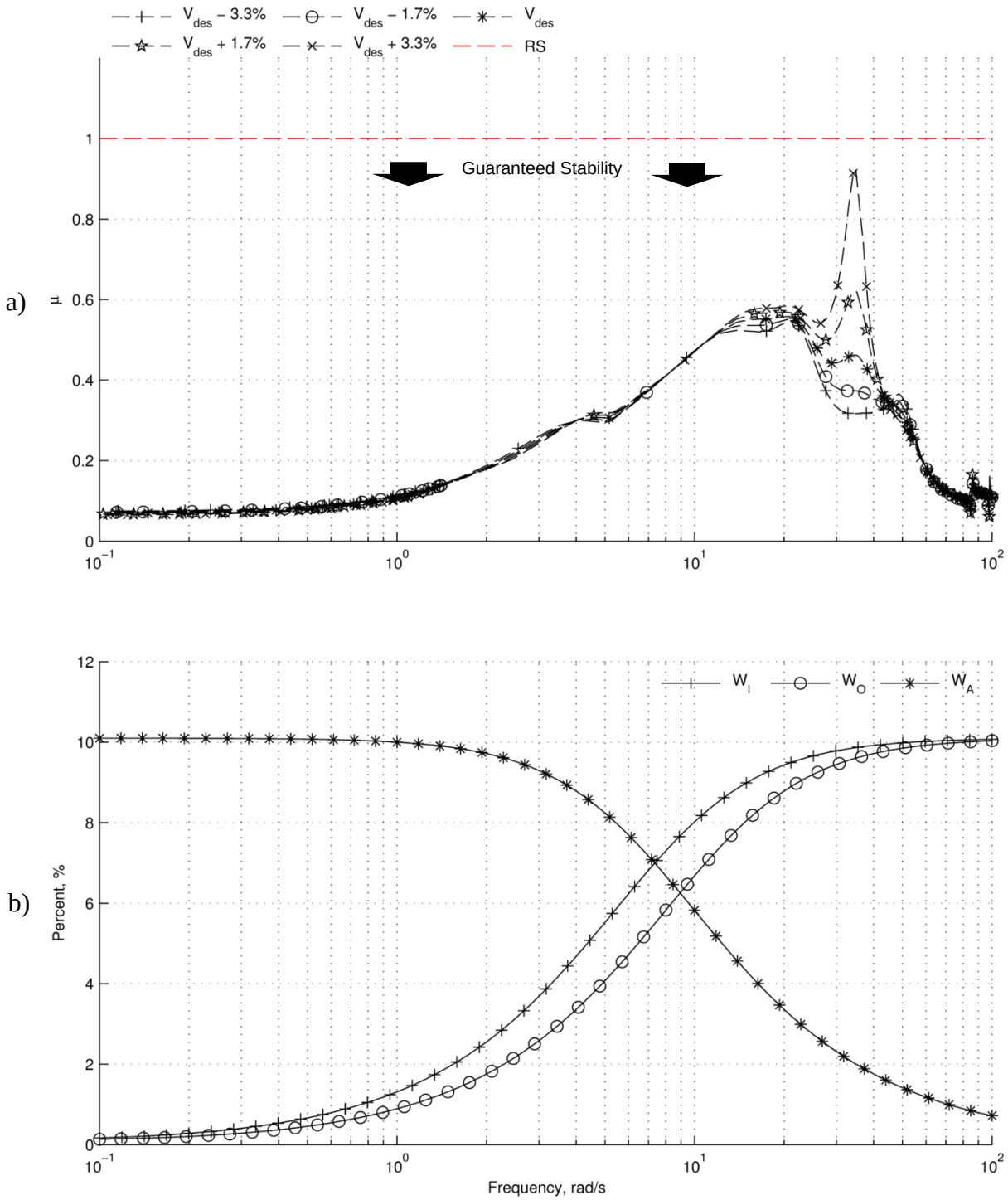

Figure 5.14: Mu Analysis over Speed Range: a) μ Chart; and b) Corresponding Uncertainty Weightings.

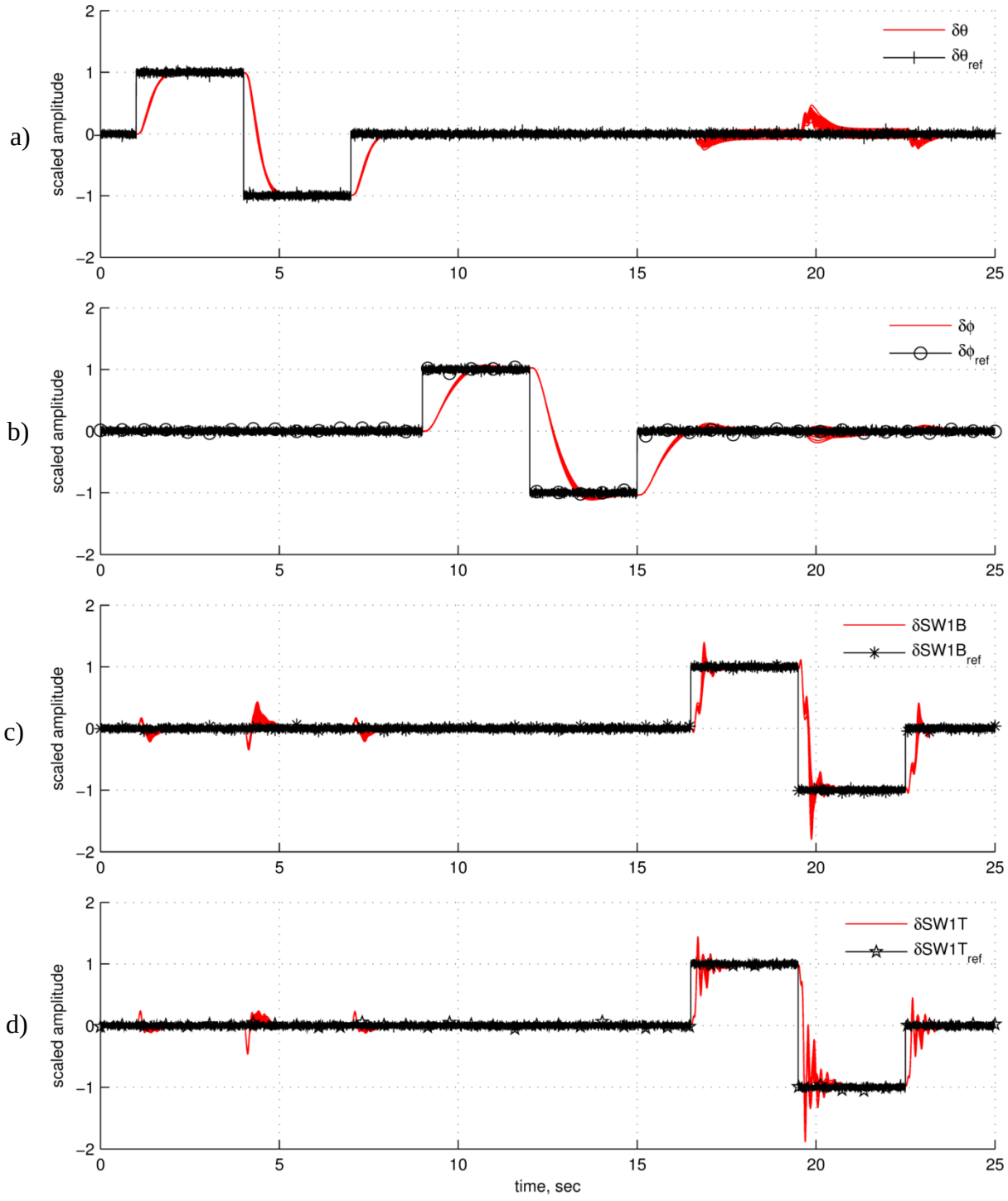

Figure 5.15: Performance with Structured Uncertainty: a) Pitch Angle Tracking; b) Bank Angle Tracking; c) SW1B Modal Displacement Tracking; and d) SW1T Modal Displacement Tracking.

It was desired that the responses of the system to a doublet have low rise time and small overshoots. This goal was for the most part achieved (See Figs. 5.13 and 5.15). All of the signals had low rise times of 0.25 s to 1.5 s. The change in pitch angle, $\delta\theta$, had excellent tracking characteristics. The change in bank angle $\delta\phi$ showed a reasonable response. The tracked modal displacements were non-minimum phase. The modal displacement, $\delta SW1T$ experienced a 25 percent overshoot, which was predicted by the singular values of T_O.

There was very little rigid body longitudinal and lateral coupling. It was interesting that the commanded rigid-body signals moved off their reference point when modes were commanded. The converse also happened; pitch angle commands tended to disturb the modal displacements. This indicates that a strong coupling between rigid body motion and flexible motion in the models exists, which cannot be easily avoided.

The normalized control movements for $\delta\theta$ and $\delta\phi$ tracking were reasonably small. In fact, the movement of the control surfaces for $\delta\phi$ tracking was almost unnoticeable. During modal displacement commands, the normalized control movements moved to a maximum amplitude of 0.4 on the body flaps. Since the outputs are scaled to half of the actuator limits, this is a relatively large control movement, but is not unreasonable. In Fig. 5.13(a) it is seen that control movement was significantly larger when commanding the modal displacements, than when commanding the flight variables.

Significant control authority is required to perturb the X-56A structure from equilibrium. However, improper scaling may be to blame. Based on this analysis, the nominal performance (NP) appears to be adequate, although it might be improved with better weights and plant scaling.

Figure 5.12 indicates that some disturbances and uncertainties are amplified; however, the actual impact of these uncertainties on the stability must be checked with a μ analysis as shown in Fig. 5.14. The μ analysis calculates robustness of the modal controller across dimensions of speed and uncertainty. For a range of plants G_V additive, multiplicative input and output uncertainties with 10 percent weightings (See Fig. 5.14[b]) was added.

The chosen shapes of the weightings were meant to replicate worst-case scenarios. Additive uncertainties may be more likely to occur in the 0.1 rad/s to 10 rad/s range due to gust disturbances. Multiplicative uncertainties may be more likely to occur at higher frequencies due to actuator dynamics and sensor uncertainties and noise. For the generalized plant with uncertainties, μ were then calculated across the operational frequency range with one controller, as shown in Fig. 5.14(b).

Recall that RS is guaranteed if the condition given in Eq. (1.14) is met. Therefore, it is desirable that μ be less than one for all structured uncertainties. The maximum μ for all perturbed plants was 0.92. Therefore, RS is achieved. The variation of μ across the frequency range shows that it tended to increase at closed loop flutter mode frequencies. The μ tended to increase for speeds past the design speed. Conversely, the μ decreased for plants below the design speed. This happens because as speed increases the margin of instability of the flutter modes increases (See Fig. 5.8[b]). The reverse happens when decreasing in speed.

Figure 5.14 indicates that the design requirement to be RS to a three percent variation in speed was met. Hence, it is shown here that the modal controller can be

designed to be a robust to modeled uncertainties. Performance at off design conditions must also be analyzed.

Robust performance (RP) is achieved if and only if the performance objectives are achieved for all possible plants about the nominal plant up to the worst-case uncertainty [103]. There were no hard performance requirements defined other than that the tracked signals have low rise times and small oscillations.

Figure 5.15 indicates that the responses from the perturbed plants was tight around the acceptable nominal plant responses shown in Fig. 5.13. The overshoots on the modal displacements for some perturbed plants did increase to 50 percent. But this overshoot increase is acceptable for the current study. Therefore, RP is achieved for these lenient performance requirements.

Since NP, RP, NS, and RS are adequately achieved, the modal controller is acceptable. It meets basic criteria necessary for utilization in an aircraft. This completes Phase I. The controller designed here is used for the virtual deformation control simulation of the X-56A. The performance and robustness results of the controller design indicate a strong positive response to Research Question 5.

5.2.5 Fiber Optic Sensor Placement

The modal filter design phase (Phase II) begins with sensor placement. Traditionally, strain sensors or accelerometers used for active structural control are placed in an optimal sense. One of the benefits of using FOS is that optimal sensor placement (OSP) routines [21, 174] lose significance.

The first few structural modes in bending and torsion are most significant to flutter, so the sensors are placed from root to wing tip to capture bending information. The sensors are laid from trailing edge to leading edge to capture torsional motion. The resulting sensor configuration looks like three claw marks across each wing. The resulting sensor configuration is given in Fig. 5.16.

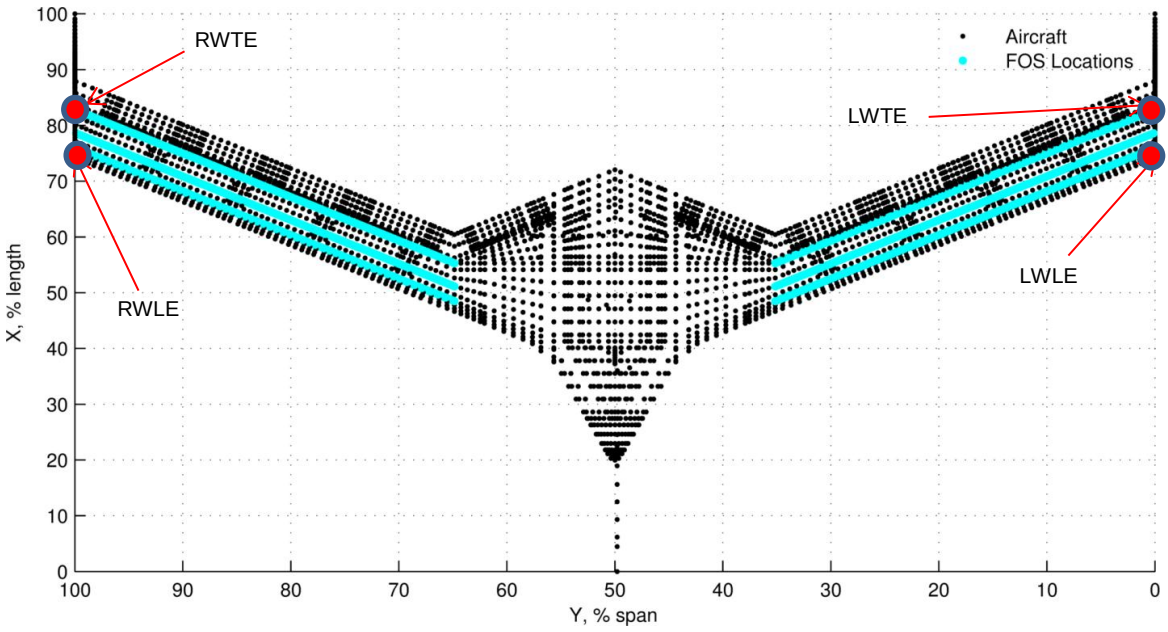

Figure 5.16: The Fiber Optic Sensor Layout on the X-56A Model.

Three fibers were chosen instead of two, for robustness considerations. If one fiber on a wing fails it may still be possible to compute torsional information with two fibers. The next section introduces the sensor strain mode shapes at the sensor locations.

5.2.6 X-56A Sensor Strain Mode Shapes

The strain and deformation modes defined at the SFOS locations are necessary to develop an operational modal filter. First the deformations at the sensor locations were

computed. This was done by laying a spline onto existing nodes of the X-56A FEM in MSC Nastran from root to tip. This was repeated for the number of fibers modeled.

The distance between each node on the spline was set at one-half-inch, which is the normal spacing between measurement gratings on the fiber [179]. At each node of the spline or sensor location a minute mass was added. The sensor nodes on the spline were then interpolated with RBE3 MSC Nastran cards. The modal analysis conducted in MSC Nastran gives sensor deformation mode shapes corresponding to each flexible mode.

The sensor deformations were used to compute sensor strain mode shapes. The conversion was implemented with Eq. (5.12). The sensor strain mode shapes were collected into the sensor strain mode matrix as in Eq. (5.13). The resulting strain modes appeared noisy. Thus, the strain was fit to a third order polynomial surface for each wing and an M-estimator [195] was utilized to trim outliers. The first four sensor strain modes used for the X-56A simulation studies are given in Fig. 5.17.

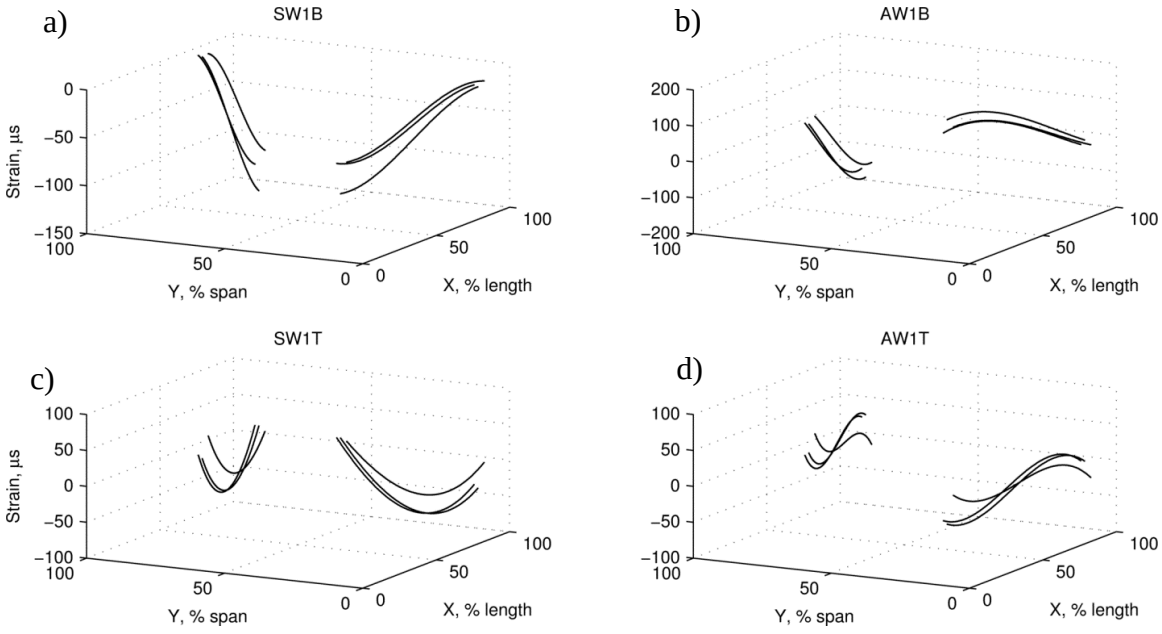

Figure 5.17: Sensor Strain Mode Shapes of X-56A Model: a) SW1B; b) AW1B; c) SW1T; and d) AW1T.

The SW1B mode has a strain distribution which starts out very high near the root of the wing (See Fig. 5.17) and goes to nearly zero at the wing tips. It is typical that in bending, strain is highest near the root of the beam [7]. The AW1B mode shows an antisymmetric strain distribution in bending. The SW1T mode shows a distribution of strain which has an inflection near zero close to the mid-span of the wing, indicating that for torsion modes where the wing is twisting, very little strain exists in the mid-span of the wing.

The AW1T mode, like the AW1B, mode has an antisymmetric strain distribution in torsion. The sensor modes are collected into the modal matrix defined in Eq. (5.13) and, together with Eq. (5.8), the modal displacement states of the aircraft can be measured.

5.2.7 Verification of Sensor Strain Mode Shapes

A moment is taken here to computationally verify the strain mode conversion procedure. It is not clear if the conversion of modal shapes to strain shapes is correct without experimental validation or at least a real simulation of strain. At least one verification step is taken here and that is show that the transformation has characteristics which satisfy the condition that the total strain is a linear combination of the modal strain shapes.

This is analogous to the concept that the total deformation can be expanded as a linear combination of modal deformation shapes. To verify that this characteristic linear relationship is achieved during the transformation, the bending mode shape is strain transformed at three separate modal displacement amplitudes, $q_1(0) = \{1,2,3\}$. Results in

Fig. 5.18. indicate that at each point, the sensor strain amplitudes increase linearly with the modal displacement amplitudes.

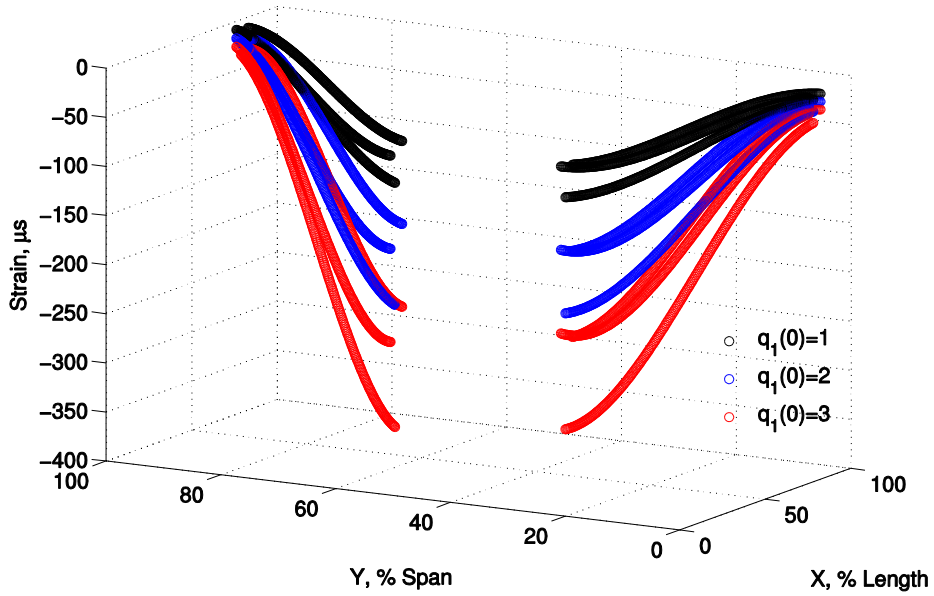

Figure 5.18: 1st Bending Strain Mode Shapes Transformed at Different Amplitudes.

Hence, the overall relationship remains linear during the displacement to strain conversion as expected. This at least confirms that the conversion technique is consistent. However, more validation is needed to determine if the strain conversion is correct. Until future experiments are completed it is assumed the strain mode transformation is valid and the following relationship indeed holds for small amplitudes:

5.2.8 Reference Signal Creation

With the strain mode matrix prepared, attention is turned to the reference signal, which is needed for virtual deformation control. For reference signal creation, the deformation free-free mode shapes shown in Fig. 5.7 are transformed according to Eq. (5.15). Four of the transformed mode shapes are given in Fig. 5.19.

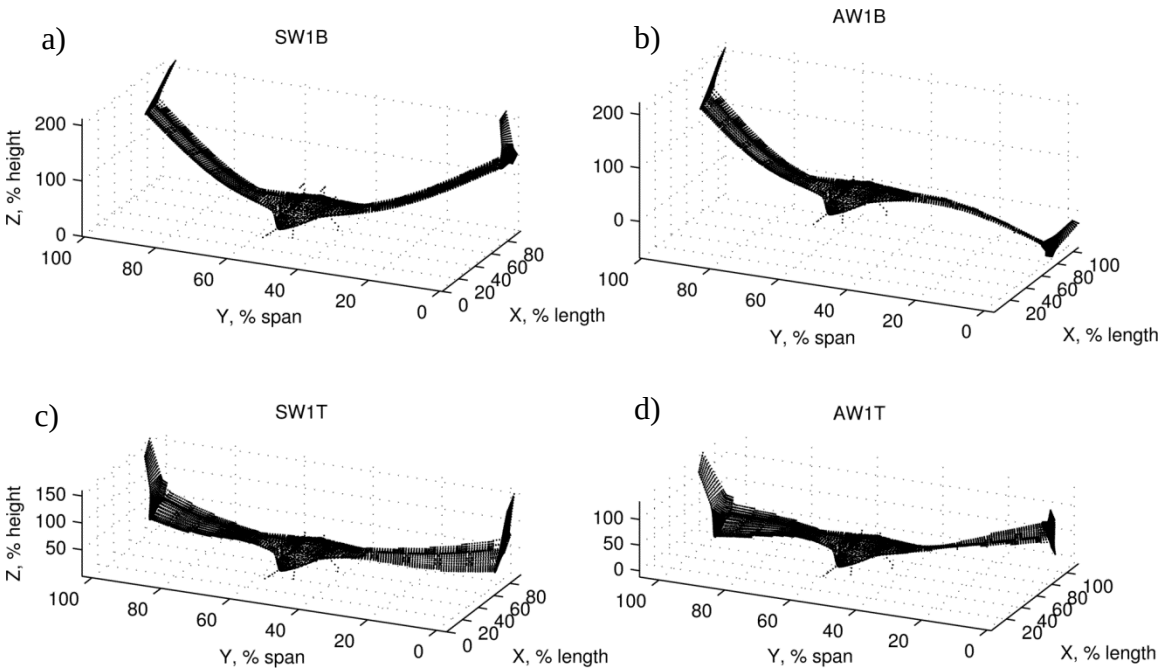

Figure 5.19: Transformed Mode Shapes of X-56A Model a) SW1B; b) AW1B; c) SW1T; and d) AW1T.

The mode shapes with rigid-body components removed (See Fig. 5.19) may be used with Eq. (5.16) to develop appropriate reference signals. Note that the flexible movement within each transformed mode shape appears amplified relative to its respective free-free mode shape presented in Fig. 5.7. Deformation commands can now be adequately transformed to achieve virtual deformation control.

Points on the aircraft must also be chosen for deformation commands. These points can be anywhere on the aircraft. A multitude of points could be chosen for total shape optimization. For proof of concept, four points were selected in this case study.

Kammer's effective independence (EI) procedure [176], was utilized to locate the four points in Fig. 5.16.. This was done to find points with the highest deformation in the

commanded mode shapes. This might reduce the chances of the reference signal from exciting residual modes better, but it is not known for sure if this is true.

The located points are right-wing trailing edge (RWTE), right-wing leading edge (RWLE), left-wing trailing edge (LWTE), and left-wing leading edge (LWLE). Their index locations in the modal matrix are referred to as l_r. As in the wing model results indicate that the wing tips carry the most modal information. Note that the selected points do not have to be on sensor locations for the virtual deformation concept to be employed.

5.3 Simulation

The modal controller derived in the previous sections adequately satisfies the robustness and performance objectives for the X-56A model. The simulation study presented here demonstrates the use of the modal filter for virtual deformation control via modal displacements of the aircraft. For demonstration, the controller designed in Phase I is put into a simulation with the modal filter designed in Phase II. The wing tips are commanded to a particular deformation using the reference signal derived in Phase III.

5.3.1 Virtual Deformation Control – Modal Displacement Tracking

The simulation architecture introduced in Fig. 5.1 represents the inner loop design for the X-56A simulation model. The exogenous inputs to the controller are references, provided by a notional outer loop control system. The references in Fig. 5.1 are separated into rigid-body commands, x_{AF}^{ref}, from the flight computer and vertical deformation

commands, d_{ref}, at selected locations (See Fig. 5.16), namely, LWLE, LWTE, RWLE, and RWTE.

The reference vertical deformations were chosen to be 0.6 percent of the span of the vehicle, which corresponds to modal displacement commands of approximately twice the scaled value. This value was thought to be reasonably small, since the control movement for scaled modal displacement commands was less than 50 percent of the actuator range as shown in Fig. 5.13(a).

Since the reference deformations were equal, a bending-type motion for the aircraft wing shape results. Different deformation choices could lead to torsion-type motion instead. The deformation references can be verified to generate a bending motion when transformed with Eq. (5.16) into a modal reference. For the following study, the airframe state references are set to 0.

The controller that was designed above (See Figs. 5.12-5.15) takes the difference of the references and the feedback signals to produce a control input signal. Multiplicative noise is added to the controller inputs, with a mean of 0 and standard deviation of 0.1. The plant takes the inputs via Eq. (5.8) and produces the state vector, x_e, in the output, which includes the measurements SW1B, SW1T, and the residual modes. The plant also outputs the rigid-body measurement vector, x_{AF}.

The SFOS measurements are simulated by multiplying the sensor strain matrix, Ψ_{FOS} , with the vector, x_e. Normal noise, n_s , with mean 0 and a standard deviation of 3 μ_s is then added to this strain vector. Since the rigid measurements are scaled, a normal distribution with mean 0 and standard deviation of .01 is added to the measurements to simulate noise. The results of the simulation to the reference are given in Fig. 5.20.

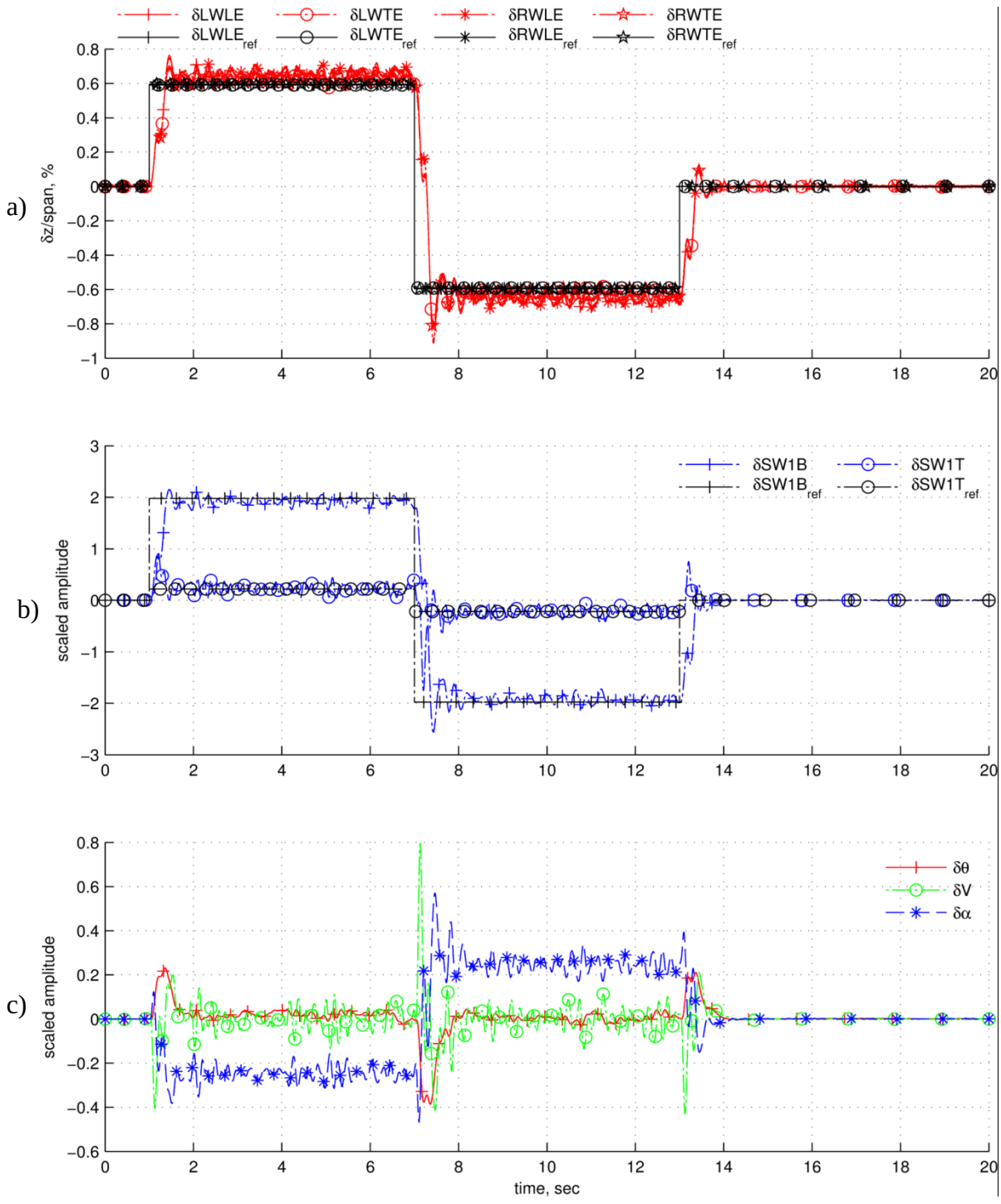

Figure 5.20: Virtual deformation tracking time history: a) deformation tracking at wing tips; b) tracked modal displacements; and c) scaled control surface movements.

The change in deformation near the wing tips (See Fig. 5.20[a]) indicates that the actual deformations moved very close to the deformation set-points. The error is due to the modal displacements from residual modes (See Fig. 4.20). This is expected, since the trailing-edge actuators are not collocated with the structure's sensors. Due to this fact and since the modes are coupled aerodynamically, independent modal control cannot be achieved [7].

The commanded modal displacements are shown in Fig. 5.20(b), and they are tracked well. Since the command is primarily due to bending, the SW1T modal reference is very small. The scaled SW1B modal displacement amplitude moves the greatest amount. Both modes had some overshoot and oscillations during the initial part of the command, which was predicted in Fig. 5.13. The steady state response has oscillations primarily due to the rather large multiplicative input noise modeled in the system.

During the shape-deformation maneuver, the aircraft experienced no enduring change of velocity or pitch angle. The angle of attack, however, achieved a steady-state change; the change in angle of attack should have also effected an enduring change in velocity. An angle-of-attack change generally leads to a drag increase or decrease, however, this was not observed, likely due to improper drag modeling.

If the results were taken as truth, it could be concluded from this analytical model that the effective lift over drag (L/D) ratio has changed. This observation could be a result of control surface movements, the bending and rotation of the wing, or both. The caveat here is that the results are achieved on a linearized plant model defined for small perturbations around the trim point. In flight, the aircraft achieves a new trim point from the angle-of-attack change, which may result in a lower or higher L/D ratio.

Outer loop control requirements are also observed from Fig. 5.20. The results indicate that the flight-path angle has changed due to shape deformation commands. Therefore, the aircraft will require a heading angle hold outer loop controller to make virtual deformation control feasible. The outer loop controller could command the pitch angle to control the flight-path angle; or it could command engine throttle settings, which are not currently modeled. If the throttle is changed to achieve trim, fuel efficiency degradation or improvement may be realizable, depending on the command to the structure.

5.3.2 Active Flutter Suppression

Previously, it was shown that the X-56A model experiences strong flutter at the design speed (See Fig. 5.9). Technically, the shape controller demonstrated above is capable of suppressing flutter. From the previous plots, this has not been shown explicitly.

To demonstrate AFS in a traditional sense, the aircraft is perturbed as before and the control system is turned on after a period of time of 1.6 s. To reduce control-induced oscillations, it was ramped in over a 1-s period, with all references set to 0. Within 2 s from the controller being turned on, the shape tracking controller achieves flutter suppression, as shown in Fig. 5.21.

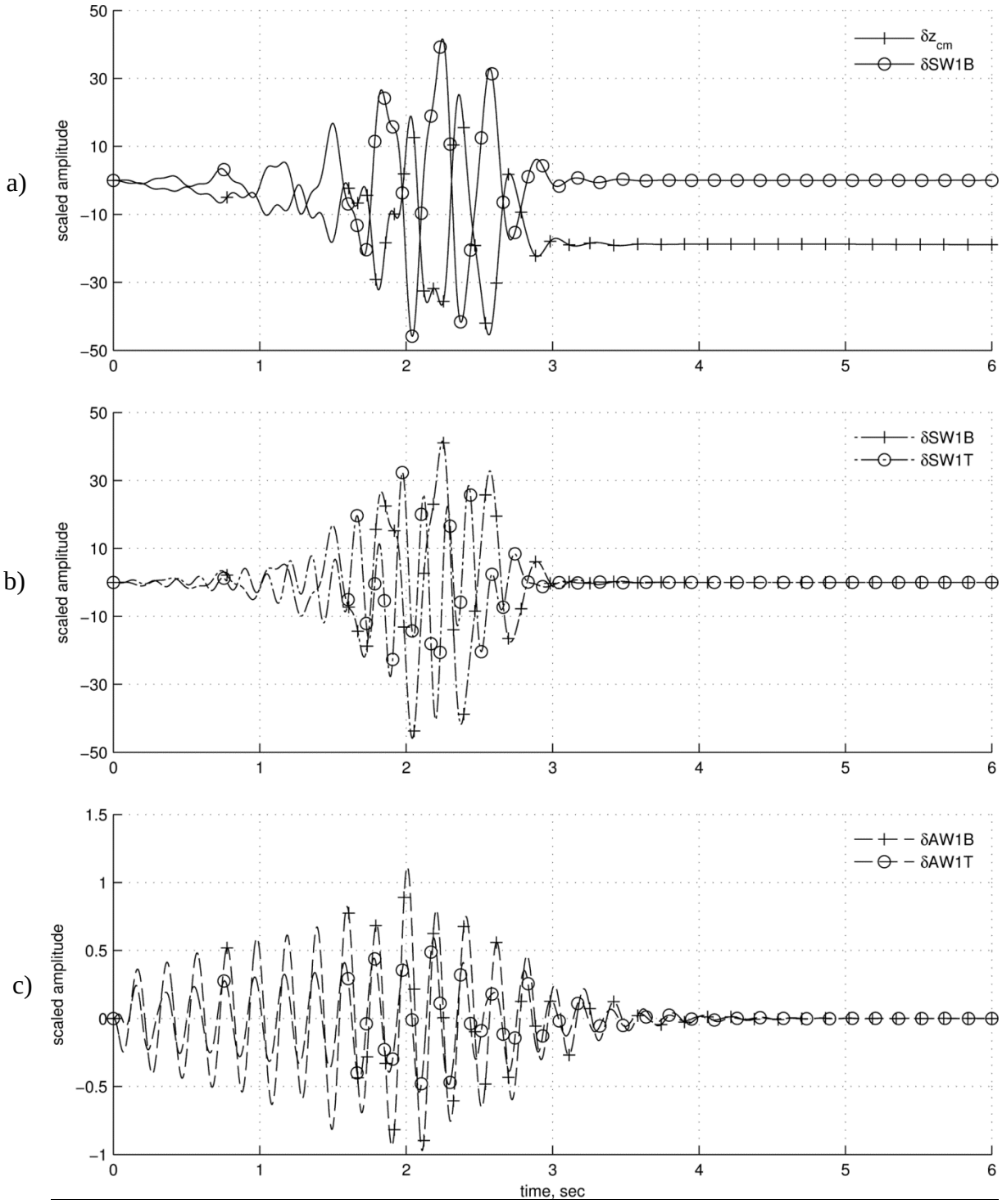

Figure 5.21: Active flutter suppression time history: a) BFF suppression; b) SWBT suppression; and c) AWBT suppression.

During AFS there was an altitude change (See Fig. 5.21[a]) observed as was discussed previously for the open loop model. What was interesting is that by commanding the symmetric modal displacements to zero, the AWBT mode was suppressed. This was unexpected, and must have been a result of coupling.

However, achieving AFS was not totally unexpected since control was implemented on a linear plant model. Nonlinear effects have not been included. Only the poles must be considered in such a model. The poles of the closed loop system have real negative parts and the closed loop system is, thus, stable. The open loop poles and the closed loop poles are plotted together in Fig. 5.22.

a)

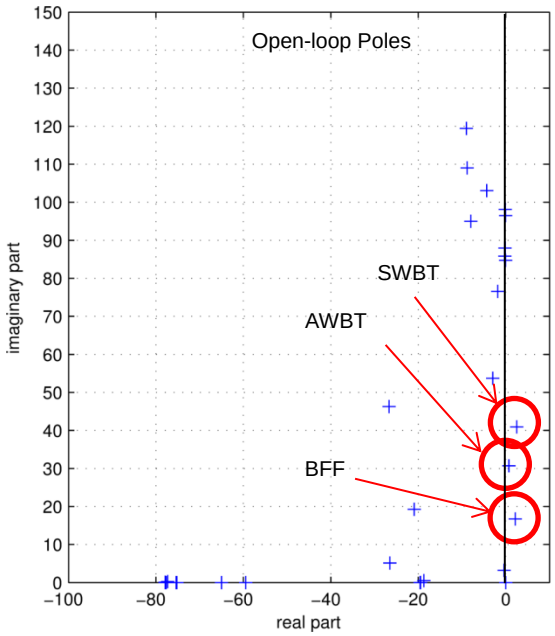

b)

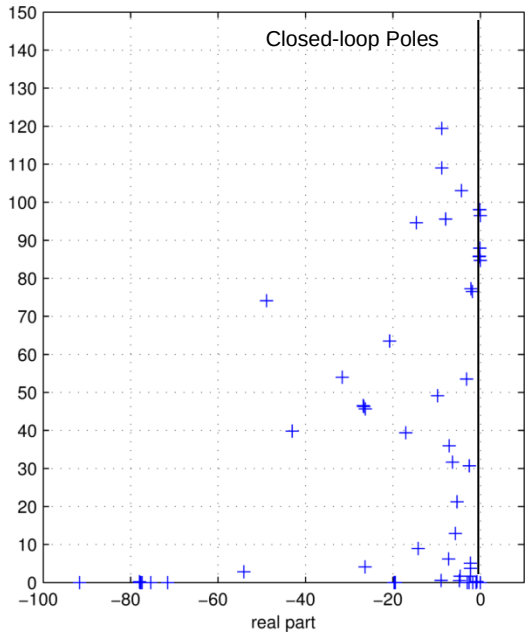

Figure 5.22: Open-loop versus closed-loop poles: a) open-loop poles; and b) closed-loop poles.

The poles of the open loop system indicate the presence of the three flutter modes identified above (See Fig. 5.8). There are also poles from lightly-damped structural

modes near the vertical axis starting at 54 rad/s. When the loop is closed with the controller, the flutter poles migrate to the stable region in the left half plane.

The lightly damping structural mode poles remain unchanged, as they are outside the controller bandwidth. The controller introduces poles seen tightly grouped near the lower right-hand corner of Fig. 5.22(b). Integrator and estimator poles are present. The lowest damping of the closed loop system poles within the actuator bandwidth is 0.08. This represents a significant improvement over the open loop BFF damping of -0.13.

5.4 Summary of X-56A Model Design Work

Recall that the original purpose of implementing a modal filter controller onto an aircraft. It was postulated that this would be a necessary verification step and the integration issues would be more complicated. This was found to be true.

Major differences were noted in how the modal filter was set up and how the reference transformation was designed. Each requires additional setup time and introduces risk into the design process. In any case, the simulation studies for the X-56A confirm the modal filtering methodology used to answer Research Question 2.

It was found that control of all three flutter modes could be completed by only feeding back two modal displacements. These modal displacements were selected intuitively and focused the control activity. This seems to be a better solution than trying to suppress all modal coordinates at once, as is required with accelerometer feedback.

Of further interest is the fact that shape control via modal filtering was handily demonstrated verified for aircraft (verifying a shape control method introduced for the Wing Model in answer to Research Question 4). The method is referred to as virtual deformation control. It was shown that the method controls displacements on an aircraft through modal referencing similar to the wing model. By using a bending command instead of a torsional command, less error was introduced by the residual modes and the shape command was accurately tracked.

A positive response to Research Question 5 was also verified. It was shown that a fully coupled rigid and flexible controller could be designing using the modal filter. However, the design was challenging. Finding the required plant scaling parameters for a modal coordinate is not intuitive. Separate break frequencies of weights may also be needed for rigid body and modal coordinate outputs. This makes the design more complex.

The remaining Chapters proceed with theoretical additions to the modal filter. This is required to make it robust to strong sensor bias. The development begins with the theoretical foundation, introduced in the next Chapter.

CHAPTER 6

THEORETICAL FOUNDATION

The previous Chapters have focused primarily on design, showing how modal filtering fits into the state space based aeroservoelastic control paradigm. A modal filtering design methodology was introduced and simulations of the wing model and X-56A were completed. It was found that the modal filter is applicable to aircraft control and enables two methods of shape control. The story continues by addressing the sensitivity of the modal filter to sensor bias.

Up till now the OLS type modal filter has been utilized. It was applied without consideration of its robustness to unexpected sensor bias. However, in order to answer Research Question 3 the modal filter must be made robust. This is the only way it can be applied to aircraft while satisfying safety concerns. It was hypothesized that a robust regression method would be necessary to shore up this limitation of the modal filter.

A review of robust regression methods is presented in this chapter. From the pool of available robust estimators, the concentration algorithms and M-estimation are postulated to be the key to deriving a robust modal filter. However these estimators may not be useful in their current forms for robust modal filtering without further manipulation.

The following sections begin with a very brief review of robust regression methods. The multivariate location and dispersion model (MLD) is introduced for a mathematical basis for the strain based modal matrix. Finally a detailed review of

concentration algorithms is presented. Concentration algorithms are reviewed in detail because they are much less well known than M-estimators.

6.1 Robust Regression Overview

There have been many developments in robust regression, with techniques for case diagnostics and robust regression. A robust estimator attempts to find a reasonable fit for the bulk of data then uses this fit to find discrepant cases, while case diagnostics use a fit to the entire data set to find discrepant cases.

In general, large residuals from an OLS parameter estimate do not confidently indicate the presence of an outlier, since an outlier may drag the fit parameters far away from the majority of the data points, and thus the residuals are no longer adequately descriptive [196, 197, 198].

Many techniques such as Least Median of Squares (LMS) [199, 200], Least Trimmed Squares (LTS) [196], S-estimators [196, 201, 202], and τ-estimators [203], follow the principle set forth by Hampel [204]. He suggested that an estimator which minimizes a highly outlier-resistant scale measure of fitted residuals would be less sensitive to outliers.

A very common implementation of this principle is to apply a practical algorithm, which subsamples the underlying data to form parameter estimates. These parameter estimates are then used to form residuals of all of the data, from which some objective

function is employed and minimization of this objective function through many subsamples of the underlying data results in an optimal parameter estimate [205].

Unfortunately, many robust regression methods are overlapping or related and it is difficult to truly tell apriori for a given problem which is better than the other. For example, the LMS estimator is a special case of the Least Quantile of Squares (LQS) estimator [196]. The LTS and LMS are also special cases of an S-estimator. The least trimmed sum of absolute deviations (LTA) [206] is found by minimizing the sum of absolute residuals similar to the M-estimator [195, 207].

Researchers focus on trading robust regression techniques off against each other in terms of consistency, Gaussian efficiency, breakdown and computational complexity [208, 209, 205]. Monte Carlo testing is often employed with varying data set types and varying degrees of contamination.

Even so, there is no commonly accepted standard for robust regression [198], thus tradeoffs based on the application and computational environment must be made. It is desirable for the present application that a robust operator be determined which can be implemented in real time and be high breakdown for all data types.

The breakdown point was first introduced by Hampel [210, 211]. Huber used it as a functional analytical procedure [207]. A simplified version for finite samples was presented by Donoho [212]. The breakdown point is the percentage of contaminated data which can exist in a data set, for which the robust regression technique can still succeed. For a problem where many sensors could fail at once such as with the FOS, a method with high breakdown (HB) is desired.

The highest theoretical breakdown point for any regression equivariant functional is 50% [196, 208], which includes estimators such as the LMS, LTS, Repeated Median (RM) [213], Minimum Volume Ellipsoid (MVE) [196], Minimum Covariance Determinant (MCD) [196, 214], Least Quartile Difference (LQD) [215] and S-estimators.

Other algorithms which are high breakdown but do not necessarily achieve 50% breakdown include the Theil-Sen Estimator [216], and Deepest Regression (DR) [217]. Low breakdown estimators include M-estimators [195, 207] assuming outliers are allowed to occur in the explanatory data. M-estimators are usually solved with an iteratively reweighted least squares (IRLS) iteration.

M-estimators have been shown to be useful, especially when small outliers exists, whereas LMS and LTS tend to classify good data points as outliers, if no gross outliers exist [209]. Hybrid M- and S-estimators known as Constrained M-estimators (CM) have combined the high breakdown point of the S-estimator and local robustness property of the M-estimator [218].

In addition to the breakdown point of an estimator, it is usually important to determine the efficiency of the estimator [219]. A fully efficient estimator should deliver the same accuracy as the maximum likelihood based estimator (which is OLS when the noise is Gaussian) when the data set contains no outliers. This is referred to as Gaussian efficiency, and is usually given as a percentage, where a higher percentage indicates the robust estimator is closer to OLS when outliers are not present. Techniques such as LMS, LTS and LTA tend to be low efficiency.

Usually a two-step process is required for an estimator to be both high breakdown and efficient, such as the Robust and Efficient Weighted Least Squares (REWLS) [220]

technique. Generally, this process consists of beginning with an initially high breakdown estimator (like LMS or LTS) and using the robust estimate to rescale the weights on the data. The second estimator usually retains its efficiency and inherits the breakdown point of the original estimator.

Data type impacts most robust regression techniques' performance. The presence of masking, swamping and leverage points is critical to how well a robust operator performs.

Masking occurs when two outliers have the effect of canceling each other out, such that the robust regression technique does not identify them as outliers [221, 222]. Swamping has the opposite effect, and occurs when a good observation is considered to be bad due to its interaction with outliers.

Leverage points are points, in the explanatory data which lie particularly far away from the majority of the observations [196]. Leverage points have a strong influence in the regression and may be good or bad, depending on the data structure and algorithm used. In the literature, LMS and LTS tend to perform the best in terms of consistency and breakdown in the presence of leverage points [209].

The LTA has been shown to be an attractive alternative to LMS and LTS when leverage points are not included in the data set [206]. Note that LMS and LTS tend to be the benchmark in robust statistics, due to both being HB and consistent in the presence of various data structures. It is clear from the optimal sensor placement discussion that operation with existing leverage points will be critical to the operation of the modal filter.

Unfortunately, in the published literature, multiple linear regression (MLR) and multivariate location and dispersion (MLD) estimators have been shown to be high

breakdown and consistent but tend to have high computational complexity $O(n^p)$, or higher where n is the sample size and p is the number of predictors [205]. Assuming the computer can perform 10^7 operations per second and $n = 100$, then any one algorithm takes $10^{(2p-7)}$seconds to complete. If the number of modal coordinates or fit parameters increases over a few, then many robust algorithms will not be implementable in real time.

Bernholt [223] suggests that the LMS, LQS, LTS, LTA, MCD, MVE, CM, projection depth [224] and Stahel-Donoho [225] estimators are hard to compute. In his unpublished manuscript *Applied Robust Statistics* [205], David Olive points out that fast algorithms for the above methods which produce good approximations are impractical except for tiny data sets. He also shows that the Generalized S-estimator (GS) [201], LQD, projection, RM and S-estimators are also impractical.

Two stage estimators that need an initial high breakdown estimator from the above list are even less practical to compute [205]. These estimators include the cross-checking [226], MM [196, 227], one step Generalized M-estimation(GM) [228], one step Generalized Rank (GR) [229], REWLS, τ- and t-type estimators [230].

Typically the implementations of these estimators are not given, impractical to compute or result in a zero breakdown estimator that is often inconsistent. Indeed, in the book *Robust Statistics*, Maronna et al. [231] indicates that S, τ, projection based, CM, MM, and Stahel-Donoho estimators may have no reliable method for computation.

A number of computationally fast, high breakdown consistent estimators have been proposed. The Fast Minimum Covariance Determinant (FMCD) was proposed by Rousseeuw and Van Driessen [232] in an effort to utilize the high breakdown MCD technique on very large sets of data (ie. $n = 137{,}256$ data points, with 27 parameter

estimates). Other practical robust regression techniques include the Median Ball Algorithm (MBA) [233], FCH [234], Recursive FCH (RFCH) [234], Recursive MVN (RMVN) [234], OGK [235], and Median Ball (MB) [233].

A recent PhD dissertation publication [236] performs a very comprehensive comparison of the "fast" robust estimators and suggests that FCH, RFCH and RMVN outperform all other compared estimators with regards to consistency and speed. These three techniques are also at least 2 orders of magnitude faster than the FMCD method and are also consistent when $n > 20p$ and $p \leq 40$. Thus, if one was tracking 5 modal coordinates, at least 100 data points would be required for consistent performance.

Olive [205] points out that FMCD is only consistent for small data sets, mainly because the algorithm still relies upon random sampling, as many practical robust regression algorithms do. Furthermore, FMCD has been delegated as an outlier diagnostic method, rather than a robust estimator, until it can be shown to be consistent [237]. Olive and Hawkins [234] recommends the FCH estimator among all of the previously mentioned estimators, and it has been shown with Monte Carlo studies to be fast, consistent, applicable to large data sets and high breakdown.

Table 6.1 summarizes this very brief review of robust regression techniques, not accounting for all of the possible advances and nuances which exist. Indeed, some information was difficult to find referenced explicitly, such as the Gaussian efficiency and leverage point influence etc. So a notes section was created which draws attention to any comments made by authors in comparative studies.

Table 6.1: Comparison of Single Step Robust Regression Methods.

Methods	Breakdown	Computational Complexity	Notes (GE- Gaussian Efficiency), convergence rate=1/consistency
OLS	1/n	$O(p^3+p^2n+pn)$	Zero breakdown as $n \to \infty$
M-estimator	1/(p+1)	$O(p^3/3+p^2n)$	sensitive to gross outliers in X-direction and leverage points; 95% GE
Theil-Sen	29.3%	O(nlog(n))	Sensitive to leverage points; fast
DGK	Low	$<O(p^3+p^2n+pnlog(n))$	$n^{1/2}$ consistent, D. Olive suggests for application
MB	High	$<O(p^3+p^2n+pnlog(n))$	small bias, D. Olive suggests for HB application
MBA	High	$O(p^3+p^2n+pnlog(n))$	
LMS	High	$O(n^{p+2})$	Low convergence rate $n^{-1/3}$, low GE
LTS	High	$O(n^p)$	More stable than LMS, 50% GE
S-estimator	High	$O(n^{p+2})$	Not a reliable method
LTA	High	$O(n^{p+1})$	
LQD	High	$O(n^{2p+4})$	67.1 % GE
MCD	High	$O(n^{1+p(p+3)/2})$	Only possible for trivial examples, similar to MVE and LTS
MVE	High	$\sim O(n^{1+p(p+3)/2})$	Only possible for trivial examples
DR	33%	$O(n^{2p-1}log(n))$	Good for asymmetric errors; simplifications for speed may exist
RM	High	$O(n^p log^p(n))$	Some simplifications may make O(n)
FMCD	High	$O(p^3+p^2n+pnlog(n))$	Not consistent, relies on resampling
OGK	High	$O(p^3+np^2log(n))$	
FCH	High	$O(p^3+p^2n+pnlog(n))$	May be too slow (suggestion by email with D. Olive)

Perhaps the most practical estimator listed in the above table is the M-estimator. It has low computational complexity and is applicable to many different data sets. In some cases, it can break down, especially if the outliers are in the explanatory data. For a sensor system, this will likely be the case as some sensors are more significant than others.

Proven computationally fast and high breakdown estimators include the concentration algorithm based estimators: FCH, MB and MBA. The weakness of concentration algorithms is that they are only applicable to data sets which are multivariate normal in nature. There are good aspects for both M and concentration type estimators. But both appear to be sensitive to leverage.

A review of the model to which these estimators apply is given next. It is also the model which is applicable to the strain mode matrix derived for the X-56A and of course, modal filters.

6.2 Multivariate Location and Dispersion

The previous section indicates that most robust regression will involve a multivariate location and dispersion (MLD) model. Herein, this model is defined and its associated popular statistics. A MLD model is a joint distribution with parameters μ and Σ, where μ is a $p \times 1$ population location vector and Σ is a $p \times p$ symmetric positive definite population dispersion (scatter) matrix [236].

Estimating μ and Σ forms the cornerstone of multivariate data analysis and estimators are widely used by many classical multivariate methods. Suppose the observed data is x_i for $i = 1, \ldots, n$ with p data parameters collected into an $n \times p$ matrix X as in Eq. (6.1).

$$X = \begin{bmatrix} x_{11} & x_{12} & \cdots & x_{1p} \\ x_{21} & x_{22} & \cdots & x_{2p} \\ \vdots & \vdots & \ddots & \vdots \\ x_{n1} & x_{n2} & \cdots & x_{np} \end{bmatrix} = \begin{bmatrix} x_1^T \\ x_2^T \\ \vdots \\ x_n^T \end{bmatrix} \tag{6.1}$$

The most commonly used estimators of multivariate location and dispersion are the classical estimator $(\bar{x}, S)$, where $\bar{x}$ is the sample mean and S is the sample covariance-variance matrix. It is the most common likely because many systems can be approximated to be multivariate normal (MVN).

For this distribution, the general location estimator of X is denoted as $T(X)$ and the general dispersion estimator as $C(T, X)$. The classical mean estimator is given as in Eq. (6.2)

$$T(X) \equiv \bar{x} = \frac{1}{n} \sum_{i=1}^{n} x_i \tag{6.2}$$

and the corresponding classical sample variance-covariance estimator may be calculated as in Eq. (6.3).

$$C(T, X) \equiv S = \frac{1}{n-1} \sum_{i=1}^{n} (x_i - T)\,(x_i - T)^T \tag{6.3}$$

If $x_1, x_2, \ldots, x_n$ are a random sample of size n from a MVN population, then $\left(\bar{x}, \frac{n-1}{n} S\right)$ is the maximum likelihood estimator (MLE) of (μ, Σ), and thus $\bar{x}$ and S are sufficient statistics and $\bar{x}$ and S are independent. An important MLD model is the elliptically

contoured $EC_p(\mu, \Sigma, \mathrm{g})$ distribution with a probability density function given as in Eq. (6.4),

$$f(x) = k_p|\Sigma|^{-\frac{1}{2}} g((x-\mu)^T \Sigma^{-1}(x-\mu)) \tag{6.4}$$

where, g is some known function and k_p is some positive constant.

A p-dimensional MVN $N_p(\mu, \Sigma)$ distribution has a probability density function given as in Eq. (6.5).

$$f(x) = \frac{1}{(2\pi)^{\frac{p}{2}}|\Sigma|^{\frac{1}{2}}} e^{-(x-\mu)^T \Sigma^{-1}(x-\mu)/2} \tag{6.5}$$

It is clear that $N_p(\mu, \Sigma)$ is a special case of $EC_p(\mu, \Sigma, \mathrm{g})$. Hotelling, a pioneer in multivariate analysis obtained that a $100(1-\alpha)\%$ p-dimensional prediction ellipsoid is given by all x satisfying Eq. (6.6).

$$(x-\bar{x})^T S^{-1}(x-\bar{x}) \leq \frac{(n^2-1)p}{n(n-p)} F_{p,n-p}(1-\alpha) \tag{6.6}$$

where $F_{p,n-p}$ is the F distribution with parameters p and $n-p$ and $P(F_{p,n-p} \leq F_{p,n-p}(1-\alpha)) = 1-\alpha$. Hence, the above prediction region for a future observed value x_i is an ellipsoid that is centered at the initial sample mean $\bar{x}$, and its axes are determined by the eigenvectors of S. Before any new observations are taken, the probability that x_i falls into the prediction ellipsoid is $1-\alpha$.

A very important statistical measure in MLD was developed by Prasanta Chandra Mahalanobis [238]. The squared sample Mahalanobis distance is a scalar and for each observation x_i is given as in Eq. (6.7).

$$D_i^2(x_i, T, C) = (x_i - T)^T \mathrm{C}^{-1}(x_i - T) \tag{6.7}$$

For distributions which are non-spherical, for instance ellipsoidal, it is expected that the probability of a future point belonging to the set depends not only on the distance from the center of mass, but also on the direction.

The Mahalanobis distance is the distance from an observation to the center of mass divided by the width of the ellipsoid in the direction of the observation. Notice that the Euclidean distance of x_i from the center of the data $T(X)$ is $D(x_i, T, I_p)$. The Mahalanobis distance differs from Euclidean distance only in that it takes into account the correlations of a data set and is scale-invariant. The classical Mahalanobis distance uses $(T, C) = (\bar{x}, S)$. The population squared Mahalanobis distance is given as in Eq. (6.8).

$$D^2(x, T, C) = (x - \mu)^T \Sigma^{-1}(x - \mu) \tag{6.8}$$

A large class of robust regression methods makes use of the Mahalanobis distance for outlier detection and removal. From Table 6.1, it was clear that robust estimators which did not rely upon pure random subsampling are based on the principle of concentration. This method is preferable to a random subsampling algorithm in order to achieve consistent estimates. Concentration algorithms are reviewed in the next section.

6.3 Concentration Algorithms

Concentration algorithms hold promise for robust modal filtering because they are fast and high breakdown. They work by iteratively approach the centroid of the

distribution through set trim percentages. Sensors used near this centroid are more likely to lead to efficient estimates of the true population estimates.

A concentration algorithm begins with an initial estimator of (μ, Σ), called a start, such as the classical estimator $(\bar{x}, S)$ of a random subset with $p+1$ cases or of the classical estimator $(\bar{x}, S)$ computed from all n cases. For each start, the concentration algorithm generates a corresponding new estimator, called an attractor. The algorithm is described here.

Let $\left(T_{0,j}, \mathrm{C}_{0,j}\right)$ be the j^{th} start, where $1 \leq j \leq K$. The Mahalanobis distances for all $1 \leq i \leq n$ observations of this start are first computed as follows

$$D_i^2\left(T_{0,j}, C_{0,j}\right) = \left(x_i - T_{0,j}(X)\right)^T \mathrm{C}_{0,\mathrm{j}}{}^{-1}(x_i - T_{0,j}(X)) \tag{6.9}$$

At the next iteration, the classical estimator $\left(T_{1,j}, \mathrm{C}_{1,j}\right)$ is computed from $c_n = \frac{n}{2}$ cases corresponding to the smallest Mahalanobis distances computed from Eq. (6.9). This iteration can be continued for k times for the j^{th} start, and a sequence of estimators can be calculated as $\left(T_{0,j}, \mathrm{C}_{0,j}\right)$, $\left(T_{1,j}, \mathrm{C}_{1,j}\right)$, …,$\left(T_{k,j}, \mathrm{C}_{k,j}\right)$. The last estimator $\left(T_{k,j}, \mathrm{C}_{k,j}\right)$ of this sequence is called the j^{th} attractor.

An empirical choice for k can range between 5-10, depending. Once all starts $1 \leq j \leq K$ have generated a set of attractors$\left(T_{k,j}, \mathrm{C}_{k,j}\right)_{1 \leq j \leq K}$, the attractor which optimizes some criterion is then chosen as the final "robust estimator". In other words, desired data parameter estimates $\beta_{1..p}$ are calculated via a least squares operation or through some other high GE operation from the set of points c_n corresponding to the optimal attractor. These points are closest to the multivariate center of the data.

Concentration algorithms assume a multivariate normal distribution in most theoretical research. However, not all data distributions can be approximated as a

multivariate normal distribution. This may be especially the case for a structure, wherein some sensor locations are far more important than others. This concept becomes significant later on in the development of the robust modal filter.

.

CHAPTER 7

ROBUST MODAL FILTERING

The theoretical foundation developed in the previous chapter is a starting point for robust modal filter design. It laid out the many choices available for estimators and identified two types of estimators which form the basis of a robust modal filter. These algorithms are based on concentration and M-estimation. However, neither algorithm type is robust to leverage or asymmetry. Asymmetric data distributions are open challenges in robust statistics.

A methodology for robust modal filtering is presented in this chapter to directly answer Research Question 3. This is developed by merging M-estimation and concentration and addressing the data distribution's particular asymmetry issues.

To begin with, a motivational example is given for why today's current robust regression methods are not applicable. Then a new robust modal filter is derived within. A sensor failure model derived from experimental data is used to test the robust modal filter. The test is conducted for three differing structural strain scenarios using a worst case break in the fiber.

For comparison, the performance of the robust modal filter is run alongside state-of-the-art robust regression M-estimators. The robust modal filter is found to outperform robust M-estimators significantly in the presence of high leverage outliers. The robust modal filter methodology is developed within the next sections.

7.1 Robust Modal Filtering Methodology

A robust modal filter must replace the OLS modal filtering method **[66]** in order to address Research Question 3. The robust modal filter is given a specific name. Here it is named as the concentrated modal estimator (CME). The name is descriptive. The modal coordinate estimate is formed from data which is iteratively concentrated around the statistical multivariate center of the data.

The CME is primarily a concentration algorithm with re-descending M-estimates used in place of OLS within the concentration steps. A major difference between the CME and other concentration operators is that it utilizes a fixed trim criterion and a more robust start. This trim criterion and new robust start is required to address asymmetry of the strain mode matrix data. The motivation to address asymmetry is reviewed in depth in the following section.

7.1.1 Motivation from Asymmetry

For the X-56A sensor system fourteen modal displacement features are included in the strain mode matrix Ψ corresponding to 1,530 sensor entries. Therefore, the problem is computationally burdensome and also multivariate. If the distribution is nominally multivariate normal, then the problem is relatively simple to solve. Most theory based robust statistics assume a nominal multivariate normal distribution. To determine if the robust strain mode estimation problem is trivial a test for normality of the sensor strain modal matrix [See Eq. (1.17)] is given. This test is completed by the Q-Q plot.

The Q-Q plot is a tool to verify if a distribution matches another distribution. If the distributions are similar, then the Q-Q plot will result in a line with a slope of 1. If the distributions are dissimilar the Q-Q plot will exhibit unusual behavior. Research confirms that the distribution of squared Mahalanobis distance [See Eq. (6.8)] of multivariate normal data assumes a chi-square distribution [239]. The squared Mahalanobis distance introduced in the previous chapter is computed for the strain mode matrix developed for the X-56A. A plot of squared Mahalanobis distance against the quantiles of a chi-square distribution is shown in Fig. 7.1:

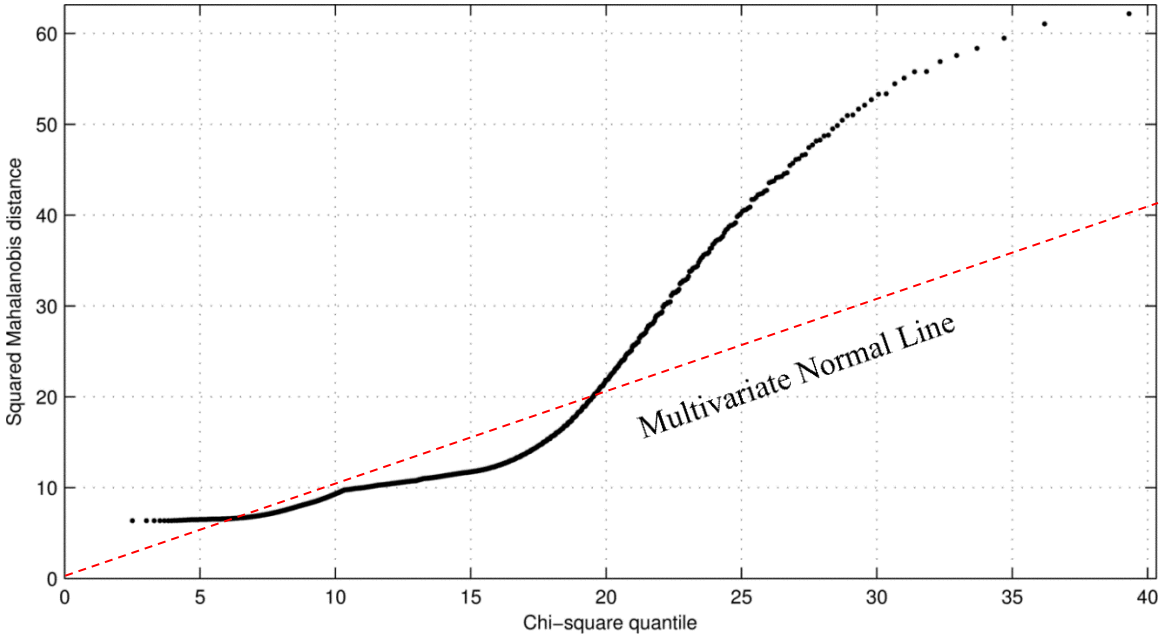

Figure 7.1: Squared Mahalanobis Distance versus Chi-square Quantiles for X-56A Model Sensor Strain Modal Matrix.

The plot of squared Mahalanobis distance skews to the right and then curves strongly upwards. The skew of the squared Mahalanobis distance is an indicator that the sensor strain data matrix is not multivariate normal. The presence of strong leverage points is obvious, from the high count of D^2 which exceeds 41.

Indeed, Mardia's skew and kurtosis estimates [240] indicate that the distribution is subject to large multivariate skew and kurtosis which is non-normal. This is also true when analyzing the multivariate skew and kurtosis corrected for small samples.

Since the measured strain is approximately a linear combination of the sensor strain data matrix, the measured strain must also be asymmetrically distributed. That is not to say the sensor noise is asymmetrically distributed. The noise for each sensor is assumed to be normal.

However, since loading will vary with aerodynamic condition, the underlying strain distribution is difficult to predict. Without a known distribution, application of most computationally efficient robust outlier detection methods is challenging. Olive suggests robust estimators can be used in place of the classical estimator for a concentration algorithm in some cases [233]. A rigorous demonstration that the strain mode filter problem can be solved using an M-estimator is introduced in the next section.

7.1.2 M-step Derivation

The CME derived herein utilizes M-estimates instead of OLS within each concentration step. M-estimators are characteristically gradient descent algorithms [138]. They are computationally efficient, affine equivariant, robust to masking effects and tend to outperform OLS when applied to many data sets [231]. Maronna's Robust M-estimator [241] and a concentration algorithm [242] have performed similarly well for contaminated data sets used in principal component analysis [243].

The asymmetric nature of the distribution (See Fig. 7.1) demands a more robust estimator such as the computationally efficient M-estimator. One could argue that the

breakdown point of an M-estimator is too low. The theoretical maximum breakdown point of $1/(m+1)$ of the M-estimator [196] is inconsequential for two reasons.

The first is that it will be shown that only fixed outliers shall exist in the explanatory data or strain mode matrix. These outliers can be accounted for with a fixed trim criterion. The second is that a concentration operator does not require a robust estimator in the concentration steps to lead to a high breakdown estimator. Therefore the following modal filter derivation follows that for M-estimators.

The strain at measurement locations may be expanded as a summation of an infinite number of orthogonal strain mode shapes (See Eq. (7.1)).

$$s_k(x_C, y_C, z_C, t) = \sum_{i=1}^{\infty} q_i(t)\psi_i(x_C, y_C, z_C) \tag{7.1}$$

To reduce model complexity, only a subset m of mode shapes which dominate the response are included in the strain modal matrix [122]. It is assumed that the subset of modes captures the contributing dynamics and the sensors are subject to random normal error. This introduces an error term into Eq. (7.1) which can be modeled as a normal distribution $\varepsilon_k \in N(\mu_n, \sigma_n)$. At any discrete time $t = \tau$, the quasi-static approximate reading of any sensor can be given as in Eq. (7.2),

$$s_k(x_C, y_C, z_C, \tau) = \sum_{i=1}^{m} q_i(\tau)\psi_i(x_C, y_C, z_C) + \varepsilon_k \tag{7.2}$$

where m is the number of mode shapes retained in the model. Consider the linear model for the k^{th} sensor measurement to be described by Eq. (7.3),

$$s_k(x_C, y_C, z_C, \tau) = \sum_{i=1}^{m} \hat{q}_i(\tau)\psi_i(x_C, y_C, z_C) + e_k = \Psi_k(x_C, y_C, z_C)\hat{q}(\tau) + e_k \tag{7.3}$$

where e_k is a finite residual (i.e. measurement error), $\Psi_k(x_C, y_C, z_C) \in \mathbb{R}^{1\times k}$ is the k^{th} row of the strain matrix. $\hat{q}(\tau) \in \mathbb{R}^{k\times 1}$ is a vector of estimated modal displacements. From the sensors readings, the objective is to estimate $\hat{q}(\tau)$. This can be solved as a maximum likelihood estimation (MLE) problem (See Huber [195]) which is posed as minimization of an equally weighted summation of a function of the residuals (See Eq. (7.4)),

$$\sum_{k=1}^{S} \rho(e_k) = \sum_{k=1}^{S} \rho\big(s_k(x_C, y_C, z_C, \tau) - \Psi_k(x_C, y_C, z_C)\hat{q}(\tau)\big) \tag{7.4}$$

where S is the set of strain sensors and $\rho(x)$ is an objective function with special properties. A reasonable $\rho(x)$ must be symmetric, zero when evaluated at zero, increasing for increasing arguments and differentiable.

Define the influence function $\varphi(x) = \rho'(x)$ as the differential of the objective function $\rho(x)$. The influence function characterizes the proportional impact of the residuals on the estimate. The impact of an OLS residual on the estimate is directly proportional to the size of the residual, which is why OLS is not robust. To find $\hat{q}(\tau)$ the summation given in (7.4) is differentiated by $\hat{q}(\tau)$ and is set equal to zero. By completing this, the following equality is achieved (See Eq. (7.5)).

$$\sum_{k=1}^{S} \varphi\big(s_k(x_C, y_C, z_C, \tau) - \Psi_k(x_C, y_C, z_C)\hat{q}(\tau)\big)\Psi_k(x_C, y_C, z_C) = 0 \tag{7.5}$$

Let $w_k(e_k) = {\varphi(e_k)}/{e_k}$ for any $\varphi(e_k)$ then the weighted objective function can be rewritten as in Eq. (7.6),

$$\sum_{k=1}^{S} w_k(e_k)\big(s_k(x_C, y_C, z_C, \tau) - \Psi_k(x_C, y_C, z_C)\hat{q}(\tau)\big)\Psi_k(x_C, y_C, z_C) = 0 \qquad (7.6)$$

which results in the weighted least squares problem [244]. Equation (7.6) can be solved as a system of equations. Under normal conditions an efficient estimate of $\hat{q}(\tau)$ can be calculated. The weights $w_k(e_k)$ are affine equivariant and modeled as functions of the residuals e_k. The residuals are dependent upon the weights.

Therefore IRLS is required. This proceeds by solving for an initial least squares estimate $\hat{q}(\tau)$ and computing the residuals and weights. Using the weighted observations a new feature estimate $\hat{q}(\tau)$ is computed and the residuals and weights are recalculated. The features or modal displacements $\hat{q}(\tau)$ of the hyperplane approximately satisfying for all sensors, Eq. (7.6) appear within a few iterations.

7.1.3 M-step Operation Within a Concentration Step

The solution of Eq. (7.6) must be computed within each concentration step, c for the proposed concentrated estimator. To improve the convergence to the unbiased solution of $\hat{q}(\tau)$ sensors which are most outlying are completely removed. For the new group of sensors, M-estimation is used to find improved feature estimates. Selection of the influence function is critical to the M-estimator's performance.

Two commonly used influence functions in M-estimation are the Huber's [195] function and Mosteller and Tukey's [245] bisquare function. While robust and efficient in many cases, Huber's influence function increases without bound as the residual departs

from 0. Therefore gross outliers still impact the feature estimates and in typical cases lead to efficiency losses of 10-20% [246].

Tukey's bisquare function belongs to a class of redescending functions [247] which account for gross outliers by gradually reducing the influence of the large residuals. Redescending M-estimators use $\varphi(x)$ influence functions which are non-decreasing near the origin, but decrease to 0 far from the origin at some minimum rejection point.

For its gross outlier rejection capability, Tukey's bisquare function is chosen to compute the weights with the residuals of the data. The bisquare weighting function $w = {\varphi(x)}/{x}$ is defined for the k^{th} sensor as in Eq. (7.7),

$$w_k^{(b,c)}\left(\frac{e_k^{(b,c)}}{\sigma_k^{(b,c)}}\right) = \begin{cases} \left(1 - \left(\frac{e_k^{(b,c)}}{\sigma_k^{(b,c)}}\right)^2\right)^2 & \left|\frac{e_k^{(b,c)}}{\sigma_k^{(b,c)}}\right| < h_0 \\ 0 & otherwise \end{cases} \tag{7.7}$$

where $\sigma_k^{(b,c)}$ is the median absolute deviation (MAD), h_0 is a tuning constant, c is a concentration step, and b is an IRLS iteration count of the M-estimator. To achieve the maximum 95% asymptotic efficiency assuming residuals have a Gaussian distribution, it has been shown that a tuning constant of $h_0 = 4.685$ is required [248].

The MAD for the k^{th} observation is calculated as in Eq. (7.8),

$$\sigma_k^{(b,c)} = {MED\left(\left|e_k^{(b,c)} - MED\left(e^{(b,c)}\right)\right|\right)}/{.6745} \tag{7.8}$$

where the constant scaling 0.6745 is required to achieve a 37% Gaussian efficient consistent estimator of the standard absolute deviation [249]. While relatively low

efficiency, the purpose of using MAD instead of using the true scale is to resist outliers. This it achieves remarkably well since the median is high breakdown.

However, The MAD is developed for symmetric distributions and does not address distribution skewness. This may be of concern since the explanatory data is multivariate skewed. Improvements of the MAD approximation for asymmetric long-tailed distributions are available if necessary (See two alternatives given in Rousseeuw and Croux's [249] work). Given the weights, $w_k^{(b,c)}$ the linear system of equations is solved for $\hat{q}^{(b,c)}(\tau)$ given sensors in subset S_g^c as in Eq. (7.9).

$$\sum_{k=1}^{S_g^c} w_k^{(b,c)} \left(\frac{e_k^{(b,c)}}{\sigma_k^{(b,c)}}\right)\Big(s_k(x_C, y_C, z_C, \tau) - \Psi_k(x_C, y_C, z_C)\hat{q}^{(b,c)}(\tau)\Big)\Psi_k(x_C, y_C, z_C) = 0 \tag{7.9}$$

The weighted least squares problem for the c^{th} concentration step is solved in the same way as Eq. (7.6). Equations (7.7)-(7.9) are the primary feature estimator equations used within the concentration operator. They are iterated within any concentration step for a specified number of M-steps, b_f resulting in $\hat{q}^{(b_f,c)}(\tau)$. The next section shows how this estimate is used to trim data through concentration before reapplying M-estimation.

7.1.4 Concentration Operation

The purpose of concentration is to iteratively remove poor observations and asymptotically approach the true statistical center of the data distribution. Utilizing sensors nearest to this centroid are assumed to give the best feature estimates. A best estimate of this center is the multivariate location T and dispersion V of the data.

Redescending M-estimators have been proposed as robust estimators of multivariate location and dispersion for theoretical asymmetric distributions [250].

Sensors furthest from this centroid are downweighted in Eq. (7.9). However, it is proposed to not just down-weight sensors, but to completely remove some from consideration [242]. The redescending M-estimator does in fact equate weights to 0 for gross outliers.

To its detriment, it tends to put some initial trust in gross leverage outliers. This has the potential to cause the feature estimates to trend towards a local minimum. It is shown in the next chapter that converged feature estimates from a redescending M-estimator may fall into local minimums due to leverage outliers.

The weighted sensor removal methodology to improve gross outlier rejection is developed here. Let the k^{th} sensor data vector be defined as in Eq. (7.10),

$$x_k \triangleq [\Psi_k(x_C, y_C, z_C) \quad s_k(x_C, y_C, z_C, \tau)] \tag{7.10}$$

Defining the data vector in this way ensures that outliers which depend on sensor readings shall not occur in the explanatory data. Only fixed outliers can occur in the explanatory data, which are to be addressed with a fixed trim criterion. From any sample sensor set $S_g^c \supseteq S$ a location vector (See Eq. (7.11))

$$T^{(b_f,c)} = \frac{1}{\sum w_k^{(b_f,c)}} \left(\sum_{k=1}^{S_g^c} w_k^{(b_f,c)} x_k \right) \tag{7.11}$$

and dispersion matrix [See Eq. (7.12)]

$$V^{(b_f,c)} = \sum_{k=1}^{S_g^c} w_k^{(b_f,c)} x_k^T x_k \tag{7.12}$$

are estimated in the c^{th} concentration step. The weightings are the result of b_f iterative M-steps over the subset of sensors S_g^c. Weighted location and dispersion matrices have led to robust affine equivariant estimators with a high breakdown point for any dimension [251], such as the Stahel [252]and Donoho [212] estimator. It was shown that if the weights are affine equivariant, that the estimates of location and dispersion are also affine equivariant. It was also shown that if the true mean and dispersion of the model has an asymptotic breakdown of 0.5, then the asymptotic breakdown point of the location and dispersion estimates also have an asymptotic breakdown of 0.5.

For the estimated location and variance, the squared Mahalanobis distance (D^2) (See Mahalanobis [238]) is computed for every sensor data point k as in Eq. (7.13).

$$D^2(x_k) = \left(x_k - T^{(b_f,c)}\right)\left(V^{(b_f,c)}\right)^{-1}\left(x_k - T^{(b_f,c)}\right)^T \tag{7.13}$$

This multivariate distance differs only from the Euclidean distance only in that it accounts for correlations between data points and is scale-invariant. If the population has a multivariate normal distribution, the D^2 is asymptotically approximated by a chi-square distribution [239]. With this knowledge, statistical cutoff points from the inverse cumulative distribution can be determined.

However, since the strain data matrix has an unknown highly skewed distribution this data removal technique will not succeed [253]. Theory based concentration algorithms which trim percentage of observations with the highest D^2 are strictly invalidated. Leverage points naturally have very large D^2. Therefore, trimming good leverage points drastically biases the feature estimates.

The amplitude of D^2 remains useful for finding outliers if the multivariate normal assumption is violated. However asymptotic theoretical cutoffs must not be relied upon. Without knowledge of the underlying theoretical distribution, an approximation is required to find the cutoff value of D^2.

The initial distribution of D^2 may be computed from the fixed modal matrix and time varying set of strain data with Gaussian noise. The maximum of the computed D^2 may be used as a upper bound for removing gross outliers. This is very similar to the empirical cutoff approach for a fixed data set in [254]. Their approach was improved with an adaptive approach taken in [253].

A shortcoming of these two methods including the one presented herein is that small outliers may be missed if sensors are removed based on a maximum threshold of D^2 or some derivative method. This is true because the initial distribution mean and covariance may be biased.

Iterative concentration steps are proposed herein to address this problem. During each concentration step gross outliers are removed and the location and dispersion are re-estimated. The sample location and dispersion more closely resemble the population location and dispersion. Therefore the small outliers become more pronounced. As the $D^2(x_k)$ increases the sensor can be identified as an outlier and removed. Outliers missed by this trim procedure will more likely be down-weighted in the M-estimate [See Eq. (7.9)].

The proposed method for finding the upper bound D_{ub}^2 is time consuming to implement requiring 1,000s of simulations since the strain is time varying. Since most of the data is described by the constant strain data matrix, an approximation can be used for

the upper bound. It can be assumed that the distribution of $D^2(x_k), k = 1 \dots S$ is equal to or greater than the distribution of $D^2\big(\Psi_k(x_C, y_C, z_C)\big), k = 1 \dots S$ if the sensor data has a Gaussian error distribution.

With this assumption, the impact of an additional feature may be assumed to change the distribution of D^2 by the additional DOF impact in a chi-square distribution. Recall that D^2 is given in units of variance. This implies that the variance will increase with the additional DOF. Therefore it can be assumed that $D^2\big(\Psi_k(x_C, y_C, z_C)\big) + \vartheta(n_s) \geq D^2(x_k)$, $k = 1 \dots S$. Assuming the adjustment of $\vartheta(n_s)$ is due to the noise of the strain data the scalar upper bound is defined as in Eq. (7.14):

$$D_{ub}^2 \triangleq P_c \max_{k \in S} D^2\big(\Psi_k(x_C, y_C, z_C)\big) \tag{7.14}$$

where P_c is a tuning constant chosen to be slightly greater than 1. The tuning constant accounts for $\vartheta(n_s)$. By removing a portion $k \in S$ sensors with $D^2 < D_{ub}^2$ a new candidate group of sensors S_g^{c+1} is found for the next concentration step, and consecutive M-steps. Simulation studies given later verify this approximation of the upper bound, D_{ub}^2 to be good for the strain mode matrix and strain data.

7.1.5 Robust Starts and Operations

Robustness for multi-stage estimators tends to come from good starts (initial feature estimates). A feature estimate from a high breakdown estimator is used to start the M-estimator for MM-estimates [227]. The robustness is inherited by the more least squares efficient M-estimator. However, this can be time consuming as most high breakdown estimators are computationally inefficient. This presents a problem for a

distributed sensor system which requires a high breakdown estimate, but must also be computationally efficient.

Other concentration operators use starts from estimates from all of the data or data closest in distance to the coordinate-wise median of the data. The median ball algorithm [233] uses feature estimates from sensors closest to the median as a robust start. This is a good start if the data can be assumed to be nominally multivariate normal and works reasonably well for nominally skewed distributions.

The first estimate of the system when τ is 0, (i.e. when the sensor system is first operational), is calculated with a non-robust least squares estimate. Since the first estimate is assumed to come from a working sensor system it is a robust estimate. The initial robust feature estimate $\hat{q}^{(0,0)}(0)$ is found by solving the least squares problem presented in Eq. (7.15),

$$\sum_{k=1}^{S_g^0} \left(s_k(x_C, y_C, z_C, \tau) - \Psi_k(x_C, y_C, z_C) \hat{q}^{(0,0)}(0) \right) \Psi_k(x_C, y_C, z_C) = 0 \qquad (7.15)$$

where S_g^0 is the set all of the available working sensors.

During operation, a robust start is paramount. A significant advantage of a time based sensor system is that previous close estimates are available. The most robust start will therefore be the estimate from the previous time step. This is because the strain change is assumed to be small between discrete time steps. Thus, the robust starts between discrete time steps are implemented as in Eq. (7.16),

$$\hat{q}^{(0,0)}(\tau) = \hat{q}^{(b_f, c_f)}(\tau - 1) \qquad (7.16)$$

where b_f is the total number of M-steps chosen and c_f is the total number of concentration steps.

The importance of starts carries over into the concentration steps themselves. In order to be high breakdown, each concentration step requires a robust start. Since the initial start $\hat{q}^{(0,0)}(0)$ is robust the final estimates at the end of each of the concentration steps: $\hat{q}^{(b_f,1)}(\tau), \hat{q}^{(b_f,2)}(\tau), \ldots \hat{q}^{(b_f,c_f-1)}(\tau)$ are robust [205].

This mean that the estimates of corresponding concentration steps are robust starts for respective next concentration steps: $\hat{q}^{(0,2)}(\tau), \hat{q}^{(0,3)}(\tau), \ldots \hat{q}^{(0,c_f)}(\tau)$. Therefore the following inheritance rule [See Eq. (7.17)] is used to generate robust starts between concentration steps:

$$\hat{q}^{(0,c+1)}(\tau) = \hat{q}^{(b_f,c)}(\tau) \tag{7.17}$$

The full steps of the CME for any discrete time step are summarized in Algorithm 1 assuming that an initial OLS feature estimate has already been computed with Eq. (7.15) at time 0.

Algorithm 1: $\{s_k(x_C, y_C, z_C, \tau), \hat{q}^{(b_f,c_f)}(\tau-1)\} \rightarrow \hat{q}^{(b_f,c_f)}(\tau)$

1) If c==0, compute $\hat{q}^{(0,0)}(\tau)$ with Eq. (7.16). Else compute $\hat{q}^{(0,c)}(\tau)$ with Eq. (7.17).

2) For b =0: b_f, Iteratively compute weights, $w_k^{(b_f,c)}$ with Eqs. (7.7)-(7.9) with $\hat{q}^{(0,c)}$

3) Compute location T (See Eq. (7.11)) and dispersion V (See Eq. (7.12)) with computed $w_k^{(b_f,c)}$

4) Compute $D^2(x_k), k = 1 \ldots S$, using Eq. (7.13) with computed T and S

5) Generate a new sensor set S_g^{c+1} by trimming sensors below cutoff D_{ub}^2 described by Eq. (7.14).

6) If $c < c_f$, Go to Step 1. Else output $\hat{q}^{(b_f, c_f)}(\tau)$.

For each time step, the M-step iteration count b_f may be initialized to be large, so that a robust redescending M-estimate initializes the CME. This improves the algorithm's stability during the concentration steps. Afterwards, single M-steps where b_f is equal to 1, may be utilized. This has the effect of improving computational efficiency.

7.1.6 Analysis of CME

The CME given by Algorithm 1 can be justified as a robust estimator, although a rigorous proof of its theoretical breakdown point presents a challenge. It may in fact be higher than 0.5, due to the use of robust starts which are estimates from previous time steps.

The use of re-descending M-estimators has been shown to give high breakdown estimates of location and dispersion [250]. Re-descending M-estimators are affine equivariant, high breakdown and robust to masking effects [251]. The MAD computed by Eq. (7.8) is also a robust estimate of scale [249]. Therefore, the breakdown point of the re-descending M-estimate is not in question. For multivariate normal distributions, concentration algorithms with OLS have been proven to have a theoretical breakdown point of 0.5 [242].

Robustness inheritance is utilized in multi-stage robust estimators [227, 233]. This implies that from the beginning of operation (i.e. sensor system turns on) till the end of operation (i.e. sensor system powers down), the CME is robust. This can be assumed to be true based on the following logic.

By assuming that the initial estimate at time 0 occurs when the sensor system is operating normally, the OLS estimate at time 0 is robust. This robust estimate is used as a robust start to the next time step; the corresponding robust estimate is used for the start in the next time step and so on. Therefore robustness is guaranteed between time steps.

Robustness is also guaranteed between concentration steps. The robust estimate from previous concentration steps are passed as robust starts to respective next concentration steps. Therefore, iterative application of the robustness inheritance concept guarantees robustness through all concentration operations.

7.1.7 Similarity of CME to Other Robust Estimators

The CME is noticeably similar to previously derived estimators. It uses concentration steps as proposed for the DGK estimator (See Olive [205]) and median ball algorithm proposed by Olive [233]. However, rather than removing a percentage of data at every concentration step, data is only trimmed if its D^2 exceeds D_{ub}^2 (See Eq. (7.14) and step 5 of Algorithm 1). Therefore, the estimator follows the Hippocratic Oath, which may be paraphrased as "do no harm".

Another difference includes robust start inheritance used between concentration steps [See Eq. (7.17)] and between time steps [See Eq. (7.16)]. The median ball algorithm uses two starts, including the median start and the classical start. It does this because access to close estimates of population parameters is not available. A previous close sample estimate will likely outperform a geometrically robust start, especially if the data is heavily skewed.

The CME is a deterministic algorithm, and requires no random subsampling. Most robust estimators rely on random subsampling; an example is the popular LTS estimator [196]. However, it has been shown that estimators with random seeds are not consistent [205]. Instability may result if large (incorrect) changes in modal displacement estimates occur between time steps. The deterministic approach of the CME leads to stable estimates which do not vary by re-running the algorithm.

It is difficult to see how the deterministic concentration procedure or the start can negatively affect the high breakdown nature of the redescending M-estimate. With robust starts and high breakdown implications over time and over concentration steps, robustness will likely be achieved by the CME. Simulation studies presented later justifies the CME as a robust estimator for several worst case asymmetric data distributions.

7.2 Concentrated Modal Estimator Simulations

The CME is demonstrated in static and dynamic simulation studies on the X-56A model. This is completed in efforts to verify the hypothesis for Research Question 3. The steps taken are as follows.

First, the sensor failure simulation is developed. An appropriate worse-case scenario failure point is determined. A failure in a fiber is induced in a critical location. Given different loading conditions this results in three different strain distribution scenarios. These scenarios include aeroservoelastic trim, torsional and bending structural

perturbations. The CME is applied to these cases for the purpose of estimating modal displacements. The MCS is used to gather error distribution estimates for the modal displacement approximation.

In an effort to compare the CME to a benchmark, the modal estimate errors are compared to the state-of-the-art robust M-estimator feature estimates. Computational time studies are completed to show that the CME has complexity similar to an M-estimator.

Finally, in the presence of 100s of sensor failures, the CME and controller designed in the previous Chapter stabilizes the flutter-unstable X-56A model. These results are presented alongside a state-of-the-art robust estimator, which the CME outperforms. The next section describes how the fiber optic sensor failures are modeled.

7.2.1 Fiber Optic Sensor Failures

Modeling the fiber optic failures is imperative for testing the robustness of the FOS based control system. Langley researchers investigated the nature of the strain data after a break in the fiber occurred [255]. A photocopy of data from the fiber break is represented in Fig 7.2.

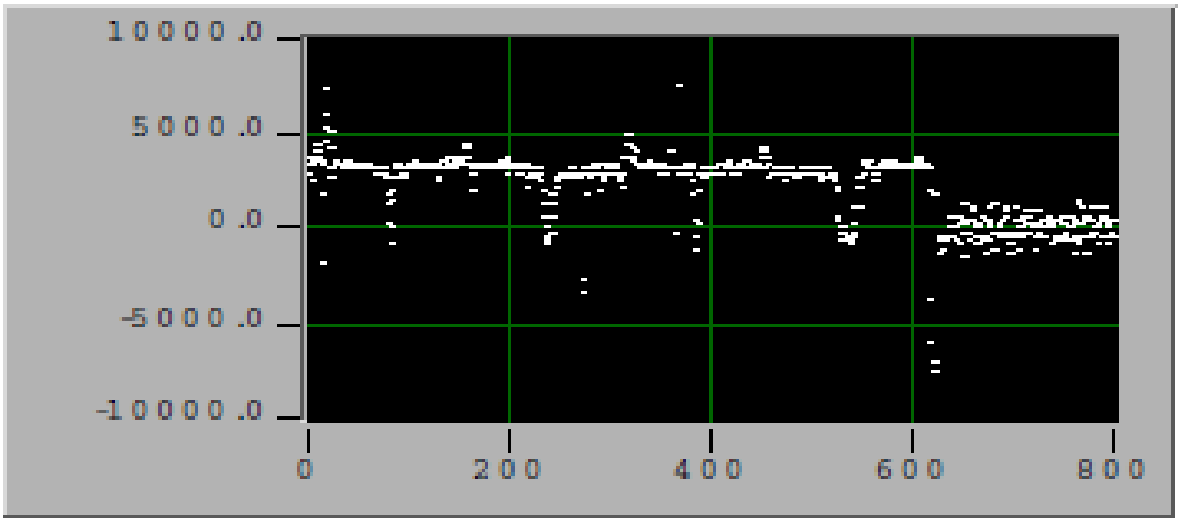

Figure 7.2: Microstrain vs. FBG Location in cm of the FBG Array Attached to a Composite Wing after Break (Courtesy of NASA Langley).

Visualization of the break near sensor 600 indicates that high bias occurs near the break. This is considered to be the first failure mode induced by a fiber break. After some discussion with subject matter experts, it was concluded that the bias can occur before or after the break in the fiber. The shape of this bias for this study is characterized by a normal distribution. However, that is not to say it will always be this way. It depends on how the fiber fractures.

Downstream of the break, the strain measurements appeared to be normally distributed with a mean of zero. This represents the second failure mode which results from one fiber break. The first failure model describing the bias added to the strain distribution is described here.

The sensor locations $P_{nf}^{s}(x, y, z)$ upstream (closer to the wing root) from the fault location $P_f(x, y, z)$ are found, within a radius, r_{nf}. The relative bias shape on the k^{th} sensor upstream of the fault is modeled by a normal distribution as in Eq. (7.18).

$$B_k^{nf} = \frac{1}{r_{nf}\sqrt{2\pi}} \exp\left(-\frac{1}{2}\left(\frac{\left\| P_f(x_C, y_C, z_C) - P_{nf}^s(x_C, y_C, z_C) \right\|}{r_{nf}} \right) \right) \tag{7.18}$$

Sensors nearest the fault are modeled to have the most bias. The sensors furthest from the fault are modeled to have the least bias. The bias is added to the sensor measurements with the following rule [See Eq. (7.19)],

$$s_k^{nf}(x_C, y_C, z_C, \tau) = s_k^{nf}(x_C, y_C, z_C, \tau) + \frac{B_k^{nf}}{\max\limits_{k \epsilon S_{nf}} \{B_k^{nf}, 1 \dots k \dots S_{nf}\}} A \tag{7.19}$$

where A is the maximum desired strain variation on sensors upstream of the fault in the fault radius.

The second failure mode is easier to model. Rather than a bias added to the existing measurement, the bias is modeled to take over the sensor measurement completely. This is modeled by replacing the sensor measurement with a sample from a normal distribution with a mean of 0 and a standard deviation of half the magnitude of A as in Eq. (7.20).

$$s_k^{af}(x_C, y_C, z_C, \tau) = N(0, \frac{A}{2}) \tag{7.20}$$

The amplitude is divided by 2 to make the error variation tighter farther from the fault. Certainly this is not a perfect model of a fiber optic sensor fault. The characteristics may vary from fault to fault and sensor to sensor.

The bias added to the sensors with Eqs. (7.18) -(7.20) is appropriate for demonstrating outlier rejection in any case. To verify that the the CME can reject any failure in the FOS a worst case break point must be identified. This is pursued in the next section.

7.2.2 Selection of Most Critical Fiber Break Point

To demonstrate robustness of CME it must be tested in a worst case scenario. Therefore the worst break possible must be identified. The worst break is one which fails sensors which coincide with leverage points. The projection (hat) matrix values of the fixed modal strain matrix can mathematically determine the location of these leverage points. This also identifies which sensors are most critical to the modal estimate [176].

The hat values for each sensor locations are calculated from the diagonals of the hat matrix as in Eq.(7.21).

$$H = \Psi_{FOS}(\Psi_{FOS}^{T}\Psi_{FOS})^{-1}\Psi_{FOS}^{T} \tag{7.21}$$

The diagonals or hat values from Eq. (7.21) are plotted on top of their corresponding sensor measurement locations (See Fig. 5.16) in Fig. 7.3.

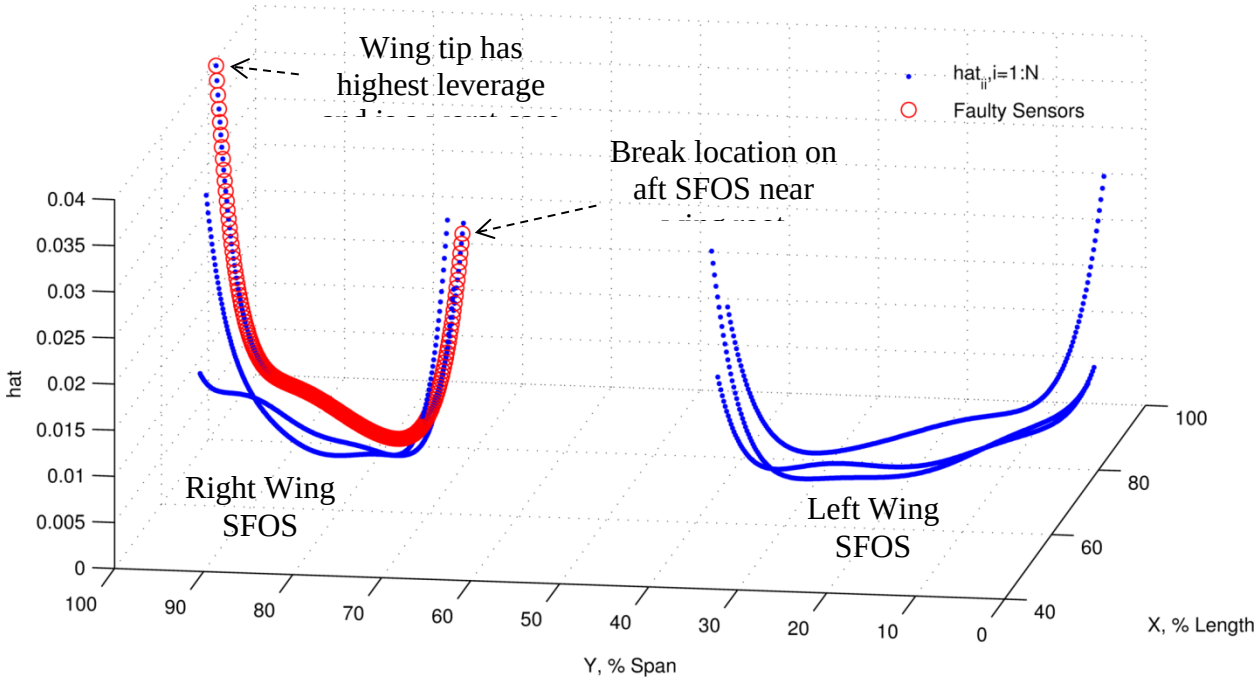

Figure 7.3: Hat values for X-56A FOS

Figure 7.3 shows that high leverage is characteristic for sensors placed near the wing root and wing tips. The location of the highest leverage is on the trailing edge tip of the right wing. Therefore the worst possible fiber break is at the wing root on the right wing aft fiber optic sensor. Figure 7.3 shows in red the biased sensors after a SFOS break near the wing root.

7.2.3 Concentrated Modal Estimator Simulation

For this break, three structural strain scenarios are analyzed. The first structural strain scenario is for aeroservoelastic trim strain at the design speed. This is a strain scenario the aircraft wing will spend the most time in. The second structural strain scenario is for a large wing tip leading edge down torsional displacement from aeroservoelastic trim. The third structural strain scenario is for a large amplitude bending displacement from aeroservoelastic trim.

It is expected that large displacements from aeroserovelastic trim may result from maneuvers, control or large disturbances. To simulate the expected failure bias during a break, the failure bias amplitude A is arbitrarily set to 30 times the standard deviation of the SFOS noise [See Eqs. (7.18)-(7.20)].

The SFOS normal error was assumed to be 3 microstrains (μs). This is because the FOS is expected to have a high signal to noise ratio. The radius r_{nf} which is used to find biased sensors upstream of the fault is set to 3 inches. The radius selection is somewhat insignificant as the worst case failure location is on the wing root.

The nominal sensor measurements for all three scenarios superimposed with suitable sensor bias for the fiber break are presented on the next page in Fig. 7.4.

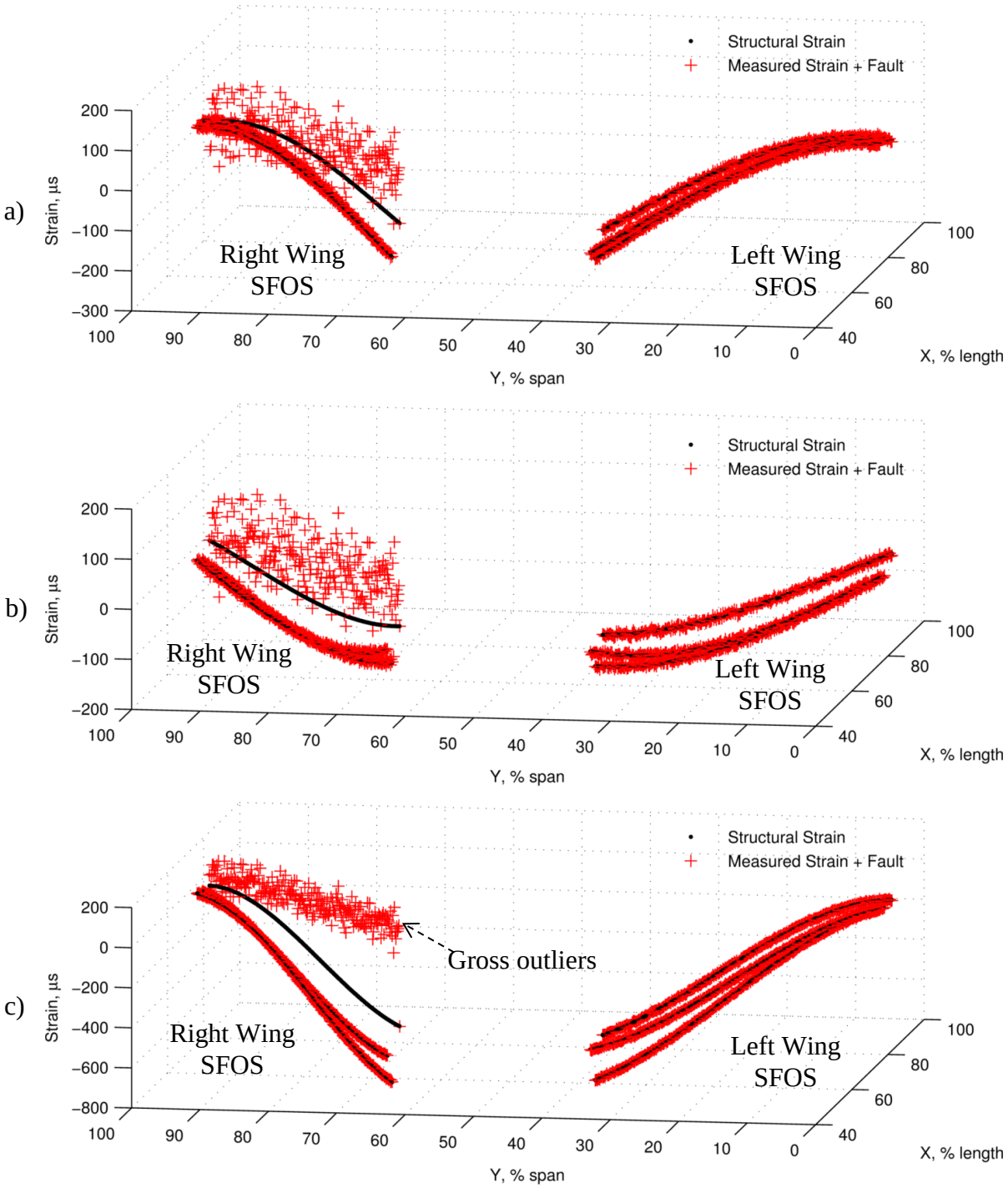

Figure 7.4: SFOS Strain with Fault + Noise: a) Trim Strain; b) Trim + Torsional Strain; and c) Trim + Bending Strain

The biased strain in Fig. 7.4(a) represents a case of small outliers. The biased strain in Fig. 7.4b represents a case of small to medium outliers. The biased strain in Fig. 7.4(c) represents a case with gross outliers. The strongly biased strain measurement data (See Fig. 7.4) presents unique challenges for a robust modal filter.

For each structural strain scenario, Algorithm 1 of section 7.1.5 representing the CME is computed for 10 concentration steps. The CME requires a robust start from a previous time step. In this case this was not available. Therefore the robust start is modeled by the true modal displacements offset by 10% of a multiplicative normal error. The relatively large offset simulates the modal displacement variation between discrete time steps τ. Recall that modal displacement estimates current discrete time steps are used as robust starts for future time steps in the CME.

The number of M-steps in C_0 is initially set to 10 to achieve a converged Tukey bisquare M-estimate and then set to 1 for all remaining concentration steps to improve computational efficiency. The tuning constant P_c for the D_{ub}^2 required for each concentration step is set to 1.1. The D_{ub}^2 works out to be 68 using Eq. (7.14). For each scenario an MCS is run and data is collected for 300 random seeds.

For the scenarios, the distribution of the relative error of the modal displacement estimates for each concentration step is recorded and plotted in Fig. 7.5.

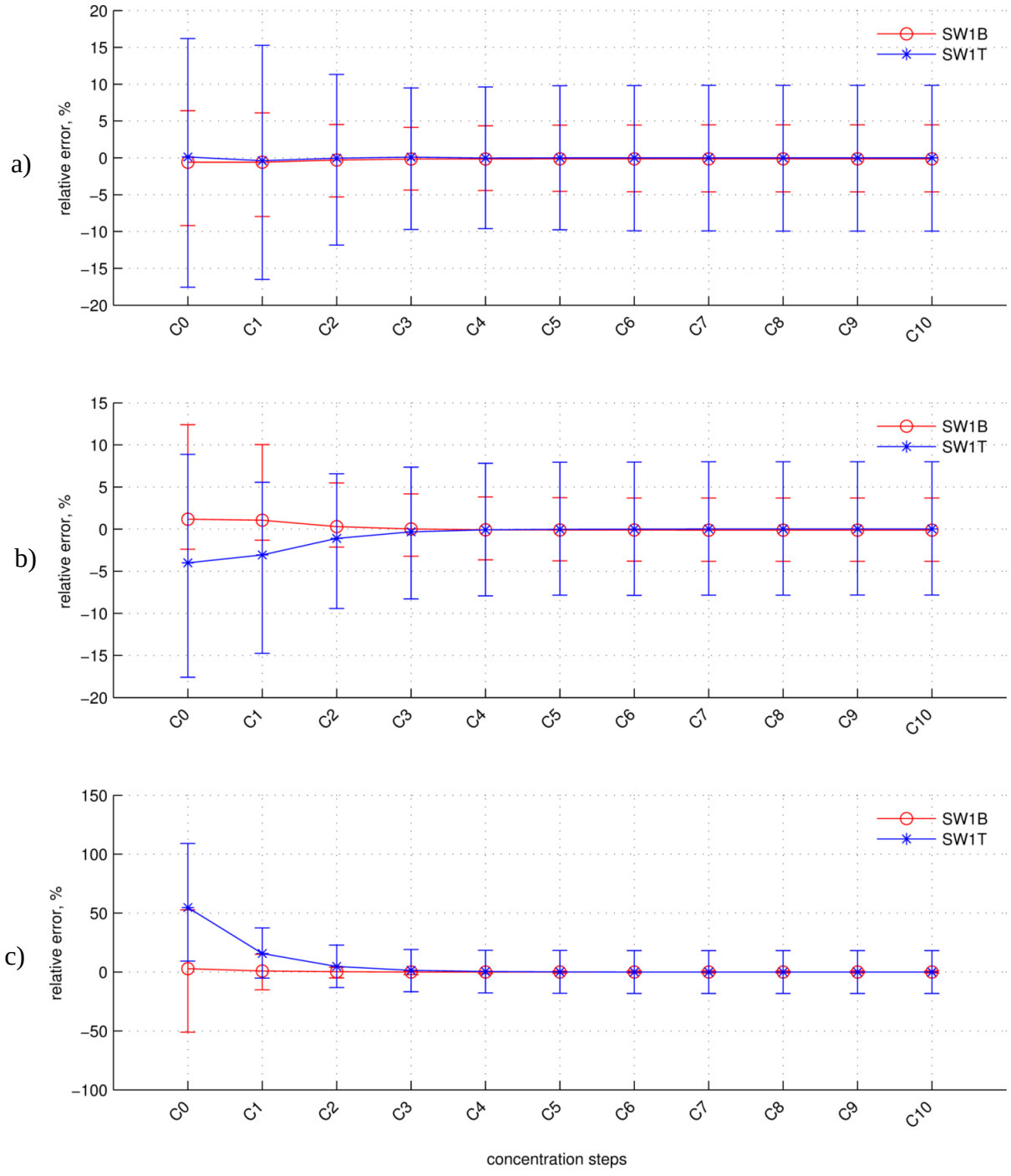

Figure 7.5: Simulation of CME on Faults: a) Trim Strain; b) Trim + Torsional Strain; and c) Trim + Bending Strain.

The first scenario is one in which the CME must perform well; the aircraft will operate normally in aeroservoelastic trim. The initial start C_0 is a converged Tukey M-estimate. Therefore the first concentration step estimate is regarded as the state-of-the-art. Any further reduction of the error and error deviation is due to the trimming concentration procedure in the CME.

The start of the first scenario (See. Fig. 7.5[a]) indicates that distribution of the SW1B modal displacement estimate is skewed with positive 1st standard deviation up to 12.5%. The SW1T modal displacement is centered near 0% but deviates to -18% error. After four concentration steps, the error distribution of both modal displacement estimates is centered at 0%. The error deviates up to 5% for the SW1B modal displacement and up to 10% for the SW1T modal displacement estimate. This represents a significant reduction in the error distribution from the state-of-the-art.

The second scenario (See. Fig. 7.5[b]) represents a particularly interesting one in which the aircraft wings have twisted leading edge down. The initial start indicates that the SW1B modal displacement error distribution is skewed as before, and the error deviates up to 13%. The SW1T modal displacement error distribution is symmetrical but is centered -4% and varies down to -18% error. After four concentration steps, the error distribution of both modal displacement estimates appears symmetrical and centers at 0%. The deviation of error of the SW1B modal displacement estimate drops to 8%. The error deviation of the SW1T modal displacement drops to 4%. This is a slightly higher reduction in error than that achieved for the aeroservoelastic trim case.

The third bending strain scenario (See. Fig. 7.5[c]) is decisively important as it clearly shows the effect of gross outliers stationed at leverage points. The initial state-of-

the-art estimates at C_0 show an error distribution of the SW1B modal displacement estimate which is symmetrical and centered at 2% and deviates up to 52%. The error distribution of the SW1T modal displacement estimate is symmetrical and centered at 54% and deviates up to 110%. Therefore, the state-of-the-art produces alarmingly bad estimates of the modal displacements in this case. After concentration up to only four steps, the error distribution of the SW1B modal displacement is symmetrically centered at 0% with insignificant error deviation. The SW1T modal displacement error distribution is symmetrically centered at 0% with error deviation up to 15%. The improvement is resounding and demonstrates the impact of concentration.

The analysis of Fig. 7.5 is useful to show the impact of concentration in the CME. However, a more visually descriptive way of comparing CME to the state-of-the-art is required. Therefore the CME final estimate is compared to the final estimates from M-estimates with Huber and Tukey bisquare weightings.

Huber's function is utilized because it down-weights but does not completely remove the presence of gross outliers. Its performance is comparable to that of OLS used by Kang et al. [66]. However it will be much more robust to outliers.

The M-estimators are given the same robust start as the CME: the true modal solution offset by 10% multiplicative normal noise. Recall that the additional noise simulates the difference in modal estimates between time steps. Each M-estimator is iterated to convergence.

Since control systems require high sampling rates, the CME must have low computational complexity. The computational processing time used for all estimators is recorded with MATLAB's profiler. The profiler estimates the total CPU time required by

processors to run functions and sub-functions. For each scenario a 2.6 GHz processor is used to compute CPU time.

Since the noise and fault conditions are characterized by normal distributions, a Monte Carlo Simulation (MCS) is run. The MCS is generated from 300 random seeds. Results are presented for percent relative error and deviation for modal bending and torsion displacement estimates. The simulation modal displacement is considered the true model of modal displacement in the system. The results of the MCS simulations for the aeroservoelastic trim case and the structurally perturbed cases are presented in Fig. 7.6.

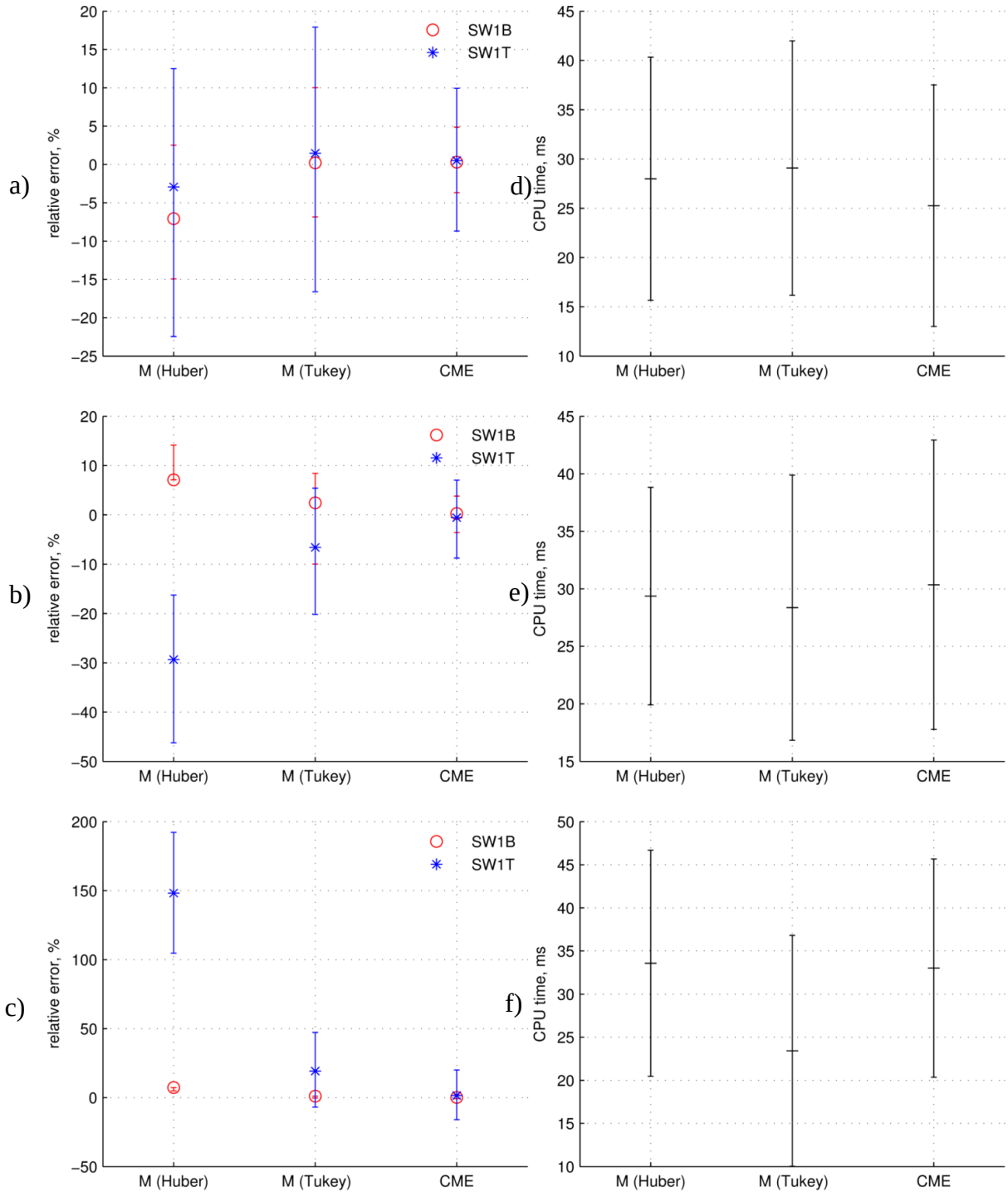

Figure 7.6: Modal Estimates during Fault: {relative error a) Trim Strain; b) Trim + Torsional Strain; and c) Trim + Bending Strain};{CPU time d) Trim Strain; e) Trim + Torsional Strain; and f) Trim + Bending Strain}.

The significance of Fig. 7.6 is primarily in the relative error comparisons. For the first scenario in Fig. 7.6(a), the relative error distribution of the SW1B modal displacement estimated with Huber weights is symmetrical and centered at -7%. The 1st standard deviation moves the overall maximum error to -15%. The SW1T modal displacement relative error distribution is skewed negatively and centered at -3%. The maximum deviation of the error moves the error to -22%.

The Tukey estimates in Fig. 7.6(a) fared better, but only slightly. The SW1B modal displacement error distribution estimated with Tukey functions is symmetrical and centered at 0%. The error deviation is up to 10%. The SW1T modal displacement error distribution is symmetrical and centered at 2%. The maximum deviation of the estimate goes up to 18%. Reduced mean errors are expected for Tukey function estimates due to the reduction of the influence of gross outliers with bounded influence functions. The error bars were nearly the same size for both estimators.

The CME estimates the SW1B modal displacement with an error distribution for both SW1B and SW1T modal displacements symmetrically centered at 0.5% in Fig. 7.6(a). The deviation of the error for the SW1B modal displacement was at a maximum of 5%. The deviation of the error for the SW1T modal displacement achieved a maximum of 10%.

When compared to state-of-the-art estimates, CME outperforms them with respect to relative error for the aeroservoelastic trim case. Figure 7.6(d) indicates that the CME is computationally comparable to the state-of-the-art estimators. The means of the CPU time for the CME was at 25 ms. The CPU time varied 18 ms from the mean.

Fig. 7.6(b) shows the relative error comparisons for the 2nd scenario, in which the wing is elastically twisted leading edge down by 3 degrees. With higher displacements from trim, the estimators are expected to perform worse, due to the growth of outliers. In fact this is the case.

The Huber SW1B modal displacement error distribution in Fig. 7.6(b) is skewed positively and centered at 7%. The maximum deviation of the error moves the relative error up to 14%. The SW1T modal displacement error distribution is skewed negatively and centered at -28%. The error variation takes the maximum error to -47%.

Tukey's estimate in 7.6(b) is better than Huber's but worse than for the aeroservoelastic trim scenario. The SW1B modal displacement error distribution is skewed negatively and centered at 3%. The maximum relative error is down to -10%. The SW1T modal displacement error distribution is symmetrical and centered at -7%. The error variation takes the error distribution to -20%.

The CME estimates for the torsional scenario (See Fig. 7.6[b]) are comparable to the aeroservoelastic trim case. The means of both modal estimates are symmetrical and centered near 0%. The SW1B modal displacement estimate varies up to 4% in either direction. The SW1T modal displacement distribution varies up to 8%.

The CME outperforms both the Tukey and Huber estimates. The CPU time for the three estimators shown in Fig. 7.6(e) is nearly the same as for the aeroservoelastic trim case. However, the CME CPU time distribution increased to 31 ms with a 17 ms variation.

In the final scenario (See Fig. 7.6[c]) the biggest improvement is seen when using the CME compared to the Huber and Tukey estimates. Huber's estimate is strongly

biased. The SW1B modal displacement error distribution is nearly a point and centered at 7%. The SW1T modal displacement error distribution is symmetrical and centered at 145%. The error varies up to 190%. The torsional modal displacement estimate is shockingly poor.

This holds true for the Tukey estimate as well in Fig. 7.6(b). The SW1T modal displacement distribution is symmetrical and centered at 20%. The error variation of the estimate is up to 48%. The CME estimate shows almost no error bias in the SW1B modal displacement. The SW1T modal displacement error distribution has longer tails than from previous scenarios, however the mean is near to 0 again. The variation is up to 20%.

The clear advantage of the CME is seen in the third scenario (See Fig. 7.6[c]). The CME easily rejects gross outliers at leverage points, dominating other robust estimators. Neither the redescending M-estimator based on Tukey's bisquare function nor the M-estimator with Huber weights considered significant removal of these leverage outliers.

7.2.4 Analysis of Concentration Steps

The previous results are telling of how the CME will outperform the state-of-the-art estimators for the asymmetrical multivariate estimation problem. The CME process of concentration is not completely intuitive without analysis of the squared Mahalanobis distance D^2 at each concentration step. For the aeroservoelastic trim strain scenario, the initial distribution of D^2 is given, along with the measured D^2 and weighted D^2 for four concentration steps is given in Fig. 7.7.

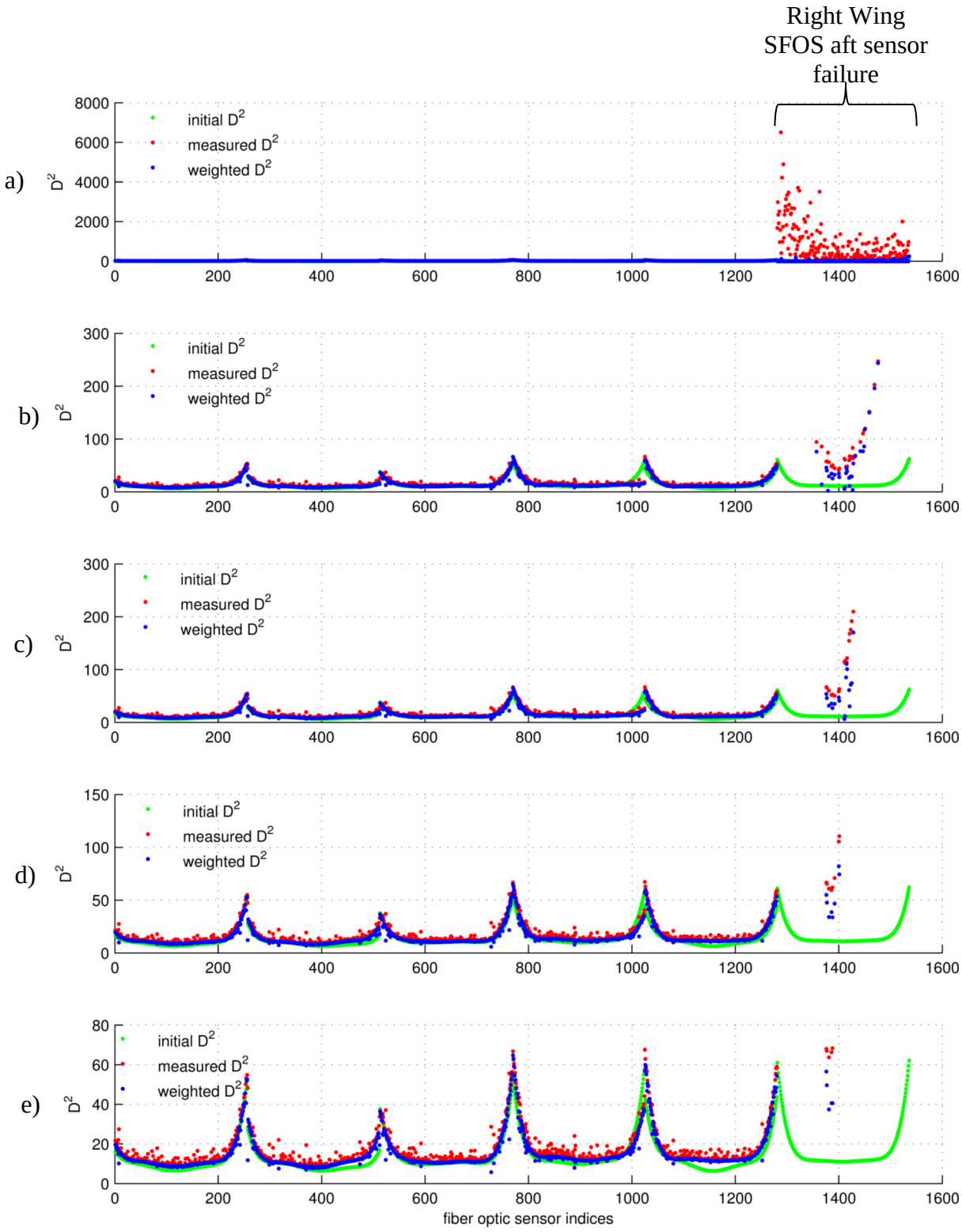

Figure 7.7: Squared Mahalanobis Distance Distribution at X-56A Model Fiber Optic Sensor Locations after each Concentration Step in Aeroservoelastic Trim Case: a) C0; b)C1; c)C2; d)C3; and e)C4.

The initial distribution is based on $D^2\left(\Psi_k(x_C, y_C, z_C)\right), k = 1 \ldots S$, where the Mahalanobis distance is computed only for the fixed strain mode matrix. The measured D^2 includes the strain mode matrix and measured strain in the computation of the Mahalanobis distance. The weighted D^2 is computed by multiplying the measured D^2 by the final weights $w_k^{(b_f,c)}$ from the CME for each sensor.

Figure 7.7 gives several indicators that the CME is operating as predicted during its derivation. The first is that the measured and weighted D^2 tends to decrease through further concentration. At the beginning of the concentration procedure (See Fig. 7.7[a]) , the measured D^2 is very large, up to 6,600. It is largest where the sensors have initially failed. The 2nd concentration step in Fig. 8b shows that the magnitude of the weighted and measured D^2 has reduced to a maximum of 250. In the final step (See Fig. 7.7[e]), the $D^2(x_k)$ of each sensor is below the D_{ub}^2 of 68.

The reason why all of the sensors cannot be detected and trimmed in the first step is because the mean and co-variance estimates are still biased. As the more biased sensors are removed, estimates of the multivariate center move closer to the true population mean and covariance. As the true population mean and covariance is approached, sensors with smaller bias begin to look more like outliers and cross the D_{ub}^2 threshold. These sensors are detected and removed, thus further improving the estimate of the mean and covariance of the distribution. This is an iterative adaptive convergent process.

Notice from Fig. 7.7 that not all of the sensors can be removed with trimming, as outliers at off-leverage points are likely to reside below the D_{ub}^2 threshold. The effects of these outliers are downweighted by the M-step reweighting procedure. Since the weighted D^2 is below that of the good leverage points the effects of these outliers have a

minimal impact on the estimate. Therefore the optimal feature estimates are pulled towards the true global optimum.

Some computational observations of theoretical predictions can be made. Note that the measured D^2 is lower bounded by the initial D^2. This supports the assumption that the addition of another feature and sensor noise to the initial D^2 increases the maximum D^2.

Therefore the utilization of Eq. (7.14) to approximate D_{ub}^2 is justified. This is best depicted in the last concentration step (See Fig. 7.7[e]), where the resolution is more pronounced. Another observation can be made about the effect of the weights on the noise.

It is clear that the CME has a side effect of down-weighting noisy sensors; the weighted D^2 appears smoother than the measured D^2. For sensors which were particularly impacted by noise, their weighted D^2 was even lower than the initial D^2. Thus, sensors with more noisy measurements than others can be identified and down-weighted within a single time step. The following section describes how the CME works in a dynamic shape control simulation with time-varying fiber optic sensor failures.

7.2.5 Dynamic Simulation – Automatic Sensor Failure Rejection

The previous static analyses show that the CME can perform adequately in the presence of unbiased and biased sensor data. But performance in a control system is a critical requirement of the CME. This is necessary to verify that a robust regression technique can satisfactorily be used to derive a robust modal filter. This would also confirm an answer to Research Question 3 and agree with the hypothesis.

Therefore the CME is tested in a dynamic simulation to verify that the estimator's interaction with the control system will not lead to instability. For this verification test, the following virtual deformation simulation control architecture is used (See Fig. 7.8).

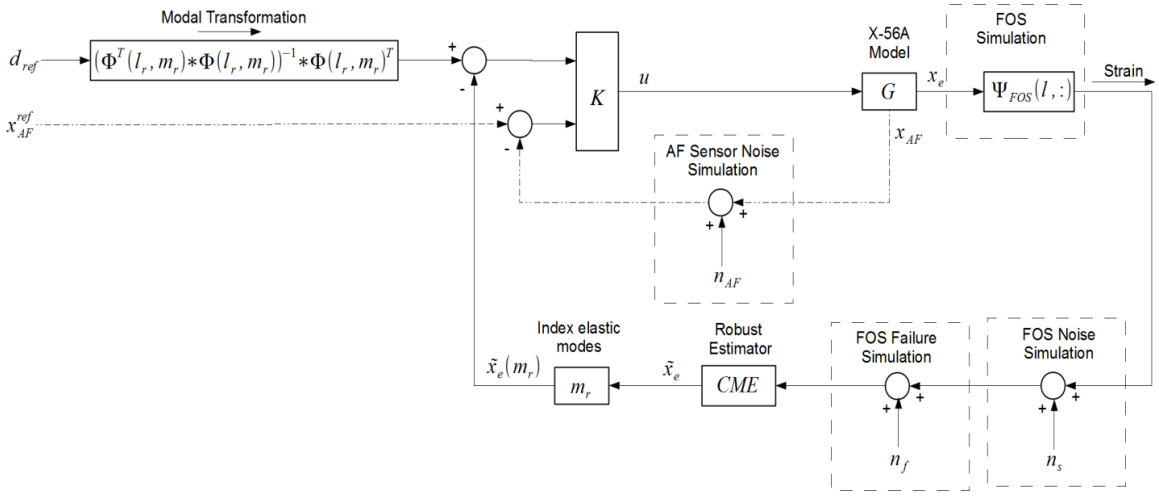

Figure 7.8: Virtual Deformation Control with Robust Modal Filter for the X-56A

Recall that virtual deformation control is the concept of controlling deformation, through modal commands. The virtual deformation control architecture represents the inner loop control system for the simulated X-56A model, where the inputs are assumed to originate from an outer loop control system.

The commands are split into deformation and airframe type and the entire simulation & controller is run at 100 Hz. This sampling rate is faster than the CME's predicted performance, but the algorithm has not yet been optimized computationally and put into hardware.

The simulated virtual deformation control system is thoroughly described in Section 5.3.1. For the present simulation, rigid body pitch θ and bank ϕ are tracked in the flight controller. Yaw axis commands are not given, because the current models do not

accurately reflect yaw dynamics. Commands of 0 deg. are given to both rigid body variables.

Points at the wing tips (See Fig. 5.16) are given opposing deformation commands. The opposing deformations correspond to a positive 3 deg. change in wing tip incidence (as in Fig. 7.4[b]). The points are tracked by commanding the first bending and torsion modal displacements.

The deformation command used previously (See Fig. 5.20) was a bending command which was nearly perfectly tracked. It becomes of interest to see if the performance in tracking torsion was characteristically similar to the performance results for a simulated clamped wing (See Fig. 4.20).

Previously the simulation in Fig. 5.1 incorporated airframe noise n_{AF} to the rigid body sensors. Only SFOS noise n_s is modeled now, so that the effect of the fault is isolated. For the current simulation, the SFOS failure bias n_f is added to faulty sensors using the same failure shown in Fig. 7.4(b). At any time after 10 seconds the sensor bias n_f impacts the sensor system.

The CME is allowed 4 concentration steps as this was the number required for convergence (See Fig. 7.5). As before, the CME is allowed 10 M-steps in the initial concentration step, C_0. A single M-step is utilized in later concentration steps up to 4 concentration steps. The D_{ub}^2 is again calculated to be 68, with P_c set to 1.1 in Eq. (7.14).

For comparison, simulation results for state-of-the-art M-estimator with Tukey bisquare weights was utilized in lieu of that by Kang et al. [66]. Clearly an OLS is an unfair comparison in the presence of such large sensor bias.

During each simulation the estimators pass their respective modal displacement estimates to the μ optimal controller. The controller achieves robust stability and performance for modeled feature and speed variations. However, it has some nominal overshoot performance issues, which may be corrected with improved weightings. It is not expected that nominal performance issues will create problems. Therefore, if instability occurs during the fault, it is not a result of an improperly designed control system. All good or bad performance is due to the estimators only. The comparative results of the dynamic simulation studies are presented in Fig. 7.9.

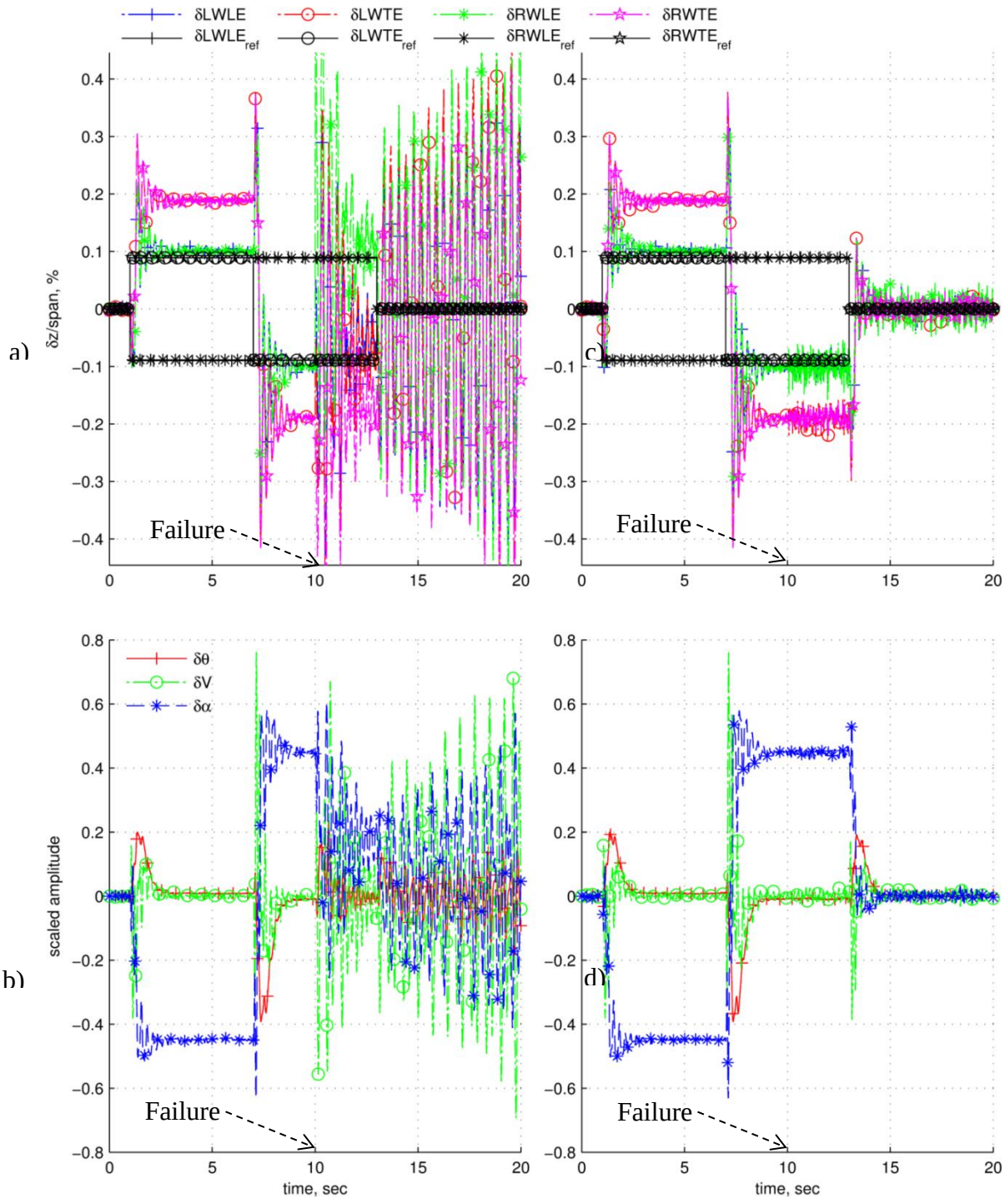

Figure 7.9: Dynamic Simulation Comparing Robust Estimators during a Simulated Fiber Optic Sensor Failure on X-56A Model: {M-estimate a) deformation tracking; and b) airframe state tracking}; {CME c) deformation tracking; and d) airframe state tracking}.

Striking differences are noted from the side by side comparison of Tukey's M-estimator (See Fig 7.9[a-b]) and CME (See Fig. 7.9[c-d]) performance. After 10 seconds, the control system with the state-of-the-art M-estimator experiences strong divergent oscillations (See Fig. 7.9[a-b]).

The oscillations appear to reduce in amplitude up to 12.5 seconds. After 12.5 seconds, the aircraft is commanded back to aeroservoelastic trim. This is when the system goes unstable. It is evident that the bias modeled by Eqs. (7.18)-(7.20), appears to either lead to control-induced instability or flutter amplification. This exposes the danger which may result from using a failed FOS system with an estimator which is not robust to leverage outliers. The situation is more terrifying if the OLS estimator used by Kang et al. [66] is utilized.

The time histories of the data (See Fig. 7.9[c-d]) in the CME supported control system show no signs of growing oscillations after the fault. However, there is an increased noise distribution on the displacements after 10 seconds. When the structure is perturbed, the noise distribution does not appear to change. This was expected due to the static simulation performances of the CME (See Fig. 7.5). It is noted that the effect of the sensor failures only slightly spill over into the rigid body variables for this case.

The dynamic performance of the CME is adequate when considering that 230 sensors have become strongly biased (See Fig. 7.4[b]). The dynamic simulation demonstrates that the robust start between discrete time steps [See Eq. (7.16)] is justified in Algorithm 1. That is, that the use of the previous modal displacement estimate can be satisfactorily used as a robust start for the CME.

More conclusions can be drawn, not just from the performance of the CME or Tukey's M-estimator. It is evident that the system has some non-minimum phase zeros in the bending and torsional modal displacement channels. The residual modes are also excited by the abrupt commands which lead to more non-minimum phase behavior. This is a property of the controller, however, and not the CME. A simple fix for this is to ramp the commands in.

Another observation is that the desired displacements for torsional control were not achieved. A roughly 1.5 deg change in wing tip incidence occurred instead of 3 deg. The wing was also corrupted by bending motion, which was not commanded. The exact nature of performance was predicted in previous research on a clamped plate model (See Fig. 4.20). and is primarily due to residual modes.

This is suggestive, since the results of that study are replicated on the aircraft. This indicates a need for improved effectors other than the present aerodynamic trailing edge control surfaces. Local effectors such as piezoelectric patches may be required to achieve improved virtual deformation control in aircraft, as non-collocated effectors tend to excite residual modes [7].

7.4 Summary of Robust Modal Filter Development

Caution demands a robust modal filter, which relies upon possibly 1,000s of sensor measurements. Indeed, if the FOS are utilized, a break of the fiber could be devastating to an aircraft control system as hundreds of sensors become biased. The

hypothesis for Research Question 3 was confirmed by developing the CME through the use of robust regression.

However, instead of using a single estimator, a hybrid estimator was required. This was developed from two existing robust estimators. When combined and an improved estimator resulted. The redescending M-estimators were used to make a concentration algorithm more robust to asymmetry. Robustness was further improved by introducing a fixed trim criterion and more robust starts.

The CME was tested in static and dynamic simulations and it was shown that it outperforms robust M-estimators. The most impressive performance was for the gross leverage outliers case. The CME experienced only small errors in the modal displacement errors when compared to other robust estimators.

The CME provides the stepping stone needed for a practical application of modal filtering in aerospace. Its applications may be broader than that which it is tested for here. Several applications of the CME are discussed in the next Chapter.

CHAPTER 8

OTHER APPLICATIONS OF ROBUST MODAL FILTERING

The previous Chapter produced the CME and showed that it is an improvement over the state-of-the-art robust estimators in the presence of strong sensor bias. It is shown in this Chapter that the CME lends itself to other applications. That is, the robust modal filter is not just derived for making a modal filter robust to sensor bias.

It is shown that the robust modal estimates recovered by the CME can also be used to estimate strain in locations of spurious measurements. This confirms a first answer to Research Question 6 which asks for further applications of the robust modal filter. A static simulation demonstrates the virtual strain reconstruction for the three strain scenarios defined in the previous chapter.

A methodology is given for identifying biased sensor locations or wing damage using residuals of the robust estimates. This is followed by a static simulation demonstrating biased sensor identification or health monitoring. This provides a second answer to Research Question 6. The methodology for virtual strain reconstruction is presented first in the next section.

8.1 Virtual Strain Reconstruction Methodology

There could be several reasons why estimating strain at biased sensor locations could be convenient or required. Virtual strain reconstruction could be required if the FOS fail while the wing is approaching a critical structural load limit. This may reduce the possibility of exceeding structural load limits in this unlikely scenario.

Virtual strain reconstruction may also be useful if the FOS is embedded in the wing structure and undergoes an age-related failure. Yet another unlikely scenario, but preparation for such events is beneficial. Indeed a strain prediction model may be required until the faulty wing sensors are serviced.

The robustly estimated modal displacements may be utilized to form a robust prediction of the true strain state at the biased sensor locations. Using the underlying data matrix or strain modal matrix, a robust estimate of the axial strain at the k^{th} sensor at any discrete time step is given as in Eq. (8.1).

$$\hat{s}_k(x_C, y_C, z_C, \tau) = \Psi_k \hat{q}^{(b_f, c_f)}(\tau) \tag{8.1}$$

Application of Eq. (8.1) to estimate strain can be considered virtual strain, which is akin to virtual deformation. The following section demonstrates this application for the three strain scenarios.

8.2 Virtual Strain Reconstruction Simulation

For all three structural strain scenarios, the virtual strain, true structural strain and measured strain are plotted together in Fig. 8.1.

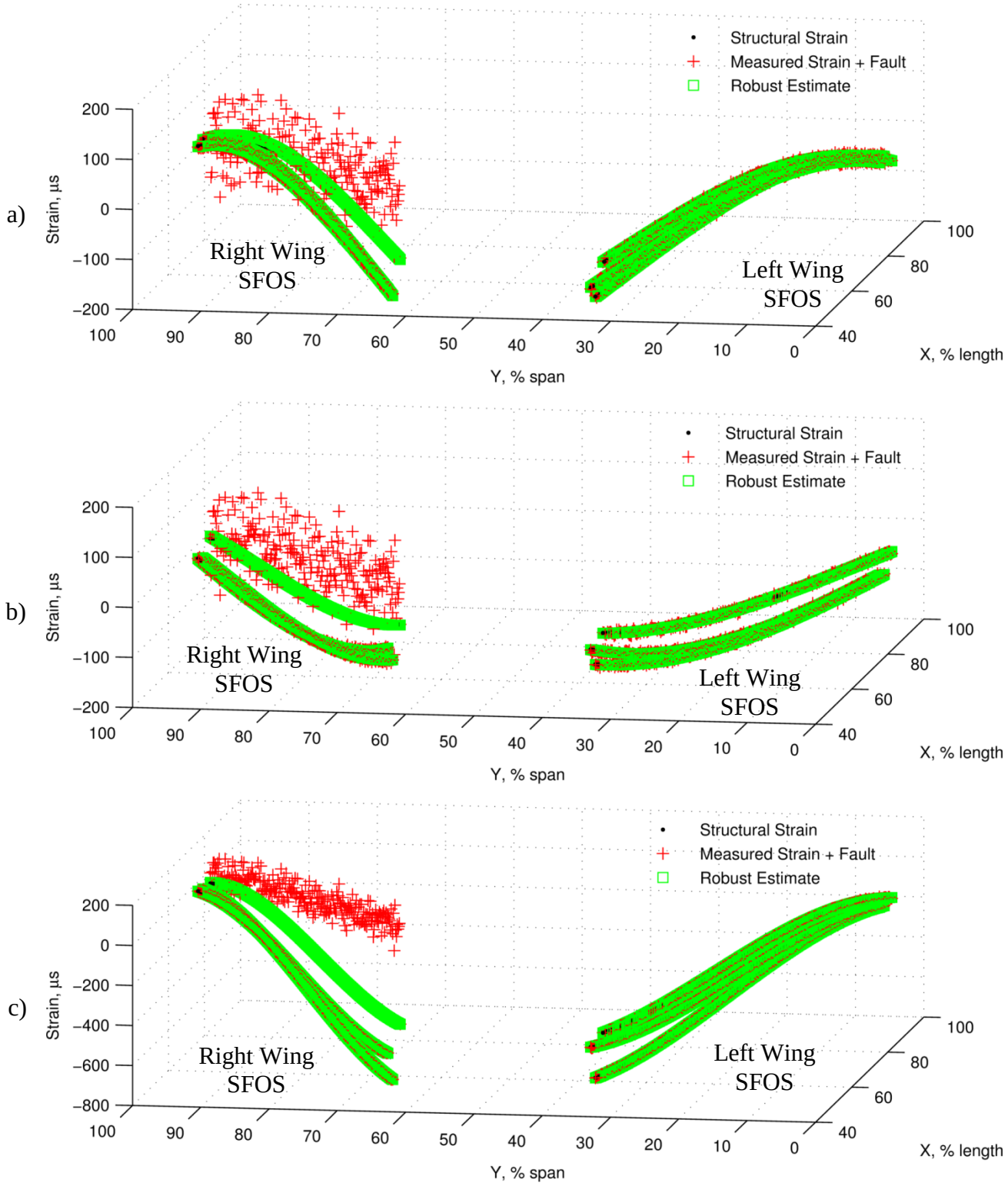

Figure 8.1: Virtual Strain Reconstruction. a) Trim Strain; b) Trim + Torsional Strain; and c) Trim + Bending Strain.

Figure 8.1 shows an overlay of the robustly estimated strain on the true structural strain in the system for each of the three scenarios. The biased strain measurements are very far away from the robustly estimated strain in most cases. Small bias is removed from the robust strain estimates.

Another conclusion can be drawn here. If the virtual strain estimated by Eq. (8.1) overlays the true structural strain, this is further confirmation that the CME is a suitable estimator. This is because the strain is modeled as a linear combination of the modal displacements. Therefore to achieve accurate strain estimates, even residual modes must be estimated well.

This excellent prediction of strain further confirms the capability of the CME to accurately predict both commanded and residual modal displacements with over 230 faulty sensors. This also further confirms the CME's operational capability in the presence of gross outliers at critical leverage points. The next section introduces another capability provided by the CME.

8.3 Sensor Fault Identification and Health Monitoring Methodology

There is at least one more answer to Research Question 6, which asks for further capabilities of the robust modal filter. This time instead of using the robustly estimated modal displacements, the robust residuals become important. A robust residual is the difference between the measurements and the estimate of the measurements computed from robust feature estimates. A large robust residual is strongly indicative of an outlier

[196]. Therefore, large robust residuals from the CME may indicate structural problems on the aircraft.

Unfortunately, these large residuals can be the result of several events. The residuals could result from poorly predicted mode shapes which no longer predict the motion of the aircraft, structural nonlinearities, and potentially damage or sensor failure. The locations of the identified outliers must be inspected by technicians to determine the cause. A description of how to find these critical locations is determined next.

The last concentration step of the CME, results in a set of "good" sensors $S_g^{c_f} \subset S$. Thus, the candidates for biased sensors or wing damage $F \supset S$ are defined to be the remaining sensors not in the set of sensors S. If the last pool of sensors only contains unbiased sensors, and the estimate is robust, then the residuals will likely assume a normal distribution of error.

It is possible that some sensors in the pool of "good" sensors remain biased, if they reside below the D_{ub}^2 threshold. Therefore the final weights are used to down-weight these observations. Let the weighted average of the residuals of the good sensor candidates be defined as in Eq. (8.2),

$$\mu_g \triangleq \frac{1}{\sum w_k^{(b_f,c_f)}} \sum_{k=1}^{s_g^{c_f}} w_k^{(b_f,c_f)} e_k^{(b_f,c_f)} \tag{8.2}$$

and the weighted standard deviation of the residuals of the good sensor candidates is defined as in Eq. (8.3).

$$\sigma_g \triangleq \sqrt{\frac{1}{\sum w_k^{(b_f,c_f)}} \sum_{k=1}^{s_g^{c_f}} \left[(\mu_g - w_k^{(b_f,c_f)} e_k^{(b_f,c_f)})^2 \right]} \tag{8.3}$$

The number of weighted standard deviations the remaining data is away from the weighted mean can be defined for the k^{th} sensor as in Eq. (8.4),

$$S_k \triangleq \frac{|\mu_g - e_k|}{\sigma_g} \tag{8.4}$$

where the robust residual for the k^{th} sensor is computed as in Eq. (8.5).

$$e_k^{(b_f,c_f)} = s_k(x_C, y_C, z_C, \tau) - \Psi_k \hat{q}^{(b_f,c_f)}(\tau) \tag{8.5}$$

By selecting a cutoff of k_O weighted standard deviations away from the mean of the residuals of the good data, outliers may be identified. The following binary logic operation [See Eq. (8.6)] is given to determine if a sensor at the k^{th} location is biased as in Eq. (8.6).

$$S_k^f = \begin{Bmatrix} 1 & S_k \geq k_O \\ 0 & else \end{Bmatrix}, \tag{8.6}$$

The sensors in the subset of candidate faulty sensors F may be good or bad. During nominal conditions Eqs. (8.2)-(8.6) guarantees that healthy sensors will not be identified to be biased if k_O is chosen intelligently. If the sensor error is normally distributed, 95% of the data will statistically fall within 2 weighted standard deviations. It is very likely that most of the data will fall within 5 weighted standard deviations from the weighted mean.

The advantage of this technique is that it provides an automated identification procedure which will improve structural diagnostics. It may also be used to permanently

remove sensors from consideration for the remainder of the flight. The simulation study demonstrating this concept is performed in the next section.

8.4 Sensor Failure Identification or Wing Damage Detection Simulation

The procedure to identify faulty sensors or wing damage defined in Eqs. (8.2)-(8.6) is tested next. For this method to work properly, a proper threshold number of deviations must be selected for biased sensor identification. Since the majority of the data will fall within five deviations of error, the number of deviations k_O in Eq. (8.6) was set to 5. The number of weighted error standard deviations away from the weighted mean of the residuals of all data is given for each sensor in Fig. 8.2.

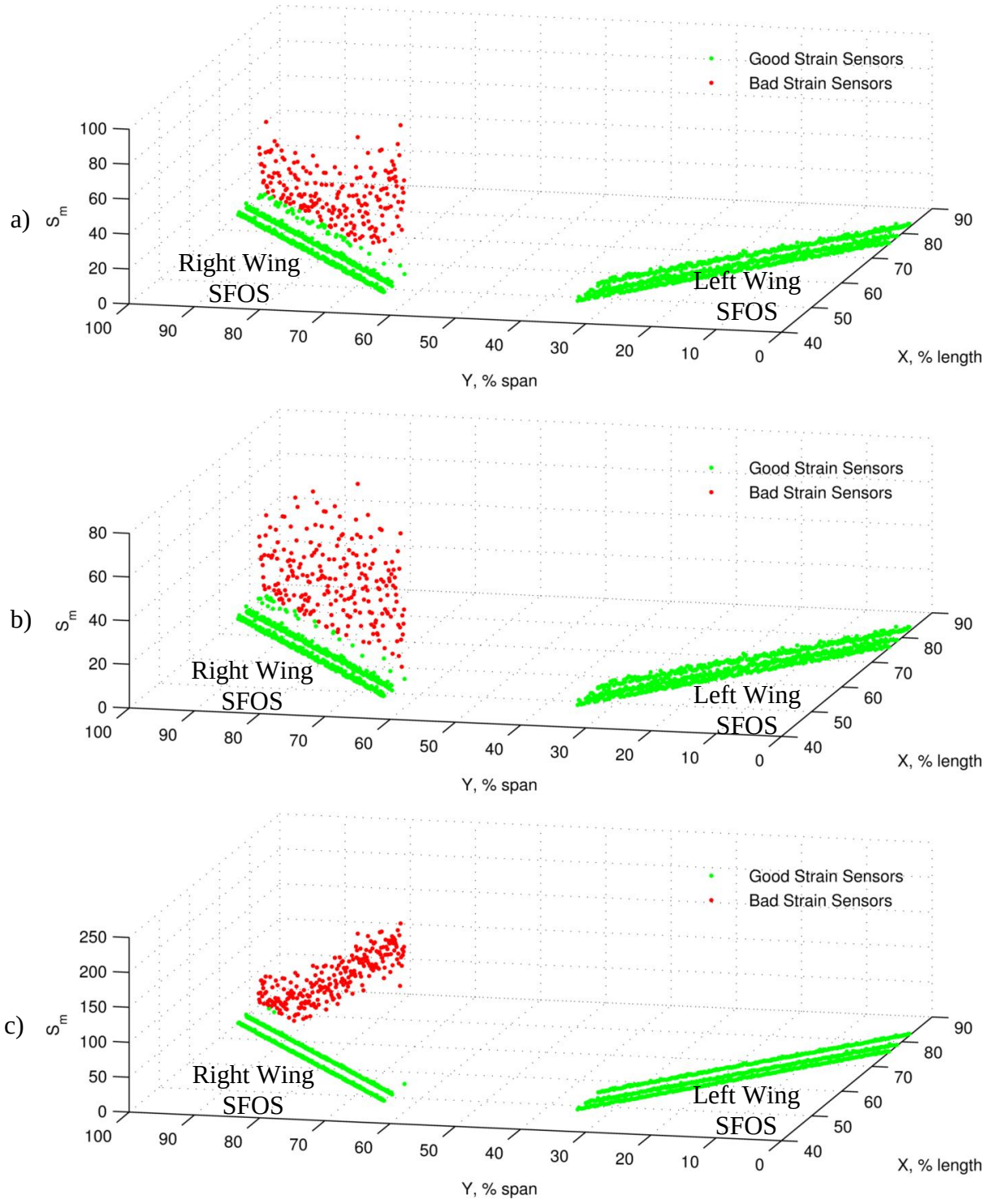

Figure 8.2: Sensor Fault or Wing Failure Detection with CME: a) Trim Strain; b) Trim + Torsional Strain; and c) Trim + Bending Strain.

Figure 8.2 shows suspicious sensors in red. Not all of the biased sensors were flagged for the three scenarios. The reason some sensors were not flagged is primarily due to the presence of small outliers [See Eq.(7.20)]. Small outliers are significantly harder to reject, as they may be mistaken for noise. This is especially true for Fig. 8.2(a), where the least biased sensors were identified.

It is clear that the sensors which most bias the estimate ($S_k > 5$) were identified in Fig. 8.2. These sensors and wing locations with very high weighted residuals are good candidates for inspection and possibly maintenance. This concludes the computational results of this dissertation. The next Chapter summarizes concepts and draws conclusions.

CHAPTER 9

CONCLUSIONS

To guide the research, six research questions were posed under the umbrella research problem. The research problem summarized much of the research objectives. This dissertation concludes by answering research questions and discussing hypotheses. The research problem is discussed and how research objectives were met.

As a result of the research activities, gaps identified previously are addressed and conclusions are drawn as to how they are filled by the modal filter. The predicted impact of the robust modal filter in aerospace is then discussed. This is followed by conclusions on the potential improvements to and follow-on activities for this dissertation. The next section proceeds with a discussion of the original research questions and hypotheses.

9.1 Research Questions and Hypotheses

In Chapter II, research questions were introduced to guide the development of this dissertation and addressed specific gaps of knowledge in the literature. Within the body of the text, these questions were answered through computational results and discussion. Here, they are given the spotlight. The research questions and their original hypotheses (if any) are represented sequentially in the following sections. Discussion is given on how the hypotheses must be modified based on all of the completed work.

1. Research Question and Hypothesis 1

Research Question 1. Is the OLS modal filter efficient for control feedback when it is utilized within an aeroservoelastic problem?

Hypothesis 1. The OLS modal filter will perform the same as it would on a static structure out of wind flow.

The original hypothesis suggests that aerodynamics have little influence on the performance of a modal filter. Mathematically, this must be true, considering the assumption upon which the state space matrices are based. This assumption is that the deformation, velocity and accelerations of all points on the structure can be approximated as a linear combination of a set of mode shapes. So, early on, this hypothesis was mathematically based.

The testing and verification of this hypothesis was answered primarily with the wing model. It was found that a modal filtering design methodology specific to this wing model was required to answer the research question. Using this three phase methodology, competent aeroservoelastic controllers were developed using the modal filter. To explore the hypothesis further, two controllers with either modal coordinate or accelerometer feedback were designed.

The modal filter based controller had no observable defects when compared to the state-of-the-art controller using accelerometers for feedback. Robustness and performance were both similar in the resulting controllers. The primary difference was the order of the controllers. For the case of the wing model, the modal filter controller had a much reduced order. The significance of this is telling, indicating the potential of the modal filter to isolate modes of importance.

2. Research Question and Hypothesis 2

Research Question 2. How should a modal filter be incorporated into the control system of a aircraft?

Hypothesis 2. The modal filter is a partial state filter in the aeroservoelastic problem. It can be placed in series with a traditional control system estimator.

The original hypothesis was mathematically based. Indeed, the relationship between the coordinates estimated by the modal filter and the states used in the aircraft state space model are the same. So the equivalence was identified early on during the Literature Review.

However, during testing of the hypothesis, it was found that the original hypothesis was too simple. While the mathematical soundness of the hypothesis holds, the application of the modal filter into the aircraft control design process is more complicated. A three phase modal filter methodology specific to an aircraft showed that several complicated steps must be taken to integrate a modal filter into an aircraft controller.

There are bandwidth limitations to be considered when choosing modal coordinates to feed back. The correct number of modes must also be chosen in order to command the structure's shape accurately. It was noted in the computational results that residual modes reduced the accuracy of the shape controller.

The methodology also addressed the complications in generating the required strain mode matrix. Experimental validation will be required for strain mode computations. Some work on this is already being considered in the literature.

The reference transformation is also of a complicated nature for an aircraft. The shape commands can be completely biased if the methodology introduced herein is not

followed. The free-free modes of the aircraft must be transformed to remove all rigid body rotation and translation, relative to the undeformed aircraft.

3. Research Question and Hypothesis 3

Research Question 3. How can the OLS modal filter be improved to be robust to sensor bias?

Hypothesis 3. A robust regression technique will provide a real time estimator which proves to be efficient and resilient to faulty sensors.

The original hypothesis was correct, and robust regression was found useful in designing a robust modal filter. This is mathematically sound considering that the modal filter uses OLS to compute modal coordinates. Robust regression is a natural solution, when considering large sensor bias.

While the original hypothesis is correct, it is not stated precisely enough. Rather it should state that a hybrid robust regression technique is applicable to this problem. In the robust modal filter development, a hybridized approach was determined to be the best solution. This was motivated by several concepts such as the discovery that most robust and efficient algorithms have two stages. The first stage is high breakdown and the second is typically Gaussian efficient. In addition, the algorithm should be consistent.

A motivation for the ingenuity introduced in this work is that the nominal multivariate data of the sensor strain modal matrix is filled with leverage points. Thus robust statistics are hard to define and theoretical robust techniques violates proof of their robustness. Randomly subsampled techniques are also strictly invalidated for the sensor strain modal filter due to the presence of leverage.

From the literature, it was found that the redescending M-estimator is both computationally simple and resistant to leverage points. However, the computational results presented here suggest that even redescending M-estimators experience too much bias from an asymmetric outlier.

To improve robustness to leverage outliers, a trim criterion had to be introduced, specific to the outliers in the explanatory data. It is discussed in the literature that robust starts are needed to improve convergence of M-estimators to the globally optimal solution. These are often geometrically based and based on the median. A better robust start is available for a time sampled system. The CME, utilizes previously computed feature estimates as robust starts throughout the operation of the sensor system. This type of start is expected to outperform statistically good starts.

It was also shown that the CME is a real time estimator as its computational complexity is comparable to that of an M-estimator. Utilizing the CME in a dynamic simulation, it was found that the CME could adequately reject over 230 faulty sensors. This confirms at least one new way to improve the modal filter to be robust against biased sensors caused by a fiber break.

4. Research Question 4

What methods of shape control may the modal filter be utilized for?

No original hypothesis was stated for this question. Instead, two techniques were introduced for aircraft shape control, utilizing modal coordinates. The techniques are both forms of what we call virtual deformation control. That is, the control of shape via modal coordinate tracking.

The first technique made the assumption that all of the modes were available for sensing. In this situation, the controller was designed to track these deflection points. These points are modeled by full rows in the output matrix relating to the modal matrix. It is limited in the number of points which can be tracked, although they can be tracked accurately using this method. The problem with this technique is that it may lead to bandwidth issues. The second technique is viewed as more practical.

The second method requires tracking of the modal coordinates, through a reference transformation. The transformation converts the desired displacements to modal references. The controller then tracks the modal references in an attempt to reduce displacement tracking error. It was found that the second method makes more sense for aircraft shape control. Primarily this is because possibly millions of points will be required to be tracked for shape optimization. It would be highly desirable from a computational and robustness standpoint to track a few modal coordinates instead.

5. Research Question 5

Can a fully coupled rigid and flexible controller be designed with the modal filter?

No original hypothesis was given for this question. The original reason for posing this question was to address the growing concept that flexible aircraft must simultaneously control both flexible and rigid variables. The issue is becoming increasingly important as modal frequencies shift towards rigid body frequencies.

This question was answered by designing a fully coupled rigid and elastic controller. It was found that excellent tracking characteristics could be achieved in the

airframe states. However, the presence of overshoots was observed in the modal displacement states, which were meant to be tracked. This is hypothesized to be coming from the closeness of the elastic frequencies and rigid body frequencies. To counteract this problem, one could simply ramp into the modal displacement commands.

Robustness appears to be degraded by designing the fully coupled tracking controller. It is hypothesized that this is because the controller bandwidth is unfavorably increased due to the requirement to track modal coordinates. However, this conclusion is shaky at best due to subjective weight design and plant scaling choices. Further weights and plant scaling design could have improved the results given here.

6. Research Question 6

Are there other uninvestigated uses for a robust modal filter?

This question was posed open ended with no original hypotheses. Two techniques were explored in answer to this research question. They both make use of robustly estimated modal coordinates.

The first technique was inspired by the concept of recreating strain at biased sensor locations. Virtual strain reconstruction was enabled by using the robustly estimated modal coordinates to recreate strain states at biased sensor locations. This was found to not only be accurate, but to confirm the CME as a robust estimator of the parameter distribution.

The second technique uses the robust modal coordinates to create robust residuals. In the literature, it is posed that a large robust residual indicates an outlier. On an aircraft

structure such an outlier could represent wing damage or a biased sensor or both. Therefore a link with health monitoring was identified and tested herein.

9.2 Findings on Research Problem

The research problem was originally posed to address gaps in the literature as well as the research objectives identified early on. The research problem is restated here:

How can high resolution distributed sensing and modal filtering be safely utilized for control feedback in flexible aircraft?

This problem was primarily supported by the research questions and hypotheses and testing discussed in the previous section. The research problem is now discussed in the context of the research objectives it supported.

By showing that the modal filter and distributed sensing could be utilized on an aeroservoelastic wing model, feasibility was demonstrated. This feasibility addresses the first research objective, which is restated here:

- **Investigate how modal filtering performs on an aeroservoelastic problem as a first application**

Application of a modal filter to control a wing model is too simple. It was necessary to incorporate the modal filter into an aircraft controller. This was done by

investigating similar modal controller designs on the X-56A model. This confirmed the modal filter was applicable to a flying aircraft. It showed the differences and what must be prepared for. It also opened up new ways of performing shape control on an aircraft. This more than met the second research objective restated here:

- **Investigate distributed sensing and modal filtering in the control system of an aircraft**

The next step was to design a robust modal filter, known as the CME, which is robust to out sensor failure model. Two ways were discovered to utilize the robust residuals to both recreate virtual strain and perform health monitoring. These steps satisfactorily addressed the thirst major research objective restated here:

- **Improve upon the sensor bias limitations of modal filtering**

The gaps are also addressed under this umbrella research problem. How the gaps were filled is outlined in the next section.

9.3 Filling Gaps

Several gaps were identified in the Literature Review. These gaps were filled by the modal filter and the design methodologies and improvements to the modal filter developed herein. The first gap in aeroservoelasticity stems from the use of point sensors to control the “distributed by nature” aeroservoelastic states.

It was shown with a comparative study, that this can be done equally well with modal filtering and distributed sensing. Modal filtering also improves the order reduction of aeroservoelastic controllers due to modal isolation.

A gap identified previously is that flexible aircraft will require active shape control in aeroservoelastic tailoring schemes at off-design conditions. Two methods of shape control were introduced all made feasible through the modal filter.

One gap which was not directly addressed in this research is how the modal filter estimates are improved with increasing numbers of sensors. This could be addressed by varying the number of sensors and computing the modal coordinates. The errors should decrease with increasing numbers of sensors. Mathematically, this is sound and bench experiments have already been conducted to show this is true. It should not be any different in an aircraft.

An important gap to fill was the knowledge of whether the modal filter is applicable in an aeroservoelastic environment. The many computational experiments completed here on the wing model and X-56A model confirm its rightful application in an aerodynamic environment.

There was also a practical gap in the modal filter itself. State-of-the-art modal filters assume the sensor error distribution can always be approximated to be normal. Therefore they are sensitive to high sensor bias. To fill this gap the robust modal filter was derived and verified in static and dynamic simulation tests. It was shown to be capable of supporting an active shape controller on the flutter-unstable X-56A model in the presence of over 230 faulty sensors.

9.4 Concluding Remarks and Follow-on Research

Three broad research activities were identified and pursued. The first activity dealt with verifying whether or not a modal filter is applicable to a structure subject to wind forces. The second activity dealt with whether the modal filter could be applied to aircraft controllers. These two activities required the development of separate modal filter design methodologies. The third activity centered on determining how to design a modal filter to be robust to strong sensor bias. This final activity was a practical requirement as well as a theoretical challenge.

In the third activity a robust modal filter was derived and it was demonstrated on a simulated flight vehicle together with simulated distributed sensing for the first time. Its purpose was to estimate aircraft flexible states under sensor fault conditions. Controllers were developed using these states for feedback. It is postulated that controllers using these states may be more trustworthy than controllers which suppress point sensors.

The modal coordinate states were used to control the shape of the vehicle in the linear simulation. Whether the control of deformation is for controlling outboard scientific instrument locations, reducing loads/gust loads or just aerodynamically optimizing shapes will be up to the designer and application. Perhaps a great follow-up research question to ask is, “What aircraft deformation shapes are best?”

Research into static aeroservoelastic trim optimization has been ongoing for decades usually linked with CFD studies. Generally aircraft wing shapes are made optimal for a specific flight condition. But now, dynamic shape optimization becomes

interesting as differing flight trim variables may be associated with differing optimal deformation shapes of the flexible flight vehicle.

It is likely (if not already known) that there is a mathematically tractable or at least learnable relationship to be found with local aerodynamic sensors and the locally deformed shape of the vehicle. This relationship could be utilized in a locally optimal shape tracking framework.

The robust modal filter will likely realize practical fast converging locally optimal intelligent control for performance. This method of optimization might be preferable over the somewhat slowly converging globally optimal intelligent control for performance studies which utilize a fuel sensor or engine thrust for feedback.

The work in this thesis is not finished. What remains is experimental testing on a flight vehicle. There are also computational avenues of research which could further support the computational work which was completed in this dissertation.

9.5 Discussion on Potential Improvements

There is more to be done, as a result of this work. However, due to time constraints, these improvements could not be made in the allotted time to finish this dissertation. Some of the improvements identified are given here, which appear to be the most outstanding. Perhaps these improvements could be addressed in future research activities:

1) The analysis could be further substantiated by utilizing a nonlinear flight simulation or experimental flight data to demonstrate the modal filter performance. Unfortunately, a nonlinear flight simulation was not available for either model during the case study simulation efforts. Linear models were relied upon for the results. Actual fiber optic failure data from a real flight experiment would also have proved very useful for validating the CME.

2) It was observed from the case studies that error in achieved deformation, during modal tracking was high in the case of commanding torsional movements. Several improvements are suggested which could lead to improved accuracy. First, the control inputs may be shaped to not excite residual modes. Another fix could be to include more modes in the reference controllers, although this is limited by controller bandwidth. Another technique would be to replace aerodynamic effectors with local collocated control effectors such as piezoelectric or piezoceramic materials. A computational fix could also be to use a learning algorithm for reference shaping.

3) Validation of shape tracking would be very useful. Demonstration of deformation tracking on a full aircraft FEM/CFD model with actual force-node conversions would identify gaps in the methodology. The FOS simulations presented in this work make the assumption that all deformations or strains are linear combinations of the deformation or strain shapes respectively. In practice, this is true but only for small deflections. A full simulation could find where linearity breaks down.

4) In this work, the strain mode conversion technique was not experimentally verified. This could have been completed on a simple cantilevered test article with fiber optic sensors attached. The strain predicted by the strain mode matrix could have been

compared to actual strain gauges readings. This in fact may be required before any true implementation work.

These identified problems are not the only issues. More will be found, especially as the robust modal filtering methodology makes its way into experimental flight testing on the X-56A. The following section concludes this dissertation work with the accomplishments made by the author and contributors.

9.6 Summarized Accomplishments and Credits

Several accomplishments were made in this thesis contributing to the field of aeroservoelasticity. Not all of the work was done by the author and credit must be given where it is due. Places where assistance with model development was received are noted in the following list. The rest of the work is the sole work of the author.

a) Developed linear finite element modeling software and aeroservoelastic code and verified both with GVT and wind tunnel experimental data (completed by author)

b) Developed and used methodology for integration of a modal filter into a flutter-unstable wing model aeroservoelastic control system (completed by author)

c) Developed and used methodology for integration of a modal filter into the shape control system of the body-freedom-flutter-unstable X-56A model (Methodology and computational studies by author, state space model development by Dr. Chan-gi Pak and Mr. Alexander Chin)

d) Demonstrated in simulation two new methods for aeroservoelastic shape control utilizing modal filtering (completed by author)

e) Devised a new way of gathering strain mode shapes from fiber optic sensor deformation mode shapes utilizing a moving particle frame. This resulted in easier implementation of the strain based modal filter (methodology and PATRAN work by author, assistance with PATRAN work by Mr. Alexander Chin)

f) Derived a fiber optic sensor failure model from experimental data published from work done at NASA Langley (completed by author, based on published work of others)

g) Derived a new multivariate location and dispersion type robust modal estimator, referred to as the CME, which is real time and robust to high leverage points (Trim criterion and robust starts derived by author, assistance in some theoretical understanding from emailed discussions on concentration operators with Dr. Olive)

h) Discovered a new loads monitoring technique under conditions of sensor abnormality (completed by author)

i) Discovered a new health monitoring solution utilizing robust residuals computed by our new robust estimator (completed by author)

REFERENCES

[1] M. I. Friswell and J. E. Mottershead, Finite Element Model Updating in Structural Dynamics, Dordrecht, The Netherlands: Kluwer Academic Publishers, 2010.

[2] H. Sumali, K. Meissner and H. H. Cudney, "A piezoelectric array for sensing vibration modal coordinates," *Sensors and Actuators A: Physical,* vol. 93, no. 2, pp. 123-131, 2001.

[3] J. G. Jones, "Nonlinear Aircraft Loads in Severe Atmospheric Turbulence," *Journal of Aircraft,* vol. 46, no. 5, pp. 1627-1633, Sept-Oct 2009.

[4] R. L. Clark, "Adaptive feedforward modal space control," *Journal of the Acoustical Society of America,* vol. 98, no. 5, pp. 2639-2650, 1995.

[5] W. L. Brogan, Modern Control Theory, New York: Quantum Publishers, 1974.

[6] M. Balas, "Active Control of Flexible Systems," *Journal of Optimization Theory and Applications,* vol. 25, no. 3, pp. 415-436, 1978.

[7] A. Preumont, Vibration Control of Active Structures An Introduction, 2nd ed., Dodrecht, The Netherlands: Kluwer Academic Publishers, 2002.

[8] J. R. Sesak and P. W. Likins, "Model error sensitivity suppression: Quasi-static optimal control for flexible structures," in *Decision and Control Including the Symposium on Adaptive Processes, 18th IEEE Conference*, 1979.

[9] L. Meirovitch and H. Baruh, "The Implementation of Modal Filters for Control of Structures," *Journal of Guidance,* vol. 8, no. 6, pp. 707-716, 1985.

[10] L. Meirovitch, Analytical Methods in Vibrations, New York: The Macmillan Company, 1967.

[11] R. W. Hornbeck, Numerical Methods, New York: QPI Publishers, 1975.

[12] J. H. Ahlberg, E. N. Nilson and J. L. Walsh, The Theory of Splines and Their Applications, New York: Academic Press, 1967.

[13] J. Robinson, Understanding Finite Element Stress Analysis, Robinson & Associates, 1981.

[14] J.-H. Hwang, J.-S. Kim and J.-S. Kim, "Effect of Modal Filter Errors on Vibration Control Characteristics," *KSME International Journal,* vol. 12, no. 5, pp. 836-846, 1998.

[15] Q. Zhang, R. J. Allemang and D. L. Brown, "Modal Filter: Concept and Applications," in *8th*

International Modal Analysis Conference, Orlando, Florida, 1990.

[16] S. Shelley, L. Freudinger, R. J. Allemang and Q. Zhang, "Implementation of a Modal Filter on a Five Meter Truss Structure," in *9th International Modal Analysis Conference*, Schenectady, NY, 1991.

[17] L. C. Freudinger, "Analysis of Structural Response Data Using Discrete Modal Filters," NASA Contractor Report 179448, 1991.

[18] S. J. Shelley, K. L. Lee, T. Aksel and A. E. Aktan, "Active-Control and Forced-Vibration Studies on Highway Bridge," *Journal of Structural Engineering,* vol. 121, no. 9, pp. 1306-1312, 1995.

[19] S. J. Shelley, R. J. Allemang, G. L. Slater and J. F. Schultze, "Active Vibration Control Utilizing an Adaptive Modal Filter Based Modal Control Method," in *11th International Modal Analysis Conference*, Kissimmee, Florida, 1993.

[20] G. L. Slater and S. Shelley, "Health monitoring of flexible structures using modal filter concepts," in *Proc. SPIE Vol. 1917 Smart Structures and Materials 1993: Smart Structures and Intelligent Systems*, Albuquerque NM, 1993.

[21] D. C. Kammer, "Sensor placement for on-orbit modal identification and correlation of large space structures," *Journal of Guidance, Control and Dynamics,* vol. 14, no. 2, pp. 251-259, 1991b.

[22] D. C. Kammer, "Sensor set expansion for modal vibration testing," *Mechanical Systmes and Signal Processing,* vol. 19, no. 4, pp. 700-713, 2005.

[23] L. Yao, W. A. Sethares and D. C. Kammer, "Sensor Placement for On-Orbit Modal Identification via a Genetic Algorithm," *AIAA Journal,* vol. 31, no. 10, pp. 1922-1928, 1993.

[24] A. Elka and I. Bucher, "Optimal Electrode Shaping for Precise Modal Electromechanical Filtering," in *ASME 2008 9th Biennial Conference on Engineering Systems Design and Analysis*, Haifa, Israel, 2008.

[25] A. Preumont, A. Francois, P. De Man and V. Piefort, "Spatial filters in structural control," *Journal of Sound and Vibration,* vol. 265, no. 1, pp. 61-79, 2003.

[26] S. E. Burke and J. E. Hubbard, "Active vibration control of a simply supported beam using a spatially distributed actuator," *IEEE Control Systems Magazine,* pp. 25-30, August 1987.

[27] C. K. Lee and F. C. Moon, "Modal sensors/actuators," *Journal of Applied Mechanics,* vol. 57, no. 2, pp. 434-441, 1990.

[28] N. Tanaka, S. D. Snyder and C. H. Hansen, "Distributed Parameter modal filtering using smart sensors," *Journal of Vibration and Acoustics,* vol. 118, no. 4, pp. 630-640, 1996.

[29] Q. Mao, "Theoretical development and experimental validation of modal sensors," *Acoustical Science and Technology,* vol. 25, no. 1, pp. 81-84, 2004.

[30] M. A. Trindade, C. C. Pagani Jr. and E. Massaroppi Jr., "Robustness of Modal Filters Using Piezoelectric Sensor Arrays Subject to Positioning Uncertainties," *Mecánica Computacional,* vol. XXIX, pp. 6865-6881, 2010.

[31] G. W. Housner, L. A. Bergman, T. K. Caughey, A. G. Chassiakos, R. O. Claus, S. F. Masri, R. E. Skelton, T. T. Soong, B. F. Spencer and J. T. P. Yao, "Structural Control: Past, Present, and Future," *Journal of Engineering Mechanics,* vol. 123, no. 9, pp. 897-971, 1997.

[32] A. Baz, S. Poh and J. Fedor, "Independent modal space control with positive position feedback," *Journal of dynamic systems and measurement and control,* vol. 114, no. 1, pp. 96-104, 1989.

[33] C. Q. Chen and Y. P. Shen, "Optimal control of active structures with piezoelectric modal sensors and actuators," *Smart Materials and Structures,* vol. 6, no. 4, pp. 403-409, 1997.

[34] H.-J. Lee, K.-M. Choi, J. Hyung-Jo and I.-W. Lee, "Experimental Study on Semiactive Modal Neuro-Control Scheme," in *The Nineteenth KKCNN Symposium on Civil Engineering*, Kyoto, Japan, 2006.

[35] J. I. Arnold and W. J. Wattman, "Supersonic Transport Flutter SAS Conceptual Study Results," D3-7600-9, 1969.

[36] C. E. Yates, N. S. Land and J. T. Foughner, "Measured and Calculated Subsonic and Transonic Flutter Characteristics of a 45 deg Sweptback Wing Planform in Air and in Freon-12 in the Langley Transonic Dynamics Tunnel. NASA Technical Note D-1616," March 1963.

[37] E. Nissim, "Flutter Suppression Using Active Controls Based on the Concept of Aerodynamic Energy," NASA TN D-6199, 1971.

[38] T. E. Noll and L. J. Huttsell, "Wing Store Active Flutter Suppression-Correlation of Analyses and Wind Tunnel Test Data," *Journal of Aircraft,* vol. 16, no. 7, pp. 491-497, 1979.

[39] The Boeing Co., Wichita Div., "Feasibility of an Active Flutter Control Demonstration," D3-8440, Wichita, Kansas, 1970.

[40] O. Sensburg, H. Honlinger, T. E. Noll and L. J. Huttsell, "Active Flutter Suppression on an F-

4F Aircraft," *Journal of Aircraft,* vol. 19, no. 5, 1982.

[41] E. Nissim and I. Lottati, "Active External Store Flutter Suppression in the YF-17 Flutter Model," *Journal of Guidance and Control,* vol. 2, no. 5, pp. 395-401, 1979.

[42] J. K. Makesh, C. R. Stone, W. L. Garrard and H. J. Dunn, "Control Law Synthesis for Flutter Suppression Using Linear Quadratic Gaussian Theory," *Journal of Guidance and Control,* vol. 4, no. 4, pp. 415-422, July-August 1981.

[43] C. Hwang and W. S. Pi, "Optimal Control Applied to Aircraft Flutter Suppression," *Journal of Guidance,* vol. 7, no. 3, pp. 347-354, 1984.

[44] R. E. Kalman and R. Bucy, "New results in linear filtering and prediction theory," *Journal of Basic Engineering,* vol. 83, no. 1, pp. 95-108, 1961.

[45] K. K. Gupta, M. J. Brenner and L. S. Voelker, "Development of an Integrated Aeroservoelastic Analysis Program and Correlation with Test Data," NASA Technical Paper 3120, 1991.

[46] N. Guy, "Aviation Week," 01 02 2012. [Online]. Available: http://www.aviationweek.com/aw/generic/story_generic.jsp?channel=aerospacedaily&id=news/asd/2012/02/01/02.xml. [Accessed 02 03 2012].

[47] G. Warwick, "Sense of Shape: NASA takes step toward active wing-shape control with flights of new fiber-optic sensor," *Aviation Week & Space Technology,* 28 July 2008.

[48] K. O. Hill, Y. Fujii, D. C. Johnson and B. S. Kawasaki, "Photosensitivity in optical fiber waveguides: Application to reflection filter fabrication," *Applied Physics Letters,* vol. 32, no. 10, pp. 674-676, 1978.

[49] C. W. Coates and P. Thamburaj, "Inverse Method Using Finite Strain Measurements to Determine Flight Load Distribution Functions," *Journal of Aircraft,* vol. 45, no. 2, pp. 366-370, 2008.

[50] B. G. Grossmann and L.-T. Huang, "Fiber optic sensor array for multi-dimensional strain measurement," *Smart Materials and Structures,* vol. 7, no. 2, pp. 159-165, 1998.

[51] A. Tessler and J. L. Spangler, "A least-squares variational method for full-field reconstruction of elastic deformations in shear-deformable plates and shells," *Computer Methods in Applied Mechanics and Engineering,* vol. 94, pp. 327-339, 2005.

[52] W. L. Ko and L. W. Richards, "Method for real-time structure shape-sensing". United States Patent 7520176, 21 April 2009.

[53] J.-C. Yu and C.-B. Lan, "System modeling of microaccelerometer using piezoelectric thin films," *Sensors and Actuators A,* vol. 88, no. 2, pp. 178-186, 2001.

[54] Q.-M. Wang, Z. Yang, F. Li and P. Smolinski, "Analysis of thin film piezoelectric microaccelerometer using analytical and finite element modeling," *Sensors and Actuators A,* vol. 113, no. 1, pp. 1-11, 2004.

[55] L.-P. Wang, R. A. Wolf, Jr, Y. Wang, K. K. Deng, L. Zou, R. J. Davis and S. Trolier-McKinstry, "Design, Fabrication, and Measurement of High-Sensitivity Piezoelectric Microelectromechanical Systems Accelerometers," *Journal of Microelectromechanical systems,* vol. 12, no. 4, pp. 433-439, 2003.

[56] T. E. Noll, J. M. Brown, M. E. Perez-Davis, S. D. Ishmael, G. C. Tiffany and M. Gaier, "Investigation of the Helios Prototype Aircraft Mishap Volume I Mishap Report," NASA Langley Research Center, 2004.

[57] A. Tessler, "Structural Analysis Methods for Structural Health Management of Future Aerospace Vehicles," NASA/TM-2007-214871, 2007.

[58] A. Chachich and M. De Vries, "Embedded fiber optic displacement sensor for concrete elements," in *11th Engineering Mechanical Conference, ASCE*, New York, New York, 1996.

[59] M. Mieloszyk, L. Skarbek, M. Krawczuk, W. Ostachowicz and A. Zak, "Application of fibre Bragg grating sensors for structural health monitoring of an adaptive wing," *Smart Materials and Structures,* vol. 20, no. 12, pp. 1-12, 2011.

[60] H. Guo, G. Xiao, N. Mrad and J. Yao, "Fiber Optic Sensors for Structural Health Monitoring of Air Platforms," *Sensors,* vol. 11, no. 4, pp. 3687-3705, 2011.

[61] W. L. Ko, L. W. Richards and V. T. Fleischer, "Applications of Ko Displacement Theory to the Deformed Shape Predictions of the Doubly-Tapered Ikhana Wing," NASA/TP-2009-214652, 2009b.

[62] N. S. Kim and N. S. Cho, "Estimating Deflection of a Simple Beam Model Using Fiber Optice Bragg-grating Sensors," *Engineering Mechanics,* vol. 44, no. 4, pp. 433-439, 2004.

[63] G. C. Foss and E. D. Haugse, "Using modal test results to develop strain to displacement transformations," in *Proceedings of the 13th International Conference on Modal Analysis*, Nashville, Tennessee, 1995.

[64] P. B. Bogert, E. Haugse and R. E. Gehrki, "Structural Shape Identification From Experimental Strains Using a Modal Transformation Technique," in *44th AIAA/ASME/ASCE/AHS Structures, Structural Dynamics, and Materials Conference*,

Norfolk, Virginia, 2003.

[65] S. Rapp, L.-H. Kang, U. C. Mueller, J.-H. Han and B. Horst, "Dynamic shape estimation by modal approach using fiber Bragg grating strain sensors," in *Proceedings of SPIE, Smart Materials and Structures 6529(2)*, San Diego, California, 2007.

[66] L.-H. Kang, D.-K. Kim and J.-H. Han, "Estimation of dynamic structural displacements using fiber bragg grating strain sensors," *Journal of Sound and Vibration,* vol. 305, no. 3, pp. 534-542, 2007.

[67] J. Lee, H. Jung and Y. Park, "Feedback FE model updating using strain mode shapes," in *ICCAS2002*, Jeonbuk, Korea, 2002.

[68] J. Treiber, U. C. Mueller, J.-H. Han and H. Baier, "Filtering techniques in dynamic deformation estimation using multiple strains measured by FBGs," in *Sensors and Smart Structures Technologies for Civil, Mechanical, and Aerospace Systems 6932*, San Diego, California, 2008.

[69] P. s. Lively, M. J. Atalla and N. W. Hagood, "Investigation of filtering techniques applied to the dynamic shape estimation problem," *Smart Materials and Structures,* vol. 10, no. 2, pp. 264-272, 2001.

[70] M. Nishio, T. Mizutani and N. Takeda, "Structural shape reconstruction with consideration of the reliability of distributed strain data from a Brillouin-scattering-based optical fiber sensor," *Smart Materials and Structures,* vol. 19, no. 3, pp. 35011-35024, 2010.

[71] M. Gherlone, P. Cerracchio, M. Mattone, M. D. Sciuva and A. Tessler, "Dynamic Shape Reconstruction of Three-Demensional Frame Structures Using the Inverse Finite Element Method," NASA/TP-2011-217315, 2011.

[72] P. V. Farrell, F.-P. Chiang, C. R. Mercer and G. Shen, "In-flight aeroelastic measurement technique development," in *Optical Diagnostics for Fluids, Solids, and Combustion II, Proc. SPIE 5191*, San Diego, California, 2003.

[73] S. S. Graves and A. W. Burner, "Development of an intelligent videogrammetric wind tunnel measurement system," NASA Langley Research Center, 2001.

[74] S. S. Graves, A. W. Burner, J. W. Edwards and D. M. Schuster, "Dynamic Deformation Measurements of an Aeroelastic Semispan Model," AIAA-2001-2454, 2001.

[75] J. KuttenKeuler, "Optical Measurements of Flutter Mode Shapes," *Journal of Aircraft,* vol. 37, no. 5, pp. 846-849, 2000.

[76] J. L. Hansen, J. E. Murray and N. V. Campos, "The NASA Dryden AAR Project: A Flight Test Approach to an Aerial Refueling System," in *AIAA Atmospheric Flight Mechanics Conference and Exhibit*, Providence, Rhode Island, 2004.

[77] G. C. Foss, "Photogrammetry of Aircraft Structures for Sensor Location," in *2005 IMAC-XXIII: Conference & Exposition on Structural Dynamics*, 2005.

[78] T. G. Ryall and C. S. Fraser, "Determination of Structural Modes of Vibration Using Digital Photogrammetry," *Journal of Aircraft,* vol. 39, no. 1, pp. 114-119, 2002.

[79] A. M. Lizotte and W. A. Lokos, "Deflection-Based Structural Loads Estimation From the Active Aeroelastic Wing F/A-18 Aircraft," NASA/TM-2005-212871, 2005.

[80] J. P. Moore and M. D. Rogge, "Shape sensing using multi-core fiber optic cable and parametric curve solutions," *Optics Express,* vol. 20, no. 3, pp. 2967-2973, 2012.

[81] R. F. O'Connel and A. F. Messina, "Development of an Active Flutter Margin Augmentation System for a Commercial Transport," *Journal of Guidance and Control,* vol. 3, no. 4, pp. 352-360, 1980.

[82] E. L. Burnett, C. Atkinson, J. Beranek, B. Sibbitt, B. Holm-Hansen and L. Nicolai, "NDOF Simulation Model for Flight Control Development with Flight Test Correlation," AIAA 2010-7780, 2010.

[83] S. Raja and A. R. Upadhya, "Active Control of Wing Flutter Using Piezo actuated Surface," *Journal of Aircraft,* vol. 44, no. 1, pp. 71-79, Jan-Feb. 2007.

[84] C. Surgenor, "GreenAironline.com," 13 12 2010. [Online]. Available: http://www.greenaironline.com/news.php?viewStory=1012. [Accessed 26 04 2012].

[85] J. Becker, B. Caldwell and V. Vaccaro, "The Interaction of Flight Control System and Aircraft Structure," RTO-MP-36, 2000.

[86] J. Levin, N. O. Pérez-Arancibia and P. A. Ioannou, "Adaptive Notch Filter using Real-Time Parameter Estimation," *IEEE Transactions on Control Systems Technology,* vol. 19, no. 3, pp. 673-681, 2012.

[87] J. Zeng, J. Wang, R. Callafon and M. Brenner, "Suppression of the Aeroelastic/Aeroservoelastic Interaction Using Adaptive Feedback Control Instead of Notching Filters," AIAA-2011-6459, 2011.

[88] K. König and J. Schuler, "Integral Control of Large Flexible Aircraft," RTO MP-36, 1999.

[89] W. J. Mykytow, "Recent Analysis Methods for Wing/Store Flutter," AGARD CP-162, 1962.

[90] G. Coupry, "Effect of Spanwise Variation of Gust Velocity on Airplane Response to Turbulence," *Journal of Aircraft,* vol. 9, no. 8, pp. 547-569, 1972.

[91] K. L. Roger and G. E. Hodges, "Active Flutter Suppression - A Flight Test Demonstration," *Journal of Aircraft,* vol. 12, no. 6, pp. 551-556, 1975.

[92] E. Nissim, "Recent Advances in Aerodynamic Energy Concept for Flutter Suppression and Gust Alleviation Using Active Controls," NASA TN D-8519, 1977.

[93] E. Nissim, "Design of Control Laws for Flutter Suppression based on the Aerodynamic Energy Concept and Comparisons With Other Design Methods," NASA Technical Paper 3056, 1990.

[94] I. Abel, J. R. Newsom and H. J. Dunn, "Application of Two Synthesis Methods for Active Flutter Suppression of an Aeroelastic Wind Tunnel Model," AIAA Paper 79-1633, 1979.

[95] V. Mukhopadhyay, J. R. Newsom and I. Abel, "Reduced-Order Optimal Feedback Control Law Synthesis for Flutter Suppression," *Journal of Guidance,* vol. 5, no. 4, pp. 389-395, July-August 1982.

[96] J. K. Mehesh, C. R. Stone, W. L. Garrard and H. J. Dunn, "Control Law Synthesis for Flutter Suppression Using Linear Quadratic Gaussian Theory," *Journal of Guidance and Control,* vol. 4, no. 4, pp. 415-422, 1981.

[97] W. L. Garrard and B. S. Liebst, "Active Flutter Suppression Using Eigenspace and Linear Quadratic Design Techniques," *Journal of Guidance, Control and Dynamics,* vol. 8, no. 3, pp. 304-311, 1985.

[98] J. R. Newsom, "Control Law Synthesis for Active Flutter Suppression Using Optimal Control Theory," *Journal of Guidance and Control,* vol. 2, no. 5, pp. 388-394, 1979.

[99] J. Beranek, L. Nicolai, M. Buonanno, E. Burnett, C. Atkinson, B. Hom-Hansen and P. Flick, "Conceptual Design of a Multi-utility Aeroelastic Demonstrator," AIAA 2010-9350, 2010.

[100] D. K. Schmidt and T. K. Chen, "Frequency Domain Synthesis of a Robust Flutter Suppression Control Law," in *AIAA/ASME/ASCE/AHS 26th Structures, Structural Dynamics and Materials Conference*, Orlando, Florida, 1985.

[101] R. Lind, "Flutter Margins for Multimode Unstable Couplings with Associated Flutter Confidence," *Journal of Aircraft,* vol. 46, no. 5, pp. 1563-1568, Sept-Oct 2009.

[102] M. R. Waszak, "Robust Multivariable Flutter Suppression for Benchmark Active Control Technology Wind-Tunnel Model," *Journal of Guidance, Control and Dynamics,* vol. 24, no. 1, pp. 147-153, 2001.

[103] S. Skogestad and I. Postlethwaite, Multivariable Feedback Control Analysis and Design, West Sussex, England: John Wiley & Sons, Inc, 2005.

[104] S. A. Marshall, "An approximate method for reducing the order of a linear system," *International Journal of Control,* vol. 10, pp. 642-643, 1966.

[105] C. B. Vishwakarma and R. Prasad, "Clustering methods for reducing order of linear systems using Padé Approximation," *IETE Journal of Research,* vol. 54, no. 5, pp. 326-330, 2008.

[106] S. Mukherjee, "Order reduction of linear systems using eigen spectrum analysis," *Journal of electrical engineering IE(I),* vol. 77, pp. 76-79, 1996.

[107] V. Mukhopadhyay, J. R. Newsom and I. Abel, "A Method for Obtaining Reduced-Order Control Laws for High-Order Systems Using Optimization Techniques," NASA Technical Paper 1876, 1981.

[108] G. Pamar, S. Mukherjee and R. Prasad, "Reduced order modeling of linear multivariable systems using particle swarm optimization technique," *International journal of Innovative Computing and Applications,* vol. 1, no. 2, pp. 128-137, 2007.

[109] P. Haley and D. Soloway, "Generalized Predictive Control for Active Flutter Suppression," *Journal of Guidance, Control and Dynamics,* vol. 24, no. 1, pp. 154-159, 2001.

[110] D.-H. Kim, J.-H. Han and I. Lee, "Application of Fiber Optice Sensor and Piezoelectric actuator to Flutter Suppression," *Journal of Aircraft, Engineering Notes,* vol. 41, no. 2, pp. 409-411, 2004.

[111] R. Scott and L. Pado, "Active Control of Wind-Tunnel Model Aeroelastic Response Using Neural Networks," *Journal of Guidance, Control, and Dynamics,* vol. 23, no. 6, pp. 1100-1108, 2000.

[112] S. N. Singh and M. Brenner, "Modular Adaptive Control of a Nonlinear Aeroelastic System," *Journal of Guidance, Control, and Dynamics,* vol. 26, no. 3, pp. 443-451, 2003.

[113] F. Bernelli-Zazzera, P. Mantegazza, G. Mazzoni and M. Rendina, "Active Flutter Suppression Using Recurrent Neural Networks," *Journal of Guidance, Control, and Dynamics,* vol. 23, no. 6, pp. 1030-1036, 2000.

[114] M. Mattaboni, G. Quaranta and P. Mantegazza, "Active Flutter Suppression for a Three-Surface Transport Aircraft by Recurrent Neural Networks," *Journal of Guidance, Control, and Dynamics,* vol. 32, no. 4, pp. 1295-1307, 2009.

[115] D. Li, J. Xiang and S. Guo, "Adaptive Control of a Nonlinear Aeroelastic System," *Aerospace Science and Technology,* vol. 15, no. 5, pp. 343-352, 2011.

[116] R. D. Milne, "Dynamics of the Deformable Aeroplane (Part I & II)," Queen Mary College, University of London, Reports and Memoranda No. 3345, 1962.

[117] K. L. Roger, "Airplane Math Modeling Methods for Active Control Design," AGARD-CP-228, 1977.

[118] R. C. Schwanz, "Consistency in Aircraft Structural and Flight Control Analysis," AGARD-CP-228, 1977.

[119] J. J. Cerra and T. E. Noll, "Modelling of Rigid-Body and Elastic Aircraft Dynamics for Flight Control Development," AIAA Paper Number 86-2232, 1986.

[120] D. H. Baldelli, P. C. Chen and J. Panza, "Unified Aeroelastic and Flight Dynamic Formulation via Rational Function Approximations," *Journal of Aircraft,* vol. 43, no. 3, pp. 762-772, 2006.

[121] M. R. Waszak and C. S. Buttrill, "Modeling and Model Simplification of Aeroelastic Vehicles: An Overview," NASA Technical Memorandum 107691, 1992.

[122] D. Schmidt, Modern Flight Dynamics, New York: McGraw-Hill, 2010, pp. 129-154.

[123] A. S. Pototzky, "Enhanced Modeling of First-Order Plant Equations of Motion for Aeroelastic and Aeroservoelastic Applications," in *AIAA Atmospheric Flight Mechanica Conference*, Toronto, Ontario Canada, 2010.

[124] M. Karpel and D. Raveh, "Fictitious Mass Element in Structural Dynamics," *AIAA Journal,* vol. 34, no. 3, pp. 607-613, 1996.

[125] M. J. Patil, D. H. Hodges and C. E. Cesnik, "Nonlinear Aeroelastic Analysis of Complete Aircraft in Subsonic Flow," *Journal of Aircraft,* vol. 37, no. 5, pp. 753-760, 2000.

[126] M. Karpel and B. Moulin, "Models for Aeroservoelastic Analysis with Smart Structures," *Journal of Aircraft,* vol. 41, no. 2, pp. 314-321, 2004.

[127] W. P. Rodden, P. F. Taylor and S. C. McIntosh , "Further Refinement of the Subsonic Doublet-Lattice Method," *Journal of Aircraft,* vol. 35, no. 5, pp. 720-727, 1998.

[128] S. H. Tiffany and M. Karpel, "Aeroservoelastic Modeling and Applications Using Minimum-State Approximations of the Unsteady Aerodynamics," NASA Technical Memorandum 101574, 1989.

[129] R. Vepa, "Finite State Modeling of Aeroelastic Systems," NASA CR 2770, 1977.

[130] IPCC, "Aviation and the Global Atmosphere: A Special Report of IPCC Working Groups I and III," Intergovernmental Panel on Climate Change, 1999.

[131] ICAO, "ICAO Environmental Report 2010," International Civil Aviation Organization, 2010.

[132] S. Heinze, Aeroelastic Concepts for Flexible Wing Structures, Stockholm, Sweden: PhD Thesis; Kungliga Tekniska högskolan, 2005.

[133] S. A. Ning and I. Kroo, "Multidisciplinary Considerations in the Design of Wings and Wing Tip Devices," *Journal of Aircraft,* vol. 47, no. 2, pp. 534-543, , March-April 2010.

[134] G. Gilyard, "Development of a Real-Time Transport Performance Optimization Methodology," AIAA Paper 96-0093, 1996.

[135] T. A. Weisshaar and D. K. Duke, "Induced Drag Reduction Using Aeroelastic Tailoring with Adaptive Control Surfaces," *Journal of Aircraft,* vol. 43, no. 1, pp. 157-164, Jan-Feb 2006.

[136] T. A. Weisshaar, C. Nam and A. Batista-Rodriguez, "Aeroelastic Tailoring for Improved UAV Performance," AIAA Paper 98-1757, 1998.

[137] C.-F. Lin, J. Ge, T. Yu and G. Gilyard, "Application of Neural Networks to Transport Performance Optimization," AIAA-98-4221, 1998.

[138] G. N. Vanderplaats, Numberical Optimization Techniques for Engineering Design, 4th ed., Colorado Springs, Colorado: Vanderplaats Research & Development Inc., 2005.

[139] B. Griffin, N. Brown and S. Yoo, "Intelligent Control for Drag Reduction on the X-48B Vehicle," in *AIAA GNC Conference*, Portland, Oregon, 2011.

[140] S. Kuzmina, F. Ishmuratov, V. Kuzmin and Y. Sviridenko, "Estimation of Flying Vehicle Induced Drag Changing Due to Deformation of Lifting Surfaces," in *Proceedings of the International Forum on Aeroelasticity and Structural Dynamics*, Amsterdam, 2003.

[141] W. P. Rodden, J. P. Giesing and T. P. Kalman, "New developments and applications of the subsonic doublet-lattice method for nonplanar configurations," AGARD CP-80-71, 1970.

[142] J. Simpson, J. Schweiger and S. Kuzmina, "Design of an Adaptive Wing Shape Control

Concept for Minimum Induced Drag of a Transport Aircraft," in *Proceedings of the International Forum on Aeroelasticity and Structural Dynamics*, Amsterdam, 2003.

[143] F. Austin, M. J. Rossi, W. V. Nostrand, G. Knowles and A. Jameson, "Static Shape Control for Adaptive Wings," *AIAA Journal,* vol. 32, no. 9, pp. 1895-1901, 1994.

[144] J. Heeg, "An Analytical and Experimental Investigation of Flutter Suppression Via Piezoelectric Actuation," AIAA-92-2106-CP, 1992.

[145] J.-H. Han, J. Tani and J. Qiu, "Active Flutter Suppression of a Lifting Surface Using Piezoelectric Actuation and Modern Control Theory," *Journal of Sound and Vibration,* vol. 291, no. 3-5, pp. 706-722, 2006.

[146] S. M. Ehlers and T. A. Weisshaar, "Static Aeroelastic Control of an Adaptive Lifting Surface," *Journal of Aircraft,* vol. 30, no. 4, pp. 534-540, 1993.

[147] C. Y. Chee, L. Tong and G. P. Steven, "A Review on the Modelling of Piezoelectric Sensors and Actuators Incorporated in Intelligent Structures," *Journal of Intelligent Material Systems and Structures,* vol. 9, no. 1, pp. 3-19, 1998.

[148] B. Bandyopadhyay, T. Manjunath and M. Umpathy, Modeling, Control and Implementation of Smart Structures, Berlin, Germany: Springer-Verlag, 2007.

[149] B. Berton, "Shape Memory Alloys Application: Trailing Edge Shape Control," RTO-MP-AVT-141, 2006.

[150] L. Barr, "Wing warping could change shape of future aircraft," 8 3 2005. [Online]. Available: http://www.af.mil/news/story.asp?storyid=123009980. [Accessed 9 2 2012].

[151] N. Nguyen, "Elastically Shaped Future Air Vehicle Concept," NASA Ames Research Center, Moffet Field, CA, 2010.

[152] N. Nguyen, "NASA Tech Briefs," 01 04 2010. [Online]. Available: http://www.techbriefs.com/component/content/article/7802. [Accessed 9 2 2012].

[153] J. Levine, "The DASP Toolbox," 19 11 2009. [Online]. Available: http://www.nasa.gov/centers/dryden/news/X-Press/aerovations/dasp_toolbox.html. [Accessed 17 02 2012].

[154] J. R. Chambers, "Innovation in Flight: Reserach of the NASA Langley Research Center on Revolutionary Advanced Concepts for Aeronautics," NASA SP-2005-4539, 2005.

[155] R. F. O'Connel, "Design, Development and Implementation of an Active Control System for

Load Alleviation for a Commercial Transport Airplane," in *49th Meeting of the AGARD Structures and Materials Panel*, Cologne, Germany, Oct. 1979.

[156] G. Rollwagen, H. Ellgoth and G. Beuck, "Identification of Dynamic Response, Simulation and Design of a Highly Nonlinear Digital Load Alleviation System for a Modern Transport Aircraft," in *17th Congress of the International Council of the Aeronautical Sciences*, Stockholm, Sweden, Sept. 1990.

[157] J. Chin, "Universal-type gust alleviation system for aircraft". Patent 4905934, 6th March 1990.

[158] J. P. Crimaldi, R. T. Britt and W. P. Rodden, "Response of B-2 Aircraft to Nonuniform Spanwise Turbulence," *Journal of Aircraft,* vol. 30, no. 5, pp. 652-659, 1993.

[159] J. Zeng, B. Moulin, R. d. Callafon and M. Brenner, "Adaptive Feedforward Control for Gust Load Alleviation," *Journal of Guidance, Control, and Dynamics,* vol. 33, no. 3, pp. 862-872, 2010.

[160] J. A. Woods-Vedeler, A. S. Pototzky and S. T. Hoadley, "Active Load Control During Rolling Maneuvers," NASA Technical Paper 3455, 1994.

[161] B. Moulin and M. Karpel, "Gust Loads Alleviation Using Special Control Surfaces," *Journal of Aircraft,* vol. 44, no. 1, pp. 17-25, 2007.

[162] M. Karpel, B. Moulin, L. Anguita, C. Maderuelo and H. Climent, "Aeroservoelastic Gust Response Analysis for the Design of Transport Aircrafts," AIAA Paper 2004-1592, 2004.

[163] R. Szilard, Theories and Applications of Plate Analysis, John Wiley and Sons, 2004.

[164] H. J. Conyers, E. H. Dowell and K. C. Hall, "Aeroelastic Studies of a Rectangular Wing with a Hole: Correlation of Theory and Experiment," in *NSBE - Aerospace Systems Conference*, Los Angeles, California, 2010.

[165] M. Blair, "A Compilation of the Mathematics Leading to the Leading to the Doublet Lattice Method," WL-TR-92-3028, 1992.

[166] J. P. Giesing, T. P. Kalman and W. P. Rodden, "Subsonic Unsteady Aerodynamics for General Configurations," AFFDL-TR-71-5 , 1971.

[167] W. P. Rodden, P. F. Taylor and S. C. McIntosh Jr., "Improvements to the Doublet-Lattice Method in MSC/NASTRAN," in *MSC 1999 Aerospace Users' Confidence Proceedings*, 1999.

[168] I. Abel, "An Analytical Technique for Predicting the Characteristics of a Flexible Wing

Equipped With an Active Flutter-Suppression System and Comparison with Wind-Tunnel Data," NASA Technical Paper 1367, 1979.

[169] E. Nissim and J. J. Burken, "Control Surface Spanwise Placement in Active Flutter Suppression Systems," NASA Technical Paper 2873, 1988.

[170] J. R. Wright and J. E. Cooper, Introduction to Aircraft Aeroelasticity and Loads, West Sussex, England: John Wiley & Sons, Ltd, 2007.

[171] W. M. Adams Jr., D. M. Christhilf, M. R. Waszak, V. Mukhopadhyay and S. Srinathkumar, "Design, Test, and Evaluation of Three Active Flutter Suppression Controllers," NASA Technical Memorandum 4338, 1992.

[172] M. Karpel, "Design for Active Flutter Suppression and Gust Alleviation Using State-Space Aeroelastic Modeling," *Journal of Aircraft,* vol. 19, no. 3, pp. 221-227, 1982.

[173] C.-G. Pak, "Unsteady Aerodynamic Model Tuning for Precise Flutter Prediction," NASA/TM-2011-215963, 2011.

[174] W. K. Gawronski, Advanced Structural Dynamics and Active Control of Structures, New York: Springer-Verlag, 2004.

[175] C. A. Pisoni, C. Santolini, D. E. Hauf and S. Dubowsky, "Displacements in a Vibrating Body by Strain Gauge Measurements," in *Proceedings of the 13th International Conference on Modal Analysis*, Nashville, Tennessee, 1995.

[176] D. C. Kammer, "A Hybrid Approach to Test-Analysis-Model Development for Large Space Structures," *Journal of Vibration and Acoustics,* vol. 113, no. 3, pp. 325-333, 1991a.

[177] T. Hanis and M. Hromcik, "Optimal sensors placement and spillover suppression," *Mechanical Systems and Signal Processing 28,* vol. 28, no. 4, pp. 367-378, 2012.

[178] P. Sjövall, T. Abrahamsson and T. McKelvey, "Indirect Vibration Sensing and Optimal Sensor Placement," in *2008 IMAC-XXVI: Conference & Exposition on Structural Dynamics*, Orlando, Florida, 2008.

[179] L. Richards, A. R. Parker, W. L. Ko and A. Piazza, "Real-time In-Flight Strain and Deflection Monitoring with Fiber Optic Sensors," in *Space Sensors and Measurements Techniques Workshop*, Nashville, Tennessee, 2008.

[180] R. I. Kroll and R. E. Clemmons, "A Computer Program to Generate Equations of Motion Matrices, L217 (EOM) Volume I: Engineering and Usage," NASA Contractor Report 2851, 1979.

[181] K.-C. Chuang, H.-T. Liao and C.-C. Ma, "Dynamic Sensing Performance of a Point-Wise Fiber Bragg Grating Displacement Measurement System Integrated in an Active Structural Control System," *Sensors,* vol. 11, no. 12, pp. 11605-11628, 2011.

[182] Y.-R. Hu and G. Vukovich, "Active robust shape control of flexible structures," *Mechatronics,* vol. 15, no. 7, pp. 807-820, 2005.

[183] S. G. Tzafestas, Applied Control Current Trends and Modern Methodologies, New York: Marcel Dekker, Inc., 1993.

[184] E. Albano and W. P. Rodden, "A Doublet-Lattice Method for Calculating Lift Distributions on Oscillating Surfaces in Subsonic Flows," *AIAA Journal,* vol. 7, no. 2, pp. 279-285, 1969.

[185] W. P. Rodden, P. F. Taylor and S. C. J. McIntosh, "Further Refinement of the Nonlinear Aspects of the Subsonic Doublet-Lattice Lifting Surface Method," *Journal of Aircraft,* vol. 35, no. 5, pp. 720-727, 1998.

[186] F. A. Woodward, "Analysis and Design of Wing-Body Combinations at Subsonic and Supersonic Speeds," *Journal of Aircraft,* vol. 5, no. 6, pp. 528-534, 1968.

[187] P. C. Chen, H. W. Lee and D. D. Liu, "Unsteady Subsonic Aerodynamics for Bodies and Wings with External Stores Including Wake Effect," *Journal of Aircraft,* vol. 30, no. 5, pp. 618-628, 1993.

[188] D. D. Liu, P. C. Chen and Z. X. Yao, "Recent Advances in Lifting Surface Methods," *Royal Aeronautical Journal,* vol. 100, no. 998, pp. 327-339, 1998.

[189] M. S. Wu, F. P. Garcia and D. D. Liu, "Potential Flow Over Bodies of Revolution in Unsteady Motion," *AIAA Journal,* vol. 27, no. 6, pp. 725-733, 1989.

[190] ZONA Technology Inc, ZAERO Theoretical Manual. Version 8.5, Scottsdale, Arizona, 2011.

[191] R. Levy and W. R. Spillers, Analysis of Geometrically Nonlinear Structures, 2nd ed., Netherlands: Kluwer Academic Publishers, 2003.

[192] L. Nicolai, K. Hunten, S. Zink and P. Flick, "System Benefits of Active Flutter Suppression for a SensorCraft-Type Vehicle," AIAA-2010-9349, 2010.

[193] NASA, The NASTRAN Theoretical Manual, Level 17.5, NASA SP-221(05), 1978.

[194] Y. Matsumura, "Spatial Filter Design for Observation Spillover Suppression," in *2005 IMAC-XXIII: Conference & Exposition on Structural Dynamics*, Orlando, Florida, 2005.

[195] P. J. Huber, "Robust Estimation of a Location Parameter," *The Annals of Mathematical Statistics,* vol. 35, no. 1, pp. 73-101, 1964.

[196] P. J. Rousseeuw and A. M. Leroy, Robust Regression and Outlier Detection, New York, New York: John Wiley and Sons, 1987.

[197] S. Hekimoglu and R. C. Erenoglu, "New Method for Outlier Diagnostics in Linear Regression," *Journal of Surveying Engineering,* vol. 135, no. 3, pp. 85-89, 2009.

[198] U. Gather, K. Schettlinger and R. Fried, "Online signal extraction by robust linear regression," *Computational Statistics,* vol. 21, no. 1, pp. 33-51, 2006.

[199] P. J. Rousseeuw, "Least median of squares regression," *Journal of the American Statistical Association,* vol. 79, no. 388, pp. 871-880, 1984.

[200] A. J. Stromberg, "Computing the exact least median of squares estimate and stability diagnostics in multiple linear regression," *SIAM Journal on Scientific Computing,* vol. 14, no. 6, pp. 1289-1299, 1993.

[201] O. Hössjer, C. Croux and P. Rousseeuw, "Asymptotics of generalized S-estimators," *Journal of Multivariate Analysis,* vol. 51, no. 1, pp. 148-177, 1994.

[202] A. Preminger and S. Sakata, "A model selection method for S-estimation," *Econometrics Journal,* vol. 10, no. 2, pp. 294-319, 2007.

[203] V. J. Yohai and R. H. Zamar, "High breakdown-point estimates of regression by means of the minimization of an efficient scale," *Journal of the American Statistical Association,* vol. 83, no. 402, pp. 406-413, 1988.

[204] F. R. Hampel, "Beyond location parameters: robust concepts and methods," *Bulletin of the International Statistical Institute,* vol. 46, no. 1, pp. 375-391, 1975.

[205] D. J. Olive, Applied Robust Statistics, unpublished manuscript available at (http://lagrange.math.siu.edu/Olive/preprints.htm)., 2008.

[206] D. M. Hawkins and D. Olive, "Applications and Algorithms for Least Trimmed Sum of Absolute Deviations Regression," *Computational Statistics & Data Analysis,* vol. 32, no. 2, pp. 119-134, 1999.

[207] P. J. Huber, Robust Statistics, New York, New York: John Wiley and Sons, 1981.

[208] D. A. Jackson and Y. Chen, "Robust principal component analysis and outlier detection with ecological data," *Environmetrics,* vol. 15, no. 2, pp. 129-139, 2004.

[209] S. Hekimoglu, R. C. Erenoglu and J. Kalina, "Outlier detection by means of robust regression estimators for use in engineering science," *Journal of Zhejiiang University Science A,* vol. 10, no. 6, pp. 909-921, 2009.

[210] F. R. Hampel, Contributions to the Theory of Robust Estimation, Berkeley, California: PhD Thesis; University of California, 1968.

[211] F. R. Hampel, "A general qualitative definition of robustness," *The Annals of Methematical Statistics,* vol. 42, no. 6, pp. 1887-1896, 1971.

[212] D. L. Donoho, Breakdown properties of multivariate location estimators, Harvard, Boston: PhD Thesis; Harvard University, 1982.

[213] A. F. Siegel, "Robust regression using repeated medians," *Biometrika,* vol. 69, no. 1, pp. 242-244, 1982.

[214] P. J. Rousseeuw, S. Van Aelst and K. Van Driessen, "Robust Multivariate Regression," *Technometrics,* vol. 46, no. 3, pp. 293-305, 2000.

[215] T. Bernholt, R. Nunkesser and K. Schettlinger, "Computing the least quartile difference estimator in the plane," *Computational Statistics & Data Analysis,* vol. 52, no. 2, pp. 763-772, 2007.

[216] H. Theil, "A rank-invariant method of linear and polynomial regression analysis," *Nederlandse Akademie Wetenchappen Series A,* vol. 53, pp. 386-392, 1950.

[217] P. J. Rousseeuw and M. Hubert, "Regression Depth," *Journal of the American Statistical Association,* vol. 94, no. 446, pp. 388-402, 1999.

[218] J. T. Kent and D. E. Tyler, "Constrained M-estimation for multivariate location and scatter," *Annals of Statistics,* vol. 24, no. 3, pp. 1346-1370, 1996.

[219] G. Beliakov, A. Kelarev and J. Yearwood, "Robust artificial neural networks and outlier detection. Technical report," Cornell University, 2011.

[220] D. Gervini and V. Yohai, "A class of robust and fully efficient regression estimators," *The Annals of Statistics,* vol. 30, no. 2, pp. 583-616, 2002.

[221] A. S. Hadi and J. S. Simonoff, "Procedures for the identification of multiple outliers in linear models," *Journal of the American Statistical Association,* vol. 88, no. 424, pp. 1264-1272, 1993.

[222] S. Hekimoglu, "Do robust methods identify outliers more reliably than conventional tests

for outliers?," *Zeitschrift für Vermessungwesen,* vol. 130, no. 3, pp. 174-180, 2005.

[223] T. Bernholt, "Robust Estimators are Hard to Compute," Technische Universität Dortmund, Sonderforschungsbereich 475: Komplexitätsreduktion in multivariaten Datenstrukturen., 2006.

[224] Y. Zuo and R. Serfling, "General Notions of Statistical Depth Function," *The Annals of Statistics,* vol. 28, no. 2, pp. 461-482, 2000.

[225] Y. Zuo, H. Cui and X. He, "On the Stahel-Donoho Estimator and Depth-Weighted Means of Multivariate Data," *The Annals of Statistics,* vol. 32, no. 1, pp. 167-188, 2004.

[226] X. He and G. Wang, "Cross-Checking Using the Minimum Volume Ellipsoid Estimator," *Statistica Sinica,* vol. 6, no. 2, pp. 367-374, 1996.

[227] V. J. Yohai, "High breakdown-point and high efficiency robust estimates for regression," *The Annals of Statistics,* vol. 15, no. 2, pp. 642-656, 1987.

[228] D. G. Simpson and V. J. Yohai, "Functional Stability of One-Step GM-Estimators In Approximately Linear Regression," *The Annals of Statistics,* vol. 26, no. 3, pp. 1147-1169, 1998.

[229] J. D. Naranjo and T. P. Hettmansperger, "Bounded-Influence Rank Regression," *Journal of the Royal Statistical Society Series B,* vol. 56, no. 1, pp. 209-220, 1994.

[230] X. He, D. G. Simpson and G. Wang, "Breakdown points of t-type regression estimators," *Biometrika,* vol. 87, no. 3, pp. 675-687, 2000.

[231] R. Maronna, D. R. Martin and V. Yohai, Robust Statistics - Theory and Methods, Hoboken, New Jersey: John Wiley & Sons, Ltd, 2006.

[232] P. J. Rousseeuw and K. Van Driessen, "A Fast Algorithm for the Minimum Covariance Determinant Estimator," *Technometrics,* vol. 41, no. 3, pp. 212-223, 1999.

[233] D. J. Olive, "A Resistant Estimator of Multivariate Location and Dispersion," *Computational Statistics and Data Analysis,* vol. 46, no. 1, pp. 93-102, 2004.

[234] D. J. Olive and D. M. Hawkins, Robust Multivariate Location and Dispersion, unpublished manuscript available at (http://lagrange.math.siu.edu/Olive/preprints.htm)., 2010.

[235] R. A. Maronna and R. H. Zamar, "Robust Estimates of Location and Dispersion for High-Dimensional Datasets," *Technometrics,* vol. 44, no. 4, pp. 295-304, 2002.

[236] J. Zhang, Applications of a Robust Dispersion Estimator. PhD Thesis, Southern Illinois University Carbondale, 2011.

[237] P. J. Huber and E. M. Ronchetti, Robust Statistics, 2nd ed., Hoboken, NJ: Wiley, 2009.

[238] P. C. Mahalanobis, "On the generalised distance in statistics," *Proceedings of the National Institute of Sciences of India,* vol. 2, no. 1, pp. 49-55, 1936.

[239] P. J. Rousseeuw and B. C. Van Zomeren, "Unmasking multivariate outliers and leverage points," *Journal of the American Statistical Association,* vol. 85, no. 411, pp. 633-651, 1990.

[240] K. V. Mardia, "Measures of multivariate skewness and kurtosis with applications," *Biometrika,* vol. 57, no. 3, pp. 519-530, 1970.

[241] R. A. Maronna, "Robust M-Estimators of Multivariate Location and Scatter," *The Annals of Statistics,* vol. 4, no. 1, pp. 51-57, 1976.

[242] R. Gnanadesikan and J. R. Kettenring, "Robust Estimates, Residuals, and Outlier Detection With Multiresponse Data," *Biometrics,* vol. 28, no. 1, pp. 81-124, 1972.

[243] S. J. Devlin, R. Gnandesikan and J. R. Kettenring, "Robust Estimation of Dispersion Matrices and Principal Components," *Journal of the American Statistical Association,* vol. 76, no. 374, pp. 354-362, 1981.

[244] D. C. Hoaglin, F. Mosteller and J. W. Tukey, Understanding Robust and Exploratory Data Analysis, New York: John Wiley and Sons, 1983.

[245] F. Mosteller and J. W. Tukey, Data Analysis and Regression, Philippines: Addison-Wesley Publishing Company Inc., 1977.

[246] F. R. Hampel, E. M. Ronchetti, P. J. Rousseeuw and W. A. Stahel, Robust Statistics: The Approach Based on Influence Functions, New York, New York: John Wiley & Sons, 1986.

[247] G. Shevlyakov, S. Morgenthaler and A. Shurygin, "Redescending M-estimators," *Journal of Statistical Planning and Inference,* vol. 138, no. 10, pp. 2906-2917, 2008.

[248] J. Fox, An R and S-plus Companion to Applied Regression, Thousand Oaks, California: Sage publications, Inc., 2002.

[249] P. J. Rousseeuw and C. Croux, "Alternative to the Median Absolute Deviation," *Journal of the American Statistical Association,* vol. 88, no. 424, pp. 1273-1283, 1993.

[250] D. P. Wiens and Z. Zheng, "Robust M-estimators of multivariate location and scatter in the presence of asymmetry," *The Canadian Journal of Statistics,* vol. 14, no. 2, pp. 161-176, 1986.

[251] R. A. Maronna and V. J. Yohai, "The Behavior of the Stahel-Donoho Robust Multivariate Estimator," *Journal of the American Statistical Association,* vol. 90, no. 429, pp. 330-341, 1995.

[252] W. A. Stahel, Robust estimation: Infinitesimal optimality and covariance matrix estimators, Zürich, Switzerland: PhD Thesis; Eidgenössische Technische Hochschule Zürich, 1981.

[253] P. Filzmoser, R. Maronna and M. Werner, "Outlier identification in high dimensions," *Computational Statistics & Data Analysis,* vol. 52, no. 3, pp. 1694-1711, 2008.

[254] R. G. Garrett, "The chi-square plot: a tool for multivariate outlier recognition," *Journal of Geochemical Exploration,* vol. 32, no. 1-3, pp. 319-341, 1989.

[255] B. Childers, M. E. Froggatt, S. G. Allison, T. C. Moore, D. A. Hare, C. F. Batten and D. C. Jegley, "Use of 3000 Bragg grating strain sensors distributed on four eight-meter optical fibers during static load tests of a composite structure," in *SPIE Smart Structures and Materials 2001*, San Diego, California, 2001.